Numerical Analysis of Propeller-Induced Higher-Order Pressure Fluctuations on the Ship Hull

Vom Promotionsausschuss der
Technischen Universität Hamburg-Harburg
zur Erlangung des akademischen Grades

Doktor-Ingenieur (Dr.-Ing.)

genehmigte Dissertation

von
Stephan Berger

aus
Dortmund

2018

Vorsitzender des Prüfungsausschusses
Prof. Dr.-Ing. Otto von Estorff

Gutachter
1. Gutachter: Prof. Dr.-Ing. Moustafa Abdel-Maksoud
2. Gutachter: Prof. Dr.-Ing. Stefan Krüger

Tag der mündlichen Prüfung
12. Dezember 2017

Am Schwarzenberg-Campus 4(C)
D-21073 Hamburg
www.tuhh.de/vss

Bericht Nr. 705
ISBN 978-3-89220-705-4

Acknowledgements

This thesis is the result of five years of participation in the KonKav II and NoiseLES projects sponsored by the Federal Ministry for Economic Affairs and Energy, whose financial support is highly appreciated. However, the person who made this all possible is my supervisor, Prof. Moustafa Abdel-Maksoud. I would like to express my gratitude for his advice and valuable suggestions and providing freedom as well as support during all stages of this research. Furthermore, I would like to thank Prof. Stefan Krüger for reviewing this thesis and Prof. Otto von Estorff for chairing the examination board.

In addition, I would like to thank the following persons and institutions for their valuable help and support: The members and former members of the *pan*MARE group at the Institute for Fluid Dynamics and Ship Theory at Hamburg University of Technology, especially Ulf Göttsche, Martin Greve, Markus Pergande and Martin Scharf; Roland Gosda for the great support in the development of the code VoCav2D and for carrying out extensive numerical studies; Christoph Wagner and Keqi Wang for generating the numerical meshes for the viscous flow simulations; Dr. Ernst-August Weitendorf for discussions, advice as well as helpful information and material regarding full-scale observations for the container vessel *Sydney Express*; the ship model basin SVA Potsdam, Germany, for extensive experimental data, photographs and videos, all of which helped me to better understand propeller cavitation processes; Dr. Stephan Helma and Yasaman Mirsadraee for discussions on propeller cavitation and tip vortices; Mecklenburger Metallguss (MMG), Waren/Müritz, Germany, for advice and for making available propeller designs and experimental data, which helped to improve the developed methods; the Institute for Optoelectronics and Photonic Systems at Rostock University, Flensburger Schiffbau-Gesellschaft and the ship model basin HSVA Hamburg, Germany, for various full-scale measurement data of the ConRo vessel *Amandine* as well as underwater photographs of the vessel's propeller. Many thanks to Jolene Mathieson, University of Hamburg, who helped me to navigate the shoals of the English language.

Because of my wonderful colleagues, the atmosphere at the Institute was always warm and friendly. I had great office mates – three in number: Nikolai Köllisch, Maria Gaschler and Hendrik Simonis. But there were also superb people to converse with in the neighbouring offices: Markus Druckenbrod, Dag Feder, Patrick Schiller and Sven Wassermann. All of them contributed directly and indirectly to the success of this research.

Doing research work can be stressful and demanding sometimes. It is good to know that my family, my friends and my girlfriend have always been there for me.

Abstract

This thesis documents and explains the development and validation of a hybrid simulation method for investigating higher-order hull pressure fluctuations induced by cavitating propellers. Two forms of propeller cavitation are considered in this work: coherent structures of sheet cavitation on the propeller blades and tip vortex cavitation. The interaction between sheet cavitation and developed tip vortex cavitation can be responsible for notable higher-order pressure fluctuations.

The essential element of this novel simulation method is *pan*MARE, the in-house panel code used to calculate the propeller flow including effects of sheet cavitation. Furthermore, relevant parts of the hull surface above the propeller are incorporated in the panel model in order to evaluate fluctuations of pressure in the aft ship region. The propeller operates in the effective wake field of the ship which results from the viscous interaction between hull and propeller flow. It is calculated by the RANSE solver ANSYS CFX in combination with *pan*MARE. A body force coupling approach is used to couple both methods. Herein, the viscous hull flow is determined by ANSYS CFX and the impact of the propeller is approximated by a corresponding distribution of body forces applied to the viscous flow which in return is calculated by means of *pan*MARE.

In order to model tip vortex cavitation, the vortex cavity is divided into a large number of cylindrical segments, where each of them are treated separately. This breaks down the formerly three-dimensional problem into a two-dimensional one, which is much easier to handle. For each segment, the momentum equations in cylindrical coordinates, leading to a Rayleigh-Plesset-like equation for the dynamical behaviour of the cavitating core, are solved by means of the newly developed code VoCav2D. Interaction with sheet cavitation is taken into account by correlating the initial cavitation radius with the cavity thickness at the trailing edge of the blade in the tip region. This and other tip vortex parameters are extracted from detailed RANS simulations of the blade tip flow made in advance for a number of representative loading conditions.

For validation purposes, three vessels are investigated. The numerical results are compared to those obtained from experiments and – if available – from full-scale measurements. Furthermore, two types of scale effects due to the Reynolds number are investigated by the method: the wake scale effect on sheet cavitation and the influence of the viscous core radius on moderate and tip vortex cavitation in the stage of formation in an idealised manner.

(Deutsch) Gegenstand der vorliegenden Arbeit ist die Entwicklung und Validierung einer hybriden Simulationsmethode zur Untersuchung propellerinduzierter Druckschwankungen höherer Ordnung in kavitierender Strömung. Es werden zwei Arten von Propellerkavitation berücksichtigt: Schichtkavitation auf den Flügeln des Propellers und Spitzenwirbelkavitation. Dabei stellt sich heraus, dass insbesondere die Interaktion zwischen Schicht- und Spitzenwirbelkavitation zu stärkeren Druckschwankungen höherer Ordnung führen kann.

Herzstück der neu entwickelten Methode ist das Paneelverfahren *pan*MARE, welches zur Bestimmung der Propellerumströmung und von Schichtkavitation eingesetzt wird. Darüber hinaus sind auch Teile des Rumpfes oberhalb des Propellers im Paneelmodell enthalten, wodurch es möglich wird, dort die propellerinduzierten Druckschwankungen auszuwerten. Der Propeller arbeitet im effektiven Nachstromfeld des Schiffes, welches aus der mit viskosen Effekten behafteten Wechselwirkung zwischen Propeller und Rumpf resultiert. Um dieses zu bestimmen, wird der RANSE-Löser ANSYS CFX in Kombination mit *pan*MARE eingesetzt. Beide Verfahren werden mithilfe eines sog. body force-Ansatzes gekoppelt. Die Rumpfumströmung wird dabei durch ANSYS CFX bestimmt und die Wirkung des Propellers durch eine äquivalente und durch *pan*MARE bestimmte Verteilung von Kräften angenähert, die in die viskose Rumpfumströmung eingebracht wird.

Um Spitzenwirbelkavitation zu simulieren, wird der kavitierende Wirbelkern in zahlreiche Segmente unterteilt, die jeweils separat betrachtet werden. Auf diese Weise wird aus dem dreidimensionalen Problem ein zweidimensionales, wodurch sich der Aufwand drastisch reduziert. Für jedes Segment werden die Impulsgleichungen in zylindrischen Koordinaten gelöst, was zu einer Gleichung ähnlich der Rayleigh-Plesset-Gleichung führt. Für die Lösung dieser zweidimensionalen Strömung eines kavitierenden Segments wird das Verfahren VoCav2D eingesetzt. Um die Interaktion mit Schichtkavitation zu berücksichtigen, erfolgt die Initialisierung des Kavitationsradius entsprechend der Dicke der Kavitation an der Austrittskante des Propellers im Bereich der Blattspitze. Dieser Parameter wird zusammen mit weiteren Parametern mithilfe fein aufgelöster RANS-Simulationen der Blattspitzenumströmung ermittelt.

Drei Schiffe dienen der Validierung und Erprobung der Methode. Die Simulationsergebnisse werden mit experimentellen Ergebnissen und – sofern vorhanden – mit Großausführungsmessdaten verglichen. Darüber hinaus werden zwei Arten von Maßstabseffekten bezüglich der Reynoldszahl behandelt: der Einfluss des Nachstromfelds auf das Verhalten von Schichtkavitation sowie der Einfluss des viskosen Kernradius auf moderate bzw. sich entwickelnde Spitzenwirbelkavitation.

Table of Contents

List of Figures

List of Tables

List of Symbols

In the following, only the most important symbols and conventions are listed. Symbols of an auxiliary character that are used only in single chapters or subchapters are not listed. For the sake of convenience, first and second time derivatives of a variable $\bullet$ can be denoted by $\dot{\bullet}$ and $\ddot{\bullet}$.

General variables	
$\mathbf{x} = (x, y, z)$	Space variable in global Cartesian coordinates
$\mathbf{X} = (X, Y, Z)$	$\sim$ in propeller-fixed Cartesian coordinates
t	Time variable

Constants	
g	Gravity constant
ρ	Density of water
μ	Dynamic viscosity of water
ν	Kinematic viscosity of water
p_v	Vapour pressure of water
n	Polytropic index

Potential flow domain Ω	
$S = \partial\Omega$	Boundary of Ω
$\mathbf{V}$, $\mathbf{U}$	Total velocity
$\mathbf{V}_\infty$	Inhomogenous inflow
$\mathbf{V}_0$	Undisturbed flow
$\mathbf{V}^+$	Induced velocity
Φ	Velocity potential in general
Φ_P, Φ_H	Velocity potential induced by the propeller and the hull
p	Pressure
μ, σ	Dipole strength, source strength

$\mathbf{X}_0$	Collocation point
$\mathbf{n}$	Normal vector of a surface element
η	Cavity thickness
$\mathbf{s} = (s_1, s_2, s_3)$	Local, non-orthogonal panel coordinate system with unit vectors $\mathbf{t}_i$, $\mathbf{t}_1$ aligned with mean flow

RANS simulation, viscous flow domain Λ

$\mathbf{u}$	Reynolds-averaged velocity
p	Reynolds-averaged pressure
τ	Reynolds-averaged stress tensor
τ_T	Reynolds stress tensor
$\mathbf{f}$	Momentum source term
$\dot{S}$	Production term
α_l	Volume fraction
$\rho^\star$	Mixture density

Flow of a vortex segment

(ξ, φ, ψ)	Local cylindrical coordinate system; ξ radial direction, φ circumferential $\sim$ and ψ axial $\sim$
u_φ, u_ξ	Local velocity in the circumferential and radial direction
Γ	Circulation in general
p_c	Pressure inside the cylindrical cavity
p_b	Pressure inside a cavitation bubble
p_D	Pressure imposed at $\xi = r_D$
r_c	Cavitation radius, i.e. radius of the cavitating vortex core
r_b	Radius of a cavitation bubble
r_B	Radius of the bubble release zone
r_D	Domain radius for vortex flow
r_a	Radius of the viscous core
T_c	Oscillation period of the cavitation radius
$\zeta = \frac{\partial^2 (r_c^2)}{\partial t^2}$	Quantity proportional to the radiated pressure of a pulsating cylindrical cavity

TVC modelling

s	Coordinate of the vortex axis starting from TE
$\Gamma^\star$	Circulation of a vortex segment

$\mathbf{x}^{\star}$	Position of a vortex segment in global coordinates
$t^{\star}$	Age of a vortex segment
$\sigma^{\star}$	Source strength of a vortex segment due to cavity volume variation
$\rho^{\star}$	Reduced density of the vortical flow surrounding a vortex segment
Φ_{TV}	Disturbance potential of the cavitating tip vortex
B_f	Solid boundary factor

Propeller and ship hull flow

$R, D = 2R$	Propeller radius, $\sim$ diameter
c, c_0	Chord length, reference $\sim$
(r, φ)	Coordinate system of the propeller plane
$\bullet_s$, $\bullet_m$	Related to the full-scale ship, $\sim$ to the model
n_b	Number of blades
n	Number of revolutions
$f_b = nn_b$	Blade frequency
V_S, V_s, V_m	Ship speed in general, $\sim$ of the full-scale ship, $\sim$ of the model
$\mathrm{Fn} = \frac{\mathscr{V}}{\sqrt{g\mathscr{L}}}$	Froude number
$\mathrm{Re} = \frac{\mathscr{V}\mathscr{L}}{\nu}$	Reynolds number
$J = \frac{V}{nD}$	Advance coefficient with propeller inflow velocity V
T, Q	Mean propeller thrust and propeller torque
$k_T = \frac{T}{\rho n^2 D^4}$ and $k_{T,\mathrm{blade}} = \frac{T_{\mathrm{blade}}}{\rho n^2 D^4}$	Thrust coefficient, $\sim$ of a single blade
$k_Q = \frac{Q}{\rho n^2 D^5}$	Torque coefficient
$\sigma_n = \frac{p_{\mathrm{ref}} + \rho g h - p_v}{1/2 \rho n^2 D^2}$ and $\sigma_{n0.8} = \frac{p_{\mathrm{ref}} + \rho g (h - 0.8R) - p_v}{1/2 \rho n^2 D^2}$	Cavitation numbers with h distance between propeller shaft and water surface
p_{ref}	Reference pressure
Γ_b	Maximum of bound blade circulation
$\Gamma_{\mathrm{ini}} = \gamma_{\mathrm{ini}} \Gamma_b$	Initial circulation of the tip vortex, directly behind TE
η_{TE}	Sheet cavitation thickness at the trailing edge near the blade tip

Auxiliary quantities	
q	Harmonic order of a fluctuation, $q = 1$: quantity fluctuates with blade frequency f_b
$\mathscr{L}$, $\mathscr{T}$, $\mathscr{V}$	Characteristic length, time and velocity (dependent on context)
$\bullet_{\mathrm{SC}}$, $\bullet_{\mathrm{TV}}$	Related to sheet cavitation, $\sim$ to tip vortex cavitation
$\bullet_{\mathrm{vs}}$, $\bullet_{\mathrm{v}}$	Related to a tip vortex segment, $\sim$ to the tip vortex
$\bullet_{\mathrm{TE}}$	Related to the trailing edge
$\bullet'$	Disturbance, e.g. p'
$\hat{\bullet}$	Amplitude of a fluctuation
$\hat{\bullet}^{[q]}$	Amplitude of the q-th harmonic component of a fluctuation
$k_\bullet$	Dimensionless representation of a quantity; sometimes $\varepsilon_\bullet$ is used
$\overline{\bullet}$	Averaged value
$\bullet_\infty$	Final state value
$\bullet_0$	Initial value
$\bullet_{\mathrm{eq}}$	Equilibrium state
$\bullet_{\mathrm{c}}$, $\bullet_{\mathrm{nc}}$	Related to cavitating, non-cavitating flow
$\bullet_u$, $\bullet_l$	Upper, lower side

Abbreviations	
HSVA	Hamburg Ship Model Basin
SVA	Potsdam Ship Model Basin
RANS	Reynolds-averaged Navier-Stokes
RANSE	Reynolds-averaged Navier-Stokes Equations
LES	Large Eddy Simulation
DES	Detached Eddy Simulation
KRISO	Korea Research Institute of Ships and Ocean Engineering
PIV	Particle Image Velocimetry
MARIN	Maritime Research Institute Netherlands
SST	Shear Stress Transport Model
TE	Trailing edge
TVC	Tip vortex cavitation
SC	Sheet cavitation

Chapter 1

Introduction

1.1 Motivation and Aim

For conventional propellers, cavitation is known as the source of numerous problems, such as noise emission, vibratory excitation of the shell plating in the aft ship region as well as erosion of propeller blades and manoeuvring devices. Thus, minimising propeller cavitation is highly desirable. However, measures aiming to reduce cavitation often lead to losses of propulsive efficiency (Patience, 1991). As a consequence, a major aim of the propeller design process is finding a satisfactory compromise between these two conflicting demands.

This compromise may look different depending on the particular type of ship for which the propeller is designed: for a container vessel bridging long distances at constant speed, low fuel costs are crucial and cavitation control is needed (only) to comply with contractual specifications regulating the maximum permissible hull vibration levels. However, anthropogenic underwater noise is a growing concern (Williams et al., 2015) and hitherto non-mandatory IMO[1] guidelines (IMO, 2014) in this respect foreshadow upcoming legal regulations for its reduction. Hence, cavitation control will gain additional importance even for cargo ships. On the other hand, for ships carrying passengers, a high comfort level is the most important factor (there may be additional nuances between a yacht and a ferry) while a certain level of propulsion efficiency has to be maintained.

Finding an ideal compromise during the design stage of ship and propeller warrants the need for efficient numerical tools that are able to predict the cavitation behaviour of a propeller. The present thesis is devoted to the development of such tools; however, the intention is not to primarily focus on the cavitation behaviour itself. Rather, pressure fluctuations induced on the hull surface by the cavitating propeller are of interest.

Nowadays, a variety of numerical methods exists for the investigation and prediction of propeller cavitation and the resultant propeller-induced pressure fluctuations. However, most of them have shortcomings:

---

[1] *IMO* is an abbreviation for *International Maritime Organization*.

(1) The prediction of first-order pressure fluctuations, i.e. fluctuations occurring with blade frequency, is possible with a sufficient degree of accuracy by most of the day-to-day simulation methods (for example, boundary element methods, vortex lattice methods, RANS methods or combinations). Apart from the finite thickness of the blades and the varying blade lift, these fluctuations are mainly related to the periodic growth and shrinkage of large and coherent sheet cavitation structures on the propeller blades – a feature which can be accounted for in these numerical simulations. When higher-order pressure fluctuations are considered (which are of equal technical relevance), there are still some discrepancies between simulation and experimental results. The reason is apparently due to the insufficient treatment of the cavitating tip vortex (van Wijngaarden, 2011, p. 118).

(2) Theoretically, it is possible to capture propeller cavitation, including the cavitating tip vortex, in a sufficiently detailed manner and the resulting pressure fluctuations of arbitrary order by a sophisticated uniform approach (for example, LES or DES methods). The numerical and modelling effort for such simulations is prohibitively large – even for simple cases – and the applicability to day-to-day industrial problems is very limited.

The aim of the present thesis is to close the gap between these two extremes. For this purpose, a day-to-day tool for simulations and investigations is developed which is able to account for tip vortex cavitation and hence better estimate higher-order hull pressure fluctuations.

1.2 Scope of the Work

Propeller cavitation and the resultant pressure fluctuations are a very complex problem and some basic assumptions and simplifications have to be met in order to construct a computational method of investigation. The most fundamental are:

(1) Only two important types of cavitation are considered – coherent sheet cavitation and tip vortex cavitation. Consequently, propellers featuring complicated and irregular cavitation patterns such as bubble and cloud cavitation during operation cannot be considered by the present method.

(2) Ship speed and number of propeller revolutions are assumed to be constant and thus propeller-induced pressure fluctuations to be periodic with blade frequency f_b, which is defined as the number of blades n_b times the number of revolutions n, hence $f_b = nn_b$. The simulation method may be adequate for analysing the propeller with respect to design operation conditions, but the simulation of propeller cavitation during extreme manoeuvres inhered with unsteadiness of ship speed and number of revolutions is beyond the scope of the thesis.

(3) Even though it is well known that the rudder can play a significant role, its influence is not considered in the present implementation of the method.

Some attention should be directed to the question of what exactly is meant by *higher-order* pressure fluctuations. Assuming constant inflow to the propeller, a constant number of revolutions and disregarding the actual physical mechanisms behind it, the pressure signal induced by the propeller at any location on the hull surface can be decomposed in a number of harmonics with frequencies qf_b. Fluctuations occurring with blade frequency $q = 1$ are referred to as first-order fluctuations. Those occurring with multiples (i.e. more than or two-times, $q = 2, 3, \dots$) of blade frequency are called higher-order fluctuations. Thus, $q = 2$ constitutes the lower frequency range limit of higher-order fluctuations, but there is also an upper limit. Pressure disturbances of a certain frequency f are propagated in the form of waves of the length $\lambda = cf^{-1}$ (e.g. Lüders and von Oppen, 2008, p. 480), where c is the speed of sound in the respective medium – water in the present case. This wave-like behaviour is due to the compressibility of the medium and generally gets important when λ is of the same order or smaller than characteristic length scales $\mathscr{L}$ of the considered problem (Söding, 1987). In the present work, however, the compressibility of water is neglected and this apparently imposes an upper theoretical limit of the ascertainable frequency range. Since pressure fluctuations on the hull are considered, a characteristic length scale of the problem may be the propeller radius R, i.e. the condition stated above yields $\mathscr{L} = R \ll \lambda$ for the incompressible solution to be valid and thus:

$$q n n_b \ll \frac{c}{R}. \tag{1.1}$$

Although somewhat arbitrary, a factor of ten between the left and right side of this inequation may be regarded as sufficient in this context. Typical values for a container vessel are, say $R = 4.0\,\mathrm{m}$, $n_b = 5$ and $n = 100.0\,\mathrm{min}^{-1}$. The speed of sound c is approximately $1500.0\,\mathrm{ms}^{-1}$ in sea water. In this particular case, fluctuations up to the fifth order can be calculated without introducing a significant error due to neglecting compressibility. It may be possible to go beyond this limit, but effects of compressibility may then become significant.

Another limitation which applies when the flow is considered to be incompressible is that the flow velocities $\mathscr{V}$ should be much smaller than the speed of sound c (Söding, 1987). Cavitation phenomena such as shock wave propagating from collapsing cavities as investigated by Budich et al. (2015) are not considered in this thesis, and at first glance, the condition of $c \gg \mathscr{V}$ seems to be fulfilled easily. However, care must be taken when considering the speed of sound for cavitating flows. Locally, the flow may be of bubbly character which leads to a significant reduction of the speed of sound (Brennen, 1995, pp. 163ff).

It is important to make a distinction between propeller-induced hull pressure fluctuations and propeller noise. Propeller noise includes the entirety of periodic and irregular pressure disturbances radiated from the propeller and comprises a wide frequency range – whatever the actual underlying physical mechanisms may be. Propeller noise is usually evaluated in the far field, i.e. distances much larger than the propeller radius are involved, and it thus becomes important to take into account the wave-like propagation of these disturbances. On the contrary, what is understood as propeller-induced hull pressure fluctuations in this thesis refers to periodic fluctuations of the pressure in the near field, i.e. on the ship hull in the vicinity of the propeller, and an upper frequency limit applies that is determined by the criterion explained above.

1.3 Approach and Development

The hypothesis which will be encountered in this study is that notable higher-order pressure fluctuations are excited by the interaction between developed tip vortex cavitation and sheet cavitation. Hence, this interaction is considered by the novel method developed here.

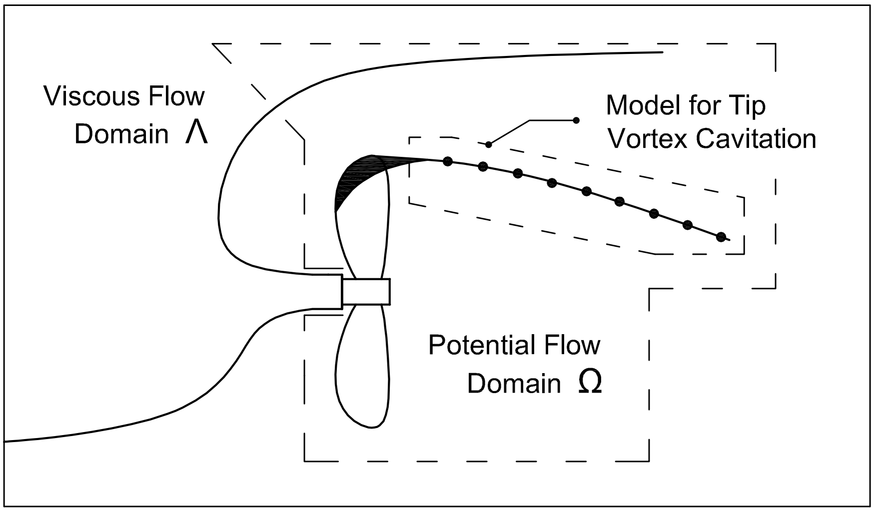

Fig. 1.1 Decomposition of the flow into a potential flow domain Ω and a viscous flow domain Λ.

The basic principle of the novel simulation method is shown in Figure 1.1. The flow is divided into two domains – the viscous flow domain Λ treated by the RANSE solver ANSYS CFX where the hull flow, i.e. the wake field of the ship is captured; and the domain of potential flow Ω treated by the panel method *pan*MARE. In the latter, the propeller flow, including effects of sheet cavitation, is considered. Furthermore, pressure fluctuations on the hull are evaluated in Ω. A coupling approach based on body forces constitutes the interface between Λ and Ω. By the suggested coupling of the two domains, a good compromise between accuracy, level of detail and computational effort can be achieved.

In order to account for tip vortex cavitation, an appropriate model has been developed within this study that is based on the solution of the two-dimensional momentum equations in cylindrical coordinates. Some basic input parameters have to be provided to the tip vortex cavitation model in every time step: the current circulation of the tip vortex, the viscous core radius and the initial cavitation radius. The model derives the unsteady tip vortex cavity shape for every time step. Equivalent potential sources are brought into the domain of potential flow in order to represent the cavitating tip vortex when assembling the signal of hull pressure fluctuations.

To account for the interaction of developed tip vortex cavitation with sheet cavitation, the cavitation radius of the tip vortex is initialised corresponding to the sheet cavitation thickness at the trailing edge of the blade in the tip region.

1.4 Structure of the Text

Following this first introductory chapter, *Chapter 2* compiles all information necessary to understand the origin and physical mechanisms behind propeller-induced hull pressure fluctuations and provides a foundation for developing the numerical methods addressed in the subsequent chapters. Chapter 2 provides an overview on general considerations as well as detailed descriptions of sheet and tip vortex cavitation. Tip vortex cavitation is given special attention in this chapter. The chapter ends with theoretical considerations on the pressure signal radiated by sheet and tip vortex cavitation.

In *Chapter 3*, current experimental and numerical methods for the prediction of hull pressure fluctuations and cavitation are reviewed. The chapter begins with an explanation of cavitation tunnel experiments and the problem of scale effects. Exemplary full-scale observation campaigns are reported. After this, numerical simulation methods for the prediction of propeller-induced hull pressure fluctuations are reviewed and relevant developments of cavitating tip vortex flow modelling are reported. For the numerical analysis of cavitation and pressure fluctuations, results of a workshop on propeller cavitation are compiled and presented.

The RANSE solver ANSYS CFX and the panel code *pan*MARE with the sheet cavitation model, which constitute the basis for the development of the hybrid simulation tool, are briefly introduced in *Chapter 4*.

Chapter 5 is devoted to VoCav2D, the newly developed model for propeller tip vortex cavitation. The chapter begins with enumerating of the necessary assumptions and simplifications made for developing the new model. After that, the idea of segmentation is explained and two different formulations of the model are introduced. Furthermore, methods for approximating the important interaction with sheet cavitation are presented. The model requires specifying a number of input parameters, such as initial tip vortex circulation, viscous core radius and initial cavitation radius. Approaches to extract these parameters from RANS simulations are proposed as well. The chapter ends with verification exercises and an elementary convergence study.

Chapter 6 integrates all the elements described before (VoCav2D, *pan*MARE and ANSYS CFX) to develop the novel hybrid simulation tool. For this purpose, appropriate interfaces between the individual submethods are established. The most important interface is the body force coupling between *pan*MARE and ANSYS CFX mentioned above. Additional measures necessary to overcome the problem of different time discretisation levels used by *pan*MARE and VoCav2D are explained.

Chapter 7 presents the validation of the (overall) hybrid simulation tool. Three cases are investigated – two container vessels and a ConRo vessel. The latter is used to validate the body force coupling algorithm by employing adequate full-scale measurement results available for this case. By means of the container vessels, the capability of the tool to predict cavitation and pressure fluctuations is demonstrated.

Scale effects on sheet cavitation and moderate tip vortex cavitation are discussed in *Chapter 8*. Two types of scale effects due to differing Reynolds numbers are discussed: (1) The effect of the hull boundary layer thickness influencing the wake field of the hull and, in turn, propeller sheet cavitation and (2) the effect of the boundary layer thickness of the propeller blades influencing the viscous core radius of the tip vortex and consequently the behaviour of cavities inside the viscous core region, respectively.

Finally, in *Chapter 9*, conclusions are drawn, results are further discussed, shortcomings are mentioned and proposals for future work are given.

Chapter 2

Flow Mechanisms Leading to Propeller-Induced Pressure Fluctuations

The basic physical mechanisms explaining the origin of propeller-induced pressure fluctuations are reviewed in this chapter. Section 2.1 provides an overview of general considerations, followed by a discussion of sheet cavitation, tip vortex cavitation and cavitation–cavitation interaction in Sections 2.3, 2.4 and 2.5, respectively. Section 2.6 explains by means of simple models how both types of cavitation contribute to the pressure signal radiated by the propeller.

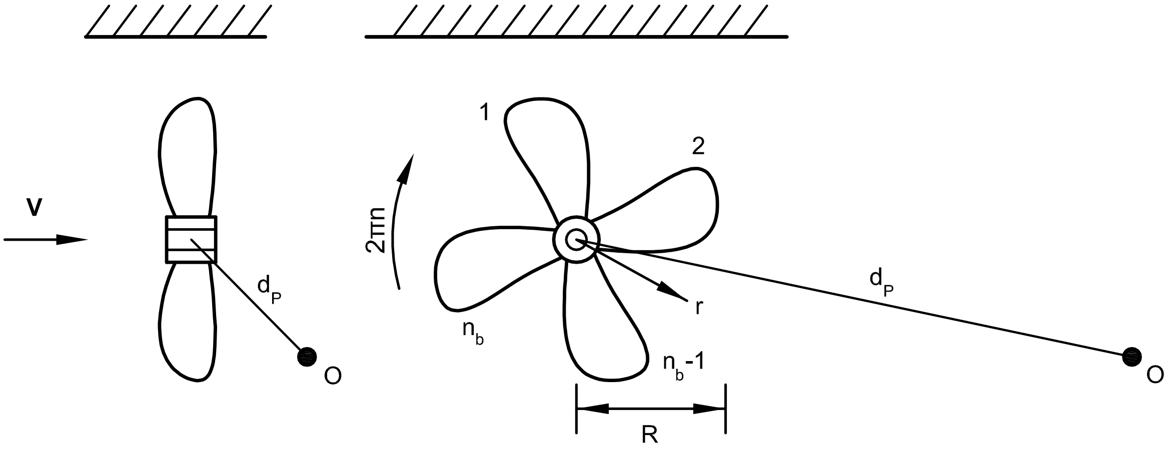

Fig. 2.1 Basic definitions and conventions used throughout this study.

Figure 2.1 illustrates a number of basic definitions and conventions used to describe the propeller flow in this study. A n_b-bladed propeller of the radius $R = \frac{D}{2}$ rotates with the angular velocity $\omega = 2\pi n$, where n is the number of revolutions. The rotating propeller is subjected to an arbitrary inflow **V** which can either be homogeneous or not. The main direction of the inflow coincides with the rotational axis of the propeller. An observer O is placed in the fluid at a fixed position relative to the propeller center; the distance between propeller and observer is denoted as d_P.

Any reasonably well-behaved P-periodic function $g(t)$ with $g(t+P)=g(t)$ can be expanded into a series of trigonometric functions. This is known as Fourier series expansion (Bronstein et al., 2005, p. 437f):

$$g(t)=\frac{a_0}{2}+\sum_{j=1}\left[\hat{a}_j\cos(j\omega t)+\hat{b}_j\sin(j\omega t)\right], \tag{2.1}$$

or, using a different notation:

$$g(t)=\frac{a_0}{2}+\sum_{j=1}\hat{A}_j\sin(j\omega t+\varphi_j), \tag{2.2}$$

where $\hat{A}_j=\sqrt{\hat{a}_j^2+\hat{b}_j^2}$, $\tan\varphi_j={}^{\hat{a}_j}/_{\hat{b}_j}$ and $\omega={}^{2\pi}/_{P}$. Accordingly, a periodic function oscillating around a mean value ${}^{a_0}/_{2}$ can be decomposed into a number of harmonics $A_j=\hat{A}_j\sin(j\omega t+\varphi_j)$ with the amplitude $\hat{A}_j$, the angular frequency $j\omega$ and the phase angle φ_j.

Under the assumption of a constant number of revolutions $n=$ const. and an inflow $\mathbf{V}=$ const. being constant in time, the propeller flow is expected to be periodic[1] with the period $T_b=(nn_b)^{-1}$. The inverse $f_b=T_b^{-1}=nn_b$ is defined as blade frequency. A common way to characterise the periodic pressure fluctuations induced by a propeller is to specify in accordance with Eq. (2.2) the amplitudes and corresponding phase angles of the harmonics of the pressure signal monitored in certain observation points. In this study,

$$\hat{p}^{[q]}$$

denotes the amplitude of the q-th harmonic of the pressure fluctuations. Corresponding notations for other quantities are possible as well. q is called the harmonic order. $q=1$ indicates the first harmonic occurring with blade frequency f_b. Higher harmonics with $q\geq 2$ are associated with integer multiples of the blade frequency $2f_b$, $3f_b$ and so on.

2.1 Basic Considerations

There is broad agreement that three main effects lead to fluctuations of the pressure field around the propeller (Huse, 1972; Skaar and Raestad, 1979, e.g.):

(1) the effect of fluid displacement due to the finite thickness of the propeller blades

(2) the pressure jump induced by the propeller blades due to the generation of lift

(3) growth, collapse and volume variation of cavitation or gas bubbles and coherent cavitation structures

While the first two effects are well understood, a simple and comprehensive explanation of how cavitation can lead to – sometimes – excessive hull pressure fluctuations does not exist (Carlton, 1994,

---

[1] In fact, the propeller flow is never perfectly periodic. The degree of deviation from periodicity depends on many factors. This and resulting implications on the frequency spectrum of the pressure fluctuations will be discussed in Section 2.6.

pp. 259ff). In the following, the influence of blade thickness and blade lift are discussed. These mechanisms lead to pressure fluctuations in every case, regardless of whether cavitation occurs or not. The discussion is then extended to cavitating flow.

2.1.1 Influence of blade lift and thickness

The simplest case is a rotating and translating propeller operating in unbounded fluid and homogeneous inflow. An observer O fixed relative to the propeller center will experience a time-dependent pressure field. Breslin and Tsakonas (1959) address this problem in a theoretical manner. They distinguish between *thickness* and *loading* effects: whenever a propeller blade passes the position of the observer, the finite thickness of the blade will induce a displacement flow which results in a varying pressure. This thickness effect can be modelled mathematically by sources and sinks distributed over the blade area. Breslin and Tsakonas show that the intensity of this effect grows linearly with an increasing thickness ratio of the blade sections, i.e. the blade thickness divided by the chord length.

The production of propeller thrust and torque is a result of the pressure jump induced by the propeller blades. With decreasing distance to blade, the pressure jump will intensify. For a rotating propeller, the distance between observer and propeller blade varies periodically and so does the induced pressure field. Breslin (1958) models this loading effect by a bound vortex rotating with the blade and a helical vortex originating from the tip of the propeller blade. He assumes constant circulation along the vortex axis and makes use of the Biot-Savart law and the Bernoulli equation in order to derive the time-dependent pressure field due to the loading effect. It turns out that the intensity of pressure fluctuations due to the loading effect are proportional to the propeller disk load $T\left(\pi R^2\right)^{-1}$, where T is the propeller thrust. In later work, Breslin and Tsakonas (1959) allow for varying circulation along the blade radius and show that the results strongly depend on the blade load near the tip.

Regarding the decay rate of the pressure disturbance induced by a non-cavitating propeller in homogeneous flow, an important conclusion can be drawn from the theoretical considerations made by Breslin and Tsakonas: modelling the thickness effect by a rotating distribution of constant sources and sinks leads to terms proportional to d_P^{-2} and d_P^{-3}; and modelling the blade lift effect leads to terms proportional to d_P^{-3}, where d_P denotes the distance from the propeller to the observation point. Consequently, the overall decay rate with increasing distance to the propeller must range somewhere between d_P^{-2} and d_P^{-3} depending on the ratio between thickness and loading effect. Following Carlton (1994, p. 260),

$$p'_{\mathrm{nc}} \propto \frac{1}{d_P^{2.5}} \tag{2.3}$$

can express the decay behaviour of the pressure disturbance p'_{nc} induced by a non-cavitating propeller in unbounded fluid an homogeneous inflow.

Pressure fluctuations induced by a propeller operating in homogeneous inflow predominantly occur with blade frequency f_b. Higher harmonics (i.e. qf_b with $q \geq 2$) virtually do not play a role in this case.

In general, the condition of unbounded fluid and homogeneous inflow is not met for a propeller operating behind a ship. The inhomogeneous wake field of the ship hull causes a time-dependent blade lift which leads to increased pressure pulses with lower decay rate compared to the case where the propeller operates in homogeneous inflow.[2] In general, these pressure fluctuations are still dominated by the first harmonic. However, higher harmonics of pressure fluctuations depending on the particular form of the inflow will arise (Vorus, 2010, pp. 19ff).

When a solid boundary is introduced in the vicinity of the propeller, this will certainly have an effect on the pressure field. In the case of a flat plate above the propeller, the pressure will increase by a factor of two compared to the free space pressure at the location of the plate; convex hull forms exhibit a lower factor (Wang, 1981). The presence of a rudder behind the propeller will also have a great impact on the pressure field induced by the propeller.

A general statement about the ratio between the blade loading and the thickness effect cannot be given – the answer depends on the particular propeller shape and on the propeller inflow.

2.1.2 Influence of cavitation

In most of the technically relevant cases, a propeller operating behind a ship will be subjected to cavitation: vapour-filled cavities will arise on the surface of the propeller as well as in its vicinity. In general, neither shape nor volume of these cavities are constant. Regardless of the exact physical principals of cavitation, which will be discussed in the next sections, the following relation holds for the pressure disturbance caused by a cavitating propeller in unbounded flow:

$$p'_{\mathrm{c}} = \frac{\rho}{4\pi d_P} \frac{\partial^2 V_{\mathrm{cav}}}{\partial t^2}; \tag{2.4}$$

see, for example, Skaar and Raestad (1979)[3]. In this relation, d_P again is the distance between propeller and the respective observation point and V_{cav} is the unsteady overall cavitation volume of the propeller. For the equation to be valid, d_P must be sufficiently large compared to the propeller dimensions. Then the cavitating propeller can be interpreted as a single unsteady monopole source of

---

[2] Huse (1972) divides the loading effect into a steady part (due to a homogeneous inflow obtained by circumferentially averaging the inhomogeneous inflow) and an unsteady part due to the variation of the blade lift caused by the inhomogeneity of the inflow. However, this separation will not be used within this thesis.

[3] Interestingly, in the discussion of this paper, Breslin argues that the relation given by Eq. 2.4 *"is entirely wrong!"*. After an elongate derivation he gives the following relation for the q-th harmonic component of the pressure fluctuations $p_{\mathrm{c}}^{[q]}$:

$$p_{\mathrm{c}}^{[q]} = -\frac{2\pi\rho n_b^3 q^2 n^2}{d_P} \mathrm{Re}\left[\widehat{V}^{[q]} \mathrm{e}^{i\cdot qz\theta}\right],$$

where $i^2 = -1$, $\hat{V}^{[q]}$ is the complex amplitude of the q-th harmonic component of the overall cavity volume and $\theta = \omega t$ denotes the blade position angle. However, the authors also show the equivalence of Breslin's relation to Eq. 2.4.

the strength $\frac{\partial V_{\text{cav}}}{\partial t}$. Considering locations close to the propeller, as, for example, the ship hull above the propeller, Eq. 2.4 yields inaccurate results since d_P is not sufficiently large in this case. The analysis of pressure fluctuations on the ship hull requires a more detailed consideration of the cavitation shape. However, despite its simplicity, some important conclusions become apparent by Eq. 2.4: The decay rate of pressure fluctuations is clearly given by

$$p'_{\text{c}} \propto \frac{1}{d_P}, \tag{2.5}$$

which is in contrast to $p'_{\text{nc}} \propto d_P^{-2.5}$ for non-cavitating propellers in homogeneous inflow.

Furthermore, as can be seen by the monopole character indicated by Eq. 2.4, the pressure disturbance radiates omnidirectionally. As a consequence, when the pressure disturbance due to cavitation at a certain instant of time is integrated over the aft ship surface, no cancellation will take place; whereas for the non-cavitating contribution due to thickness and lift of the blades, such a cancellation can be observed.[4] Figure 2.2 illustrates this in a schematic manner. Evidently, pressure disturbances due to cavitation are much more serious for hull vibration than the contributions due to blade lift and thickness.

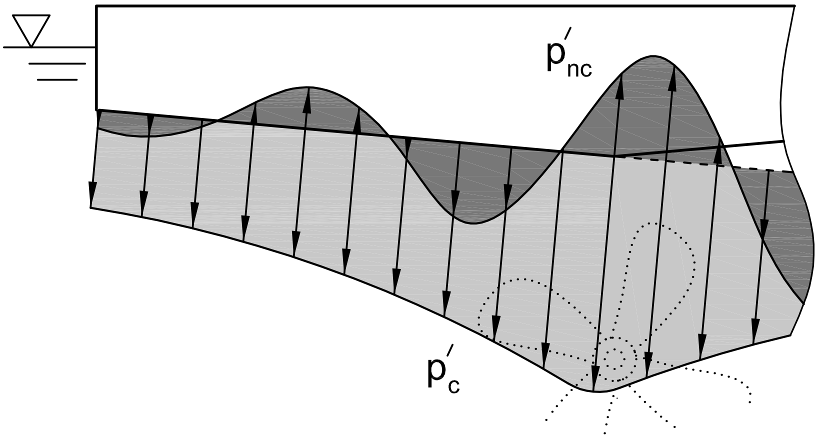

Fig. 2.2 Schematic distribution of the pressure disturbance due to blade thickness, blade lift and cavitation on the aft ship hull for a certain instant of time; adopted from Söding et al. (2014).

In general, cavitation can lead to increased pressure fluctuations of the first order and to increased fluctuations of higher order. A more precise statement requires some insights into the behaviour of cavitation occurring at the particular types of propellers. This will be addressed in the next sections.

A universal rule of thumb regarding the relation between the strength of pressure fluctuations induced by blade lift and blade thickness and the strength of pressure fluctuations due to cavitation cannot be given. Abels (2006a) states that modern propeller designs with skewed blades as they are used for passenger ships, for example, exhibit first-order pressure amplitudes measured on the hull of, say, 1.0…1.5 kPa, whereof approximately 1.0 kPa are due to blade load and thickness. A

---

[4] Integrating the pressure disturbance over an infinite plate induced by a non-cavitating propeller operating under this plate leads to vertical force equal to zero. This is known as *Breslin condition* (Vorus, 2010, p. 19, p. 21).

cavitating propeller of a container vessel typically exhibits first-order amplitudes of $4.0 \ldots 8.0\,\mathrm{kPa}$ and approximately $1.0 \ldots 2.5\,\mathrm{kPa}$ in non-cavitating flow. Examples will be given in Chapters 7 and 8.

2.2 Propeller Cavitation

Cavitation is a phenomenon where coherent or isolated regions of the fluid start to evaporate due to the ambient pressure in the vicinity of these regions being lower than a certain critical pressure. In this context, regions of evaporated fluid are called cavities.

The critical pressure is supposed to be the equilibrium vapour pressure p_v of the fluid medium at a given temperature (e.g. $p_v = 2339\,\mathrm{Pa}$ at 20°C (Lucas, 2006, p. 539)). One has to note that this is an oversimplification of the actual physical problem since there are a number of other factors influencing the inception of cavitation (Carlton, 1994, pp. 199ff). However, the investigation of cavitation inception is not addressed primarily in this thesis and one can agree upon the general rule that if the pressure in the fluid falls below the equilibrium vapour pressure of the medium, cavitation is very likely to occur:

$$p \leq p_v \quad \text{for the presumable occurrence of cavitation.} \tag{2.6}$$

The pressure distribution on the surface of an operating propeller and within close vicinity of the operating propeller very often shows regions where the absolute pressure falls below vapour pressure. Because the pressure distribution on the propeller blades is more or less similar within certain ranges for all propellers – at least as far as conventional propellers are concerned – the typical patterns of propeller cavitation shown in Figure 2.3 are also more or less similar for all conventional propellers, even though the presence and dominance of a certain cavitation type depends on the exact pressure distribution of the particular propeller. Regions of low pressure and therefore with increased likelihood of cavitation are:

(1) the suction side of the blade

(2) the leading edge of the blade

(3) the system of trailing vortices, i.e. tip vortex and hub vortex

In the following, typical forms of cavitation regarding propeller flow are listed and shown in Figure 2.3. This classification is based on the introductory explanations made by Carlton. Sheet cavitation (2) usually starts at the leading edge of the propeller where large suction pressures occur. This type of cavitation extends over portions of the suction side of the blade appearing as a coherent sheet as depicted in the figure. Sections of the blade operating at negative incident angles often show sheet cavitation on the face side. Cloud cavitation (4) can occur downstream of developed sheet cavitation due to the separation of flow taking place at the closure of sheet cavitation. This form of cavitation – as indicated by its name – has a cloudy appearance and consists of agglomerations of small cavities which are swept away by the flow. The origin of bubble cavitation (1) is the low-pressure region near the position of maximum blade thickness or rather close to the mid-chord region of the blade sections. If the pressure in this region is low enough, individual bubbles travelling over the blade arise and collapse when entering regions of higher pressure.

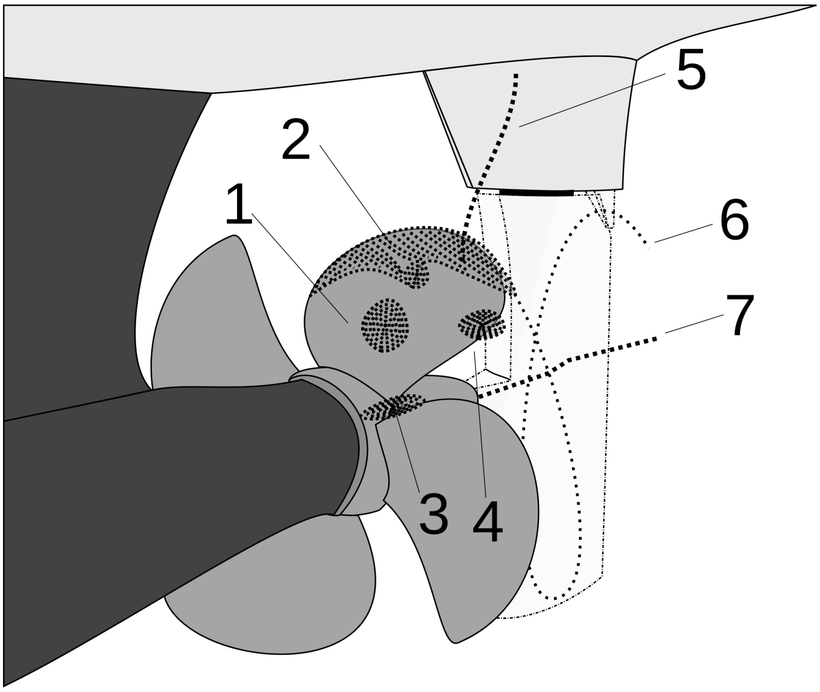

Fig. 2.3 Different types of propeller cavitation (Wikimedia Commons, 2008).

The operation of the propeller is associated with the formation of prominent vortices, mainly the tip vortices (6) emanating from the blade tips and a hub vortex (7) which is the result of the combination of the blade root vortices. Flow separation at the leading edge will result in a leading edge vortex – an effect which can be observed at large positive or negative incident angles. The pressure in the core of these vortices can fall far below vapour pressure and consequently these vortices are susceptible to cavitation. Other forms of cavitation observed on propellers are blade root cavitation (3) and – rarely – propeller–hull vortex cavitation (5).

In general, all these forms of propeller cavitation are unwanted because of the harmful effects they have. Apart from increased pressure fluctuations, erosion is a serious problem.

Again, cavitation inception is not an issue of the present thesis and in the following it is assumed that cavitation – regardless of the particular type of cavitation – is fully developed. Furthermore, only two types of cavitation are studied: tip vortex and sheet cavitation. These two cavitation types and their influence on the radiated pressure signal are discussed below in greater detail.

2.3 Sheet Cavitation on Propeller Blades

Sheet cavitation appears to be a large-scale coherent structure covering portions of the blade surface. Depending on the local angle of incident, this can be either the pressure or – more likely – the suction side or sometimes both. A typical case of sheet cavitation is shown in Figure 2.4.

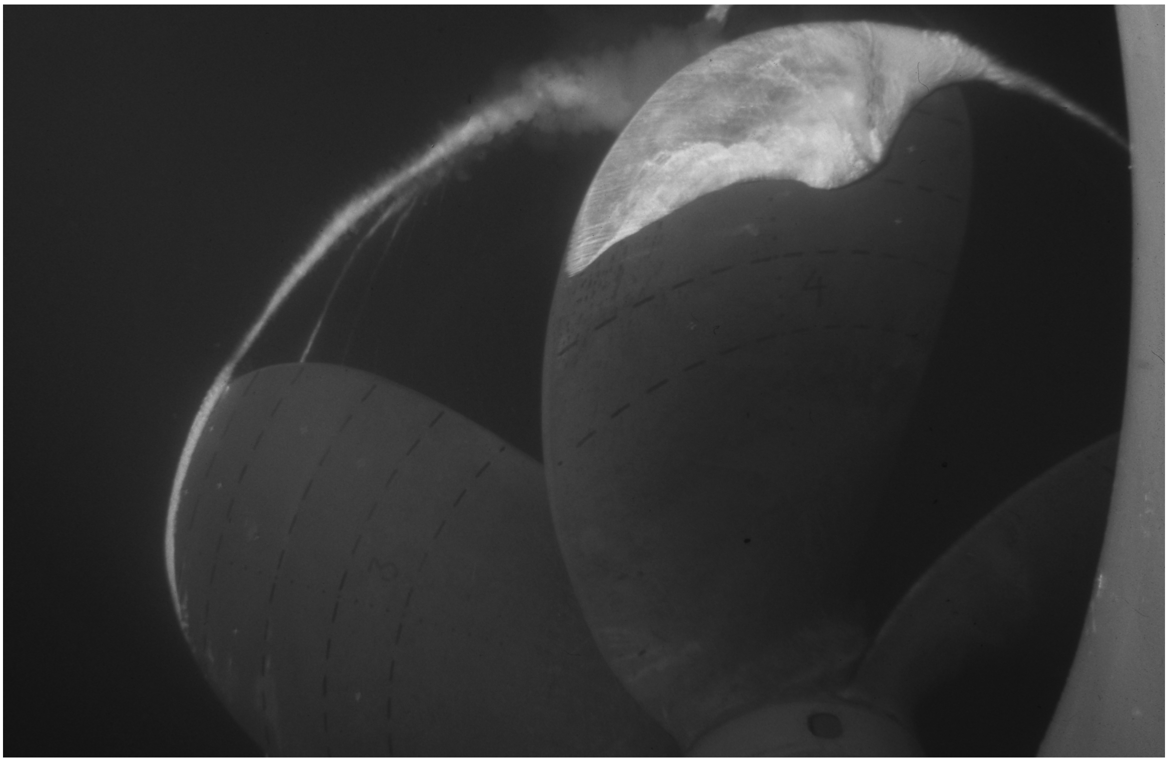

Fig. 2.4 Full-scale observation: Sheet cavitation on the suction side of the propeller of the container vessel *Sydney Express* (Keller and Weitendorf, 1979). Courtesy: E. A. Weitendorf.

Sheet cavitation usually starts to grow first from the leading edge of the propeller blade and then propagates in the streamwise direction towards the trailing edge. It is possible for sheet cavitation to even exceed the trailing edge. Two mechanisms are known for evoking unsteadiness of the cavitation volume and consequently inducing pressure fluctuations in terms of Eq. (2.4):

(1) Due to the inhomogeneous wake field of the ship and the related fluctuation of incident angle and blade load, the sheet cavitation volume changes accordingly. The maximum cavity volume occurs in the region of the wake peak and may entirely vanish when the blade is unloaded.

(2) The second mechanism is related to shedding taking place in the closure region of the sheet cavity, leading to a rather cloudy appearance of cavitation and a highly vortical flow. In Figure 2.4, this cloud formation in the closure region can be observed.

Falcão de Campos et al. (2006) investigated the first effect mentioned above in a systematic numerical study by applying a panel method similar to the one presented in Section 4.2. For this purpose, the case of a two-dimensional cavitating hydrofoil subjected to an unsteady inflow $(V_0, V_w(t))$ in the chordwise direction and perpendicular to it, respectively, and resultant changing angle of attack was considered. The key findings of this work, which are assumed to be applicable to unsteady propeller flow, are that the unsteady cavity volume in terms of cavity length and thickness significantly depends on the reduced frequency $K = 0.5\omega c V_0^{-1}$, a characteristic number, with ω and c being the oscillation frequency and the chord length, respectively, as well as on the non-dimensional amplitude $\mathit{\Delta} V_w V_0^{-1}$ with $\mathit{\Delta} V_w = V_{w,\max} - V_{w,\min}$. For fixed $\mathit{\Delta} V_w V_0^{-1}$, it can be stated that the higher the reduced frequency K, the smaller the maximum cavitation volume. This indicates the importance of inertia effects when sheet cavitation is concerned.

Volume fluctuations due to shedding are related to details of the flow in the closure region of sheet cavitation. Directly downstream of the cavity, a re-entrant jet forms, travelling upstream and separating a certain portion of the sheet cavity from the surface of the body (Franc and Michel, 2005, pp. 131ff). When this separated portion is convected into regions of higher pressure, it collapses and cloud cavitation may occur. This cyclic process and the corresponding cavity volume fluctuation can be both periodic and irregular. An important parameter in this respect is cavity thickness, which must be sufficiently large in order to give rise to noticeable cavity shedding.

A large number of numerical and experimental investigations is devoted to this flow feature (Arndt et al., 2000; Ji et al., 2015; Leroux et al., 2004, e.g.). In many of these publications, a foil under steady inflow conditions is considered; similar investigations with respect to unsteady propeller flow are not known to the author; a few remarks on this issue are given by Kuiper (2001).

At this point, the following question may arise: When addressing pressure fluctuations induced by a cavitating propeller, how important are these two effects in comparison with each other? For a two-dimensional foil with constant inflow, situations have been reported where a thick cavitation sheet develops and the re-entrant jet literally shears off the entire sheet (Franc and Michel, 2005, pp. 141ff). Such an extreme behaviour is rare for propeller flow. The reason may be that the cavity thickness on the blades of a propeller under moderate operation conditions is not large enough and only becomes critical in the closure region itself. Thus, shedding and the formation of cloud cavitation is limited to the, say, last ten percent of the cavity sheet (as shown in Figure 2.4). It can be assumed, then, that the most important contributor to periodic propeller-induced pressure fluctuations is the part of cavity volume fluctuation that results from changing inflow.

2.4 Tip Vortex Cavitation

Whenever a three-dimensional wing or hydrofoil, which also comprises the blades of a propeller, produces lift, this is intrinsically tied to the generation of tip and – in the case of the propeller – hub vortices. In the core region of these vortices, the pressure drops and cavitation may occur.

With respect to marine propellers, isolated tip vortex cavitation or – to be more precise – trailing vortex cavitation as shown in Figure 2.5 for the case of an elliptical hydrofoil, is rarely observed; a combination with other types of cavitation is more likely.

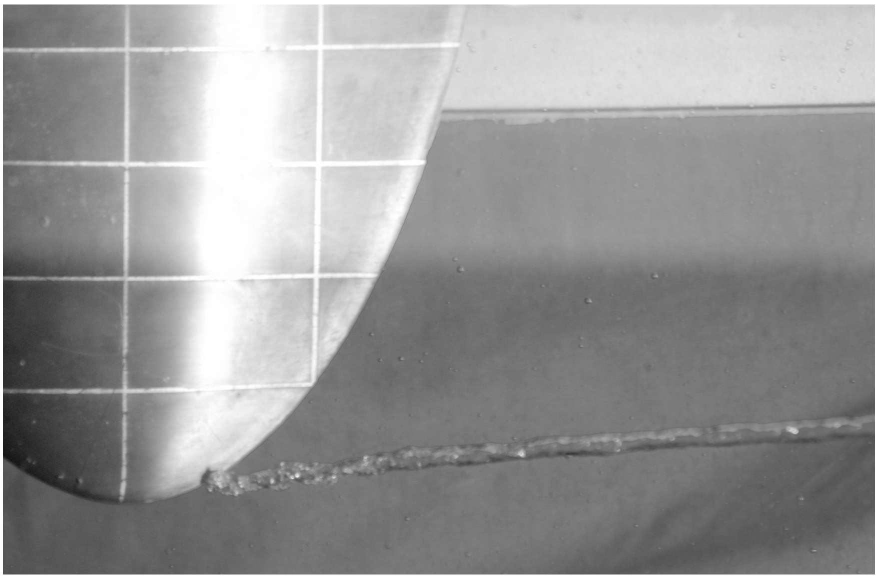

Fig. 2.5 Trailing vortex cavitation on an elliptical hydrofoil. Courtesy: SVA Potsdam GmbH, Potsdam, Germany.

Figure 2.5 already reveals two important aspects of fully developed vortex cavities: A cavitating vortex typically exhibits a – roughly – circular cross section and an elongated structure, which means that the radius of the cavity is significantly smaller than the length of the vortex. These observations are essential for the development of the numerical methods addressed in Chapter 5.

In this section, the origin of cavitating tip vortices and relevant phenomena are explained. The investigation of vortices in the hub region of the propeller is beyond the scope of this thesis. There is a great body of literature dealing with the behaviour of the flow over symmetric wings or foils and the formation of trailing vortices behind these bodies; most of the literature is related to application in aircraft design. However, it can be assumed that the basic mechanisms are applicable to propeller flow.[5]

In the following, insights on the formation of the tip vortex for non-cavitating flow are given in Section 2.4.1, and cavitating flow with fully developed tip vortex cavitation is discussed in Section 2.4.2. In many cases, tip vortex cavitation may be an important source of hull pressure fluctuations. Relevant mechanisms are presented in Section 2.5. Furthermore, simple analytical approaches for the estimation of the frequency range of radiated pressure fluctuations are shown in Section 2.6.2.

2.4.1 Non-cavitating propeller tip vortex flow

With respect to propeller flow, the tip vortex is understood as a combination of more than one vortical flow structure originating from different regions of the propeller. The particular contributions are often difficult to identify since modern conventional propeller designs feature a smooth transition

---

[5] An idea which seems to be justified: *"The blade of an orthodox screw propeller is a hydrofoil with no end plate at its tip, an inadequate end plate at its root, and some circulation along its entire length."* (Saunders, 1957, p. 250).

from the leading edge over the blade tip to the trailing edge. Nevertheless, three distinct vortical structures can be distinguished with varying degrees from case to case:

(1) The most important contribution is due to the vorticity shed from the trailing edge which forms a highly unstable shear layer that undergoes a roll-up process. The result is a compact *trailing vortex*.

(2) Under certain operation conditions, the flow around the leading edge of the propeller cannot follow the high curvature of the blade sections in the tip region of the propeller blade. Separation will then take place giving rise to a *leading edge vortex* (Kuiper, 2001). This vortex can arise on both the suction and the pressure sides of the blade, depending on the local angle of attack (see Section 2.5.2).

(3) Locally at the blade tip and due to the compensating flow whistling around the blade from the higher to the lower pressure level, a *local tip vortex* originates due to separation (Hirschel, 1996)[6].

Evidently, the occurrence of these three species may vary from propeller to propeller and highly depends on the operation conditions. In particular, it is difficult to separate the local tip vortex from the trailing vortex. In the following, it is assumed that the trailing vortex is the dominant part and the other vortical structures merge smoothly without disturbing the trailing vortex in a significant way. This merged structure is now denoted as propeller tip vortex. The assumption of a smooth mergence may be justified in many cases, although there are cases in which massive disturbances can occur. This is addressed in Section 2.5.2.

Figure 2.6 shows the pressure distribution around the tip of a conventional propeller blade at moderate operation conditions.[7] A compensating flow propagating from the pressure side of the blade towards the suction side is clearly visible in the middle subfigure. Furthermore, the right subfigure depicts isolines of pressure at the blade tip for different intersecting planes perpendicular to the propeller plane. Plane (c) is located downstream of the tip and exhibits one agglomeration of circular isolines indicating the presence of a prominent tip vortex. In plane (a), the isolines indicate the presence of a weak leading edge vortex, and a local tip vortex joins in plane (b). In plane (c), the three species are no longer distinguishable. Again, it is important to highlight that this situation can be entirely different for other propeller shapes and operation conditions.

For the trailing vortex, a theoretical concept exists and will be addressed. The explanatory model comprises two steps: the origin of a shear layer carrying trailing vorticity and the roll-up process this shear layer undergoes. For the sake of simplicity, steady flow conditions are assumed for the following explanations. An experimental investigation of the complicated trailing vortex system for

---

[6] In this reference, the mentioned flow phenomenon is solely denoted as ‘tip vortex’. In order to avoid confusion, the adapted expression ‘local tip vortex’ is used here. Kuiper (2001) also applies this term. However, he gives a slightly different explanation for the origin of the phenomenon. Most likely, he means the same.

[7] The figure depicts results obtained by a numerical simulation with a RANS method. Details on this method can be found in Section 4.1.

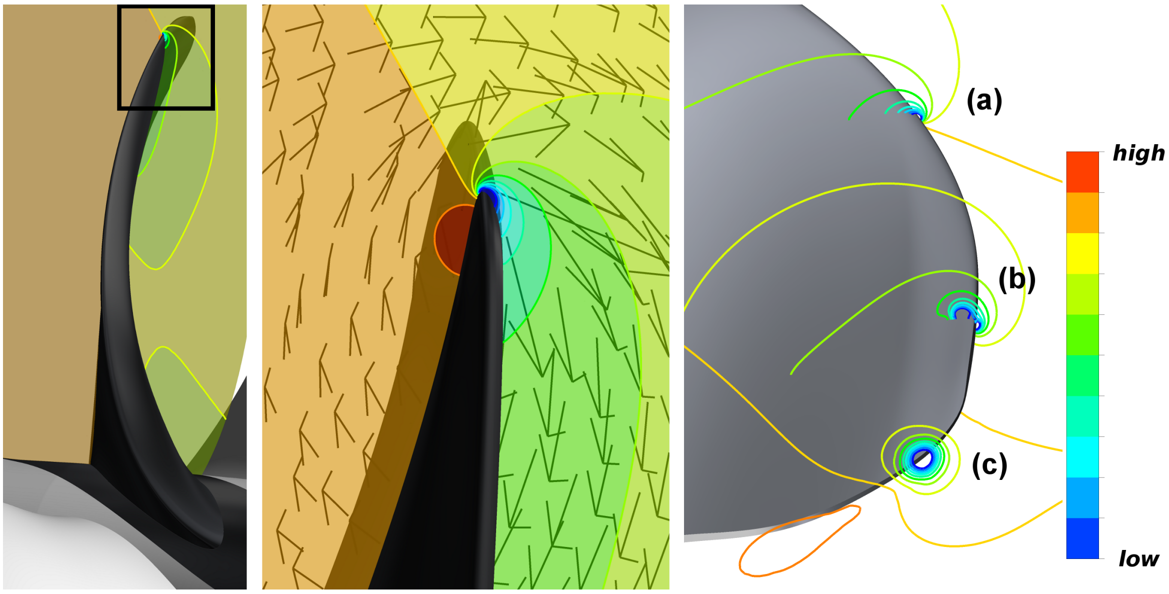

Fig. 2.6 Pressure distribution around a propeller blade in a plane perpendicular to the propeller plane. Left: overview; middle: detailed view of the propeller tip with arrows indicating the direction of the local flow velocity; right: pressure isolines in three planes (a, b and c) perpendicular to the propeller plane.

unsteady inflow conditions was conducted by Hart et al. (1992) by means of an oscillating hydrofoil. A dominant parameter influencing the characteristics of the trailing vortex system is the reduced frequency $K = 0.5\omega c V_0^{-1}$, where – again – ω is the frequency of changing angle of attack, c the chord length and V_0 the inflow velocity. The lower K, the smaller the difference between steady and unsteady flow conditions. When developing the tip vortex cavitation model later in Chapter 5, K is assumed to be small, although this might not be entirely the case under certain conditions.

Trailing vorticity and trailing vortex To begin with, consider a hydrofoil of finite length and sharp trailing edge as depicted in Figure 2.7 being subjected to steady inflow under a moderate angle of attack. A coordinate system (x,y,z) is introduced with the x-axis pointing in the direction of the chord, the y-axis in the spanwise direction and z is the third axis to complete the right-handed coordinate system. The velocity is denoted as $\mathbf{u} = (u_x, u_y, u_z)$. The foil is assumed to be symmetric, with $y = 0$ being the symmetry plane, which also indicates symmetry of the flow. For convenience, the foil is assumed to be very thin, so that the z-direction is approximately normal to the surface of the foil. Furthermore, only the semi-span with $y > 0$ is considered in the following.

Exclusively owing to viscosity, the flow around the foil will smoothly transit the trailing edge (Wu et al., 2015, pp. 283ff)[8] leading to a flow pattern where the circulation Γ around a curve $\mathscr{C}$ enclosing

---

[8] Wu et al. (2015, pp. 269ff) report detailed studies of the complicated flow around the trailing edge of a foil which is accelerated from a state of rest to a constant velocity.

an arbitrary cross section of the foil will be non-zero. The circulation is defined as

$$\Gamma = \oint_{\mathscr{C}} \mathbf{u}\,\mathrm{d}\mathbf{l}, \tag{2.7}$$

with the curve element $\mathrm{d}\mathbf{l}$ (Greitzer et al., 2004, p. 130). According to the theorem of Kutta-Joukowsky (Truckenbrodt, 1989, pp. 217ff), a body featuring a non-zero circulation $\Gamma = \Gamma(y)$ will experience a lift force $\mathrm{d}L = \rho V \Gamma(y)\mathrm{d}y$ acting on a body section of the width $\mathrm{d}y$ and being normal to the inflow velocity V. Obviously, the lift force has to be equivalent to the integrated pressure difference between the lower and upper side of the foil. At both ends of the foil, however, this pressure difference will vanish due to a compensating flow from the lower to the upper side (where the pressure level is lower in the present example) and the resulting lift force will fall to zero. Being tied to the lift by the Kutta-Joukowsky theorem, the circulation bound to the body is also zero at the ends, whereas it reaches its maximum at $y = 0$. Due to the compensating flow, apart from the components $u_{x,l}$ and $u_{x,u}$ in the direction of x at the lower $\bullet_l$ and upper side $\bullet_u$ of the foil, the flow over the foil has also components $u_{y,l}$ in the direction of y on the lower side and $u_{y,u}$ on the upper side in the direction of $-y$. These components gain intensity with decreasing distance to the ends of the foil – in the middle at $y = 0$, these components are zero, $u_{y,l} = u_{y,u} = 0$. Other velocity components are not relevant for the considered case. Certainly, the velocity directly on the surface of the body is zero because of the no-slip condition applying to solid surfaces. The velocities mentioned above refer thus to the inviscid flow outside the boundary layer. Due to convection, the boundary layer is extended in the form of a thin fluid layer far beyond the trailing edge.

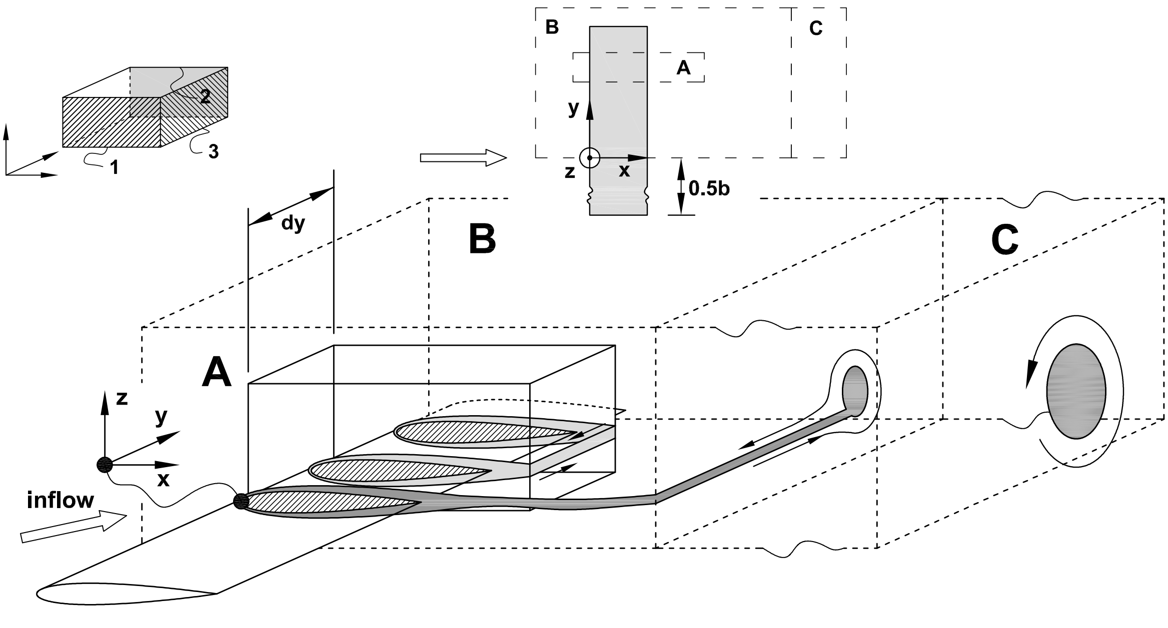

Fig. 2.7 Trailing vorticity sheet and formation of the trailing vortex (schematic).

In this context, it is important to note that what is interpreted as bound circulation around the body is exclusively contained in its boundary layer (Greitzer et al., 2004, pp. 142ff). The vorticity of the flow $\boldsymbol{\omega} = (\omega_x, \omega_y, \omega_z)$ is introduced, which is defined as

$$\boldsymbol{\omega} = \nabla \times \mathbf{u}, \tag{2.8}$$

with $\nabla = \left({}^{\partial}/_{\partial x}, {}^{\partial}/_{\partial y}, {}^{\partial}/_{\partial z}\right)$. Being the curl of the velocity field $\mathbf{u}$, the vorticity field is divergence-free per definition (Wu et al., 2015, p. 71):

$$\nabla \cdot \boldsymbol{\omega} = 0, \tag{2.9}$$

or, by applying Gauss' theorem, brought to an integral form (Wu et al., 2015, p. 72):

$$\int_{\partial V} \boldsymbol{\omega} \cdot \mathbf{n} \mathrm{d}S = 0, \tag{2.10}$$

where ∂V is the boundary surface of an arbitrary control volume V in the fluid domain and $\mathbf{n}\mathrm{d}S$ an orientated surface element.

Inside the boundary layer, which is indicated by the colour grey in Figure 2.7, concentrated vorticity is present, whereas $\boldsymbol{\omega} = \mathbf{0}$ outside the boundary layer. At high Reynolds numbers, the boundary layer thickness is sufficiently thin and the vorticity vector can be simplified to (Hirschel, 1982):

$$\boldsymbol{\omega} = \left(-\frac{\partial u_y}{\partial z}, \frac{\partial u_x}{\partial z}, 0\right). \tag{2.11}$$

Of particular interest is the vorticity vector at the trailing edge of the foil. An explanation is given by Eberle et al. (1992, pp. 303ff), for example. Whereas on the foil surface, the vorticity vector has two components as stated by Eq. (2.11), at the trailing edge where the flow transits smoothly, the ω_y-component of the lower and upper sides cancel each other out when the boundary layers merge to the trailing fluid layer and what remains is the component ω_x. Assuming a small thickness δ_t of the trailing fluid layer, the magnitude of ω_x equals $\|u_{y,l} - u_{y,u}\| {\delta_t}^{-1}$. Obviously, the intensity of the vorticity at the trailing edge increases towards the end of the foils since the difference between these spanwise velocities at the upper and lower side increases. Because of the velocity jump across the trailing fluid layer, it is also denoted as shear layer. It can be observed that such a shear layer is not stable and it tends to undergo a roll-up process, and what started as a flat and thin sheet is concentrated in a vortical structure with a roughly circular cross section – a trailing vortex at each end of the foil (Green, 1995).

There is a close relation between circulation and vorticity. Let A be a surface bounded by $\mathscr{C}$ and $\mathbf{n}$ the corresponding surface normal. Then:

$$\Gamma = \oiint_{A} \boldsymbol{\omega} \cdot \mathbf{n} \mathrm{d}A, \tag{2.12}$$

which is a result of Stoke's theorem (Greitzer et al., 2004, p. 130). In order to gain some insight into the structure of the trailing vortices, consider the control volume V_A enclosing a spanwise fraction of the foil as depicted in Figure 2.7. The spanwise distance between the left and right facet A_1 and A_2 is dy. Having in mind that vorticity is concentrated in the boundary layer, it is obvious that only the facets A_1, A_2 and A_3 are relevant for balancing the flux of vorticity. Per definition, the flux of vorticity through A_1 equals the bound foil circulation $-\Gamma_1$ at the spanwise location of A_1. Likewise, the flux through A_2 is Γ_2. Again, the circulation bound to the foil falls to zero when approaching the ends of the foil and hence $\Gamma_1 \neq \Gamma_2$. In order to comply with the solenoidality of the vorticity field stated by Eq. (2.10), there must be a flux $\Gamma_1 - \Gamma_2$ through A_3 in terms of $\omega_x \mathrm{d}y \delta_t$ leaving the trailing edge of the foil. In other words, when a small portion of the foil is considered, a change dΓ of bound circulation over a span dy results in a portion d$y\delta_t$ carrying shed vorticity with the circulation $\mathrm{d}\Gamma = \left({}^{\mathrm{d}\Gamma}/_{\mathrm{d}y}\right) \mathrm{d}y$ (Green, 1995).

Next, consider the control volume V_B. It encloses half of the span and also the foil end. B_1 is located at $y = 0$ where the bound circulation is maximal. The maximum circulation is now denoted as Γ_b. As indicated in the figure, the shear layer already starts to wind and a region with circular cross section arises, which is shown in the B_3-plane. The flux of vorticity through B_3 is obviously equal to Γ_b since no vorticity passes B_2. Balancing the vorticity flux through control volume C shows that all the vorticity flux or circulation Γ_b at $y = 0$ is contained in the developed trailing vortices, which is an important result. This academic example can be considered as a simplified model for the propeller flow.

Flow models for the developed tip vortex The tip vortex is regarded as developed when sufficiently far away from the trailing edge and propeller tip or the foil end, respectively, the roll-up process is completed and the influence of other vortical structures vanishes. The resulting flow field is more or less axisymmetric towards the vortex axis and characterised by a region of the radius r_a where concentrated vorticity is present. The so-called radius of the viscous core r_a is not constant but will grow continually due to diffusion with increasing distance from the trailing edge. It is useful to use a cylindrical coordinate system (ξ, φ, ψ) with ψ pointing along the vortex axis, φ being the circumferential and ξ the radial direction. The flow is generally dominated by the circumferential velocity u_φ; however, the axial velocity component u_ψ may also undergo substantial changes in the radial direction, i.e. the axial velocity in the core region can differ from the flow outside the core. Batchelor (1964) was one of the first authors to discuss this problem. In the present thesis, such effects are not considered when tip vortex cavitation is modelled.

A simple model for describing the flow pattern $u_\varphi(\xi)$ of such a developed tip vortex with the circulation Γ and the viscous core radius r_a is the Rankine vortex (Schade and Kunz, 1989, pp. 267f):

$$u_\varphi(\xi) = \frac{\Gamma}{2\pi r_a} \cdot \begin{cases} \frac{\xi}{r_a} & \text{if } \xi \leq r_a \\ \frac{r_a}{\xi} & \text{if } \xi \geq r_a \end{cases} \tag{2.13}$$

Inside the viscous core, the fluid is assumed to behave like a rigid body; while outside the viscous core it behaves like an inviscid potential vortex (see Figure 2.8 for a visualisation). The Rankine vortex suffers from an unrealistic discontinuity of the velocity profile at $\xi = r_a$.

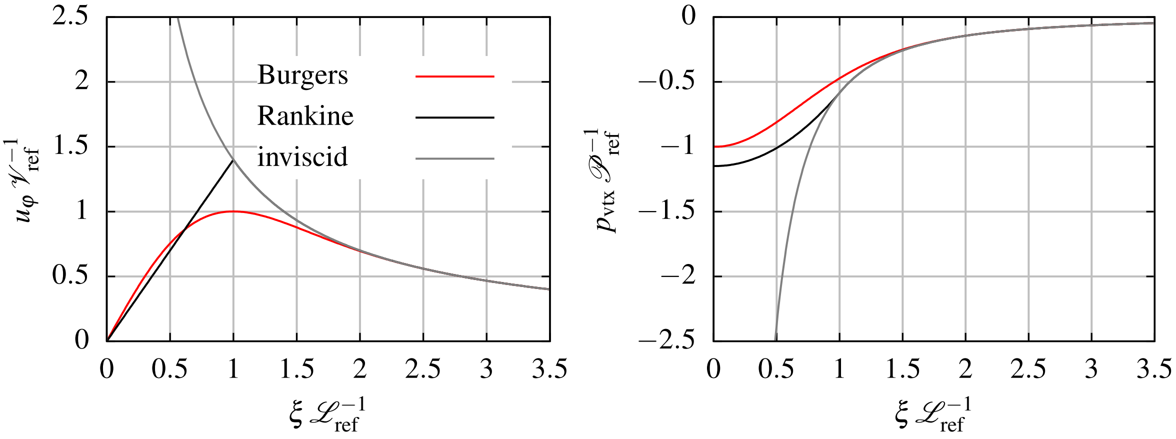

Fig. 2.8 Velocity and pressure for a Rankine vortex, a Burgers vortex and an inviscid potential vortex. Results are made dimensionless by $\mathscr{V}_\mathrm{ref} = 0.715\Gamma\,(2\pi r_a)^{-1}$, which is the maximum velocity of a Burgers vortex and the minimum pressure $\mathscr{P}_\mathrm{ref} = 0.871\rho\Gamma^2\,(2\pi r_a)^{-2}$ in a Burgers vortex (Franc and Michel, 2005, pp. 232ff); $\mathscr{L}_\mathrm{ref} = r_a$.

A more realistic model is the Burgers vortex (Franc and Michel, 2005, pp. 232ff), where the distribution of circumferential velocity is given by:

$$u_\varphi(\xi) = \frac{\Gamma}{2\pi\xi}\left[1 - \exp\left(\frac{-\beta\xi^2}{r_a^2}\right)\right]. \tag{2.14}$$

Here, $\beta = 1.256$ ensures that the maximal circumferential velocity occurs at $\xi = r_a$. This model results from a solution of the Navier-Stokes equations. It ensures a smooth transition from the viscous core region into the outer regime of inviscid flow (see Figure 2.8). The vortex flow can be described by the two parameters Γ and r_a, the influence of which is shown in Figure 2.9. It can be seen that r_a influences the solution in the region of the viscous core and especially the minimum pressure at $\xi = 0$. The Burgers vortex is only one of many vortex models. A summary and evaluation of alternative vortex models with respect to tip vortex flow is given by Hommes et al. (2015). An earlier study was carried out by del Pino et al. (2011), who compared theoretical models and experimental data with respect to both circumferential and axial velocities.

Notes on the formation process and role of turbulence in the core That the maximum bound circulation Γ_b equals the circulation of the trailing vortices can be entirely explained by purely kinematic relations governed by Eq. (2.9). However, in order to understand the roll-up process of the shear layer, dynamic relations are needed. As already indicated, this is due to the instability of the

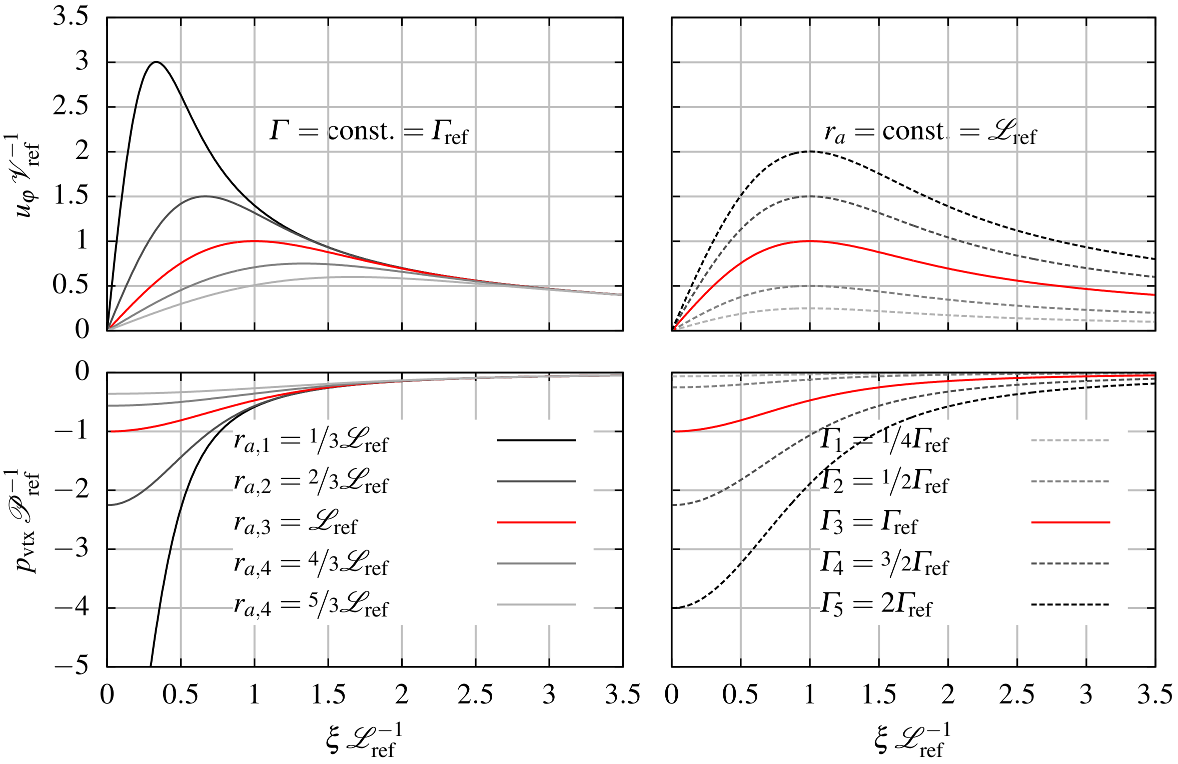

Fig. 2.9 Velocity and pressure for a Burgers vortex with varying parameters. Left: variation of r_a; right: variation of Γ. Results are made dimensionless by $\mathscr{V}_{\text{ref}} = 0.715\Gamma\left(2\pi r_{a,3}\right)^{-1}$ and $\mathscr{P}_{\text{ref}} = 0.871\rho\Gamma^2\left(2\pi r_{a,3}\right)^{-2}$; see Figure 2.8 for an explanation.

shear layer. A study of the roll-up process has not been carried out in this work, but a simple heuristic model will be used for this purpose when tip vortex cavitation is to be simulated (see Chapter 5).

Phillips (1981) describes the roll-up process as a merging process, where the initially planar shear sheet is wound up into a spiral with a continuously increasing number of turns. The innermost turns have a circular shape and the vorticity contained in the shear layer is reorganised by a diffusive blurring when the distance between the turns gets small enough. Phillips calls this merged region the trailing vortex.[9]

Clearly, the roll-up process will be influenced by many factors, including the distribution of trailing vorticity and hence the circulation $\Gamma(y)$ or $\Gamma(r)$, respectively, as well as by the geometry of the tip of the lifting body – see, for example, Astolfi et al. (1999) or Fruman et al. (1995). Furthermore, it is not clear in how far effects due to the local tip vortex and the formation of the trailing vortex can be distinguished, especially in the region very close to the tip of the propeller blade. The tip vortex cavitation model developed in Chapter 5 neglects these effects. With respect to propeller flow, the roll-up process is completed surprisingly fast. For instance, Kuiper (2012) states that typically 80 %

---

[9] Unlike a vortex tube or vorticity tube for which Helmholtz's vortex laws apply (Schade and Kunz, 1989, pp. 265f), the circulation of such a trailing vortex as defined by Phillips is not constant.

of the blade circulation is concentrated in the tip vortex after a blade rotation of 40°. Surely, the exact value depends on the particular blade shape and the operation conditions.

Phillips also pointed to the important role of turbulence during the initial stage of the merging process of the shear layer forming the trailing vortex. On the other hand, according to Zeman (1995), the far field evolution of the tip vortex, i.e. the widening of the viscous core radius of the developed tip vortex, seems to be controlled by viscosity and not by turbulence. Further detailed studies involving experiments and theoretical analysis are presented by Devenport et al. (1996). The authors conclude that turbulence plays only a minor role when the core region of a developed tip vortex is concerned.

2.4.2 Propeller tip vortex with cavitating core

The minimum pressure in the core of tip vortex can reach values low enough to give rise to cavitation. The onset of cavitation is not discussed here and fully developed cavitation is assumed for the moment.

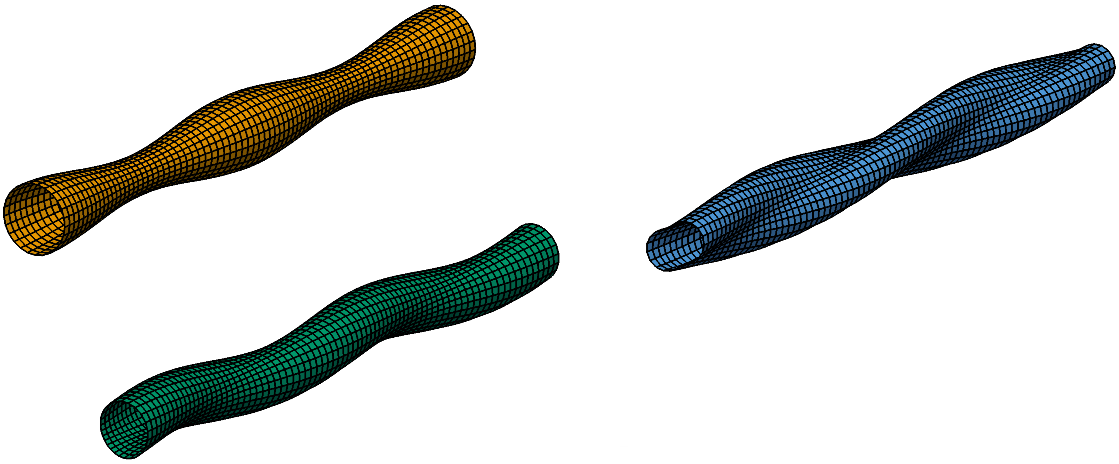

Fig. 2.10 Different modes of a vibrating hollow core vortex. Breathing mode $n = 0$ (orange, top left), bending mode $n = 1$ (green, bottom left) and double helix mode $n = 2$ (blue, right).

The interface between fluid and vapour constitutes a deformable surface and as such it acts as a carrier of waves travelling along this surface. Such mechanisms were first investigated by Thompson (Lord Kelvin) (1880), then continued by Morozov (1974), and recent contributions have been provided by Bosschers (2009a). In a general form, the local (complex) cavitation radius η_c of a columnar vortex with hollow core is given by

$$\eta_c = r_{c0} + \hat{\eta}_c \exp\left[i\left(k_\psi \psi + n\varphi - \omega t\right)\right], \tag{2.15}$$

where k_ψ is the axial wave number, n the azimuthal wave number, ω the angular frequency and $\hat{\eta}_c$ the complex amplitude in the cylindrical coordinate system (ξ, φ, ψ), which has been introduced in the previous section. The azimuthal wave number is an integer, and depending on this number, different modes of vibration, as shown in Figure 2.10, occur. For $n = 0$, the axisymmetric breathing mode results. The serpentine-like mode with $n = 1$ is called bending mode and involves a displacement of the vortex center line. Finally, for $n = 2$, the double helix mode arises with a deformation of the cross section. The only mode involving volume variations and therefore relevant for cavity-induced pressure fluctuations is the breathing mode with $n = 0$ (Bosschers, 2009a).

It is possible to derive dispersion relations for these waves, which relate wave numbers and frequency ω. Morozov did this in a linearised manner by assuming that the amplitude of the cavitation radius is small compared to the mean radius, i.e. $\hat{\eta}_c \ll r_{c0}$. For the case of $n = 0$ and long wave lengths, he gives the following asymptotic dispersion relation:

$$T_c = \frac{4\pi^2 r_{co}^2}{\Gamma} \sqrt{\ln\left(\frac{2}{\gamma k_\psi r_{c0}}\right)}, \tag{2.16}$$

where $T_c = 2\pi\omega^{-1}$ and γ denotes the Euler constant. It can be seen that for this case (i.e. $2\pi k_\psi^{-1} \gg r_{c0}, \hat{r}_c$), the dispersion is relatively weak, which is not surprising, since, for long wave lengths, the interaction forces acting between adjacent cross sections of the hollow vortex are relatively small. The disadvantage of such an investigation is the lack of information on the amplitude $\hat{\eta}_c$. So far, a non-linear and three-dimensional investigation is not known to the author. However, for the two-dimensional case, it is possible to formulate a Rayleigh-Plesset-like equation describing the oscillation of the cavity radius r_c of a cylindrical cavity inside a vortex (Chahine, 1995; Choi et al., 2009). These equations are derived and discussed in Chapter 5 in greater detail:

$$\left(r_c \ddot{r}_c + \dot{r}_c^2\right) \ln\left(\frac{r_D}{r_c}\right) + \frac{r_c^2 \dot{r}_c^2}{2}\left(\frac{1}{r_D^2} - \frac{1}{r_c^2}\right) = \frac{1}{\rho}\left(p_c - p_{\mathrm{vtx}}\right) \tag{2.17}$$

with

$$p_{\mathrm{vtx}}\left(r_c\right) = p_D - \rho \int_{r_c}^{r_D} \frac{u_\varphi^2}{\xi} \mathrm{d}\xi, \tag{2.18}$$

where the variable p_c denotes the pressure inside the cavity and equals vapour pressure p_v for the moment, and r_D is the outer integration radius and will be discussed later. The influence of the vortex flow around the cavity is represented by u_φ. Eq. (2.17) describes a non-linear oscillation of the cavity radius r_c. Thus, once excited by deflection or a change of the surrounding vortex flow, the cavity radius will undergo oscillations. It is possible to truncate those terms containing $\ddot{r}_c$ and to approximate u_φ by a Rankine vortex (Eq. (2.13)), which leads to the frequency of a small oscillation around the cavity radius r_{c0} (Franc and Michel, 2005, p. 227):

$$T_c = \frac{4\pi^2 r_{c0}^2}{\Gamma} \sqrt{\ln\left(\frac{r_D}{r_{c0}}\right)}. \tag{2.19}$$

The relation of this equation to Eq. (2.16) is obvious. Instead of the (unknown) wave length, r_D appears as a parameter. This indicates that, for long wave lengths, the solution behaves similarly to the two-dimensional solution.

It is important to note that the presence of cavitating tip vortex does not necessarily involve the generation of pressure fluctuations (Pennings et al., 2016, e.g.). It has been noted in Section 2.1.2 that cavitation-induced pressure fluctuations are related to a significant variation of the cavitation volume. If, for example, a purely sinusodial disturbance of the cavity radius along the vortex axis with moderate amplitude and a not too long wave length is present, then the overall variation of the cavitation volume observed from a point far away from the vortex (i.e. $d_P \gg 2\pi k_\psi^{-1}$), will vanish and no fluctuations of pressure will be detected, although this may be the case in the direct vicinity of the vortex. Hence, a substantial excitation of the cavity inside the vortex and a certain degree of irregularity of the cavitation shape along the vortex axis are required as necessary conditions for the radiation of effective pressure fluctuations. This is addressed in the following section.

2.5 Phenomena Related to Cavitation–Cavitation Interaction

With regard to propeller flow, isolated tip vortex cavitation is rarely found. Interaction with other types of cavitation, other distinct vortex cavities propagating from the blade and the interaction with the rudder become relevant. Several aspects of propeller cavitation, interaction mechanisms and the resultant pressure fluctuations are reviewed by Kuiper (2001), van Terwisga et al. (2007, 2006), van Wijngaarden et al. (2005) as well as Carlton and Fitzsimmons (2004). Having the essential results of these works in mind, cavitation interaction phenomena are described in the following by means of selected examples.

2.5.1 Tip vortex–sheet cavitation interaction

The propeller depicted in Figure 2.11 is designed for a container vessel and shows a typical cavitation behaviour for this type of propeller. Before entering the zone of the highest velocity deficit at 0°, sheet cavitation arises between $r/R = 0.7$ and $r/R = 0.95$. A cavitating leading edge vortex can be observed turning into the cavitating tip vortex. Approaching the angular position 10°, the zone of sheet cavitation grows and the leading edge vortex can no longer be distinguished from sheet cavitation. The cavitating tip vortex gains in size and appears to be a continuation of sheet cavitation at the blade tip. At the position 20°, sheet cavitation gets more pronounced and the spanwise extent becomes larger. The tip vortex cavitation radius at the blade tip is significantly influenced by sheet cavitation. After leaving the wake peak zone (30°), the sheet cavitation regime exceeds the trailing edge and disintegrates. Fragments of the formerly coherent sheet cavitation structure seem to migrate into the tip vortex. Also visible – albeit weakly – are remnant parts of the re-entrant jet vortex interacting with the tip vortex.

A similar behaviour can be observed in the case of the propeller of the container vessel *Sydney Express*. The photographs in Figure 2.12 show the real propeller of the ship during a full-scale measurement campaign (Keller and Weitendorf, 1979) (see Section 3.1.2 for more information). Cavitating tip vortices emerge from every single blade of the propeller. Directly at the blade tip, a

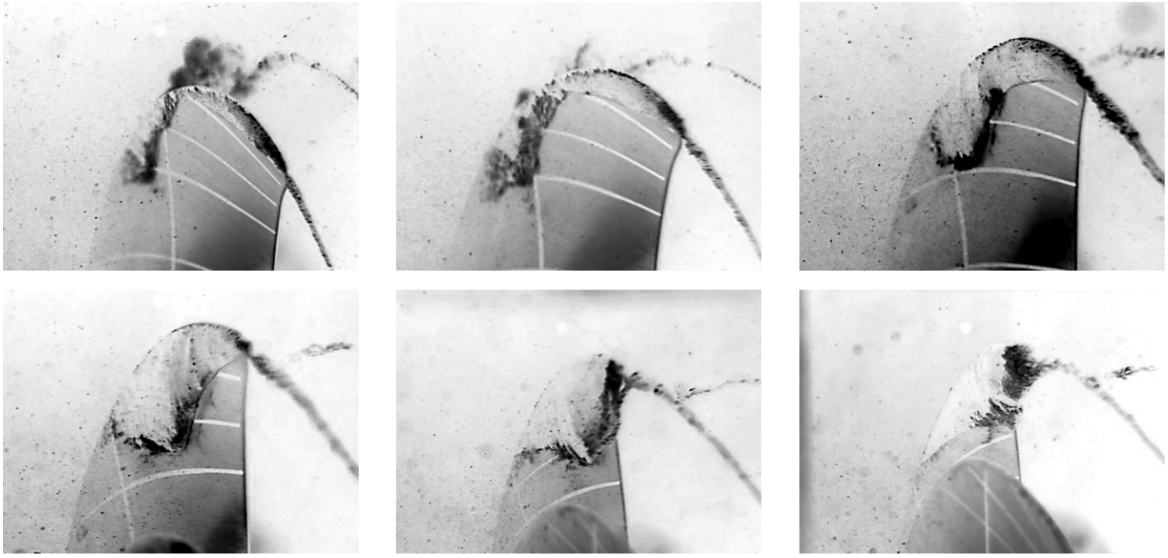

Fig. 2.11 Model test observations (model scale conditions; inverted colours): cavitating propeller of a container vessel in six angular positions (from top left to bottom right: 350°, 0°, 10°, 20°, 30° and 40°; see Figure 4.1 in Chapter 4) passing the wake peak in the 12 o'clock position; extensive sheet cavitation interacting with the cavitating tip vortex. Courtesy: SVA Potsdam GmbH, Potsdam, Germany.

local tip vortex arises due to the flow strongly circulating around the blade tip. This merges perfectly with the trailing vortex and both then constitute the (overall) tip vortex. There is a significant tendency of sheet cavitation protruding from the trailing edge which heavily influences the cavitation radius of the tip vortex. This is particularly visible in the angular positions of 15° and 25° depicted in Figure 2.12.

Consider now the antecedent blade in the positions of 345° and 0° (photographs at the top of Figure 2.12), which has already left the region of the wake peak. It can be observed that the portion of the tip vortex having absorbed the remaining parts of sheet cavitation maintains it widened shape and that this portion is swept towards the rudder. This effect is regarded as an important source of higher-order pressure fluctuations and will be resumed in Section 5.3.

When approaching the leading edge of the rudder, the tip vortex structure becomes rather cloudy and the tip vortex axis loses its clear helical shape. However, inspecting the background of the photographs reveals a complete recovery of the helical form. The mechanism demonstrated here is what is commonly understood as vortex bursting or vortex blow up (Kuiper, 2001). It has to be stated that neither the definition of this phenomenon is absolutely clear nor the underlying mechanisms are entirely understood, and a comprehensive explanatory model does not exist at present. English (1979) was one of the first to document the phenomenon. Further experimental and theoretical investigations have been carried out by Konno et al. (2002) and Lücke (2006), and full-scale observations are reported by Carlton and Fitzsimmons (2004). It can be stated that in almost every documented case

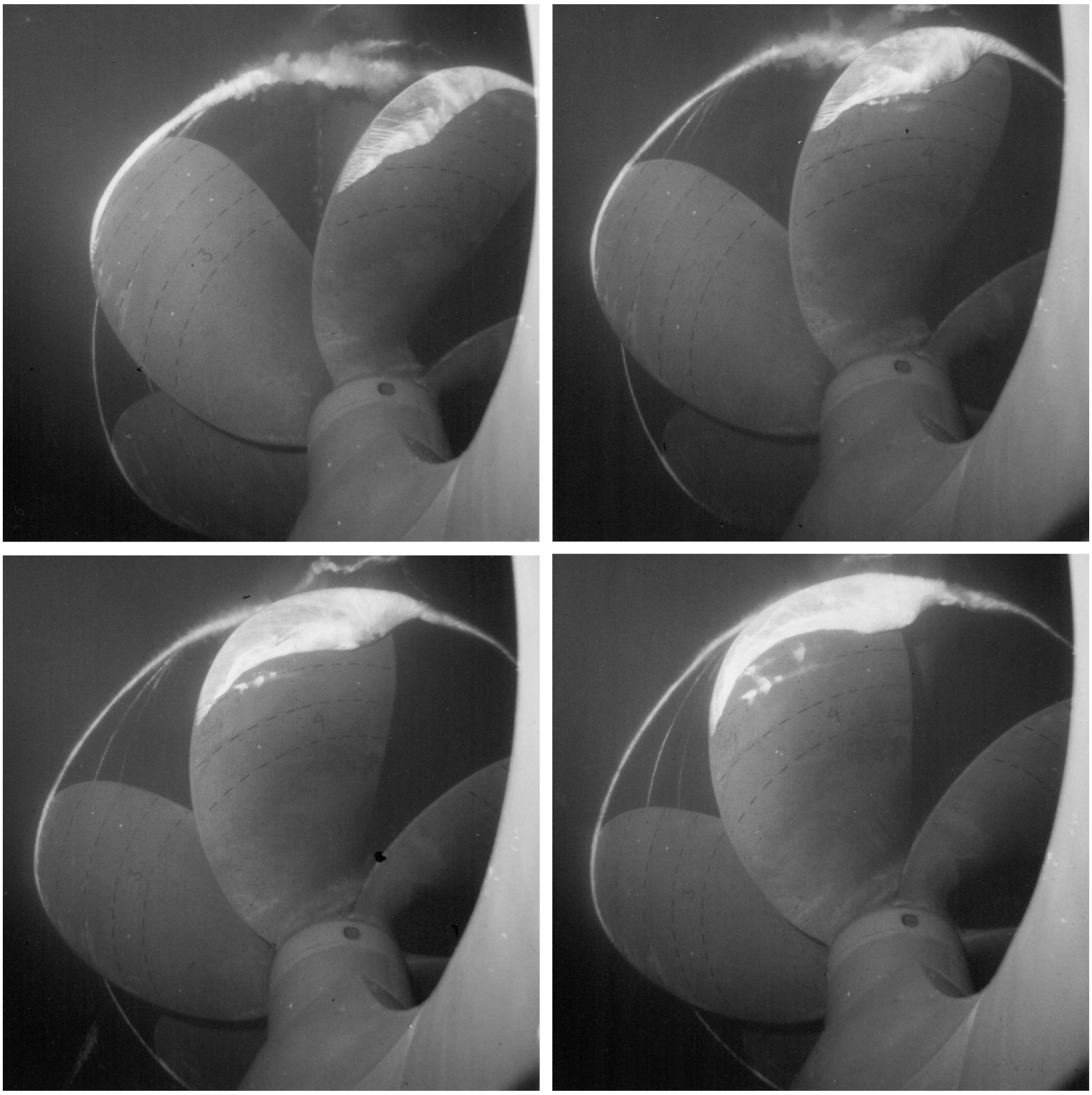

Fig. 2.12 Full-scale observations: blade passage through the wake peak in the 12 o'clock position of cavitating propeller of the container vessel *Sydney Express* in four angular positions (from top left to bottom right: 345°, 0°, 15° and 25° referring to the blade with developed sheet cavitation; see Figure 4.1). Courtesy: E. A. Weitendorf.

excessive sheet cavitation interacting with the cavitating tip vortex is present.[10] A possible explanation for this mechanism is that, apparently, the combination of entrained and violently twisted remainders of sheet cavitation and the resultant irregular widening of the tip vortex cavity is a fragile formation and the pressure gradient imposed by the rudder leads to a further destabilisation and finally to a burst. The tip vortex itself is not affected significantly by these mechanisms and proceeds persistently

---

[10] Lücke, e.g., points out a second mechanism for the occurrence of tip vortex bursting involving an instability of the vortex flow itself. It remains unclear how this can be accommodated with the entire recuperation of the tip vortex downstream of the location where vortex bursting is detected.

downstream of the burst. Figure 2.13 shows a cavitating tip vortex impinging the rudder without pronounced sheet cavitation in the blade tip region. No bursting is observed in this case, albeit a distinct deformation of the helical vortex axis appears. This indicates that the presence of sheet cavitation due to a high blade load in the wake peak region is an important parameter for tip vortex bursting.

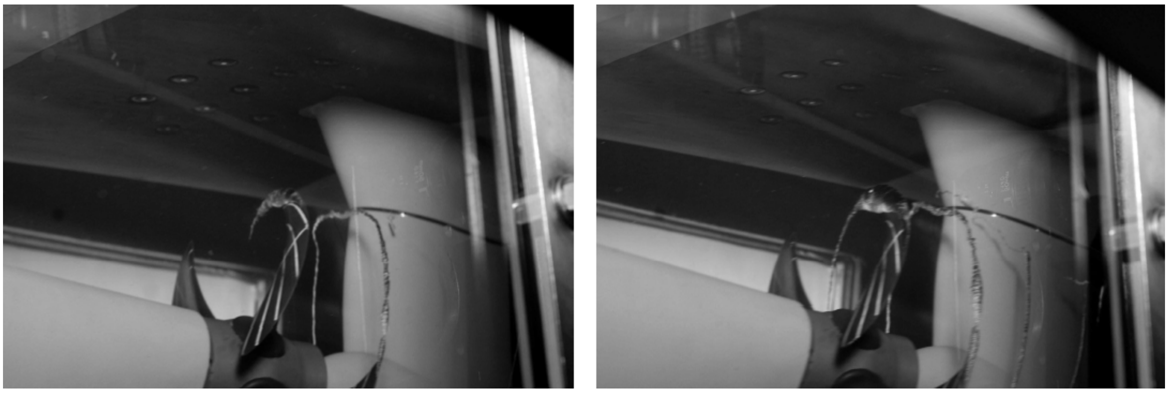

Fig. 2.13 Tip vortex impinging the rudder without vortex bursting for $\sigma_n = 0.22$. Left: $k_T = 0.22$; right: $k_T = 0.29$. Courtesy: SVA Potsdam GmbH, Potsdam, Germany.

Apart from the reasons and physical mechanisms behind this phenomenon, wide agreement exists regarding the character of the emitted hull pressure signal. If vortex bursting appears, owing to the irregularity of the burst, broadband pressure fluctuations are likely to occur (Kuiper, 2001; van Wijngaarden et al., 2005, e.g.).[11]

2.5.2 Vortex–vortex interaction

It has been said at the beginning of Section 2.4.1 that different types of vortices originating from the tip region of the propeller blade undergo a smooth merging process resulting in a unique tip vortex. This may be the case in general, but there are situations where serious vortex–vortex interaction can occur, giving rise to higher-order pressure fluctuations. The interaction of two or more vortices has been investigated in a general fashion by many authors (Bristol et al., 2004; Williamson et al., 2014, e.g.). The resulting flow pattern is highly unsteady and depends on various factors, such as vortex strength, distance between the vortices and orientation.

Figure 2.14 shows photographs taken during a full-scale measurement campaign carried out for a ConRo vessel (Lücke, 2014). More details on this campaign are provided in Section 3.1.2. The vessel is equipped with a controllable pitch propeller and was operated with reduced pitch during the campaign. To elucidate this further, RANS simulations have been carried out for equivalent operation conditions. Because of the negative incident angle, a pronounced leading edge vortex arises at the pressure side of the blade that has an even stronger intensity than the trailing vortex originating from

---

[11] Interestingly, English relates pressure fluctuations of the second and third harmonic order to the phenomenon of vortex bursting, which contradicts the findings of other authors.

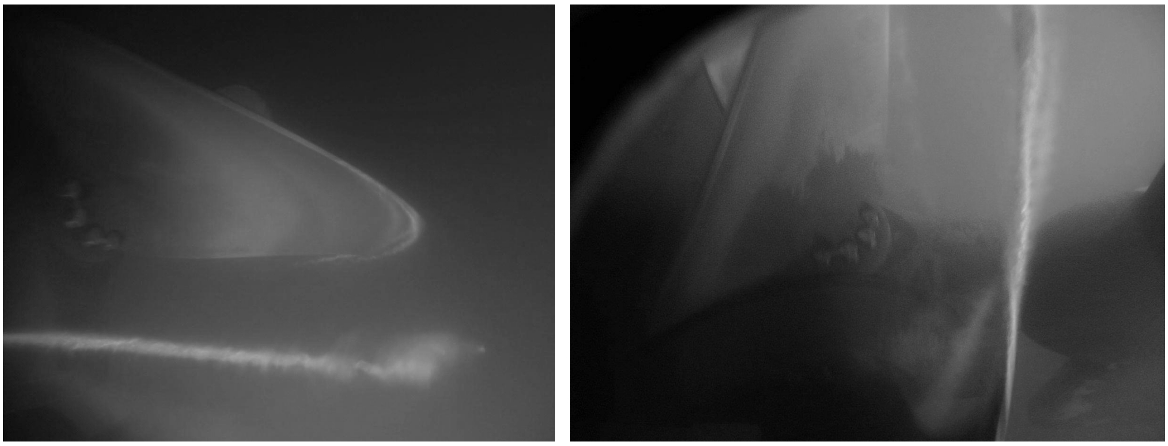

Fig. 2.14 Observation during a full-scale measurement campaign: interaction between a leading edge vortex originating from the pressure side of the blade and the trailing vortex (Lücke, 2014). Courtesy: HSVA Hamburg GmbH, Hamburg, Germany.

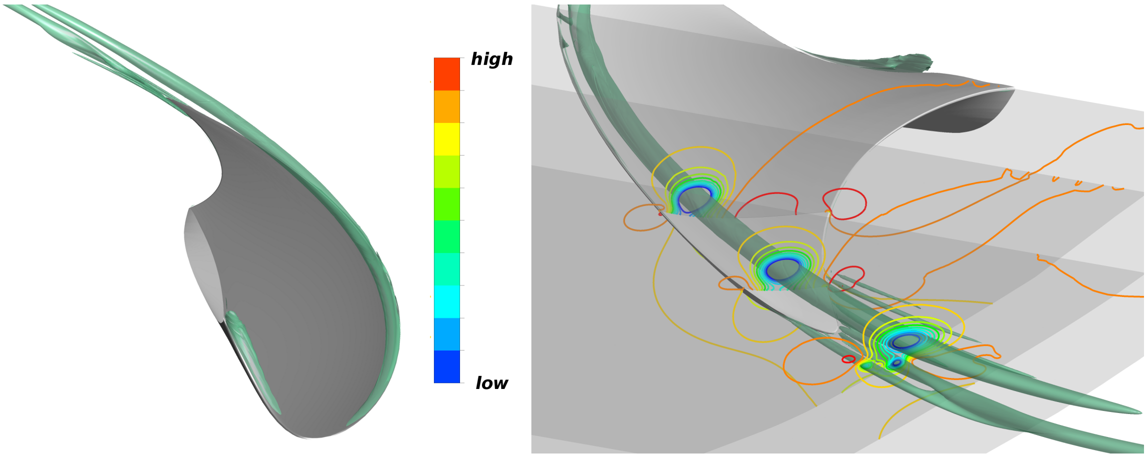

Fig. 2.15 RANS simulation of a propeller blade with large advance coefficient leading to a negative anlge of attack. Vortices are made visible by the λ_2-criterion.

the tip. These vortical structures are also discernible in Figure 2.14. According to Lücke, strong interaction was observed leading to pronounced pressure fluctuations of higher order. A similar case of vortex–vortex interaction is documented by Carlton and Fitzsimmons (2004) for a cruise vessel. Further detailed studies on this issue were carried out by Okamura et al. (1994) together with a simplified theoretical analysis. They investigated a controllable pitch propeller in off-design conditions with reduced pitch that also resulted in a strong vortex–vortex interaction and significantly increased broadband pressure fluctuations.

2.6 Theoretical Considerations of Propeller-Induced Pressure Fluctuations

In this section, theoretical considerations are made which explain how sheet cavitation and tip vortex cavitation contribute to higher-order pressure fluctuations. Usually, two parts of the frequency spectrum are distinguished: (1) discrete harmonic components of the amplitude spectrum occurring at multiples $q = 1,2,\ldots$ of the blade frequency $f_b = nn_b$ and (2) broadband components spread over the whole frequency range (see Figure 2.16).

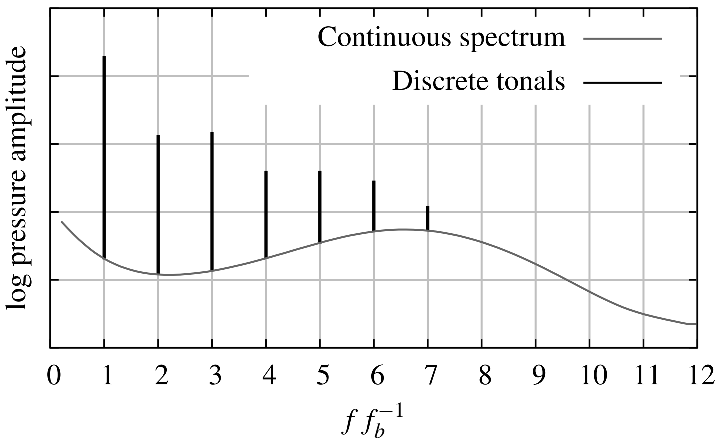

Fig. 2.16 Exemplary, schematic frequency spectrum of a cavitating propeller, reproduced and schematised from Bosschers (2009a).

A widely accepted explanation for the existence of the discrete components at frequencies qf_b is the periodic volume variation of cavitation structures on the propeller and its vicinity. The origin of the broadband part is assumed to be the random violent collapse of cavitation fragments (Bark and van Berlekom, 1978), which also comprises phenomena related to vortex bursting, and the deviation from perfect periodicity which can be observed under real conditions.

Modelling effects which contribute to the broadband part of the spectrum is beyond the scope of the thesis and the focus is put on the discrete components.[12] The effect of slight aperiodicity is discussed in a qualitative manner in Section 2.6.3. For the moment, perfect periodicity is assumed.

2.6.1 Influence of sheet cavitation

The periodic process of growth and shrinkage of sheet cavitation on the propeller blades has been described in Section 2.3. The question may arise whether this process being periodic with f_b can contribute in a noteworthy way to higher-order pressure fluctuations occurring with $2f_b$, $3f_b$ and so on. To answer this question, a generic growth and shrinkage process of sheet cavitation according to

---

[12] In fact, frequency spectra shown later in the thesis also exhibit a broadband part, which is merely a pseudo broadband part due to leakage effects and numerical inaccuracies.

Bark and van Berlekom (1978) is investigated and plotted in a dimensionless manner in Figure 2.17. A key parameter of this process is the life span T_{lc} of the sheet cavity. In the figure, five variations of the generic process are investigated (depicted in the top row): three variations (a–c) of the peak cavitation volume and the ratio between life span T_{lc} and the blade passage period $T_b = f_b^{-1}$ ranging from $T_{lc}f_b = 0.75$ to $T_{lc}f_b = 1.25$; and, in particular for $T_{lc}f_b = 1.0$, two variations of the curve shape in the final stage of the shrinkage process: Curve (d) exhibits a more abrupt collapse, and an additional cavity rebound has been added in order to obtain curve (e).

In the second row of the figure, the pressure signals according to Eq. (2.4) are approximated. The single and non-repetitive signal, i.e. the pressure disturbance induced by one single blade passage, can be transferred in the frequency domain by Fourier transformation, leading to a continuous frequency spectrum. The continuous spectra corresponding to the respective pressure signals are shown in the third row of Figure 2.17. Once the frequency spectrum of the single signal is known, the resultant discrete frequency spectrum of the T_b-periodically continued signal can be easily identified as discrete samples of the continuous spectrum at qf_b multiplied by the constant T_b^{-1}. In other words, all the information on the periodic signal is already contained in the single and non-repetitive signal.[13] The last row of the figure shows the ratio between the higher harmonic amplitudes $\hat{p}^{[q]}$ and the first harmonic $\hat{p}^{[1]}$.

First, consider the influence of the ratio $T_{lc}T_b^{-1} = T_{lc}f_b$ (curves a–c on the left side of Figure 2.17). A clear tendency becomes apparent: the shorter the life span of the cavity, the more pronounced the higher harmonics are. Considering the present generic growth and shrinkage process, the second harmonic even exceeds the first harmonic amplitude for $T_{lc}f_b = 0.75$. If the life span is rather large and sheet cavitation is present on the blades for more than, for example, a third propeller revolution as it may occur at real propellers ($T_{lc}f_b \geq \frac{5}{3}$ for a five-bladed propeller, e.g.), the induced pressure disturbance will presumably be dominated by the first harmonic amplitude and higher harmonics will play only a minor role.

In the next step, the focus is put on the influence of the final stage of the sheet cavitation shrinkage (curves b, d and e on the right-hand side of Figure 2.17). The life span of the generic examples of sheet cavitation is the same in all cases as well as the peak volume. Comparing curves (b) and (d), it can be asserted that the more collapse-like shrinkage of the cavitation volume represented by curve (d) leads to a more intense pressure peak shortly before the cavity disappears and to stronger higher harmonics. The first harmonic amplitude is nearly the same. An additional cavity rebound, as it is the case for curve (e), leads to even more pronounced higher harmonic amplitudes. As an important

---

[13] Mathematically, the single and non-repetitive signal can be interpreted as a well-behaved and rapidly decaying function $f(t)$ and the repetitive signal as its P-periodic summation $f_P(t) = \sum_n f(t+nP)$. It is then possible to express the periodic function f_P in terms of a Fourier series and to recover the discrete complex Fourier coefficients c_j from the continuous Fourier transform $\mathscr{F}(f)$ of f:

$$c_j = \frac{1}{P}\mathscr{F}(f)\left(\frac{j}{P}\right). \tag{2.20}$$

This result can be obtained by the Poisson summation formula (Wikipedia Encyclopedia, 2017).

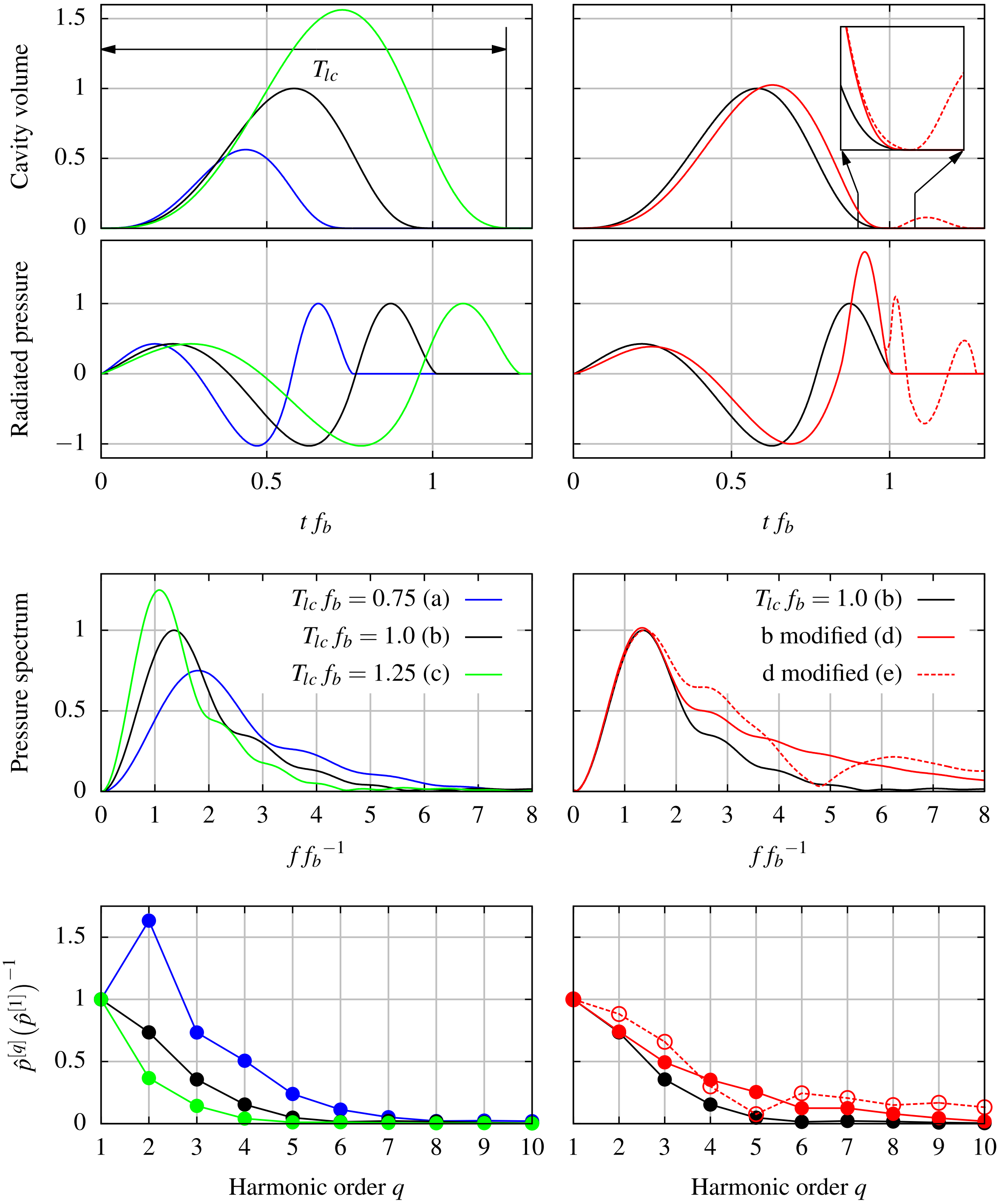

Fig. 2.17 Generic growth and shrinkage of sheet cavitation, adopted from Bark and van Berlekom (1978). Left part: various life spans T_{lc} and peak volumes, all having the same curve shape (a–c). Right part: different curve shapes in the final stage of the shrinkage process (curves d and e).

consequence, when higher-order pressure fluctuations are concerned, it is important to accurately capture the details of the final stage of the shrinkage process.

2.6.2 Influence of tip vortex cavitation

What is the contribution of the cavitating tip vortex to the frequency spectrum of pressure fluctuations? An order-of-magnitude estimate shall answer this question. Again, perfect periodicity is assumed. The maximum bound blade circulation $\mathit{\Gamma}_b$ of a propeller with diameter D can be approximated by

$$\mathit{\Gamma}_b \approx \frac{1}{\kappa}\frac{32}{\pi^2}\frac{k_T}{n_b}nD^2, \tag{2.21}$$

where $\kappa = 1.7\ldots 1.9$ depending on the blade shape and k_T is the thrust coefficient (Isay, 1991). The flow field of the developed tip vortex can be roughly approximated by an inviscid line vortex of strength $\mathit{\Gamma}_b$, for which the equilibrium cavity radius $r_{c,\mathrm{eq}}$ is given by (Franc and Michel, 2005, p. 227):

$$\frac{\mathit{\Gamma}_b^2}{8\pi^2 r_{r_{c,\mathrm{eq}}}^2}\left[1-\left(\frac{r_{c,\mathrm{eq}}}{r_D}\right)^2\right] = \frac{p_\infty - p_c}{\rho}, \tag{2.22}$$

where p_∞ is the ambient pressure, ρ the density of the fluid, p_c the pressure in the cavitating core (here $p_c = p_v$ with p_v being the vapour pressure) and r_D is the outer boundary of the flow domain. The period of oscillation $T_c = f_c^{-1}$ of such a line vortex performing a small oscillation around the equilibrium cavitation radius is given by Eq. 2.19, which has been introduced in Section 2.4.2. Using the equilibrium cavitation radius $r_{c,\mathrm{eq}}$ one obtains:

$$T_c = \frac{4\pi^2 r_{c,\mathrm{eq}}^2}{\mathit{\Gamma}_b}\sqrt{\ln\left(\frac{r_D}{r_{c,\mathrm{eq}}}\right)}. \tag{2.23}$$

Combining Eqs. (2.21), (2.22) and (2.23) leads to the ratio between the oscillation frequency f_c of the cavitating vortex and the blade frequency nn_b:

$$\alpha \equiv \frac{f_c}{nn_b} = \frac{1}{\varepsilon}\frac{\sigma_n}{k_T}. \tag{2.24}$$

Here, $\sigma_n = 2\,(p_\infty - p_v)\,\rho^{-1}n^{-2}D^{-2}$ and all constants are included in $\varepsilon = 2.7$, for which $r_D/r_{c,\mathrm{eq}} = 10$ and $\kappa = 1.8$ have been assumed. For a propeller operating at $k_T = 0.190$ and $\sigma_n = 1.8$, the ratio becomes $\alpha = 3.5$.

Consider now a small portion of the cavitating tip vortex of the length $\mathrm{d}s = 1$ performing oscillations of the amplitude $\hat{r}_c$ with only one frequency f. Then, the unsteady radius can be described by

$$r_c = r_{c0} + \hat{r}_c\cos(\omega t), \tag{2.25}$$

with $\omega = 2\pi f$, and the unsteady volume is easily obtained by $V_c = \pi r_c^2$. For distances $d \gg r_{c0}$, the pressure disturbance p_c' caused by a vibrating vortex cavity is simply $p_c'(t) \propto d^{-1}\ddot{V}_c$ (ref. Eq. (2.4)) and hence:

$$p_c' \propto r_{c0}\hat{r}_c\omega^2\cos(\omega t) + \hat{r}_c^2\omega^2\cos(2\omega t)\,. \tag{2.26}$$

For small oscillations with $\hat{r}_c \ll r_{c0}$, the radiated pressure fluctuates with frequency f, larger amplitudes $\hat{r}_c$ make additional contributions arise, occurring with $2f$. Certainly, these findings are valid for any harmonic oscillation of r_c.

The rule of thumb given by Eq. (2.24) assumes uniform tip vortex characteristics at any time for a given propeller and only small oscillations around the equilibrium cavity radius $r_{c,\mathrm{eq}}$. None of these conditions, however, is met for a propeller operating in inhomogeneous inflow: the bound blade circulation Γ_b varies continually depending on the blade load. Due to the roll-up process, the vortex strength does not become equal to the bound blade circulation immediately but gradually increases from an initial value until it reaches a value close to the bound blade circulation. Furthermore, it is very likely that the amplitude $\hat{r}_c$ is not sufficiently small for Eq. (2.19) to be entirely valid and r_{c0} is not necessarily equal to $r_{c,\mathrm{eq}}$.

As a consequence, if a single blade passage is considered, the cavitating tip vortex does not induce a pressure disturbance at only one frequency f_c; rather, it is a range of frequencies around f_c. Having in mind the assumption of perfect periodicity, the same mechanisms explained for sheet cavitation in the previous section apply when the frequency spectrum of a single blade passage is converted to the discrete spectrum of the T_b-periodically continued signal of the pressure disturbance induced by the cavitating tip vortices of the entire propeller.

2.6.3 Influence of deviation from periodicity

As indicated several times in this chapter, the condition of perfect periodicity does not apply for real propeller flow, even at laboratory conditions. Possible reasons for this are:

(1) changes of the propeller inflow conditions induced by the ships's motion

(2) imperfections of the fabricated propeller

(3) large-scale turbulent, vortical flow structures of the viscous hull flow changing randomly the local angle of attack and hence the propeller load

(4) wave loads due to seaway

(5) random changes in the local water quality

Certainly, the importance of these mechanisms is different and may depend on the particular ship type and the operation conditions of the vessel.

Baiter (1992) discusses the influence of aperiodicity in the context of propeller cavitation based on the work of McFarlane. Baiter et al. (1982) offer an advanced holistic model for the formation of the sound spectrum due to cavitating propellers. An important conclusion is that deviation from periodicity results in the appearance of a broadband spectrum, which typically exceeds the discrete components in magnitude when higher frequencies are concerned, as shown in Figure 2.16. For the ratio between discrete and continuous spectra, the parameter $s_\triangle f_b$ is important. Here, f_b is again the blade frequency and $s_\triangle$ is the standard deviation of the random deviations from periodicity (Baiter, 1992). For $s_\triangle f_b > 0.13$, the discrete spectrum is hidden in the continuous spectrum. For $s_\triangle f_b = 0$, the spectrum is entirely discrete and, according to the example given by Baiter, if $s_\triangle f_b = 0.07$, the first three harmonics become visible. Further theoretical investigations regarding aperiodicity with regard to time and amplitude have been carried out by Bosschers (2015).

Many authors agree (for example, Bosschers (2009a) or Berghult (2000)) that the cavitating tip vortex is – under certain conditions – responsible for the broadband hump often found at frequencies around the *seventh* harmonic order in the frequency spectrum of cavitating propellers (see Figure 2.16). The exact location and the width of this hump can vary from author to author. However, using the rule of thumb given in Eq. (2.24) and using typical values for k_T and σ_n as input parameters, it turns out that frequencies between the *third* and *fourth* harmonic order are affected by tip vortex cavitation. Yet none of the literature sources mention the lower frequency range between the third and fourth harmonic order as possible locations for the center of the broadband hump. Why is this the case?

One possible explanation is inhered in Eq. 2.26. An oscillation of the cavity with radius r_c and frequency f results in radiated pressures with also frequency f and, assuming sufficiently large amplitudes $\hat{r}_c$, $2f$. Those portions occurring with $2f$ may contribute to the frequencies around the seventh harmonic order. Since tip vortex cavitation is always affected by a notable amount of aperiodicity, it is very likely that discrete tonals do not exist in this higher frequency range and a broadband hump arises apart from the contributions to the third and fourth order mentioned above.

Chapter 3

Prediction of Propeller-Induced Pressure Fluctuations

In the previous sections and chapters of this thesis, it has become clear that the problem of propeller-induced hull pressure fluctuations is complex, and this is certainly reflected in the prediction of pressure fluctuations. The experimental prediction carried out by ship model basins is still the method of choice for reliable results. However, in parallel to this, theoretical concepts yielding various numerical approaches have arisen in the past century, some of which show a surprisingly good agreement with the experimental methods – keeping in mind the complexity of the problem. In this reviewing chapter, the state of the art shall be reported briefly.

Achievements and various experiences with respect to the investigation of cavitating propeller flow and hull pressure fluctuations can be found in a comprehensive but condensed form in the reports of ITTC[1]. Van Wijngaarden (2011, pp. 15ff) has summarised the information contained therein. A broad overview can be found in Carlton's book (Carlton, 1994, pp. 197ff, pp. 259ff, pp. 335ff). Further reviews are given by van Terwisga et al. (2007), Johannsen (1998) and Heinke (2003), for example.

This chapter consists of two sections. In Section 3.1, some problems regarding the experimental prediction (model scale test and full-scale observations) are discussed. In Section 3.2, aspects and challenges of numerical prediction are dealt with.

3.1 Experimental Prediction

3.1.1 Cavitation tunnel experiments

Nowadays, cavitation tunnel experiments are a commonly-accepted tool for commercial propeller tests. The aim of these tests is to predict the cavitation behaviour of the full-scale propeller by investigating a model which is scaled by a factor λ. When propeller-induced pressure fluctuations are of concern, tests are carried out with ship model, propeller and rudder. The ship model is equipped with pressure

---

[1] *ITTC* is an abbreviation for *International Towing Tank Conference*.

transducers located on a raster on the hull surface above the propeller. For the experiments to be entirely portable to full-scale conditions, geometrical and flow similarity must be conserved (Carlton, 1994, pp. 219ff).[2] Geometrical similarity can be obtained by maintaining a certain level of accuracy when the model prototype is fabricated.

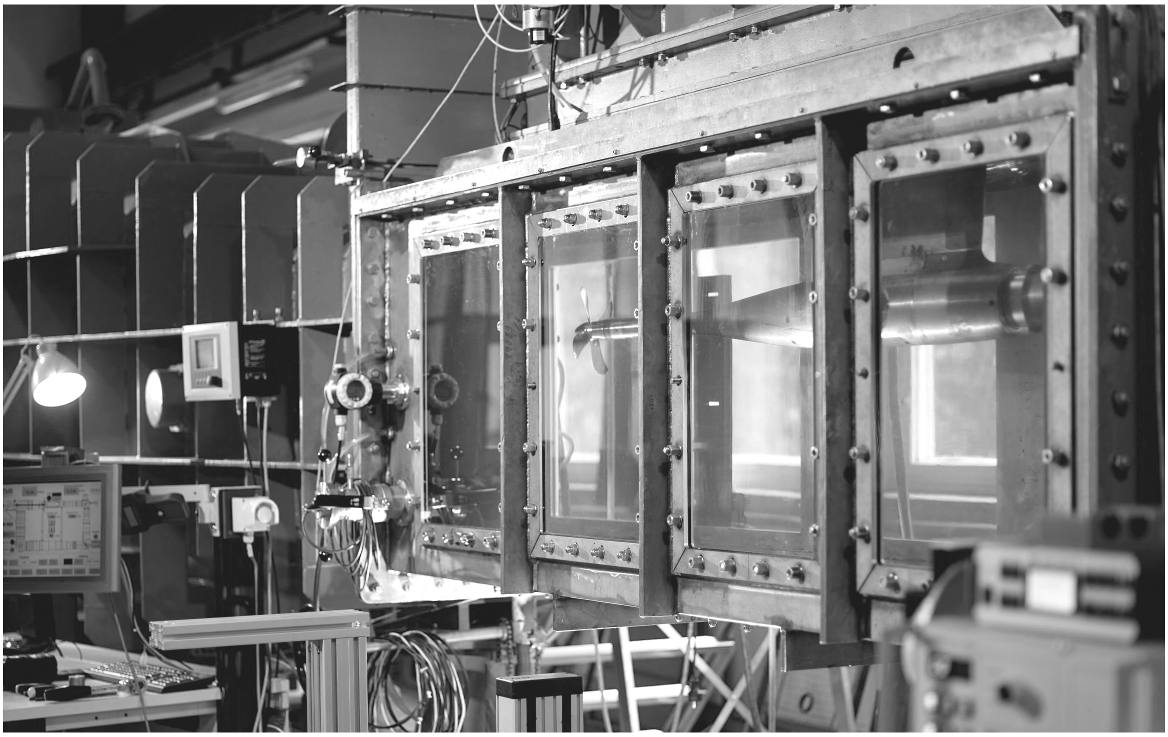

Fig. 3.1 Cavitation tunnel K15A of SVA Potsdam with square test section and propeller prepared for open-water cavitation experiments. Partially visible in the photograph: the strengthened circulatory tunnel; not visible: the impeller and driving motor approximately ten meters below the test section. Courtesy: SVA Potsdam GmbH, Potsdam, Germany.

According to Carlton, ensuring identity of the following characteristic numbers enables flow similarity between model and full-scale ship: the Froude number $\mathrm{Fn} = \mathscr{V}\left(g\mathscr{L}\right)^{-0.5}$, the Reynolds number $\mathrm{Re} = \mathscr{V}\mathscr{L}\nu^{-1}$, the Weber number $\mathrm{We} = \rho\mathscr{V}^2\mathscr{L}S^{-1}$, the advance ratio $J = V\left(n\mathscr{L}\right)^{-1}$ and the cavitation number $\sigma = \left(p - p_v\right)\left(0.5\rho\mathscr{V}^2\right)^{-1}$, with $\mathscr{V}$ and $\mathscr{L}$ being a characteristic velocity and length, respectively, as well as p being the pressure in the flow, V the ship speed and n the number of revolutions. ρ, μ, g, S and p_v are the density, the viscosity, the gravitational constant, the surface tension and the vapour pressure, respectively. The influence of We is not discussed here since this number governs predominantly the onset of cavitation, which is not the focus of the present thesis.

Obviously, it is not possible to arrange an experimental setup where the identity of all the characteristic numbers for model and full-scale ship is satisfied simultaneously and thus a compromise is needed.[3] What this compromise looks like exactly depends on the particular model basin carrying

---

[2] Flow similarity may be decomposed into kinematic and dynamic similarity (van Wijngaarden, 2011, pp. 39ff).

[3] For instance, adhering to Re-identity and assuming constant viscosity, the model speed is λ-times *higher* than the full-scale ship speed; adhering to Fn-identity, it is $\sqrt{\lambda}$-times *lower*.

out the experiments and the constraints imposed by the particularities of the respective cavitation tunnel. The basic idea, however, is the same in most cases. It is assumed that the influence of the hull-induced wave system can be neglected when propeller cavitation is investigated, which allows for dropping the Froude number Fn and carrying out cavitation tests without considering the free water surface.[4] Within the limitations of the tunnel capacities, the ship speed, i.e. the inflow velocity, and the number of revolutions of the propeller are set as high as possible while maintaining J-identity in order to keep the difference between full-scale and model Reynolds number as small as possible. Also owing to these aims, the diameter of the model propeller is chosen to be as large as possible. It then may happen that the test section is not long enough to house the entire model of the ship hull. For this reason, the claim of global geometrical similarity is abandoned and dummy models with shortened mid ship section and a simplified bow geometry are used if necessary. In these cases, geometrical similarity is only maintained locally in the region of the aft ship and the only characteristic length $\mathscr{L}$ which can consistently be used is the propeller diameter D.

Another implication of abandoning identical Froude numbers is that the equality of the cavitation number σ can only be claimed for a specified reference location and not for the entire fluid domain (Isay, 1989, pp. 373ff).

Even the minimised difference of Re between model and full-scale variant is not small enough to prevent Reynolds number scale effects entirely. These scale effects are dealt with in Chapter 8 and can be roughly classified as follows:

(1) The viscous hull flow, i.e. the wake field, of the model often differs significantly from the one of the full-scale ship in terms of axial velocity deficit in the 12 o'clock position and the velocity components in the direction of y and z. In particular, the velocity deficit in the wake peak region is significantly higher for the geometrically similar model than for the full-scale ship. This is called wake scale effect here and has a direct influence on the propeller load and the cavitation behaviour.

(2) The viscous boundary layer flow of the propeller blades is different for model and full-scale propeller. As the tip vortex originates from the rolled-up shear layer shed from the trailing edge, there is a strong correlation between the boundary layer thickness and the radius of the viscous vortex core, which will influence the behaviour of tip vortex cavitation.

Each ship model basin pursues a different strategy to overcome the incorrect representation of the full-scale wake field. The basic idea, however, is always the same and consists of achieving the best possible local similarity of the flow in the vicinity of the *propeller* wilfully sacrificing global geometrical and flow similarity.

A superior condition towards this is to ensure an average J-identity of the propeller flow between model $\bullet_m$ and full-scale propeller $\bullet_s$ and it is assumed that this is equivalent to the identity of the

---

[4] In fact, there are some test facilities with free water surface; for example, the depressurised wave basin *DWB* of MARIN in Wageningen, The Netherlands.

thrust coefficient $k_T = T\rho^{-1}n^{-2}D^{-4}$, which is much easier to monitor. A direct consequence of this demand is that a *global* J-identity can no longer be maintained since the inflow velocity of the model will be relatively higher than the advance velocity of the full-scale ship due to compensating the overstated wake peak. On account of this, the inflow velocity is no longer a suitable reference velocity for the formulation of the cavitation number. Instead, the product of propeller diameter and number of revolutions nD is used as reference velocity, and the cavitation number gets:

$$\sigma_n = \frac{p_{\text{ref}} - p_v}{\frac{\rho}{2} n^2 D^2}, \tag{3.1}$$

where the reference pressure p_{ref} is chosen as the hydrostatic pressure p_{stat} at the propeller axis or at a distance of $0.8R$ above the propeller axis where most of the propeller cavitation is assumed to occur. To sum it up, the two most important conditions for flow similarity in the experimental procedure are identity of the thrust coefficient and the cavitation number between model $\bullet_m$ and full-scale ship $\bullet_s$:

$$k_{T,m} = k_{T,s} \tag{3.2}$$

and

$$\sigma_{n,m} = \sigma_{n,s}. \tag{3.3}$$

Adhering to average J-identity or k_T-identity, respectively, does not solve the problem entirely since the velocity gradients and distribution in the wake field are still not converted correctly. The following examples illustrate how ship model basins correct this error:

(1) When a dummy model with shortened mid ship section as depicted in Figure 3.2 is used, additional wake screens are attached to the model. By means of a viscous flow simulation with a RANSE solver (see Section 4.1) of the full-scale ship hull, the nominal wake field, i.e. the velocity field under absence of the propeller, is calculated. The wake screens are then adjusted in size and position until the manipulated nominal wake field of the dummy model fits the previously simulated full-scale counterpart (Heinke, 2003). This procedure is an intelligent try-and-error method involving the experience and knowledge of the ship model basin. This approach is used by SVA Potsdam, for example. The model test results used later in Chapter 7 have been obtained by this approach.

(2) Alternatively, none of these corrections is applied and a geometrically similar model of the hull is used. The overestimation of pressure fluctuations due to the wake scale effect is then counteracted by empirical methods. It is also possible to desist from claiming J-identity in the propeller plane (and consequently k_T-identity) and to enforce a local J-identity in the wake peak region. The rationale for this approach is that cavitation is particularly active in this blade position (Johannsen et al., 2012; Schuiling et al., 2011).

(3) A novel concept is the *Smart Dummy* approach which has been developed at MARIN. It attempts to modify the form of the ship model in a way that the wake field of the modified

model resembles the wake field of the full-scale ship. A RANSE solver is used to perform this inverse design process. Practical limitations have to be obeyed when the *Smart Dummy* is designed (Schuiling et al., 2011).

It is important to note that these corrections only apply to the wake scale effect. The viscous boundary layer of the propeller blades is still not correctly extrapolated from the model to the full-scale propeller. This problem will be addressed in Section 8.2.2.

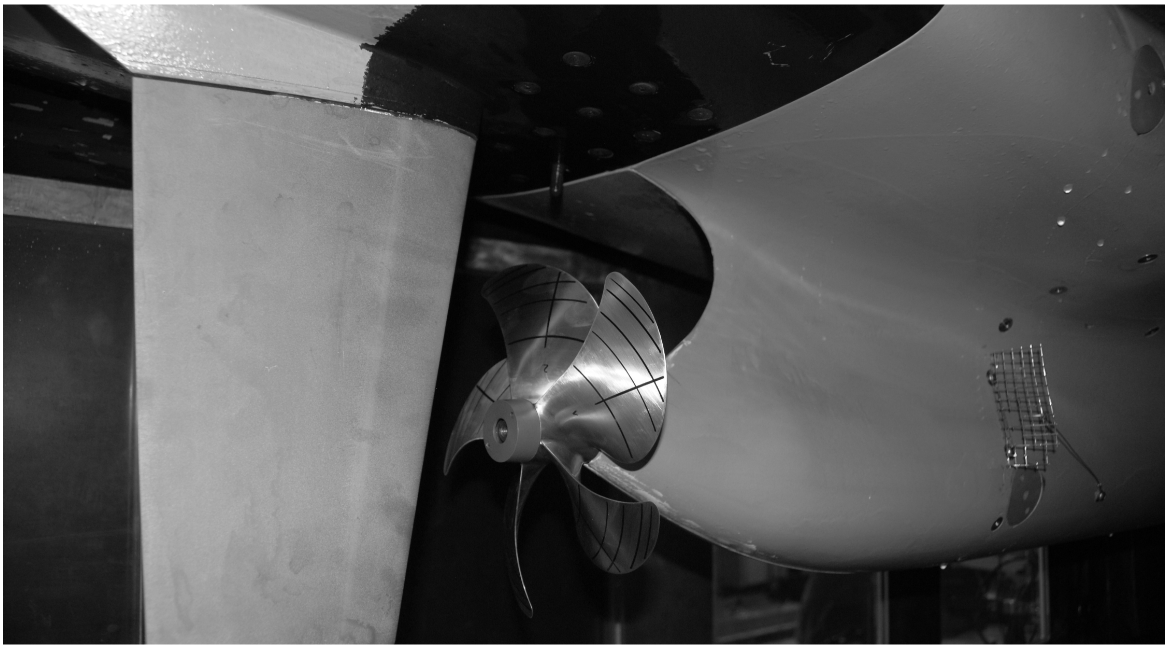

Fig. 3.2 Dummy model of a container vessel equipped with propeller, rudder and wake screens (wire mesh visible in the right part of the photograph attached to the hull). Such models are commonly used at SVA Potsdam for cavitation experiments. Courtesy: SVA Potsdam GmbH, Potsdam, Germany.

Apart from these considerations, a lot of other problems must be addressed when a certain level of accuracy shall be achieved. These are, for example, the influence of the walls of the test section and problems caused by vibration of the cavitation tunnel itself. A great concern is the influence of the water quality in terms of gas content and nuclei concentration.

3.1.2 Full-scale observations

Full-scale observations and measurements are of great importance for the validation of experimental and numerical methods of prediction. In contrast to model tests, measuring flow quantities of any kind needs to be performed from the inside, which often leads to complications. Sophisticated measurement techniques are required; most of them make it necessary to drill holes in the shell plating or to flame-cut openings for underwater observation windows. Furthermore, all full-scale measurements usually have to be conducted during the regular service operation, which often leads to very imprecise information on the operation and surrounding conditions. However, even with these limitations, useful insights with respect to the correlation between experimental and numerical prediction and the full-scale ship can be extracted from those measurements.

Fig. 3.3 Exemplary equipment for full-scale measurements. Left and center: laser and camera for PIV measurements of the velocity field in front of the propeller (Damaschke et al., 2014); right: pressure transducers for measuring propeller-induced hull pressure fluctuations and observation window (Lücke, 2014). Courtesy: Institute for Optoelectronics and Photonic Systems at Rostock University and HSVA Hamburg GmbH, Hamburg, Germany.

A general problem of full-scale observations is that the measurement equipment usually has to be installed in void spaces between engine and rudder where the room can be very constricted. Noise, extreme temperatures as well as insufficient aeration create a stressful working atmosphere. Furthermore, the structure often vibrates heavily, all of which needs to be taken into consideration when measurement equipment is installed (Keller and Weitendorf, 1979). Vibrations can be excited by the propeller or by the machinery in the aft ship region. Disregarding the actual source, these vibrations can significantly affect the accuracy of the measurements. Huse (1968) has recognised this problem and reports some theoretical considerations yielding to a quantitative estimation.

In the 1970s, there was an abrupt rise in scientifically evaluated full-scale measurement and observation campaigns in the non-military field. In fact, propeller cavitation had been already an issue before this time. However, it started to become a serious problem when container vessels were equipped with powerful engines and propellers transmitting this power into the water. A number of full-scale observation campaigns on container vessels were reported on the occasion of the *Symposium on propeller induced ship vibration* held in London in 1979 (RIN, 1979). Johnsson et al. (1976) reports on the correlation between full-scale observations and model tests made for a triple-screw high-speed container vessel. Furthermore, Carlton and Fitzsimmons (2004) present some full-scale observations obtained more recently by the minimally invasive borescope technique. Their observations of cavitation pattern comprise a wide range of vessel types. In the following, two examples of full-scale observation campaigns will be described in greater detail:

Container vessel Sydney Express One of the first full-scale measurement campaigns was conducted in the late 1970s during the voyage of the container vessel *Sydney Express* (Keller and Weitendorf, 1979). This campaign was the result of a collaboration of several German research institutes. The primary goal was to gather information on the water quality in terms of bubble and particle concentration, which had been acknowledged as an important parameter for determining the cavitation behaviour of propellers. For this purpose, a novel optical measurement technique based on laser light was used. Additionally, by the same technique, the flow velocity in front of the propeller was obtained. Due to a lack of time, the measurements could only be carried out for a single location. Strain gauges were attached to the shaft in order to measure the shaft power. Beyond the openings in the shell plating necessary for the laser beams and the optical sensors, conversions were conducted in order to install cavitation observation windows and pressure transducers. During the journey, a number of high-quality photographs were taken which are shown in Figures 2.4 and 2.12.

Pressure fluctuations up to the third order are documented for this case. The results of this campaign were widely used for validation purposes and investigations related to the correlation of cavitation effects between model and full-scale conditions. Such activities are documented in the ITTC Cavitation Committee reports of the years 1981 – 1990 (ITT, 1981, 1984, 1987, 1990).

ConRo vessel Amandine More recently, within the research project KonKav II, several measurement campaigns were conducted aboard the ConRo vessel *Amandine*, a freight ferry with controllable pitch propeller operating in the North Sea. The vessel had already been equipped with observation windows in the aft ship and no conversions of the hull structure were carried out. The primary goal of these campaigns was to obtain information on the velocity field directly in front of the propeller and hence on the effective wake field. The optical measurement technique applied was based on a PIV[5] methodology (see Damaschke et al. (2014) for more information). In contrast to the Sydney Express measurements, several control volumina were sampled which helped to determine the velocity distribution in the wake peak region. Additionally, strain gauges were used to record the mean propeller torque and the torque fluctuations transmitted by the shaft (Stoye, 2014). Use will be made of these data later in Section 7.2.

Cavitation observations and measurement of pressure fluctuations made for the vessel when operating with reduced propeller pitch reveal a complicated interaction between leading edge and trailing vortex emanating from the tip, which has already been shown in Figure 2.14 and explained in Section 2.5.2. In this particular case, pressure fluctuations of the fifth order even exceed first-order fluctuations – a very rare finding which was related to the complex unsteady cavitation pattern (Lücke, 2014). Complementary model test experiments were carried out by two model basins for operation conditions similar to those identified during the full-scale observations. Although a similar cavitation pattern could be observed in the model test with an increase of higher-order fluctuations, the full-scale measurement results could not be reproduced entirely (Heinke and Richter, 2014; Lücke, 2014).

---

[5] *PIV* is an abbreviation for *Particle Image Velocimetry*.

3.2 Numerical Prediction

The numerical prediction of propeller-induced hull pressure fluctuations is an appealing alternative to the experimental prediction because of possible savings of time and cost. In this context, the field of numerical simulation comprises various subordinate problems, such as the simulation of the viscous hull flow, the simulation of the propeller flow and cavitation modelling. The review to be made in this section will not address all the achievements in these subordinate fields of research and development. Rather, the focus is put on reviewing existing (overall) approaches for determining pressure fluctuations. However, because of its relevance, some achievements of tip vortex cavitation modelling are reported.

3.2.1 Overview and development of numerical prediction methods

For the investigation of propellers considering the interaction with the ship hull, which also includes the prediction of propeller-induced pressure fluctuations, the available methods can roughly be classified into three groups (see Figure 3.4):

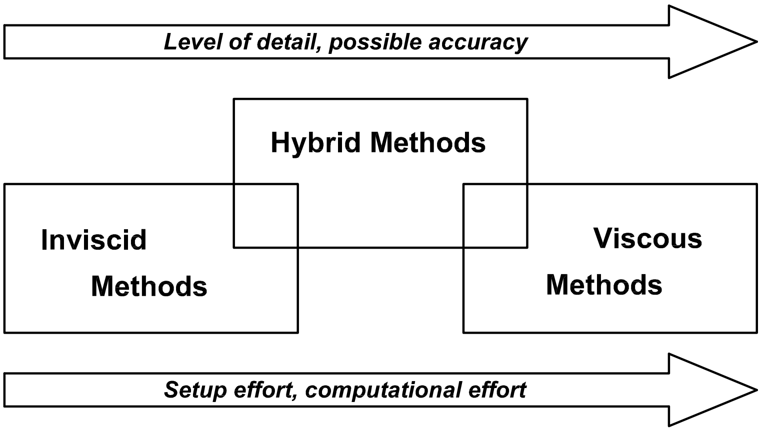

Fig. 3.4 Different groups of methods for predicting propeller-induced pressure fluctuations.

(1) *inviscid methods* for irrotational flow based on potential theory as, for example, panel methods, vortex lattice methods or methods based on wing section theory

(2) *viscous methods* based on the solution of the Navier-Stokes equations

(3) *hybrid methods* being a suitable combination of the aforementioned methods

In the following, some representative examples for the three groups of methods are given and their historical development is briefly sketched.

Inviscid methods Because computation capacity was quite limited five or six decades ago, the first attempts to numerically simulate propeller-induced pressure fluctuations were based upon inviscid methods. One of the first engineers to investigate pressure field disturbances induced by a rotating propeller were Breslin (1958) and Breslin and Tsakonas (1959). Neither cavitation nor effects due the inhomogeneity of the inflow were taken into account, but some valuable knowledge about propeller-induced pressure fluctuations was acquired. These works have been cited in Section 2.1.

Huse (1972) and Weitendorf (1976, 1977) took into account the effect of cavitation by using a corresponding distribution of sources to represent the cavity volume. However, the extent and the volume of cavitation could not be calculated by their methods and experimental data had to be used in order to predefine the unsteady behaviour of cavitation in the numerical model. Interestingly, both authors already considered the cavitating tip vortex in their calculations. In Huse's work, the radius of the vortex cavity is assumed to be a small constant portion of the propeller radius. Not surprisingly, the contribution to hull pressure fluctuations of a cavitating tip vortex modelled in such a way is almost zero. Inspired by Ackeret's (1930) work, Weitendorf (1977) considered the fluctuations of the cavitation radius in his calculations. The amplitudes and the cavitation radius had been determined experimentally. In doing so, he was able to demonstrate that the cavitating tip vortex contributes significantly to higher-order pressure fluctuations.

One of the next steps was to develop a model that was able to forecast the dynamical behaviour of cavitation on a propeller in unsteady flow. This was an important step towards making real numerical predictions of propeller-induced pressure fluctuations. At the beginning of the 1980s, two research groups made advances in this regard. Alwardt et al. (1982) used a stripe method based on wing section theory to calculate the cavitating propeller flow in inhomogeneous inflow. They introduced additional unknown sources and vortex distributions in order to take into account sheet cavitation. Determining these unknown singularities requires additional boundary conditions:

(1) the *dynamic boundary condition* requiring the pressure to equal vapour pressure on the cavity surface

(2) the *kinematic boundary condition* requiring that no flow penetrates the cavity surface

In other words, the cavitation problem is interpreted as a free streamline problem with predetermined pressure on the streamline (Streckwall, 2003). This formulates the basic concept of sheet cavitation modelling in potential flow theory.

Breslin et al. (1982) used a boundary element method with sources and dipoles located on the camber surface of the blades that took into account inhomogeneous inflow. In order to reduce the computational effort, the key blade concept was used. Boundary conditions similar to those used by Alwardt et al. were applied in order to derive the cavity shape of each radial stripe of the propeller geometry. The resulting pressure fluctuations were evaluated on the hull surface, which was also considered in the numerical model.

More recently, Abels (2006a,b) used a vortex lattice method that contained a model for sheet cavitation. He accounted for the effective wake field when determining the propeller inflow. The effective wake field was obtained by a conversion of the measured nominal wake field considering the contraction of the propeller stream. The developed simulation method was tested for a number of vessels and showed satisfactory results for first-order pressure fluctuations.

The computational effort of these purely inviscid methods is relatively low compared to alternative concepts. However, when sheet cavitation is to be simulated, the computational effort increases significantly because most of the cavitation models incorporated in inviscid simulation methods require an iterative solution procedure. This, in turn, is because the cavity planform is part of the solution sought (see Section 4.2). Furthermore, inviscid methods require the specification of the ship's wake field, which is not the case for hybrid or fully viscous approaches.

Hybrid methods An example for hybrid methods involving the combined use of more than one method is given by van Wijngaarden (2011). His strategy consists of applying a RANSE solver for the prediction of the nominal wake field and performing a subsequent conversion to the effective wake field. Using this as inflow, the instationary propeller load and the varying extent of propeller sheet cavitation are simulated by a panel method for potential flow with sources and dipoles distributed over the blade surface. Sheet cavitation is modelled using a formulation proposed by Fine (1992). Hull pressure fluctuations and radiated far field sound are analysed by an acoustic scattering method based on the Kirchhoff-Helmholtz integral equation.

The advantage of hybrid approaches is the good compromise between efficiency and the level of detail. This makes it particularly suitable for propeller optimisations. Such attempts were made by Larsson et al. (2006) and Vesting (2015). In both works, propellers in behind-conditions were optimised with respect to efficiency and cavitation behaviour as well as pressure fluctuations by means of appropriate optimisation algorithms. Propeller–hull interaction is modelled by a body force coupling approach between a RANSE solver and an inviscid method for predicting the cavitating propeller flow. A disadvantage of hybrid methods is that, because more than one method is involved, inaccuracies and additional effort due to the presence of interfaces between the respective methods may become a problem.

With respect to first-order pressure fluctuations, the agreement between simulation and experiment or full-scale observation is acceptable in most cases. When second or higher-order fluctuations are considered, results obtained by numerical methods often exhibit deviations compared to experimental results. Van Wijngaarden (2011, p. 118) considers the incomplete representation of the cavitating tip vortex as one of the reasons for the unsatisfactory results. Owing to this, tip vortex cavitation modelling is of great importance when numerical methods are developed.

Viscous methods Purely viscous methods are computationally more expensive. In return, they do not have the disadvantage of interfaces being necessary between different methods and, from a theoretical standpoint, they inherently capture the propeller tip vortex and cavitation. However, as shown by Hsiao and Chahine (2008), a fine grid resolution and diligent turbulence modelling is required to capture the high velocity gradients in the tip vortex region. Generally, if not paying attention to this, tip vortex cavitation is not even rudimentarily detectable in such simulations.

Two classes of cavitation models can be distinguished when using a viscous method based on the solution of the Navier-Stokes equations – following Yakubov et al. (2011):

(1) *Euler–Euler* cavitation models, where it is commonly assumed that both the vaporous and the liquid phase share the same pressure and velocity field. An additional variable, the volume fraction, is introduced and a transport equation with a source term is employed in order to close the system of equations governing the flow. Cavitation modelling manifests in the formulation of a source term for which certain variants exist. Generally, these models need to be calibrated, which is – according to Yakubov et al. – considered to be questionable. Nevertheless, they can lead to reasonable results for engineering problems at an acceptable computational effort.

(2) *Euler–Lagrange* cavitation models take into account the motion, growth and shrinkage of individual bubbles governed by the Rayleigh-Plesset equation. The behaviour of the bubbles results from the pressure and velocity field of the the non-dispersed phase. If cavitation becomes developed and extends over substantial regions of the fluid, it may become important to allow for a two-way coupling, i.e. to consider the effect of the vaporous phase on the liquid non-dispersed phase. Theoretically, Euler–Lagrange cavitation models are more accurate than Euler–Euler cavitation models. However, the computational effort is very high, which is why they are not commonly employed for industrial applications.

A purely viscous simulation of ship and propeller was carried out by Paik et al. (2013a,b) using a RANSE solver. In order to model cavitation, an Euler–Euler single-fluid two-phase mixture flow approach was employed in their simulations. More recently, Fujiyama (2015) performed a numerical study similar to Paik et al., but with more attention paid to a better resolution of the propeller tip region. The results reveal a good agreement with the experimental data for first-order and second-order pressure fluctuations. Tip vortex cavitation is visible, although vanishing quite close to the propeller tip.

Attempts to simulate cavitation and propeller-induced pressure fluctuations with a cavitation model based on an Euler–Lagrange approach were made by Abdel-Maksoud et al. (2013) for a hull–propeller configuration. The presented results are very promising. However, one has to keep in mind the huge computational effort of such simulations.

Shin (2016) performed a DES simulation of a propeller–rudder configuration using an Euler–Euler single-fluid two-phase mixture flow approach to model cavitation. Special attention was paid to a fine resolution of the entire tip vortex helix. Unfortunately, neither results with respect to pressure fluctuations are reported nor any information on computation time is given; however, the cavitating tip vortex is quite persistent, giving rise to confidence with respect to future developments.

3.2.2 Remarkable developments in tip vortex cavitation modelling

In this section, a few examples of innovative concepts for modelling tip vortex cavitation comprising a wide range of complexity and computational effort are reported.

Hsiao et al. (2015) presented a multi-scale Euler–Lagrange two-phase cavitation model applicable to propeller flow. The micro-scale level comprises the tracking of small bubbles and cavitation nuclei as well as their growth. On the macro-scale level, larger coherent cavities are considered. In their approach, additional models are included to consider the coalescence of bubbles or the disintegration of formerly coherent structures. The published snapshots of the simulations show a realistic cavitation behaviour. Pressure fluctuations were not taken into consideration.

Instead of using an extremely fine mesh in the tip vortex region, Hachmann et al. (2011) pursued a different strategy. They applied vortex confinement to prevent unphysical decay of vortex strength, i.e. anti-diffusive correction terms were added to the Navier-Stokes equations. The challenge is to reliably detect the prominent vortex structures and perform the respective manipulations only in restricted regions encompassing the tip vortex. Their approach can be combined with an Euler–Lagrange cavitation model and the presented results reveal an improved persistence of the cavitating tip vortex – a significant step towards the real physical situation. Results with respect to pressure fluctuations were not reported.

Obviously, the computational effort for capturing the cavitating tip vortex by a purely viscous approach is very significant and the applicability of these approaches to day-to-day simulations methods is limited. Attempts have been made to address the problem of tip vortex cavitation prediction by alternative methods.

Berghult (2000) offers a noise prediction method based on empirical formulae. These were developed based on the analysis of data which was generated by the experimental investigation of more than 300 propellers. A similar approach was chosen by Raestad (1996) using a much smaller data set. Certainly, if the propeller design undergoes only changes in nuances, such regression formulae are an appropriate measure to predict the level of pressure fluctuations radiated by the tip vortex. A deeper insight in the physical processes cannot be achieved by such methods.

Lee (2002) enhanced a panel method by introducing additional panel elements along the tip vortex. The shape of the vortex cavity is then determined in an iterative manner until additional adequate boundary conditions on the cavity surface similar to those mentioned above are fulfilled. However, no results with respect to pressure fluctuations induced by the cavitating vortex were published by the author. Szantyr (2006) as well as Kanemaru and Ando (2015a,b) consider discrete segments of the cavitating tip vortex and make use of the Rayleigh-Plesset equation in order to calculate the dynamical behaviour of the segments. The driving pressure field of the vortex is approximated by a vortex model in their methods and the induced pressure fluctuations are obtained under the assumptions of incompressible potential flow. In an earlier work, Ligneul (1989) also applied a Rayleigh-Plesset-type equation for determining the unsteady cavitation radius; however, he took into account the compressibility of the fluid when calculating the radiated pressure disturbances.

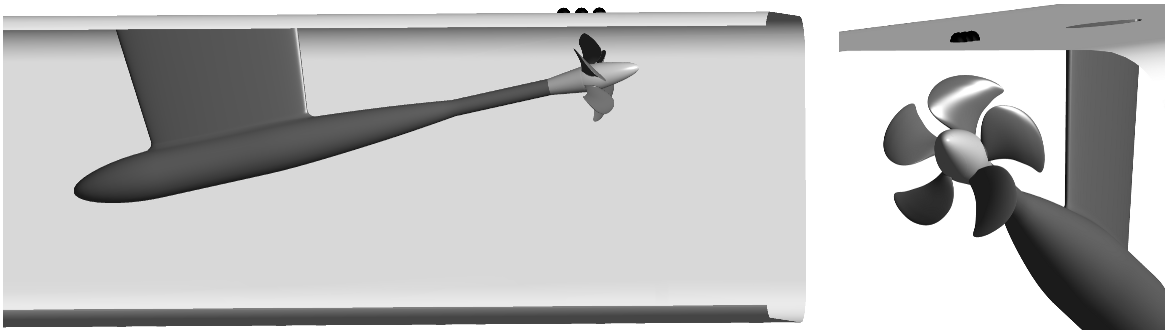

Fig. 3.5 Test scenario to be investigated during the workshop and position of the three monitoring points.

3.2.3 Accuracy of numerical predictions

Certainly, any advanced simulation tool used for design purposes should be able to perform reliable predictions with a reasonable accuracy. The results presented at the *Second Workshop on Cavitation and Propeller Performance* (Abdel-Maksoud et al., 2015) indicate that even predicting first-order pressure fluctuations for both non-cavitating and cavitating flow is not a trivial task. In this workshop, the PPTC propeller[6] was investigated numerically in the oblique flow configuration shown in Figure 3.5.

The following aspects were investigated: mean thrust and torque for cavitating and non-cavitating flow, behaviour of cavitation in terms of cavity extent and distribution as well as pressure fluctuations monitored in three observations points above the propeller at $x = x_p$, $x = x_p - 0.2D$ (downstream of the propeller) and $x = x_p + 0.2D$ (upstream of the propeller) for both cavitating and non-cavitating flow. The workshop was intended to be a blind workshop, i.e. experimental data was not provided in advance. Roughly a dozen research institutions joined the workshop and about 15 numerical state-of-the-art simulation methods applicable to propeller design were involved, most of them viscous methods using Euler–Euler cavitation models (RANS codes, group 2) and a few of them inviscid panel methods (group 1 mentioned in the previous section). The reported results are not entirely complete since some of the institutions did not simulate all of the requested test scenarios.

Whereas a relatively good agreement was obtained for the thrust and torque for non-cavitating flow, the thrust deduction due to cavitation was predicted inaccurately in some cases. Owing to the oblique inflow and the corresponding change of angle of attack, the cavitation behaviour of the propeller is quite complicated – a mixture of sheet cavitation on the pressure and on the suction side, intense tip vortex cavitation as well as bubble, cloud and root cavitation (see Figure 2.3 in Section 2.2 for an explanation). Not surprisingly, the predicted cavity extent on the blades was different from contribution to contribution. However, a rough agreement with experimental data could be obtained in most cases.

---

[6] The *PPTC* (Potsdam Propeller Test Case) propeller has been designed as a modern propeller for benchmark tests of numerical simulation methods (SVA, 2017).

Results of propeller-induced pressure fluctuations are of particular interest. A compilation of these results is shown in a dimensionless manner in Figure 3.6 in terms of harmonic amplitudes of first and second order $k_{\hat{p}[q]}$ occurring with blade frequency f_b and $2f_b$, respectively. The workshop report does not contain any information on fluctuations with a frequency higher than $3f_b$.

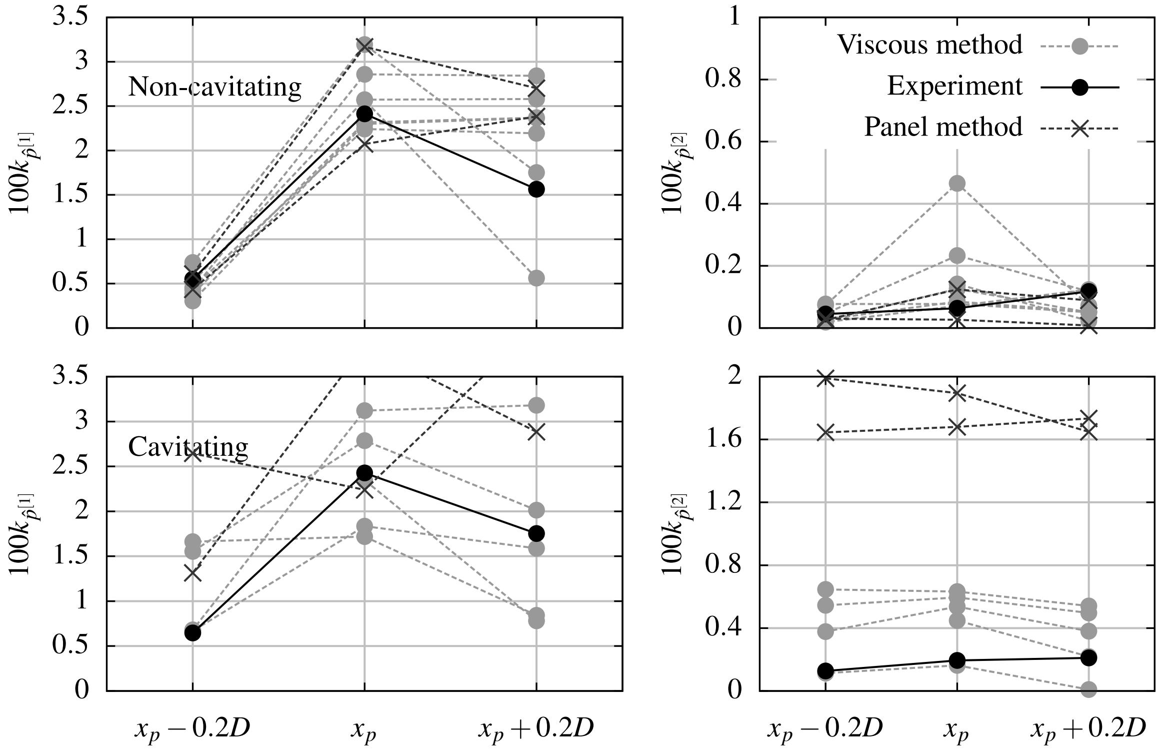

Fig. 3.6 Results with respect to propeller-induced pressure fluctuations presented at the workshop for three monitoring points; $x_p + 0.2D$ is located upstream of the propeller.

For non-cavitating flow, the agreement between simulation and experiment is acceptable, albeit, for $k_{\hat{p}[1]}$, a larger variance of the results for the observation point upstream of the propeller can be observed. With respect to cavitating flow and $k_{\hat{p}[1]}$, the agreement between simulation and experiments is acceptable in some cases, in other cases only a roughly correct reproduction of the general tendency of decaying amplitude with growing distance from the propeller can be reproduced; in a few cases even this is not achieved.

Indeed, the unsteady cavitation pattern of the PPTC propeller in oblique flow is admittedly very complicated, which makes it literally an academic benchmark test. Presuming moderate operation conditions, most of the propellers which are investigated in the present thesis exhibit a well-behaved cavitation behaviour.

Chapter 4

Underlying Numerical Methods

In this chapter, the underlying numerical methods that provide a basis for the simulation models developed in this thesis are reviewed. These are a finite volume method for the solution of the RANS equations describing the behaviour of viscous turbulent flow (referred to as *RANSE solver*) and a panel method solving Laplace's equation for potential flow. Nowadays, both methods are technically matured and a great amount of literature exists that address the description and the application of these methods.

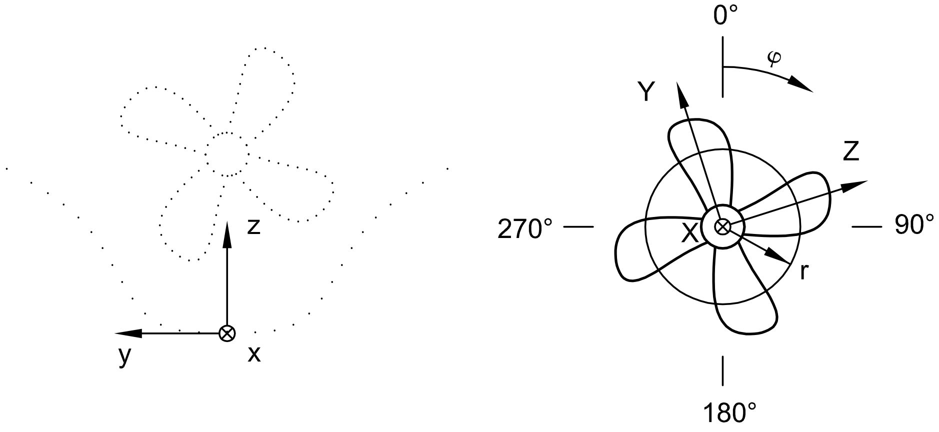

Fig. 4.1 Coordinate systems used throughout the thesis, view from behind.

The global coordinate system with $\mathbf{x} = (x, y, z)$ used for the majority of the thesis is Cartesian, right-handed and the origin is located at the aft perpendicular of the ship on the baseline (see Figure 4.1). Some of the mathematical formulations are given in a body-fixed coordinate system with $\mathbf{X} = (X, Y, Z)$ rotating with the propeller. The origin of this system is the propeller center. In order to address positions in the propeller plane, the angle φ and the radius $r = \sqrt{Y^2 + Z^2}$ as depicted in Figure 4.1 are introduced.

4.1 RANSE Solver

In this section, the RANSE solver for the simulation of unsteady three-dimensional viscous flow taking into account effects of turbulence and cavitation is described. The applied software is the commercial code `ANSYS CFX` and this section sums up all the relevant information from the user's manual (ANSYS, 2014).

It has been indicated in Chapter 1 and will be explained in greater detail in Chapters 5 and 6 that `ANSYS CFX` will be primarily used to calculate the viscous hull flow and to carry out some auxiliary simulations with respect to propeller cavitation. Here, flow details in the blade tip region are of special interest (see Section 5.4). However, for convenience, the outline of the theory starts with the case of the viscous hull flow.

4.1.1 Governing equations for non-cavitating flow and boundary conditions

The fluid of the density ρ and of the dynamic viscosity μ is considered to be Newtonian as well as incompressible and the behaviour of the flow can thus be described by the continuity equation:

$$\nabla \cdot \mathbf{u} = 0, \tag{4.1}$$

and the momentum equation:

$$\rho \left(\frac{\partial}{\partial t} + \mathbf{u} \cdot \nabla \right) \mathbf{u} = -\nabla p + \nabla \cdot \tau + \mathbf{f}, \tag{4.2}$$

for all $\mathbf{x} \in \Lambda$, where Λ is defined as the viscous flow domain and $\nabla = ({}^{\partial}/_{\partial x}, {}^{\partial}/_{\partial y}, {}^{\partial}/_{\partial z})$. Equations (4.1) and (4.2) are denoted as Navier-Stokes equations.[1] In the above equations, $\mathbf{u} = \mathbf{u}(\mathbf{x},t)$ is the velocity, $p = p(\mathbf{x},t)$ the pressure, $\tau = \tau(\mathbf{x},t)$ the viscous stress tensor with $\tau_{ij} = \mu \left(\frac{\partial u_i}{\partial x_j} + \frac{\partial u_j}{\partial x_i} \right)$ and $\mathbf{f} = \mathbf{f}(\mathbf{x},t)$ a body force source term which is regarded as a known quantity and may contain gravitational forces, for example. This term will become important later in Section 6.1.

In order to describe the flow field by Eqs. (4.1) and (4.2), appropriate boundary conditions have to be fulfilled on $\partial\Lambda$. In the following, it is assumed that $\partial\Lambda$ is invariant in time (i.e. parts of $\partial\Lambda$ do not change their position relative to each other over time). This limitation does not hold generally, but it simplifies the explanations given in the following. Different types of boundary conditions exist and the user has to assign them to the different parts of $\partial\Lambda$ in physically meaningful manner. At the inlet $W_{\text{in}} \subset \partial\Lambda$, usually the velocity is defined:

$$\mathbf{u} = \mathbf{u}_{\text{in}}, \quad \text{for all } \ \mathbf{x} \in W_{\text{in}}. \tag{4.3}$$

---

[1] Sometimes in the literature, only Eq. (4.2) is called Navier-Stokes equation.

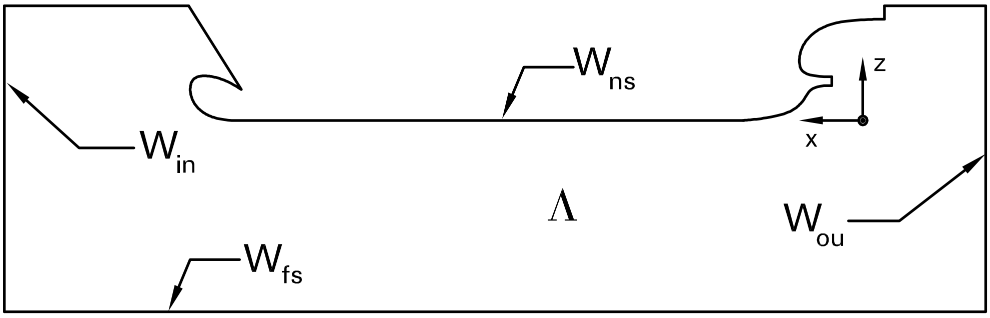

Fig. 4.2 Different parts of the boundary $\partial\Lambda$ of the viscous flow domain Λ.

In general, no information on the velocity distribution at the outlet $W_{\mathrm{ou}} \subset \partial\Lambda$ is available. Hence, a suitable reference pressure is imposed here:

$$p = p_{\mathrm{ref}}, \quad \text{for all} \;\; \mathbf{x} \in W_{\mathrm{ou}}. \tag{4.4}$$

The velocity at impermeable no-slip walls $W_{\mathrm{ns}} \subset \partial\Lambda$ is zero:

$$\mathbf{u} = \mathbf{0}, \quad \text{for all} \;\; \mathbf{x} \in W_{\mathrm{ns}}. \tag{4.5}$$

For an impermeable free-slip wall W_{fs}, only velocity components normal to the wall and the wall shear stress $\tau_{\mathrm{W}} \subset \partial\Lambda$ are set to zero:

$$\mathbf{u} \cdot \mathbf{n} = 0 \;\; \text{and} \;\; \tau_{\mathrm{W}} = 0, \quad \text{for all} \;\; \mathbf{x} \in W_{\mathrm{fs}}, \tag{4.6}$$

where $\mathbf{n} = \mathbf{n}(\mathbf{x})$ is the normal vector on the surface.

4.1.2 Turbulence modelling

Most of the flows which are encountered within this thesis have high Reynolds numbers, and effects related to turbulence will therefore become important. One way to account for turbulence in a macroscopic manner (i.e. without resolving the turbulent structures in detail) is to decompose velocity and pressure into average values and fluctuations due to turbulence[2] according to $\phi(\mathbf{x},t) = \overline{\phi}(\mathbf{x},t) + \phi'(\mathbf{x},t)$. Inserting a corresponding decomposition for pressure and velocity into Eqs. (4.1) and (4.2) and subsequent averaging introduces an additional term to Eq. (4.2) which can be interpreted as an additional stress tensor:

$$\rho\left(\frac{\partial}{\partial t} + \mathbf{u} \cdot \nabla\right)\mathbf{u} = -\nabla p + \nabla \cdot (\tau + \tau_{\mathrm{T}}) + \mathbf{f}. \tag{4.7}$$

---

[2] For the decomposition to be valid, it is necessary that the turbulent time scales are much smaller than characteristic time scales of the mean flow.

Here, τ_T with $\tau_{\mathrm{T}ij} = -\rho\overline{u_i'u_j'}$ is called the Reynolds stress tensor and additional models are required in order to approximate it. Eqs. (4.1) and (4.7) form the Reynolds-averaged Navier-Stokes (RANS) equations.

Most of the turbulence models applied in engineering activities are based on the Boussinesq eddy-viscosity principle, which reduces turbulent effects to an additional isotropic turbulent viscosity $\mu_\mathrm{T} = \mu_\mathrm{T}(\mathbf{x},t)$. In other words, the problem of modelling the components $-\rho\overline{u_i'u_j'}$ of the Reynolds stress tensor τ_T is shifted to the problem of modelling the additional turbulent viscosity, hence:

$$-\rho\overline{u_i'u_j'} = \mu_\mathrm{T}\left(\frac{\partial u_i}{\partial x_j} + \frac{\partial u_j}{\partial x_i}\right) - \frac{2}{3}\rho k \delta_{ij}, \tag{4.8}$$

where $k = {}^1\!/\!{}_2\overline{u_i'u_i'}$ is defined as the turbulent kinetic energy and δ_{ij} is called the Kronecker delta with $\delta_{ij} = 1$ if $i = j$ and $\delta_{ij} = 0$ else. The additional term constitutes a pressure and is necessary to handle normal turbulent stresses, i.e. $j = i$ (Rodi, 1993, pp. 10f).

Two-equation eddy viscosity turbulence models and their derivatives are commonly applied for most engineering problems. There are roughly two groups of two-equation models.

(1) k–ε models relate the turbulent kinetic energy $k = k(\mathbf{x},t)$ and the turbulence dissipation $\varepsilon = \varepsilon(\mathbf{x},t)$ to the turbulent viscosity:

$$\mu_\mathrm{T} \propto \frac{k^2}{\varepsilon}. \tag{4.9}$$

For the quantities k and ε, two extra equations have to be solved. The structure of these equations is similar to the structure of Eq. (4.2). However, source terms which have an heuristic character are added.

(2) k–ω models are motivated by the assumption that the turbulent viscosity is linked to the turbulent kinetic energy and the turbulent frequency $\omega = \omega(\mathbf{x},t)$:

$$\mu_\mathrm{T} \propto \frac{k}{\omega}. \tag{4.10}$$

The Boussinesq eddy-viscosity approximation can lead to good results for many engineering problems. However, one has to keep in mind that this approximation will fail in cases where the streamline curvature is high or in vortical flow (Wilcox, 2006, pp. 303f). Nevertheless, in this thesis, tip vortex characteristics are simulated by means of this method and a certain error is accepted.

4.1.3 Cavitation modelling

Cavitating flow is regarded as homogeneous multiphase flow. This means that the fluid is now a mixture of two phases: water $\bullet_l$ and its vapour $\bullet_v$. Both phases are assumed to share the same pressure and velocity field, i.e. they can be treated as one fluid. One is left with introducing the volume fraction α as a new variable, for which

$$\alpha_l + \alpha_v = 1 \tag{4.11}$$

holds. The density of the mixture $\rho^\star$ is obtained by

$$\rho^\star = \alpha_l \rho + \alpha_v \rho_v, \tag{4.12}$$

where ρ is the density of water and ρ_v the density of water vapour. Since the density $\rho^\star$ of the mixture is no longer a constant, Eqs. (4.1) and (4.2) look slightly different:

$$\frac{\partial \rho^\star}{\partial t} + \nabla \cdot (\rho^\star \mathbf{u}) = 0 \tag{4.13}$$

and

$$\left(\frac{\partial}{\partial t} + \mathbf{u} \cdot \nabla\right)(\rho^* \mathbf{u}) = -\nabla p + \nabla \cdot (\tau + \tau_\mathrm{T}) + \mathbf{f}. \tag{4.14}$$

Introducing a new variable to the problem requires an additional equation in order to find a solution. For this purpose, transport and production of the volume fraction are balanced and one obtains:

$$\frac{\partial}{\partial t}(\alpha_l \rho) + \nabla \cdot (\alpha_l \rho \mathbf{u}) = \dot{S}_l, \tag{4.15}$$

where the source term of the liquid phase $\dot{S}_l$ is simply related by $\dot{S}_l = -\dot{S}_v$ to the source term of the vaporous phase $\dot{S}_v$. Determining the source term $\dot{S}_v$ is the task of the particular cavitation model. In this case, the cavitation model described and developed by Bakir et al. (2004) is used. Apart from some material and empirical constants, the source term is proportional to

$$\dot{S}_l \sim -F_c \sqrt{|p_v - p|}\ \mathrm{sgn}\,(p_v - p), \tag{4.16}$$

with p_v being the vapour pressure of water, $F_c = 50$ for $p_v - p > 0$ and $F_c = 0.01$ for $p_v - p < 0$. The relation in Eq. (4.16) originates from the idea that a volume unit contains a number of vapour bubbles whose growing and shrinking behaviour is modelled by means of the Rayleigh-Plesset equation. In order to simplify the model, the higher-order terms of this equation are truncated.

4.1.4 Numerical solution

In the following, some details of the numerical solution are presented. However, one has to keep in mind that these details are only a small part of what comprises the whole flow solver. In this context, a major problem encountered when constructing the numerical solution procedure is the decoupling of pressure and velocity. Details on strategies to overcome this problem and other measures to, for example, accelerate, stabilise and parallelise the solution procedure can be found in the manual of ANSYS CFX (ANSYS, 2014).

Discretisation For convenience, the discretisation is illustrated using the example of non-cavitating flow. In order to solve Eqs. (4.1) and (4.7) numerically, a finite volume method is applied. The viscous flow domain Λ is therefore divided into a number of control volumes V_m having the surface S_m. Integration of Eqs. (4.1) and (4.7) over V_m leads to

$$\int_{S_m} \mathbf{u} \cdot \mathrm{d}\mathbf{S} = 0 \tag{4.17}$$

and

$$\rho \left(\frac{\partial}{\partial t} \int_{V_m} \mathbf{u} \,\mathrm{d}V + \int_{S_m} \mathbf{uu} \cdot \mathrm{d}\mathbf{S} \right) = \int_{S_m} p \,\mathrm{d}\mathbf{S} + \int_{S_m} (\tau + \tau_\mathrm{T}) \cdot \mathrm{d}\mathbf{S} + \int_{V_m} \mathbf{f} \,\mathrm{d}V, \tag{4.18}$$

for all V_m, with $\mathrm{d}\mathbf{S} = \mathbf{n}\mathrm{d}S$ being an oriented element of S_m. Use has been made of Gauss' divergence theorem in order to convert volume integrals involving the operator ∇ to surface integrals. In ANSYS CFX, the control volumes V_m are constructed around the nodes $\mathbf{x}_m$ of the mesh (vertices) (see Figure 4.3). All variables are stored in the mesh nodes. The approximation of volume integrals is done in a straightforward manner by

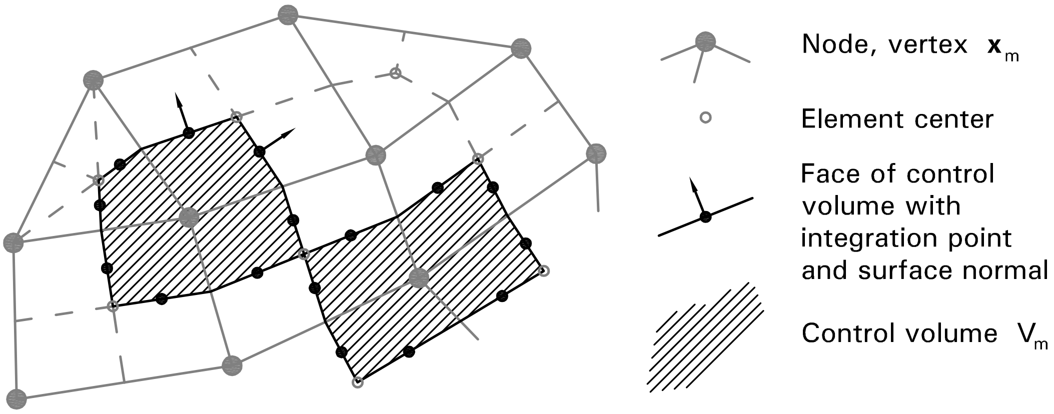

Fig. 4.3 Discretisation strategy in ANSYS CFX.

$$\int_{V_m} \phi \,\mathrm{d}V \approx \phi \, V_m, \tag{4.19}$$

where ϕ is an arbitrary scalar or vectorial variable. This approximation is of second-order accuracy if the node is located in the center of the control volume – a condition which is met inherently by the given arrangement of the control volumes. However, when surface integrals are considered, difficulties may arise. For the approximation, the variable ϕ needs to be evaluated at every integration point (ip) j that is associated with the control volume V_m:

$$\int_{S_m} \phi \,\mathrm{d}\mathbf{S} \approx \sum_j \phi_{\mathrm{ip},\,j} \, \Delta S_j \mathbf{n}_j. \tag{4.20}$$

This requires an interpolation of the quantity ϕ from the vertices to the integration points. Depending on the physical character of the integrand ϕ, i.e. diffusive or advective, different interpolation schemes have to be applied in order achieve numerical stability and accuracy. For the interpolation of advective terms, ANSYS CFX applies a high-resolution scheme for the interpolation in order to maximise the numerical accuracy for a given mesh configuration.

For the approximation of time derivatives, ANSYS CFX uses either a first-order backward Euler scheme with

$$\frac{\partial \bullet}{\partial t} \approx \frac{\bullet - \bullet^{\circ}}{\Delta t}, \tag{4.21}$$

where $\bullet$ is an arbitrary quantity as, for example, a variable or an integral appearing in Eq. (4.18), Δt is the time step size and $^{\circ}$ denotes the previous time level, or a second-order backward Euler scheme with

$$\frac{\partial \bullet}{\partial t} \approx \frac{3\bullet - 4\bullet^{\circ} + \bullet^{\circ\circ}}{2\Delta t}. \tag{4.22}$$

In this case, storing the solution of two past time levels is required. For most of the simulations carried out within this thesis, the latter variant is applied.

Numerical treatment of turbulence Without going into further detail, two major problems concerning turbulence modelling should be mentioned here, apart from the general shortcomings of the Boussinesq approximation: (1) In general, turbulence models are not universally applicable. Some of them are more accurate when flows near walls are concerned, some of them are advantageous for the simulation of free stream flows. (2) Turbulent flows exhibit strong gradients normal to walls and the results are very sensitive towards the spatial discretisation. In order to overcome these difficulties to a certain degree, ANSYS CFX provides the SST turbulence model with an automatic near-wall treatment. Depending on the distance to the nearest surface in the vicinity, the SST turbulence model blends the Wilcox k–ω model and a k–ε model which has been cast into a k–ω-like formulation. In order to overcome numerical difficulties arising from the discretisation near no-slip walls, the automatic near-wall treatment switches from a direct computation of the boundary layer flow (which requires a fine grid resolution normal to walls) to an empirical approximation based on wall functions whenever the grid resolution is too coarse for a direct computation. Additionally, a correction for flows with high streamline curvature is available.

Simulation of propellers in homogeneous inflow In this thesis, use will be made of ANSYS CFX to simulate the cavitating flow of the propeller with special interest on details of the flow near the propeller blade tips. These simulations are carried out for homogeneous inflow and it becomes advantageous to only consider one blade of the propeller contained in a domain similar to a distorted pie slice and to prescribe a periodic boundary condition on the walls defining the side faces of this slice (see Figure 4.4). Then, the equations are solved in a propeller-fixed coordinate system with $\mathbf{X} = (X, Y, Z)$ rotating according to the number of revolutions of the propeller. Additional body forces due to the Coriolis force and the centrifugal force have to be considered in the momentum equation.

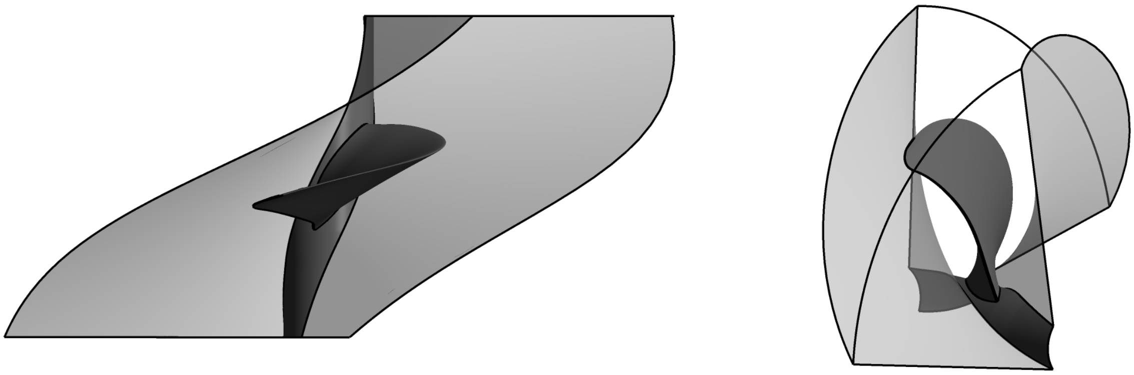

Fig. 4.4 Rotational domain enclosing one single blade with periodic boundary conditions (respective location are marked grey opaque); different views.

Memory Management System and User Coding Despite being a commercial code, ANSYS CFX allows some manipulation of the program routines. This means that users can incorporate their own physical models. By means of the *Memory Management System*, every flow variable can be accessed during the solution process. Furthermore, it is possible to apply user-specified distributions of body forces. These facilities are the framework for the implementation of the coupling approach described in Section 6.1.

Usually, the solver distributes the flow simulation over more than one partition, each handled by a separate processor, i.e. the mesh is split into several fragments which partially overlap. Some bookkeeping is needed therefore in order to enable parallelisation of the user coding routines.

4.2 Panel Method with Sheet Cavitation Model

The panel method *pan*MARE, developed at Hamburg University of Technology, is applied to the simulation of the inviscid unsteady propeller flow including effects of sheet cavitation on the blades. Detailed information on the underlying theory can be found in Katz and Plotkin (2001), and information on the present implementation is documented by Hundemer (2013), Greve (2015) and Gaschler (2017), for example. Because of the exhaustive documentation that already exists, the following review only briefly illustrates the basic principles.

The main idea behind panel methods is to describe the flow in the entire flow domain by a discrete distribution of sources and dipoles on the body surrounded by the flow. This converts the three-dimensional flow problem into a two-dimensional one, which is defined by the surface of the body of interest. This leads to a reduced computational effort. Appropriate boundary conditions have to be fulfilled: zero flow normal to the body surface, decaying influence of the body with growing distance and in case of lifting bodies, flow separation from the trailing has to be enforced. The choice of sources and dipoles is somewhat arbitrary, i.e. the conditions mentioned above can be fulfilled by more than one combination of sources and dipoles depending on the particular formulation of the method (Hess, 1990).

4.2.1 Governing equations for non-cavitating flow and boundary conditions

The domain of potential flow is named Ω and initially only contains the propeller as a solid body with blades having a distinct trailing edge. It is assumed that the total velocity field $\mathbf{V}$ in Ω can be regarded as a superposition of the undisturbed flow $\mathbf{V}_0$ and the velocity field $\mathbf{V}^+$ induced by the propeller, which is considered to be incompressible and irrotational. Hence, a velocity potential Φ exists for $\mathbf{V}^+$ with $\mathbf{V}^+ = \nabla\Phi$ and

$$\mathbf{V} = \mathbf{V}_0 + \nabla\Phi. \tag{4.23}$$

The problem is formulated in the body-fixed coordinate system (X,Y,Z), which implies $\nabla = (\partial/\partial X, \partial/\partial Y, \partial/\partial Z)$. In the general case, $\mathbf{V}_0 = \mathbf{V}_\infty + \mathbf{V}_{\mathrm{mot}}$ is the combination of an inhomogeneous inflow (effective wake field) $\mathbf{V}_\infty$ and velocities $\mathbf{V}_{\mathrm{mot}}$ due to the rotation of the propeller. Unsteadiness is introduced to the problem by the rotation of the propeller blades because the inhomogeneous inflow $\mathbf{V}_0$ faced by the propeller will change with time.

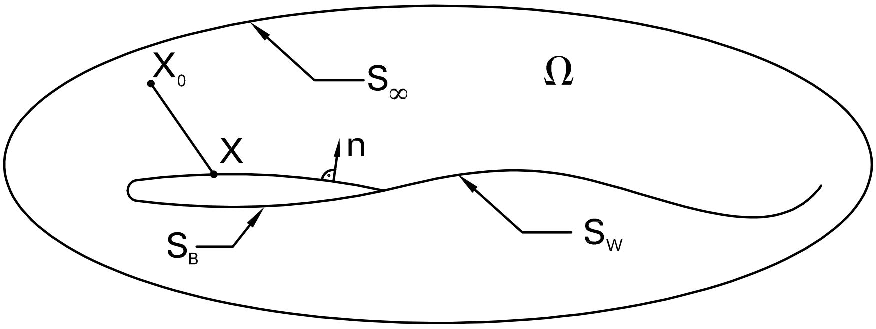

Fig. 4.5 Schematic illustration of the boundaries of the potential flow domain Ω.

Because of the assumptions made, the governing flow equations simplify to Laplace's equation for the potential Φ and Bernoulli's equation for the pressure p:

$$\nabla^2\Phi = 0 \tag{4.24}$$

and

$$p + \frac{1}{2}\rho|\mathbf{V}|^2 + \rho\frac{\partial\Phi}{\partial t} + \rho g z = p_{\mathrm{ref}} + \frac{1}{2}\rho|\mathbf{V}_0|^2, \tag{4.25}$$

with p_{ref} being a suitable reference pressure. For the moment, only the propeller blade enclosed by the surface $S_B \subset \partial\Omega$ is considered (see Figure 4.5); the boundary S_W will be introduced later. The task is to find an appropriate potential Φ satisfying the following boundary conditions:

(1) With growing distance to the body, the influence of the induced velocity must decrease and finally vanish:

$$\mathbf{V}^+ = \nabla\Phi = \mathbf{0}, \quad \text{for all } \mathbf{X} \in S_\infty, \tag{4.26}$$

where $S_\infty \subset \partial\Omega$ is the virtual surface at infinity.

(2) On the surface S_B of the solid body, the impermeability condition is applied, stating that no flow is allowed to penetrate the surface:

$$\mathbf{V} \cdot \mathbf{n} = (\mathbf{V}_0 + \nabla \Phi) \cdot \mathbf{n} = 0, \quad \text{for all } \ \mathbf{X} \in S_B. \tag{4.27}$$

It can be shown that such a velocity potential exists and that the velocity potential in a point $\mathbf{X}_0$ can be expressed in terms of the potential $\Phi(\mathbf{X})$ on the surface S_B, i.e. $\mathbf{X} \in S_B$, and its normal derivative $\nabla \Phi(\mathbf{X}) \cdot \mathbf{n}(\mathbf{X})$:

$$\varepsilon \Phi(\mathbf{X}_0) = \int_{S_B} \left(\frac{1}{d} \nabla \Phi - \Phi \nabla \left(\frac{1}{d} \right) \right) \cdot \mathbf{n} \mathrm{d}S, \ \ \mathbf{X} \in S_B, \tag{4.28}$$

where $\mathbf{n}$ is the normal vector of the surface element $\mathrm{d}S$ pointing into the fluid and $d = \|\mathbf{X} - \mathbf{X}_0\|$. This is a form of one of Green's identities. For ε, the following applies:

$$\varepsilon = \begin{cases} 2\pi & \text{if } \mathbf{X}_0 \text{ lies on the surface} \\ 4\pi & \text{if } \mathbf{X}_0 \text{ lies outside the body.} \\ 0 & \text{if } \mathbf{X}_0 \text{ lies inside the body} \end{cases} \tag{4.29}$$

In Eq. (4.28), $\nabla \Phi \cdot \mathbf{n}$ can be identified as a source strength and Φ as a dipole strength. Thus, the following substitution is made:

$$\sigma = -\nabla \Phi \cdot \mathbf{n} \ \text{ and } \mu = -\Phi, \ \ \mathbf{X} \in S_B. \tag{4.30}$$

From this relation and Eq. (4.27), it follows automatically that

$$\sigma = \mathbf{V}_0 \cdot \mathbf{n}. \tag{4.31}$$

This means that the normal derivative of the potential in terms of the source strength σ is already known and the problem remains to specify the potential itself or – equivalently – the dipole strength μ on the body. For this purpose, use can be made of Eqs. (4.28) and (4.29) by adjusting μ in a way that for a given source strength σ the potential vanishes inside the body. However, the solution found will not be unique and does still not reflect the real flow behaviour because the fluid can flow off anywhere but not necessarily at the trailing edge (Katz and Plotkin, 2001, pp. 209ff). It has been mentioned in Section 2.4 that viscosity is the exclusive reason for the flow detaching at the trailing edge. Since viscosity is not taken into account within the underlying theory of potential flow, an alternative concept is required in order to model the controlled detachment from the trailing edge: the Kutta condition stating that

$$\Delta p = 0, \quad \text{for all } \ \mathbf{X} \in \text{trailing edge}, \tag{4.32}$$

where $\Delta p = p_u - p_l$ is the pressure jump between the pressure value on the upper and lower side of the trailing edge, or equivalently:

$$\nabla \Phi < \infty, \quad \text{for all } \mathbf{X} \in \text{trailing edge}, \tag{4.33}$$

which means that the flow velocity has to be finite at the trailing edge. This would not be the case if the flow whistled around the trailing edge.

Furthermore, it has been shown in Section 2.4 that the flow over a body with a distinct trailing edge such as the blade of a propeller (i.e. a flow featuring the conditions posed by Eqs. (4.32) and (4.33)) is generally associated to a certain non-zero circulation that is bound to the body and which varies in the spanwise direction. Because of the solenoidality of the vorticity field, a sheet carrying trailing vorticity is shed from the trailing edge of the body. This sheet of vorticity can be idealised by an infinitesimally thin vortex layer, which is the reason for introducing the additional boundary surface $S_W \subset \partial\Omega$ to the problem (see Figure 4.5). Equivalently, all the features of a vortex layer can also be represented by a distribution of dipoles on S_W (Kornev, 2009, p. 158).

The condition given by Eq. (4.32) can be approximately fulfilled by Morino's Kutta condition:

$$\mu_W = \mu_u - \mu_l, \tag{4.34}$$

defining the relation between the dipole strength at the upper and lower side of the trailing edge and the dipole strength at the wake surface S_W for a certain spanwise (or radial) position of the trailing edge. This linearisation holds if the flow direction is perpendicular to the trailing edge, which constitutes a two-dimensional flow – an approximation which holds for major parts of the propeller radius except for the region near the blade tip.

4.2.2 Numerical solution

Now, it becomes possible to construct a unique solution of the flow problem approximating the real behaviour of the flow over the blades. To become more specific, the surfaces S_B and S_W are discretised by N_B and N_W quadrilateral panels, respectively (see Figure 4.6a). Dipole strengths μ_k and source strengths σ_k are associated with each panel on the boundary S_B and only dipole strengths μ_i are placed on the panels of S_W. Both dipole and source strengths are assumed to be constant over one panel. N_B collocation points $\mathbf{X}_{0,j}$ are introduced, each one associated to a panel of S_B and slightly shifted into the body.

Under these conditions and considering the additional dipole strenghts μ_i on the surface S_W, Eq. (4.28) yields a system of linear equations:

$$\sum_{k=1}^{N_B} (C_k\mu_k + B_k\sigma_k) + \sum_{i=1}^{N_W} C_i\mu_i = 0 \quad \text{for each internal point } \mathbf{X}_{0,j}, \quad j = 1, \dots, N_B, \tag{4.35}$$

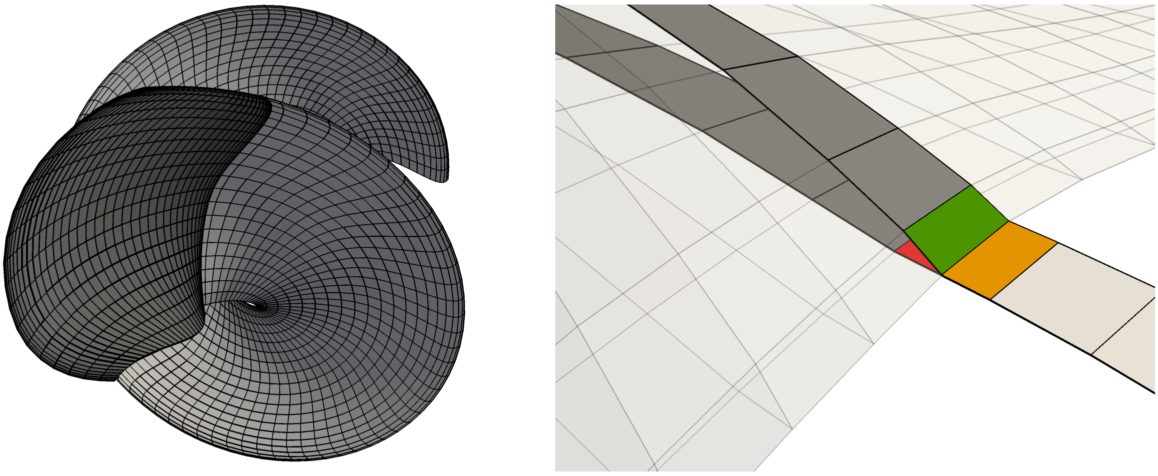

(a) Discretisation of S_B (dark grey) and S_W (light grey).

(b) Panel arrangement at the trailing edge.

Fig. 4.6 Left: discretisation of the propeller blade by quadrilateral panel elements; right: panel arrangement at the trailing edge. Upper panel with μ_u (green), lower panel with μ_l (red) and wake panel carrying μ_W (orange); see Eq. (4.34).

where C_k, C_i and B_k are known influence coefficients, which only depend on shape and position of the panels. In the equation, σ_k is a known quantity specified by Eq. (4.31). What remains are $N_B + N_W$ unknown dipole strengths and only N_B equations. To fix this problem, Morino's linearised Kutta condition (Eq. (4.34)) is applied and the final system of linear equations to be solved reads:

$$\sum_{k=1}^{N_B} A_k \mu_k = -\sum_{k=1}^{N_B} B_k \sigma_k \quad \text{for each internal point } \mathbf{X}_{0,j}, \quad j = 1, \ldots, N_B, \tag{4.36}$$

where $A_k = C_k \pm C_t$ for panels at the trailing edge (C_t is the influence coefficient of the adjacent wake panel located on S_W; see Figure 4.6b) and $A_k = C_k$ for all other panels on S_B. The solution vector contains the unknown dipoles strengths μ_k and can be found easily by the Gauss method.

Nothing has been said so far about the exact shape of the surface S_W. Representing the sheet of trailing vorticity, the extent in the downstream direction should be as large as possible. Furthermore, no lift is produced by this surface since it is only an imaginary surface and not a solid one. This condition is equivalent to aligning S_W along the streamlines of the velocity field $\mathbf{V}$. In *pan*MARE this is performed in an iterative manner, which, however, entails a huge computational effort, especially if the discretisation of the wake surface is fine. Alternatively, the shape of the surface S_W can be predefined and considered to be indeformable during the simulation.

It has already been said at the beginning of this section that the problem is of an unsteady nature in general. Within a panel method, the treatment of unsteady flow is not very different from steady flow simulations (Katz and Plotkin, 2001, pp. 369ff). Unsteadiness is introduced by the time-dependent inflow $\mathbf{V}_0$ and manifests in the term $\partial\Phi/\partial t$ in Eq. (4.25), which can easily be derived by a first-order backward Euler scheme (see Eq. (4.21)), and in the treatment of the wake panels discretising S_W.

Here, *pan*MARE introduces a new row of panels in the radial direction at the trailing edge in every time step fulfilling the Kutta condition (Eq.(4.34)) and the panel row being previously attached to the trailing edge is swept away by the flow carrying its primary distribution of dipole strength. This procedure may be sufficiently accurate if the change of the inflow with respect to time is not too large (Katz and Plotkin, 2001, p. 375).

4.2.3 Modelling of sheet cavitation

The sheet cavitation model incorporated in *pan*MARE is based on the works of Vaz (2005) and Fine (1992). It has been originally implemented and validated by Gaschler (2017) and enhanced by Scharf (2014). The model is able to simulate partial sheet cavitation on both the pressure and the suction side of the propeller blades. It is linearised in the sense that the respective boundary conditions are fulfilled on the blade surface $S_{B_C} \subset S_B$ and not on the cavity surface. According to Fine, a considerable amount of computation time can be saved and the additional error introduced by this simplification is only small.

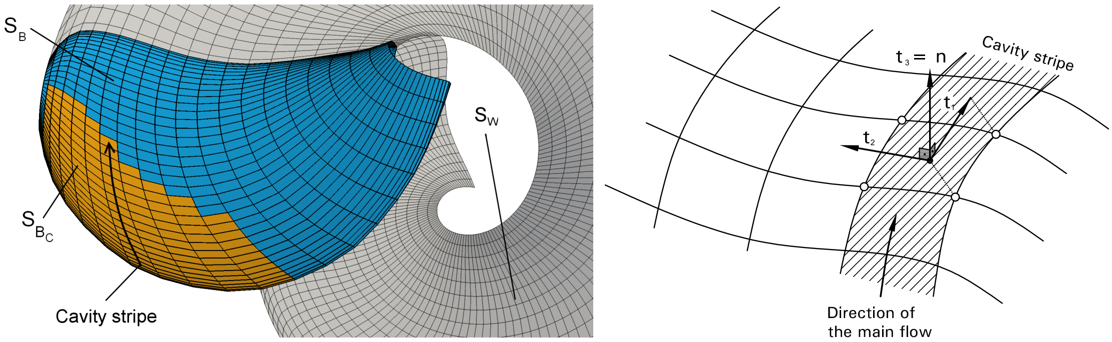

(a) Boundaries S_B and S_{B_C} on the blades.

(b) Local non-orthogonal coordinate system on the propeller surface.

Fig. 4.7 Additional boundaries and local coordinate system introduced for modelling partial sheet cavitation.

In order to approximate the physics of sheet cavitation, additional boundary conditions are necessary to find a solution for the cavitating propeller flow (see Section 3.2):

(1) The dynamic boundary condition states that the pressure on the cavitating part S_{B_C} of the blade must be equal to vapour pressure p_v:

$$p = p_v, \quad \text{for all } \mathbf{X} \in S_{B_C}. \tag{4.37}$$

(2) The cavity surface is regarded as a material surface and as such, no flow is allowed to penetrate this surface. This can be formulated as follows:

$$\frac{D}{Dt} F(\eta(s_1, s_2, t), s_3) = 0, \quad \text{for all } \mathbf{s} \in S_{B_C}, \tag{4.38}$$

where η is the cavity thickness and $F(\eta(s_1,s_2,t),s_3) = s_3 - \eta(s_1,s_2,t)$ is a function for the cavity shape. The variables s_1, s_2 and s_3 are the coordinates of the local non-orthogonal coordinate system of a panel element which are introduced in the following.

A fundamental assumption made from now on is that the flow on the blade follows primarily the radial sections of the blade, i.e. it streams in chordwise direction. (This assumption has already been met when the linearised form of the Kutta condition was applied; see Eq. (4.34)). It is then beneficial to introduce a local panel coordinate system (s_1,s_2,s_3) with the basis vectors $\mathbf{t}_1$, $\mathbf{t}_2$ and $\mathbf{t}_3$. Here, $\mathbf{t}_1$ is chosen in a way that it coincides with the direction of the panel edge parallel to the main flow (see Figure 4.7), $\mathbf{t}_2$ is parallel to the other edge and $\mathbf{t}_3 = \mathbf{n}$ is perpendicular to $\mathbf{t}_1$ and $\mathbf{t}_2$. The basis vectors $\mathbf{t}_1$ and $\mathbf{t}_2$ parallel to the panel edges enclose the angle θ, which is rectangular for an orthogonal grid. One has to note that the assumption regarding the flow direction may be an appropriate simplification for large parts of the propeller radius. However, at the propeller tip, this assumption definitively will not hold and difficulties are inevitable when a solution for the cavity shape is sought.

Using the dynamical boundary condition represented by Eq. 4.37 and neglecting velocities in the normal s_3-direction, the Bernoulli equation (4.25) can be cast in a Dirichlet-like formulation for the potential Φ on the cavitating part of the blade S_{B_C}:

$$\Phi = \Phi_0 + \int_{s_0}^{s_t} \left[V_{s_2}\cos\theta + \sin\theta \sqrt{\frac{2}{\rho}\left(p_{\text{ref}} - p_v\right) - 2\frac{\partial \Phi}{\partial t} + |\mathbf{V}_0|^2 - 2gz - V_{s_2}^2} - \mathbf{V}_0 \cdot \mathbf{t}_1 \right] \mathrm{d}s_1, \quad (4.39)$$

where the integral has to be evaluated between the detachment point $s_1 = s_0$ and the reattachment point $s_1 = s_t$. Because of Eq. (4.30), the dipole strength distribution on S_{B_C} is settled by this expression.

The kinematic boundary condition stated by Eq. (4.38) can be brought to the form:

$$A\frac{\partial \eta}{\partial s_1} + B\frac{\partial \eta}{\partial s_2} = C\left(V_{s_3} - \frac{\partial \eta}{\partial t}\right) \quad (4.40)$$

with $A = V_{s_1} - V_{s_2}\cos\theta$, $B = V_{s_2} - V_{s_1}\cos\theta$ and $C = \sin^2\theta$. This results in one equation for each panel and a system of equations when all panels belonging to S_{B_C} are considered.

The assumption of the flow having a primarily chordwise orientation allows for developing an algorithm which operates on chordwise panel stripes (see Figure 4.7).[3]

When the cavity shape is computed, the detachment point ($s_1 = s_0$) and the reattachment point ($s_1 = s_t$) require special attention. The detachment point is assigned to the first panel of each stripe where $p \leq p_v$, or, leading to a simpler implementation, the panel nearest to the leading edge – for a discussion see Gaschler (2017, pp. 51f).

In the closure region of the sheet cavity, i.e. the transition from the sheet cavity to the wetted surface of the blade defining the reattachment point, complicated and highly unsteady flow phenomena will take place that involve the formation of a re-entrant jet (see Section 2.3). This effect cannot be

---

[3] This does not mean that the influence of neighbouring stripes is neglected. In fact, Eqs. (4.39) and (4.40) include the crossflow velocity term V_{s_2}.

handled by the present method. Thus, during the transition from S_{B_C} to S_B defining the reattachment point, the term $p_{\mathrm{ref}} - p_v$ in Eq. (4.39) requires a special treatment. In order to approximate the flow behaviour in this region, pressure recovery models are applied to blend the pressure from $p_{\mathrm{ref}} - p_v$ to $p_{\mathrm{ref}} - p_{w1}$ when transiting from sheet cavitation to the wetted part downstream of the cavitation, with p_{w1} being the pressure of the first panel located on S_B downstream of the cavitation (Scharf, 2014, pp. 12f).

The system of linear equations represented by Eq. (4.36) is modified when cavitating flow is considered. The body or the blade surface, respectively, is discretised now by $N_B - N_{B_C}$ panels on the non-cavitating part $S_B \setminus S_{B_C}$ and by N_{B_C} panels on the cavitating part S_{B_C}. Whereas for $S_B \setminus S_{B_C}$ the source strengths σ are settled prior to solving, for S_{B_C} the dipole strengths are determined by Eq. (4.39). Thus, a system of linear equations has to be constructed based on Eq. (4.28) for $N_B - N_{B_C}$ unknown μ_k and N_{B_C} unknown σ_k:

$$\sum_{k=N_{B_C}+1}^{N_B} A_k \mu_k + \sum_{k=1}^{N_{B_C}} B_k \sigma_k = -\sum_{k=1}^{N_{B_C}} A_k \mu_k - \sum_{k=N_{B_C}+1}^{N_B} B_k \sigma_k \quad \text{for each internal point } \mathbf{X}_{0,j}, \tag{4.41}$$

$j = 1, \ldots, N_B$, where the right-hand side consists of known quantities. Further substitutions are required by the fact that Φ_0 in Eq. (4.39) depends on the solution of the wetted surface upstream of the inception point (Scharf, 2014, pp. 15ff).

For the formulation of the model it has been assumed so far that the cavity planform S_{B_C} is known. This, however, is not the case and an iterative procedure is necessary in order to calculate sheet cavitation. The procedure comprises the following steps:

(1) First, the boundary value problem is set up and solved numerically without taking sheet cavitation into account. The distribution of pressure on the body is calculated and the initial cavity length is estimated by the criterion $p \leq p_v$ leading to a first guess of S_{B_C}.

(2) Then, a new boundary value problem with the particular boundary conditions for non-cavitating regions ($S_B \setminus S_{B_C}$) and cavitating regions (S_{B_C}) is set up, yielding an updated distribution of pressure and velocity.

(3) By means of Eq. (4.40), the cavity thickness η is derived for every panel of S_{B_C}. For every stripe at $s_1 = s_t$, the cavity thickness should vanish. This, however, will not be the case in general. Rather, the cavity thickness will have a finite positive or negative value.

    - If the value is positive, the cavity length $s_t - s_0$ is extended in the downstream direction,
    - if it is negative, one or more panels are removed from the panel stripe starting from the downstream end, i.e. the cavity length is reduced.

    This adjustment leads to an updated cavity planform S_{B_C} and step 2 is repeated until convergence is reached.

The cavity shape computation is considered to be converged when the sum of the cavity thickness of every stripe at $s_1 = s_t$ is smaller than a certain threshold δ:

$$\sum_{\text{stripes}} \left\| \eta \left(s_1 = s_t \right) \right\| \leq \delta. \tag{4.42}$$

The steps mentioned above are repeated for every time step of the simulation. It can be advantageous to initialise the cavity planform of the new time step not by the fully wetted solution but by means of the results obtained from the previous time step.

Certainly, the sheet cavitation model of *pan*MARE described so far is not able to resolve all sophisticated phenomena of sheet cavitation. Furthermore, the current implementation does not consider sheet cavitation exceeding the trailing edge of the blade. To model this effect, an enhancement of the method would be necessary. However, it is assumed that the model reproduces the bulk of sheet cavitation to a sufficiently accurate degree and that it approximates the unsteady behaviour appropriately. It has already been mentioned that numerical problems are likely to occur at the blade tip where high velocities in the crosswise s_2-direction dominate the flow. For this reason, when details of the cavitating blade flow are needed, additional viscous flow simulations are carried out by means of ANSYS CFX. This is described in greater detail in the next chapter.

Chapter 5

Modelling of Tip Vortex Cavitation

The cavitating tip vortex and its interaction with sheet cavitation in the blade tip region are major contributors to higher-order pressure fluctuations. This has been introduced in Chapter 2. In the present chapter, the developed code `VoCav2D` for modelling tip vortex cavitation is explained. The discussion starts in Section 5.1, where the assumptions and simplifications for developing the model are listed. Solving the momentum equations for two-dimensional axisymmetric flow constitutes the core of the model. In this respect, two formulations exist. These are presented in Section 5.2. Modelling the interaction between sheet and tip vortex cavitation is addressed in Section 5.3. A verification study and a convergence analysis complete this chapter.

5.1 Basic Considerations

In order to make the complex problem of tip vortex cavitation accessible to a numerical treatment, some assumptions and simplifications are necessary. The most fundamental issues are the following:

(1) For most conventional propellers, the cavitating tip vortex is a well-defined flow structure which can be clearly distinguished from the ambient flow. This is illustrated in the fact that, from a theoretical point of view, the circulation Γ_b bound at the blade is completely concentrated in the tip vortex, with the vortex radius being much smaller than characteristic length dimensions of the propeller blade. This warrants the separate consideration of the nearly axisymmetric tip vortex flow and the ambient flow.

(2) Additionally, the tip vortex is an elongated structure, which implies that changes in the axial direction can be neglected. Because of the approximate symmetry with respect to the vortex axis, changes in the circumferential direction can also be neglected. Proceeding from these assumptions, it is possible to treat the cavitating tip vortex as a two-dimensional problem, which helps to drastically ease the implementation and to reduce computational effort.[1]

---

[1] It will turn out that the actual solution of the problem only involves one spatial dimension – namely the cavitation radius r_c.

(3) Compared to the radius of the tip vortex cross section, the curvature radius of the vortex axis is very large. Furthermore, the distance between one tip vortex and the tip vortices of the other blades is large. This allows for neglecting the helical shape of the tip vortex trajectory and the interaction between the individual tip vortices when the dynamical behaviour of the vortex cavity is modelled.

(4) In Section 2.4 it has been explained that what is understood as propeller tip vortex is a combination of up to three species of vortices, with the trailing vortex being the most dominant one – for moderate operation conditions of the propeller. This distinction is abandoned from now on, i.e. only a single merged vortical structure that propagates from the propeller tip is considered, disregarding its actual genesis.

(5) The fluid is assumed to be Newtonian and incompressible. Turbulence is not taken into consideration when the tip vortex flow is simulated. Indeed, Isay (1991) proposes a method for approximating the resulting Reynolds stresses; Devenport et al. (1996) show that turbulence in the viscous core region of a developed tip vortex plays only a minor role and the flow is rather of laminar character. Thus, the laminar solution is considered as a sufficient approximation.

(6) Thermodynamic effects on cavitation are neglected.

The second assumption may evoke a critical discussion. It has already been stated in Section 2.4 that disturbances of the interface between water and vapour propagate in the form of Kelvin waves, and vibration modes different from axisymmetric deflection may arise. This has been investigated by Pennings et al. (2015) in a detailed experimental campaign with an elliptic hydrofoil in homogeneous inflow. They confirm the existence of Kelvin waves that show a specific behaviour of dispersion. This effect can only be explained by a three-dimensional vortex model. Nevertheless, there are reasons which justify the use of a two-dimensional approximation: Pennings et al. do not only show the existence of Kelvin waves on the cavitating core of a vortex, they also show the possibility of disturbances being convected with the flow – an important feature with respect to the interaction with sheet cavitation, which is ascertainable by the current formulation because interaction forces between adjacent cross sections are of little importance in this case. Furthermore, according to their work, substantial excitement of the relevant breathing mode – i.e. axisymmetric deflection of the cavity surface – happens at relatively low frequencies and therefore long wavelengths. A close relation between the two-dimensional and three-dimensional formulation for the limiting case of long wave length has already been indicated in Section 2.4.

5.2 Description of the Tip Vortex Cavitation Model

The two-dimensional approximation applied to the simulation of the tip vortex cavitation dynamics is based on the ideas of Szantyr (2006) and Ligneul (1989). The tip vortex is split into numerous segments and each segment is treated separately, i.e. the (assumably) small interaction forces acting between the segments cannot be considered. In this context, a vortex segment is defined as a small axial portion of the tip vortex with a developed cavitating core of the radius r_c and the surrounding vortical flow. In Figure 5.1, the segmentation scheme is shown. A segment k originates at the propeller tip at $t = t_{0,k}$. The age of the k-th segment is denoted as $t_k^\star$ and is simply the time passed since the birth of the segment. Each segment has a certain position $\mathbf{x}_k^\star = \mathbf{x}_k^\star\left(t_{0,k}, t_k^\star\right)$, which is given by

$$\mathbf{x}_k^\star\left(t_{0,k}, t_k^\star\right) = \mathbf{x}_{0,k}^\star + \int_{t_{0,k}}^{t_{0,k}+t_k^\star} \mathbf{v}_w \mathrm{d}t, \tag{5.1}$$

with the initial position $\mathbf{x}_{0,k}^\star$ depending on the angular position of the propeller tip at $t = t_{0,k}$. In this equation, $\mathbf{v}_w$ is the velocity of the fluid in the slipstream of the propeller in the coordinate system fixed to the ship. In fact, this velocity is not constant, but for the purpose of approximating the position of the cavitating tip vortex it is assumed that using a constant value is sufficiently precise. For convenience, $\mathbf{v}_w \approx (-V_S, 0, 0)$ with the ship speed V_S is used in the present case and the errors introduced are neglected. The element length $\mathrm{d}l_k = \mathrm{d}l = \mathrm{d}t\sqrt{(\pi n D)^2 + (v_w)^2}$ is then a constant and Eq. (5.1) reduces to

$$\mathbf{x}_k^\star\left(t_k^\star\right) = \mathbf{x}_{0,k}^\star + \mathbf{v}_w t_k^\star. \tag{5.2}$$

The position $s_k^\star$ relative to the blade tip is the number of segments upstream of the segment k multiplied with dl.

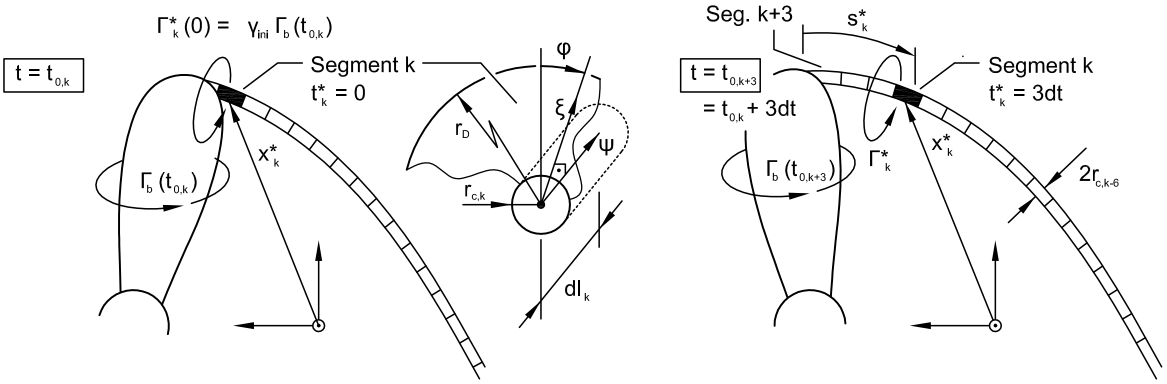

Fig. 5.1 Segmentation scheme of the tip vortex cavitation model.

Furthermore, two fundamental parameters describing the vortical flow of each segment are introduced: the circulation $\Gamma_k^\star = \Gamma_k^\star\left(t_{0,k}, t_k^\star\right)$ and the radius of the viscous core $r_{a,k} = r_{a,k}\left(t_{0,k}, t_k^\star\right)$. Both quantities will grow as the segment travels downstream starting from an initial value depending on the characteristics of the flow at the propeller tip at $t_{0,k}$. This is addressed in greater detail in Section 5.4. The quantity $r_{c,k} = r_{c,k}(t)$ is the time-dependent cavitation radius of the segment k.

So far, the framework for the vortex model has been given: numerous independent segments arranged at the vortex axis and being convected downstream by the flow. Knowing the cavitation radius $r_{c,k}(t)$, it is straightforward to obtain an approximation for the pressure disturbance. This is explained in Section 6.2. The question remains how to calculate $r_{c,k}(t)$ for each single segment.

For this purpose, the code `VoCav2D` is applied. It calculates the vortical cavitating flow under the assumption of two-dimensionality.

The treatment for every segment is the same and thus the index k is omitted from now on. For the axisymmetrical local tip vortex flow with a cavitating core of the radius r_c at its center, it is convenient to use cylindrical coordinates; in the present work these are denoted as (ξ, φ, ψ) in the radial, circumferential and axial direction (see Figure 5.1).

In accordance with the simplifications made above, i.e. $\partial/\partial\psi = 0$ (neglect of changes in the axial direction), $\partial/\partial\varphi = 0$ (assuming axisymmetric flow), $\rho = \text{const.}$ and $\mu = \text{const.}$, the following underlying equations in cylindrical coordinates are obtained (Chahine, 1995). The continuity equation:

$$\frac{1}{\xi}\frac{\partial\left(\xi u_{\xi}\right)}{\partial\xi} = 0, \tag{5.3}$$

the momentum equation for ξ:

$$\rho\left(\frac{\partial u_{\xi}}{\partial t} + u_{\xi}\frac{\partial u_{\xi}}{\partial\xi} - \frac{u_{\varphi}^{2}}{\xi}\right) = -\frac{\partial p}{\partial\xi} + \mu\frac{\partial}{\partial\xi}\left(\frac{1}{\xi}\frac{\partial\left(\xi u_{\xi}\right)}{\partial\xi}\right) \tag{5.4}$$

and the momentum equation for φ:

$$\rho\left(\frac{\partial u_{\varphi}}{\partial t} + u_{\xi}\frac{\partial u_{\varphi}}{\partial\xi} + \frac{u_{\xi}u_{\varphi}}{\xi}\right) = f_{\varphi} + \mu\frac{\partial}{\partial\xi}\left(\frac{1}{\xi}\frac{\partial\left(\xi u_{\varphi}\right)}{\partial\xi}\right). \tag{5.5}$$

The body force term f_{φ} will become important later; for the moment, it is set to zero.

It can be seen that the viscous term in Eq. (5.4) vanishes because of the symmetry assumed and the continuity equation (5.3). Also originating from continuity of the flow, the kinematic relation between cavity radius r_c and radial velocity $u_{\xi} = u_{\xi}\left(\xi\right)$,

$$u_{\xi} = \frac{\dot{r}_c r_c}{\xi}, \tag{5.6}$$

can be formulated. Substituting the radial velocity component u_{ξ} in Eqs. (5.4) and (5.5) by Eq. (5.6) yields

$$\rho\left(\frac{\ddot{r}_c r_c + \dot{r}_c^{2}}{\xi} - \frac{\dot{r}_c^{2} r_c^{2}}{\xi^{3}} - \frac{u_{\varphi}^{2}}{\xi}\right) = -\frac{\partial p}{\partial\xi} \tag{5.7}$$

for the radial momentum equation, and

$$\rho\left(\frac{\partial u_{\varphi}}{\partial t} + \frac{\dot{r}_c r_c}{\xi}\left(\frac{\partial u_{\varphi}}{\partial\xi} + \frac{u_{\varphi}}{\xi}\right)\right) = f_{\varphi} + \mu\frac{\partial}{\partial\xi}\left(\frac{1}{\xi}\frac{\partial\left(\xi u_{\varphi}\right)}{\partial\xi}\right) \tag{5.8}$$

for the equation of circumferential momentum. Obviously, both equations constitute a system of coupled differential equations and the change of cavitation radius is influenced by the pressure gradient and the surrounding flow u_φ. On the other hand, u_φ is affected by the presence of a cavity with varying a radius inside the core of the vortex.

Integrating the radial momentum equation (5.7) from a certain outer boundary radius r_D to the radius of the (unknown) cavitating core $r_c > 0$ results in the two-dimensional form of the Rayleigh-Plesset equation (Choi et al., 2009; Gosda, 2016, e.g.):

$$\left(r_c\ddot{r}_c + \dot{r}_c^2\right)\ln\left(\frac{r_D}{r_c}\right) + \frac{r_c^2\dot{r}_c^2}{2}\left(\frac{1}{r_D^2} - \frac{1}{r_c^2}\right) = \frac{1}{\rho}\left(p_c - p_{\text{vtx}}\right), \tag{5.9}$$

where

$$p_c = p_v + p_{g0}\left(\frac{r_{c0}}{r_c}\right)^{2n} - 2\mu\frac{\dot{r}_c}{r_c} - \frac{S}{r_c} \tag{5.10}$$

and

$$p_{\text{vtx}}\left(r_c\right) = p_D - \rho\int_{r_c}^{r_D}\frac{u_\varphi^2}{\xi}\mathrm{d}\xi. \tag{5.11}$$

This equation has already been introduced in Section 2.4. In Eqs. (5.9) and (5.10), p_c is the pressure inside the cavity, which depends on the vapour pressure p_v of water and the partial pressure $p_{g0}\left(r_{c0}r_c^{-1}\right)^{2n}$ of non-condensable gases with the polytropic index $n = 1$ for isothermal processes. The last two terms in Eq. (5.10) are contributions from viscosity μ and interfacial tension S. Furthermore, p_{vtx} describes the influence of the vortical flow around the cavitating core; p_D is the ambient pressure far away from the vortex axis at $\xi = r_D$.

Choi et al. (2009) mention the problem caused by the appearance of r_D as an argument of the ln-function in Eq. (5.9) (just as in Eq. (2.19) in Section 2.4). Since $\ln x$ is unbounded for $x \to \infty$, r_D has to be chosen with caution. In their work, a numerical study is carried out in order to show the influence of r_D on the results. They suggest using a finite but large value of r_D. In this work, $r_D r_{c,\text{eq}}^{-1} \gtrsim 10$ is used in most cases. The influence of r_D on the results is investigated in Sections 5.5.2 and 7.4.

The Burgers vortex model has been introduced in Section 2.4.1:

$$u_\varphi\left(\xi\right) = \frac{\Gamma}{2\pi\xi}\left[1 - \exp\left(\frac{-\beta\xi^2}{r_a^2}\right)\right]. \tag{5.12}$$

It is a solution of Eq. (5.8) for the case $r_c = 0$ and $\dot{r}_c = 0$ and describes the distribution of circumferential velocity. Due to diffusion, the viscous core radius is not constant and will grow with time. This relation will be used later.

Two implementations of the method VoCav2D exist: VoCav2D-f1 with a strong bidirectional coupling between the radial and the circumferential momentum equation and VoCav2D-f2, where the influence of the cavitating core on the surrounding vortex flow is neglected; however, by an enhancement, it provides the possibility of capturing the influence of disintegrated remainders of sheet cavitation surrounding the tip vortex cavity.

5.2.1 Formulation f1

The coupled system of equations formed by Eq. (5.8) and Eqs. (5.9) through (5.11) can be solved numerically. For the solution of the problem, appropriate initial and boundary conditions have to be prescribed (Bosschers, 2009b):

(1) At $t = t_0$, the initial cavitation radius r_{c0} has to be defined. This can be the equilibrium radius or any other value in this range. In all cases, $\dot{r}_{c0}$ is set to zero for $t = t_0$.

(2) Furthermore, at $t = t_0$, the velocity distribution $u_\varphi(\xi)$ is initialised. For this purpose, the Burgers vortex model given by Eq. (5.12) with $\Gamma = \Gamma^\star$ and r_a at $t = t_0$ is applied.

(3) For the solution of the circumferential momentum equation, the boundary condition at $\xi = r_c$ reads:

$$\frac{\partial u_\varphi}{\partial \xi} = \frac{u_\varphi}{\xi}, \text{ for } \xi = r_c, \tag{5.13}$$

stating that no shear stresses act across the liquid-vapour interface.

(4) For $\xi \geq r_D$, the outer domain radius, the velocity is thought to behave similarly to a potential vortex.

Applying these boundary and initial conditions, a numerical solution procedure as proposed by Chahine (1995) can be constructed: A central finite difference scheme is used to solve the radial momentum equation (Eqs. (5.9), (5.10) and (5.11)), and the circumferential momentum equation (5.5) is solved by the Crank-Nicolson method. Both equations are solved sequentially in an iterative manner; consult Gosda (2016) for details.

Due to the roll-up process, the circulation of a vortex segment will increase with time. Certainly, it is not possible to model the roll-up process itself by means of the present two-dimensional approach and a method is required to mimic this process. In VoCav2D-f1, this is achieved by a manipulation of the source term f_φ in Eq. (5.8). The approximate relation between the change of circulation $\partial\Gamma^\star/\partial t$ and the source term is given by

$$f_\varphi = \rho \frac{\partial \Gamma^\star}{\partial t} \frac{1}{2\pi\xi} \left[1 - \exp\left(\frac{-\beta \xi^2}{r_{a0}^2} \right) \right]. \tag{5.14}$$

To obtain this approximation, Eq. (5.12) has been combined with $\rho \partial u_\varphi/\partial t = f_\varphi$, which is a truncated variant of Eq. (5.5) neglecting the influence of viscosity.

The accuracy and convergence of the numerical solution depends on the spatial discretisation and on the selected time step size. In order to choose an appropriate time step size, the expected period of the oscillations is approximated by Eq. (2.19). Then, the time step size is determined so that one period is discretised by at least 200 time steps. The spatial domain considered in the circumferential momentum equation (5.5) is $[r_c, r_D]$. Since $[r_c, r_D]$ changes with r_c, the equation is transformed to an invariant grid that consists – in the present cases – of 5000 points in the radial direction; see Gosda (2016) for details.

5.2.2 Formulation f2

Whereas the `f1`-formulation enables a strong coupling between the radial the and circumferential momentum equation, the `f2`-formulation only considers the influence of the vortex flow on the cavitating core. The vortex flow itself remains undisturbed by the cavity. For this purpose, the radial momentum equation (Eqs. (5.9), (5.10) and (5.11)) is solved by a fourth-order Runge-Kutta scheme and u_φ in Eq. (5.11) is modelled by the Burgers vortex given by Eq. (5.12) using $\Gamma = \Gamma^\star(t_0, t^\star)$ and $r_a = r_a(t_0, t^\star)$. The advantage of this formulation is a significantly reduced computational effort.

Full-scale and model test observations reveal a bubbly flow surrounding the cavitating tip vortex (see Section 2.5). These bubbles are assumed to originate primarily from two mechanisms:

(1) Disintegrating sheet cavitation yields to a high number of bubbles circulating around the cavitating vortex core and finally being absorbed by the tip vortex.

(2) The assumption of a cavitating core with an exact circular shape and a sharp interface between water and vapour is a strong simplification. In fact, when the tip vortex cavity undergoes strong oscillations, the interface between both phases gets disturbed and bubbles start to disassociate.

Even though the formation mechanism of these bubbles cannot be modelled by the present model, it does try to capture their influence on the cavitating core. In order to achieve this, a number of spherical bubbles m each having the radius $r_{b,m}$ is placed around the cavitating core of each vortex segment. An illustration of the idealised situation is given in Figure 5.2.

The assumption made here is that the entirety of all bubbles has an impact on the density ρ of the flow surrounding the cavitating core, so that p_vtx in Eq. (5.11) changes to

$$p_\text{vtx}(r_c) = p_D - \int_{r_c}^{r_D} \rho^\star \frac{u_\varphi^2}{\xi} \mathrm{d}\xi, \tag{5.15}$$

where $\rho^\star = \rho^\star(t_0, t^\star)$ is the density of the fluid which is reduced by the presence of the bubbles. The bubbles are released at $t = t_0$ in a zone r_B around the vortex core and the reduced density is then approximated by

$$\rho^\star = \rho\left(1 - \frac{\sum_m r_{b,m}^2}{r_B^2}\right). \tag{5.16}$$

The choice of r_B and the distribution of $r_{b,m}$ at $t = t_0$ remain to be determined.

The index m is omitted from now on since the treatment for every bubble is the same. To determine the radius $r_b = r_b(t)$ of a bubble at the radial position ξ_b, the spherical Rayleigh-Plesset equation (Brennen, 1995, pp. 36f) is applied, neglecting surface tension and viscous effects:

$$r_b \ddot{r}_b + \frac{3}{2}\dot{r}_b^2 = \frac{1}{\rho}\left(p_b - p_\text{vtx}(\xi_b)\right), \tag{5.17}$$

with $p_b = p_v + p_{g0}\left(r_b r_{b0}^{-1}\right)^{3n}$. Due to the pressure gradient $\partial p / \partial \xi$, the bubbles are carried to the center of the vortex and a simplified equation of motion adopted from Abdel-Maksoud et al. (2010) describes how the bubbles travel from their initial position ξ_{b0} to the core at $\xi = 0$. For the motion of the bubble, only radial bubble velocities and forces are taken into consideration, i.e. for the circumferential direction $u_{\varphi,b} = u_\varphi$ is assumed and since the vortex flow is described as Burgers vortex, the radial flow velocity u_ξ is zero. Hence:

$$\frac{2}{3}\pi\rho r_b^3 \dot{u}_{\xi,b} = F_D + F_p + F_v, \tag{5.18}$$

where F_D is the drag force with

$$F_D = -C_D \frac{\rho}{2}\pi r_b^2 |u_{\xi,b}| u_{\xi,b}, \tag{5.19}$$

$C_D = 24\,(1+C)\,\mathrm{Re}_b^{-1}$ and $\mathrm{Re}_b = \rho |u_{\xi,b}| 2 r_b \mu^{-1}$, F_p is the pressure force:

$$F_p = -2\pi r_b^3 \frac{\partial p}{\partial \xi}, \tag{5.20}$$

and F_v is denoted as the volume force with

$$F_v = -2\pi\rho r_b^2 \dot{r}_b u_{\xi,b}. \tag{5.21}$$

Combining Eqs. (5.18) through (5.21) leads to the following relation:

$$\dot{u}_{\xi,b} = -\frac{3}{2}\,\frac{\left[6\,(1+C)\,\mu + 2\rho r_b \dot{r}_b\right] u_{\xi,b} + 2 r_b^2\, {}^{\partial p}/_{\partial \xi}}{\rho r_b}, \tag{5.22}$$

where $\dot{u}_{\xi,b} = \ddot{\xi}_b$. Eqs. (5.17) and (5.22) can be solved by the Runge-Kutta scheme similar to the solution process of Eq. (5.9). In the present work, delimiters for the growth of r_b are defined that prevent the bubbles from unphysical strong growth when approaching the core. Once a bubble reaches the core, the bubble will be eliminated.

Within VoCav2D-f2, two levels of time discretisation exist: the level $\tilde{t}_{[k]}$ for which data exchange with external methods is performed (see Section 6.3) and a finer level $\tilde{\tilde{t}}_{[j]}$ applied to the Runge-Kutta scheme. The influence of time discretisation on the results obtained by VoCav2D-f2 is discussed later in this chapter.

5.3 Interaction with Sheet Cavitation

One of the key assumptions of this thesis is that the interaction between sheet and tip vortex cavitation is important for the generation of higher-order pressure fluctuations. Based on observations and the conclusions drawn by other authors reported in Section 2.5, the following idealised model for the interaction mechanisms is deduced and illustrated in Figure 5.2.

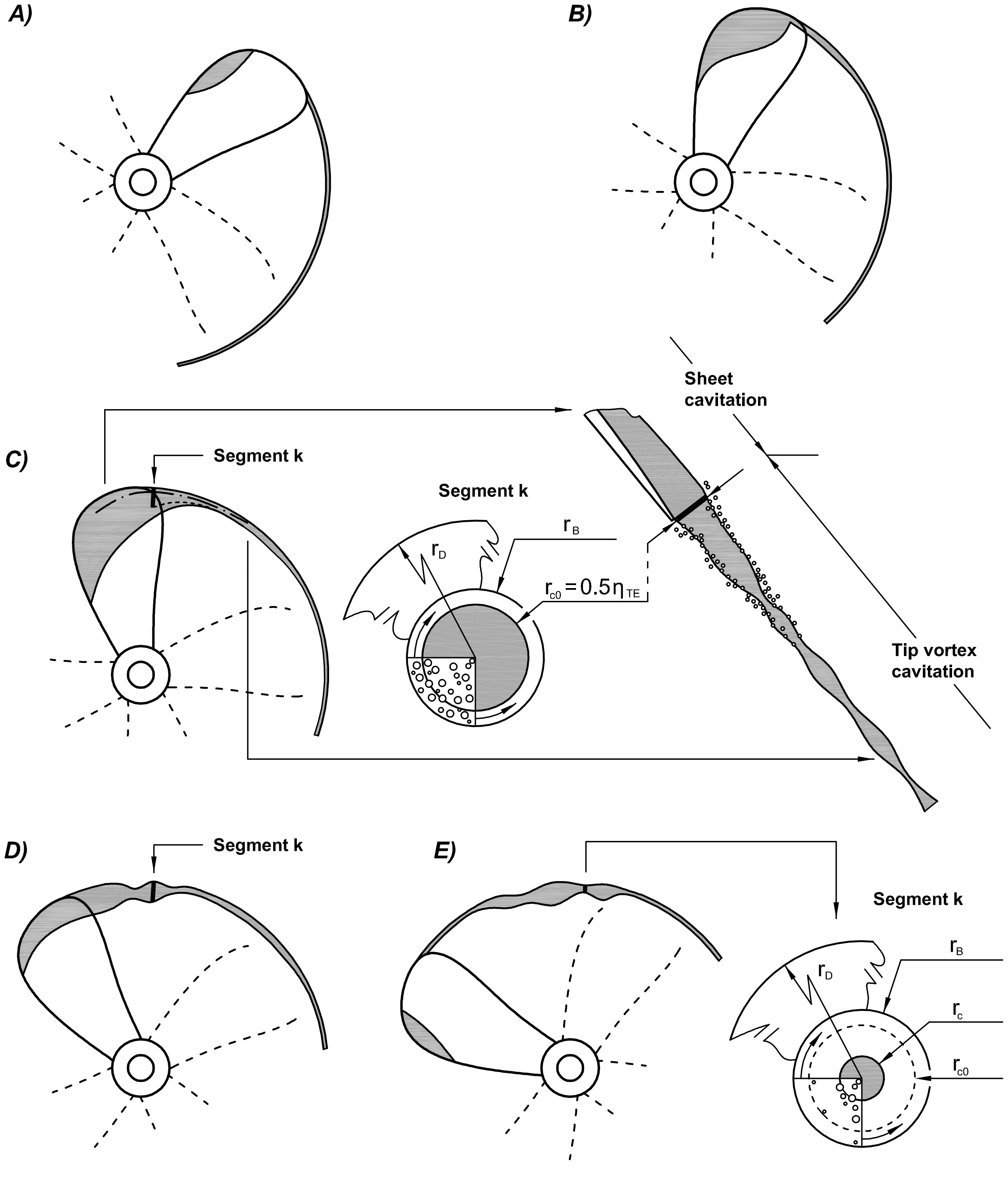

Fig. 5.2 Interaction between sheet cavitation and tip vortex cavitation (schematic).

When approaching the wake peak in the 12 o'clock position, sheet cavitation is present near the leading edge and continually grows in the chordwise direction (see subfigures A and B). With further rotation of the propeller, sheet cavitation reaches the trailing edge and widens the cavitating core of the tip vortex (subfigure C). At a certain point, the sheet cavitation starts to disintegrate and large scale fragments as well as bubbles broken out of the formerly coherent sheet cavity are swept away by the flow and absorbed by the tip vortex. Thus, when sheet cavitation reaches the trailing edge, the following heuristic condition for the initial cavitation radius r_{c0} of a vortex segment can be justified:

$$r_{c0} = \max\left\{\frac{\eta_{\mathrm{TE}}}{2}, r_{c,\mathrm{eq}}\right\}, \tag{5.23}$$

where η_{TE} is the cavity thickness at the trailing edge and $r_{c,\mathrm{eq}}$ is the equilibrium cavity radius for the given flow conditions.

In subfigures (D) and (E), the blade is leaving the wake peak zone and a common observation is that sheet cavitation on the blade shrinks. This shrinking process starts from the inner radii and may be retarded by the upward velocity component of the wake field which increases the propeller load. Those segments born during the sojourn of the blade in the wake peak region have a large initial cavitation radius, undergo strong fluctuations and are finally swept away by the flow. This part of the cavitating tip vortex is responsible for significant fluctuations of the pressure on the hull. It is important to note that the segments maintain their angular position in the model because of the assumption made when formulating Eq. (5.2).

5.4 Determination of Vortex Parameters

Up to this point, the numerical model for the cavitating tip vortex has been described in a general fashion. However, to really apply this model to cavitating propeller tip flow, a number of governing parameters of the tip vortex flow have to be estimated in a quantitative manner. The basic idea is to carry out RANS simulations of the propeller by means of ANSYS CFX with a special focus put on the flow in the tip region. The flow in this region is rather complex, strongly influenced by viscous effects and characterised by large spatial gradients. Consequently, the grid resolution has to be fine, which leads to a high computational effort. In order to limit the effort to an acceptable level, simulations of the propeller flow are carried out for a number of representative operation conditions with homogeneous inflow, and the results in terms of vortex parameters $\bullet$ for the propeller operating in the wake field of the ship are found by interpolation, depending on the current blade load:

$$\{\bullet \mid \text{RANS, tip flow}\}\left(k_T n_b^{-1}\right)\Big|_{\text{homogeneous}} \rightsquigarrow \{\bullet \mid \mathsf{VoCav2D}\}\left(k_{T,\text{blade}}\right)\Big|_{\text{wake field}}$$

The results presented later in Chapter 7 will be anticipated here for a discussion of the problem. Figure 5.3 shows the flow details at the tip of the propeller of a container vessel simulated by the RANS method ANSYS CFX. For non-cavitating flow conditions (subfigure A), a compact and clearly discernible tip vortex can be seen. The pressure distribution shown at planes perpendicular to the vortex axis indicates axisymmetry of the flow.

When cavitation takes place, this has a significant influence on the flow conditions at the propeller tip (subfigures B and C). The tip vortex still has a compact structure; however, the intensity is lower compared to the non-cavitating case. This can be seen by inspection of the pressure isolines in the

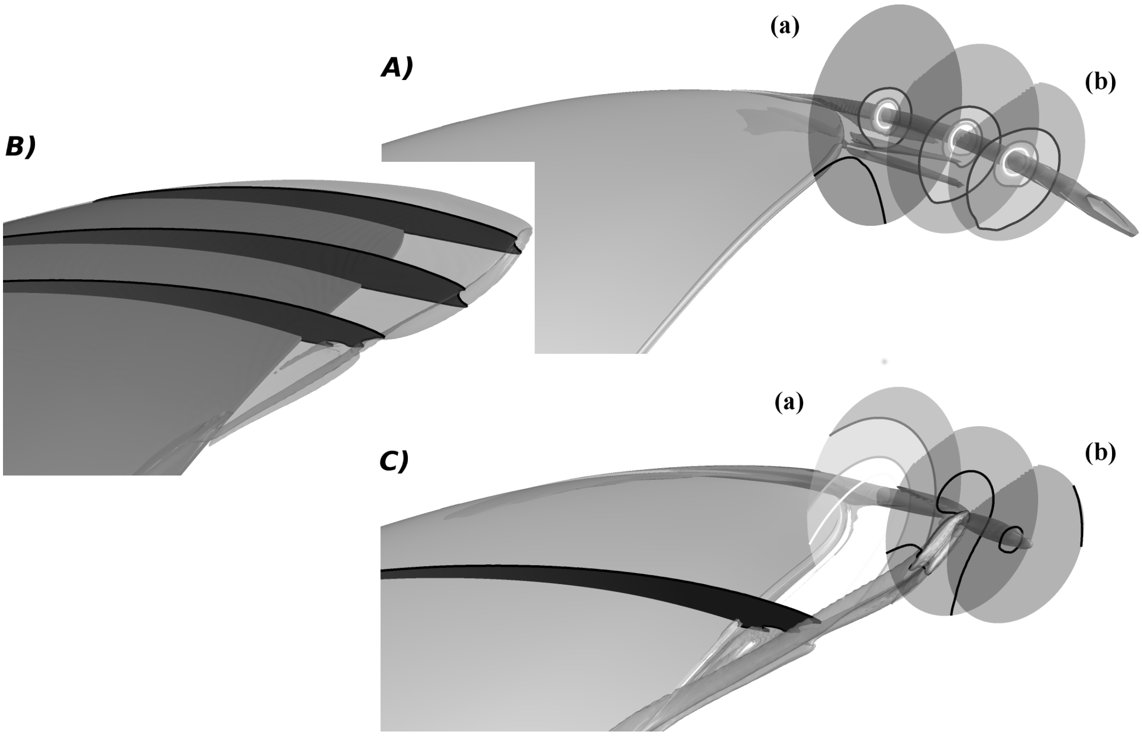

Fig. 5.3 Simulation results for the tip flow of the propeller of a container vessel (referred to as P00C in Table 7.1) in homogeneous inflow for $J = 0.65$. Subfigure (A): non-cavitating flow conditions, vortex structures made visible by the λ_2-criterion (ANSYS, 2014) and pressure distribution at circular planes perpendicular to the vortex axis. Subfigures (B) and (C): cavitating flow conditions; extent of sheet cavitation (B) and vortex structure (C). An inverted colour scale has been used for the isolines of pressure: the brighter the colour, the higher the pressure drop towards the vortex center.

figure. Furthermore, another prominent vortex structure arises. This vortex structure is aligned with the closure of the sheet cavity and can be identified as the re-entrant jet vortex merging with the tip vortex. Directly at the propeller tip (plane a), the flow is far from being axisymmetric. However, downstream of the closure of sheet cavitation (plane b), this condition is met again. Any conclusions drawn from Figure 5.3 concerning the streamwise change of intensity of the tip vortex must be handled with some care, since, as shown by Hsiao and Chahine (2008), RANS methods tend to give erroneous predictions of the streamwise development of tip vortices. However, also shown by Hsiao and Chahine, directly behind the trailing edge, RANS methods are able to deliver reliable results. This insight leads to the following procedure for finding adequate input parameters for the cavitating vortex model.

5.4.1 Circulation of the vortex

It has been stated in the previous section that the flow of the tip vortex is assumed to be representable by the Burgers vortex model given by Eq. (5.12). Hence, the tip vortex flow is described by two parameters, the circulation Γ and the radius of the viscous core r_a. This parametrisation is adopted for the flow surrounding the segments of the cavitating tip vortex, where the circulation of a segment is denoted as $\Gamma^{\star}(t_0, t^{\star})$ and the radius of the viscous core becomes $r_a(t_0, t^{\star})$. Due to the roll-up process of the tip vortex, the circulation will gradually increase from an initial value $\Gamma^{\star}(t_0, 0)$ to a value close to the bound blade circulation $\Gamma_b(t_0)$ as the segment travels downstream. Astolfi et al. (1999) suggest a power law formulation for the increase of the strength of a tip vortex with increasing distance from the trailing edge. In this work, the following formulation based on the exponential function is chosen:

$$\Gamma^{\star}(t_0, t^{\star}) = \Gamma_b(t_0)\left(1 - (1 - \gamma_{\text{ini}})\exp\left(-\kappa t^{\star}\right)\right), \tag{5.24}$$

where γ_{ini} is the ratio between the initial circulation $\Gamma^{\star}(t_0, 0) = \Gamma_{\text{ini}}$ of the tip vortex segment and the maximum bound circulation $\Gamma_b(t_0)$. The parameter κ is adjusted in a way that the maximum circulation is reached after a specified segment age.

For determining γ_{ini}, the considered propeller is analysed numerically by means of the RANS method ANSYS CFX. Obviously, $\gamma_{\text{ini,c}} = \gamma_{\text{ini,c}}(J, \text{Re}, \sigma)$ for cavitating and $\gamma_{\text{ini,nc}} = \gamma_{\text{ini,nc}}(J, \text{Re})$ for non-cavitating flow will be different. Presuming

$$\gamma_{\text{ini,c}} = \gamma_{\text{ini,nc}}\varepsilon_1\varepsilon_2, \tag{5.25}$$

the procedure is to determine the ratio $\gamma_{\text{ini,nc}}$ for non-cavitating flow and the correction factors $\varepsilon_1(J, \sigma) = \Gamma_{b,\text{nc}}\Gamma_{b,\text{c}}^{-1}$ and $\varepsilon_2(J, \sigma) = \Gamma_{\text{ini,c}}\Gamma_{\text{ini,nc}}^{-1}$.

The procedure starts with the simulation of the propeller in homogeneous inflow and for non-cavitating conditions obeying the correct propeller scale for various advance coefficients J. The distribution of bound circulation can be determined by integration of the velocity along a closed curve around the propeller blade at $r = \text{const.}$, which is shifted slightly away from the propeller surface in order to be outside of the boundary layer. The maximum of this distribution is assumed to equal Γ_b.

In order to estimate the initial circulation of the tip vortex $\Gamma_{\text{ini,nc}}$ in close vicinity of the trailing edge, the velocity distribution $\widetilde{u}_{\varphi}$ and $\widetilde{u}_{\xi}$ on a circular plane of the diameter e_p perpendicular to the tip vortex axis is analysed (see Figure 5.3). Flow components in the ψ-direction are not considered. In the following, $\widetilde{\bullet}$ is used to distinguish between propeller tip flow quantities obtained by a RANS simulation from those used in VoCav2D. Although the tip vortex flow is very compact and concentrated, $\widetilde{u}_{\varphi}$ and $\widetilde{u}_{\xi}$ will be affected by the ambient background flow and these portions need to be filtered out. Since $e_p \ll D$, the background flow will be almost constant over the whole plane and can easily be identified, and what remains after filtering is a distribution of circumferential velocities $\widetilde{u}_{\varphi} = \widetilde{u}_{\varphi}(\xi)$ and vanishing radial velocities $\widetilde{u}_{\xi}$. The parameters Γ and r_a of the Burgers vortex $u_{\varphi}(\Gamma, r_a, \xi)$ are then adjusted, so that:

$$\int_0^{e_p/2} \left[\widetilde{u}_{\varphi}(\xi) - u_{\varphi}(\Gamma, r_a, \xi)\right]^2 \mathrm{d}\xi \to \min. \tag{5.26}$$

For this purpose, a Gauss-Newton algorithm can be applied. Determining $\gamma_{\text{ini,nc}} = \Gamma_{\text{ini,nc}}\Gamma_{\text{b,nc}}^{-1}$ for various J is straightforward then.

For the estimation of the factors ε_1 and ε_2, RANS simulations for cavitating flow have to be carried out. The cavitation number σ has to be chosen appropriately. Eq. (2.21) states that $\Gamma_b \propto k_T n D^2$ and thus simply $\varepsilon_1 \approx k_{T,\mathrm{nc}} k_{T,\mathrm{c}}^{-1}$ for all J taken into consideration. Determining ε_2 is more complicated. It can be seen in Figure 5.3 that for the non-cavitating case, the tip vortex is attached to the blade tip (plane a), whereas for the case of cavitating flow, a developed tip vortex with axisymmetric flow emerges from the closure of the sheet cavity (plane b). Due to the presence of the cavitating core, the fitting procedure described by Eq. (5.26) will not lead to reasonable results since the Burgers vortex is a model for non-cavitating flow. However, far away from the cavitating and the viscous core, the flow field behaves like a potential vortex with $u_\varphi(\xi) = \Gamma (2\pi\xi)^{-1}$ and this yields a possibility to determine ε_2: A circular plane is placed on the vortex axis at a position close behind the closure of the sheet cavitation. In Figure 5.3, this corresponds to plane (b). At the same location, a similar plane is placed in the non-cavitating flow scenario and $\varepsilon_2 \approx u_{\varphi,\mathrm{c}}\left({}^{e_p}/_2\right)\left[u_{\varphi,\mathrm{nc}}\left({}^{e_p}/_2\right)\right]^{-1}$ might be used as an approximation.

5.4.2 Initial cavitation radius and bubble distribution

It has been justified in Section 5.3 to initialise the cavitation radius of a new tip vortex segment r_{c0} with half of the cavity thickness at the trailing edge η_{TE} – for the case of sheet cavitation exceeding the trailing edge. Extracting η_{TE} from the solution obtained by a RANS method is straightforward (see Figure 5.3). First, the curve $\mathscr{C}_{\eta,0.95}$, which is defined as

$$\mathscr{C}_{\eta,0.95} = \left\{ \mathbf{X} = (X,Y,Z) \mid \sqrt{Y^2+Z^2} = 0.95R \text{ and } \alpha_l(\mathbf{X}) = 0.5 \right\}, \tag{5.27}$$

has to be extracted from the flow field, where α_l is the volume fraction (see Section 4.1.3). With $\mathbf{X}_{\mathrm{TE},0.95}$ being a point located on the trailing edge of the propeller at $r = 0.95R$, the cavity thickness η_{TE} is the distance to $\mathscr{C}^*_{\eta,0.95}$:

$$\eta_{\mathrm{TE}} = d\left(\mathbf{X}_{\mathrm{TE},0.95}, \mathscr{C}^*_{\eta,0.95}\right), \tag{5.28}$$

with $\mathscr{C}^*_{\eta,0.95} = \left\{\mathbf{X} \,|\, \mathbf{X} \in \mathscr{C}_{\eta,0.95} \wedge \mathbf{X} \text{ between cavitation inception and closure point}\right\}$. The distance d can be found easily by formulating a minimisation problem.

Bubbles travelling along the tip vortex due to disintegration of sheet cavitation and disassociation from the tip vortex cavity are released around the tip vortex, leading to reduced density $\rho^\star$ according to Eq. (5.16). In order to reduce computation time, only a representative sector with $0 \le \varphi \le {}^{\pi}/_2$ and $0 \le \xi \le r_B$ is considered when the propagation of bubbles and the size of the bubbles is simulated. The choice of r_B in this model is arbitrary to a certain extent; however, it may be reasonable to select a value slightly larger than r_{c0}. For the initial distribution of bubbles, a uniform distribution of the initial bubble locations $(\varphi_{b0,m}, \xi_{b0,m})$ is expected, whereas for the initial bubble radius $r_{b0,m}$ with $m = 1,\ldots,N_b$ a Gaussian distribution is postulated. The number of bubbles seeded in the flow around a vortex segment at $t = t_0$ can be determined if $\rho^\star(t_0)$ and an average bubble radius are known.

5.4.3 Radius of the viscous core and ambient pressure

The initial radius of the viscous core r_{a0} depending on the blade load can be adopted from the fitting procedure necessary for the calculation of the initial circulation ratio $\gamma_{\mathrm{ini,nc}}$. Certainly, the presence of a cavitating core will have an influence on the viscous core radius; however, for determining r_{a0}, this is neglected. When the f1-formulation is used, the viscous core will only be used for the initialisation at $t = t_0$ and the model will automatically determine the evolution of the circumferential velocity distribution u_φ. However, when the f2-formulation is used, u_φ is defined by a Burgers vortex (see Eq. (5.12)) which requires specifying the temporal evolution of the viscous core radius. A formulation similar to Eq. (5.24) is applied.

For locations far away from the propeller, the ambient pressure far away from the vortex axis p_D equals the hydrostatic pressure due to the hydrostatic head above the vortex segment. In the direct vicinity of the propeller, p_D is affected by the propeller flow. Thus, the ambient pressure p_D will change while the segment travels downstream.

5.5 Verification of the Model

Prior to simulating the entire problem of hull pressure fluctuations induced by a cavitating propeller, the code VoCav2D is subjected to a couple of preliminary tests and verification studies. In these studies, only a single segment is considered. At the beginning of this section, a validation of the method VoCav2D-f1 is carried out using experimental data made available by Choi and Ceccio (2007) and data obtained by a numerical simulation with a different code published by Bosschers (2009c). Thereafter, the behaviour of a vortex segment with increasing circulation is examined and some results obtained by the f2-formulation are presented.

In Figure 5.4, the most important difference between both formulations of VoCav2D are shown. For the f2-formulation, the distribution of circumferential velocity is not affected by the presence of the cavity in the core of the vortex; in other words, there is no difference between cavitating and non-cavitating flow. However, the f1-formulation takes this effect into account and the vortex flow is strongly modified by the radial growth and shrinkage of the vortex cavity. This depends particularly on the ratio between cavity radius r_c and the radius of the viscous core r_a. If the cavitation radius is larger than the viscous core radius as shown in Figure 5.4a, the velocity extremum seems to be pushed in the outward direction by the growing cavity. On the other hand, if the shrinking cavitation radius gets significantly smaller than the radius of the viscous core, a high circumferential velocity occurs (see Figure 5.4b).

It can also be observed in the figure that the distribution of circumferential velocity without a cavity being present in the core always lies between the distributions associated with the minimal and maximal cavitation radius. This justifies the assumption that the f2-formulation leads to reasonable results within certain limits.

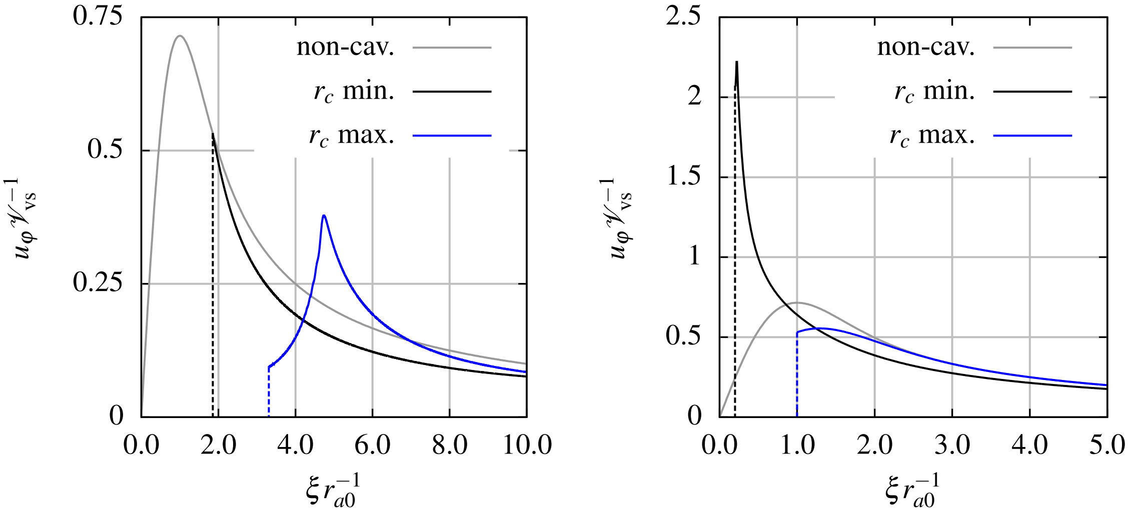

(a) Case $r_{c0} > r_{a0}$ **(b)** Case $r_{c0}, r_c \leq r_{a0}$

Fig. 5.4 Two exemplary distributions of circumferential velocity for a cavitating vortex for different relations between initial cavitation radius r_{c0} and viscous core radius r_{a0}. See Section 5.5.2 for the meaning of $\mathscr{L}_{\mathrm{vs}}$ and $\mathscr{V}_{\mathrm{vs}}$.

5.5.1 Comparison to experimental data and third-party codes

Choi and Ceccio (2007) carried out a number of experiments in a cavitation tunnel for the purpose of investigating the growth of cavitation nuclei in the center of a tip vortex. The results can be used to validate the method VoCav2D-f1 for cases in which the radius of the cavity is significantly smaller than the viscous core radius. In their experiments, vortical flow was generated by a cambered hydrofoil. Downstream of the foil, a Venturi section was placed around the tip vortex in order to enforce a change of the ambient pressure of the vortex. Laser pulses were used to create cavitation nuclei at the vortex axis in a controlled manner upstream the Venturi section. The results depicted in Figure 5.5a have been obtained following the procedure described by Choi et al. (2009): For the vortex properties $0.252\,\mathrm{m^2/s} < \Gamma < 0.302\,\mathrm{m^2/s}$ and $3.75\,\mathrm{mm} < r_a < 5.15\,\mathrm{mm}$ given by Choi and Ceccio, a nucleus of the size $r_{c0} = 100.0\,\mu\mathrm{m}$ is placed at the center of the vortex. The outer domain radius is set to $r_D = 0.2\,\mathrm{m}$ and the pressure p_{g0} is adjusted so that the nucleus is in an equilibrium state initially for a given core cavitation number σ_{C0}. Then, starting from σ_{C0}, the ambient pressure is reduced until the desired value of σ_C is reached. The non-dimensional results shown in Figure 5.5a are in good agreement with the experimental data. The vertical bars in the figure indicate variations in the results when the vortex parameters are changed within the range mentioned above.

Bosschers (2009c) applied a similar numerical method like VoCav2D-f1 for the investigation of two-dimensional cavitating vortex. His method is based on the same underlying equations and boundary conditions. In Figure 5.5b, the resonance frequency of a cavitating vortex depending on the ratio between equilibrium cavity radius $r_{c,\mathrm{eq}}$ and the radius of the viscous core r_{a0} is shown. The

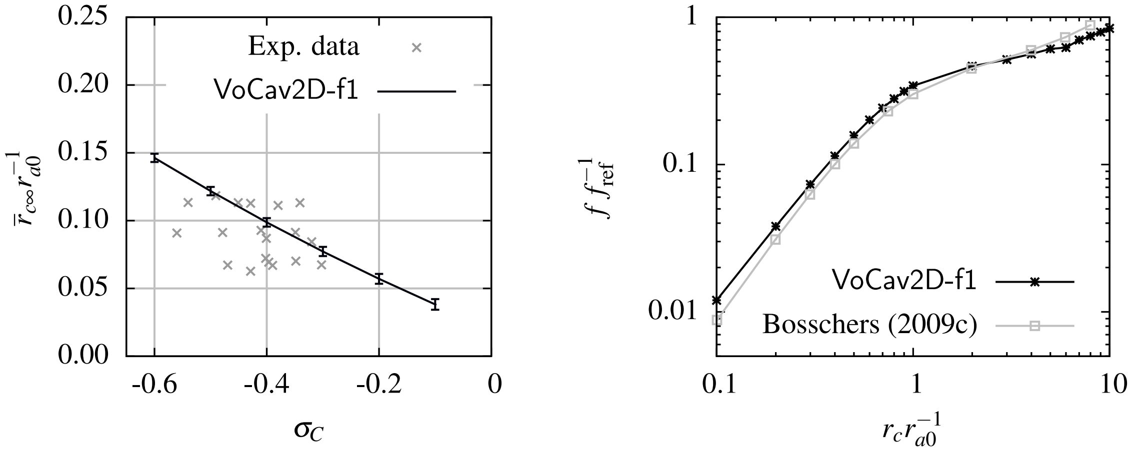

(**a**) Final radius $\bar{r}_{c\infty}$ of a small cylindrical bubble placed in the vortex core against σ_C.

(**b**) Resonance frequency of a vortex cavity against $r_{c,\mathrm{eq}} r_{a0}^{-1}$.

Fig. 5.5 Validation of the method VoCav2D-f1 by means of experimental data and data obtained by a third-party simulation method.

reference frequency f_{ref} is obtained by Eq. (2.19). Both methods predict a similar trend regarding the influence of viscosity on the resonance frequency: The larger the cavity radius is compared to the viscous core radius, the smaller the influence of the viscous core radius becomes. The solution tends then to the inviscid solution. This is reasonable and to be expected.

5.5.2 Vortex segment with a generic increase of circulation

In the previous section, the circulation of the vortex segment remained constant during the entire duration of simulation. In the following, the circulation of the vortex is increased during the simulation starting from different initial values. The study carried out here aims to investigate the influence of various initial conditions on the dynamical behaviour of a vortex segment. The values and quantities used for the study are listed in Table 5.1 and have been chosen to meet the flow conditions occurring at full-scale propeller flow. The results were obtained by using the f1-formulation.

The initial partial pressure p_{g0} of non-condensable gases has been set to 5000.0 Pa and $r_D = 0.5\,\mathrm{m}$ has been used in all cases. Additionally, all constants have been chosen according to the properties of water. Starting from an initial circulation $\Gamma_{\mathrm{ini}} = \gamma_{\mathrm{ini}} \Gamma_b$, the circulation is increased gradually as described by Eq. (5.24). Each segment is observed for a duration of $T_{\mathrm{sim}} = 2.0\,\mathrm{s}$, and κ in Eq. (5.24) is chosen so that 99% of Γ_b are reached after 0.4 s. The results are brought to a dimensionless representation of the following length and time scales: $\mathscr{L}_{\mathrm{vs}} = r_{a0,2}$ for all length quantities and $\mathscr{T}_{\mathrm{vs}} = 4\pi^2 r_{a0,2}^2 \Gamma_b^{-1}$ for all quantities related to time. Velocities are made dimensionless by $\mathscr{V}_{\mathrm{vs}} = 2\pi \mathscr{L}_{\mathrm{vs}} \mathscr{T}_{\mathrm{vs}}^{-1}$.

Table 5.1 Relevant conditions for the numerical investigation of the dynamical behaviour of a single vortex segment.

Quantity			Value
Max. circulation	Γ_b	$\left[\mathrm{m}^2/s\right]$	7.0
Ini. circulation ratio	γ_{ini}	[-]	0.4, 0.7, 1.0
Ini. core radius	$r_{a0,i}$	[m]	0.01, 0.03, 0.07
Ini. cavitation radius	r_{c0}	[m]	0.0005...0.1
	$\dot{r}_{c0}$	$\left[\mathrm{m}/s\right]$	0
Ambient pressure	p_D	[Pa]	130000.0
Outer domain radius	r_D	[m]	0.5

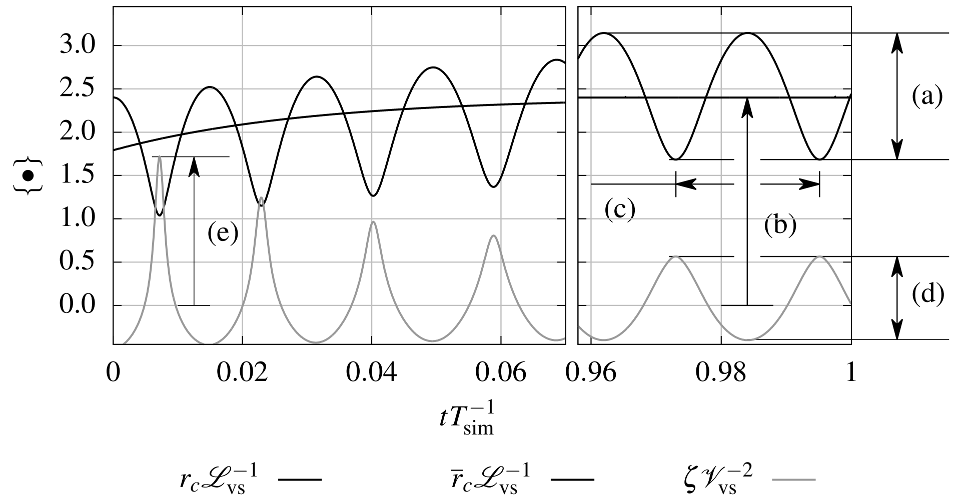

Fig. 5.6 Exemplary time history of a vortex segment illustrating the evaluated quantities: (a) $2\hat{r}_{c\infty}$, (b) $\overline{r}_{c\infty}$, (c) $T_{c\infty}$, (d) $2\hat{\zeta}_\infty$ and (e) ζ_{max}. See text for explanations.

In Figure 5.6, an exemplary result of the simulation campaign is shown. In particular, the following quantities are of greater interest: (a) the amplitude $\hat{r}_{c\infty}$ and (b) the average cavitation radius $\overline{r}_{c\infty}$ as well as (c) the period $T_{c\infty}$ at the end of the simulation.

In Section 2.1.2 it is explained that the acceleration of the cavity volume $\ddot{V}_c$ is proportional to the pressure fluctuations induced by cavitation. Hence, the quantity

$$\zeta \equiv \frac{\partial^2 \left(r_c^2\right)}{\partial t^2} \tag{5.29}$$

is an adequate measure for the pressure fluctuations caused by the cavitating vortex segment. This quantity is evaluated by means of (d) the amplitude $\hat{\zeta}_\infty$ at the end of the simulation and (e) the maximum value ζ_{max} occurring during the lifetime of the segment. It can be observed in Figure 5.6

that high values of ζ occur when the cavitation radius runs through the first minimum where the curvature of $r_c(t)$ is very high.

Due to the direct relation between ζ and r_c, the diagrams shown in the upper part of Figure 5.7 and in Figure 5.8 should be discussed in one context. All curves exhibit a distinctive minimum where both the amplitude $\hat{r}_{c\infty}$ is nearly zero and ζ vanishes. The position of the minimum can be related to the equilibrium radius $r_{c,\text{eq}}$ depending on the respective value for γ_{ni} and the conclusion can be drawn that a vortex segment initialised in an equilibrium state will not contribute to pressure fluctuations in a significant manner. However, when deviating from the equilibrium state, oscillations of the cavity will be stimulated. Viscosity can have an important influence on the amplitude if the radius of the viscous core is equal or greater than the cavitation radius.

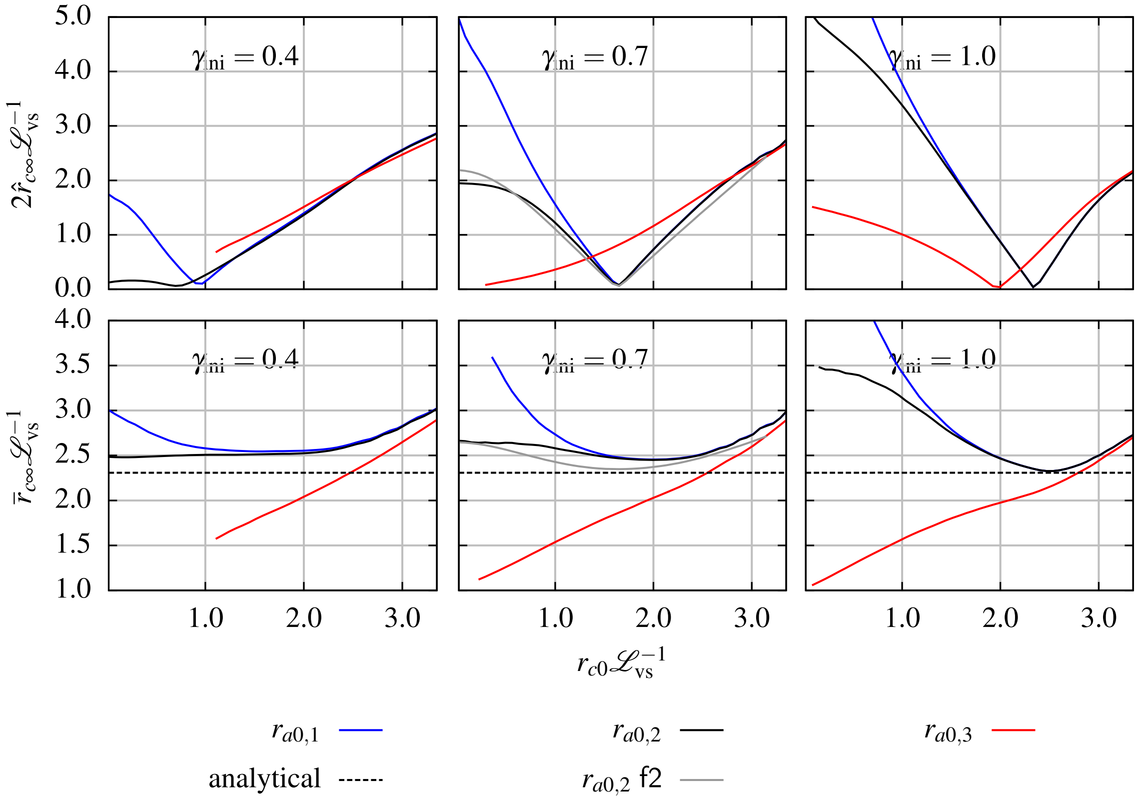

Fig. 5.7 Amplitude $2\hat{r}_{c\infty}$ of the oscillation of the cavitation radius (upper diagrams) and mean cavitation radius $\bar{r}_{c\infty}$ (lower diagrams) for a single vortex segment at the end of the simulation.

The results for cases with an initial cavitation radius being much smaller than the equilibrium radius have to be interpreted with some caution. The data shown in Figure 5.8 suggest that large values of $\zeta_{\max}$ appear when the chosen initial cavitation radius is substantially smaller than the equilibrium radius. However, one has to keep in mind that in these cases, $r_c(t)$ starts with a minimum and the cavitation radius will rapidly adjust to higher values, which results in a huge curvature and thus also in high values for $\zeta_{\max}$. The oscillations stimulated by such a deflection are large, which results in

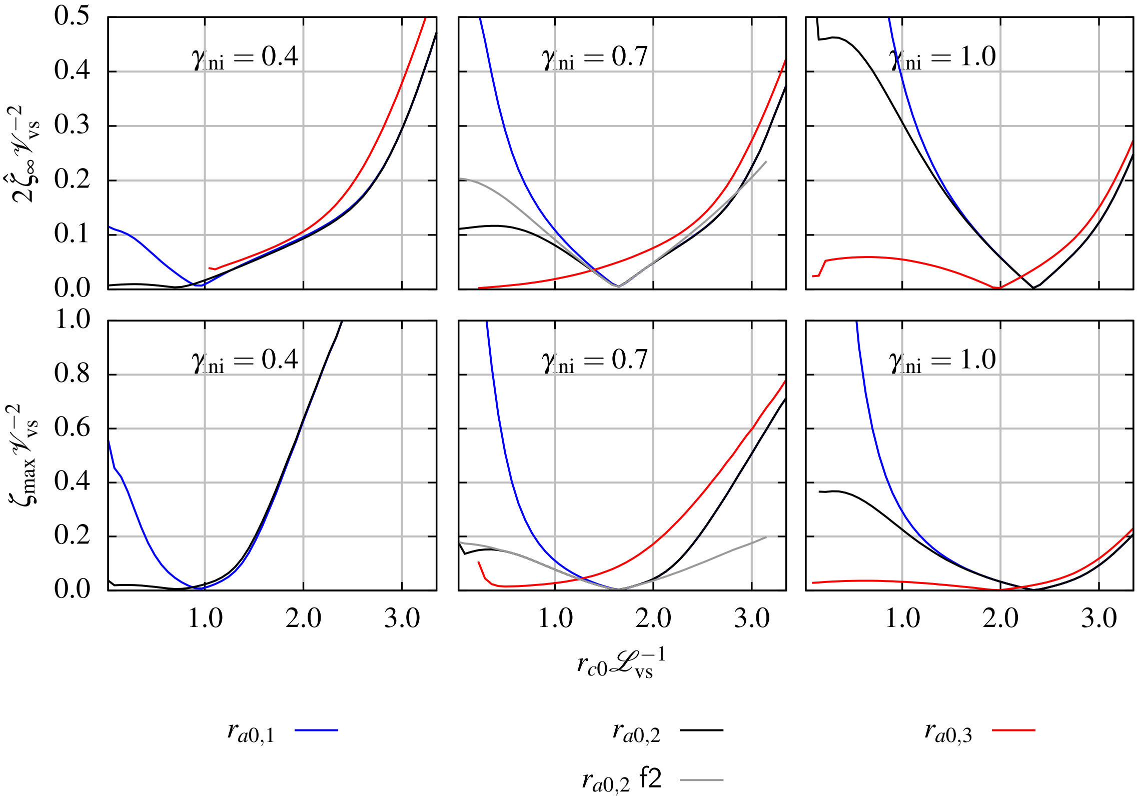

Fig. 5.8 Radiated pressure $2\hat{\zeta}_\infty$ for a single vortex segment at the end of the simulation and maximum radiated pressure $\zeta_{\max}$ occurring during the simulation.

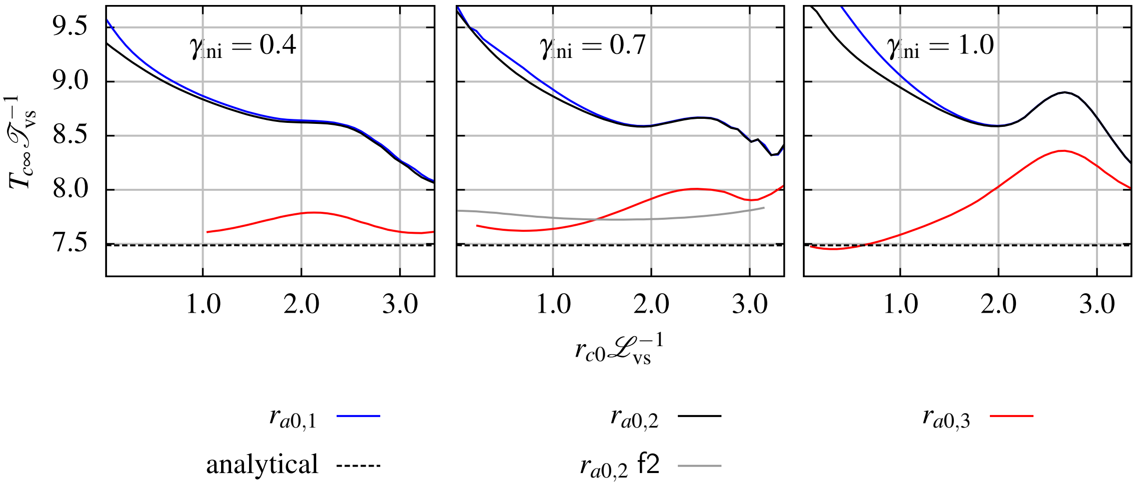

Fig. 5.9 Oscillation period $T_{c\infty}$ of a single vortex segment.

bigger amplitudes $\hat{r}_{c\infty}$ and $\hat{\zeta}_\infty$. In real flows, such a constellation is very unlikely – therefore the data right of the equilibrium radius are of greater practical relevance.

The results obtained by the f2-formulation for the case $\rho^\star = \rho$ are also shown in the figures. No significant differences occur except for very small values of r_c compared to the viscous core radius. This becomes relevant when either r_{c0} is small or r_c approaches small values during the life of a segment. The latter case explains the differences in the predicted results for $\zeta_{\max}$ shown in the lower part of Figure 5.8.

In Figure 5.9, the oscillation period $T_{c\infty}$ of a segment at the end of the simulation time is shown. The analytical results obtained by Eq. (2.19) neglecting the influence of viscosity describe the lower limit of possible values for the period $T_{c\infty}$. Furthermore, the f1-formulation predicts a dependency between the period and the initial cavitation radius r_{c0}. This is due to the effect that the amplitude of oscillation is affected by the choice of r_{c0} and so is the period of the (non-linear) oscillation.

The average cavitation radius at the end of the simulation $\bar{r}_{c\infty}$ depending on the initial value of r_{c0} is illustrated in the lower part of Figure 5.7. The results are compared to the analytically determined equilibrium radius according to Eq. (2.22). Similar to the period of oscillation, the overall growth depends strongly on the selected initial circulation and the initial cavitation radius. Again, viscosity plays a significant role if the core radius is larger than the initial cavitation radius.

Note that in all cases considered here, the major characteristic of the vortex – the maximum circulation Γ_b – is the same. However, depending on the initial conditions, the dynamical behaviour of the vortex cavity can differ in a considerable manner from case to case. This underlines the importance of finding suitable initial conditions when the effect of propeller tip vortex cavitation on propeller-induced pressure fluctuations is considered.

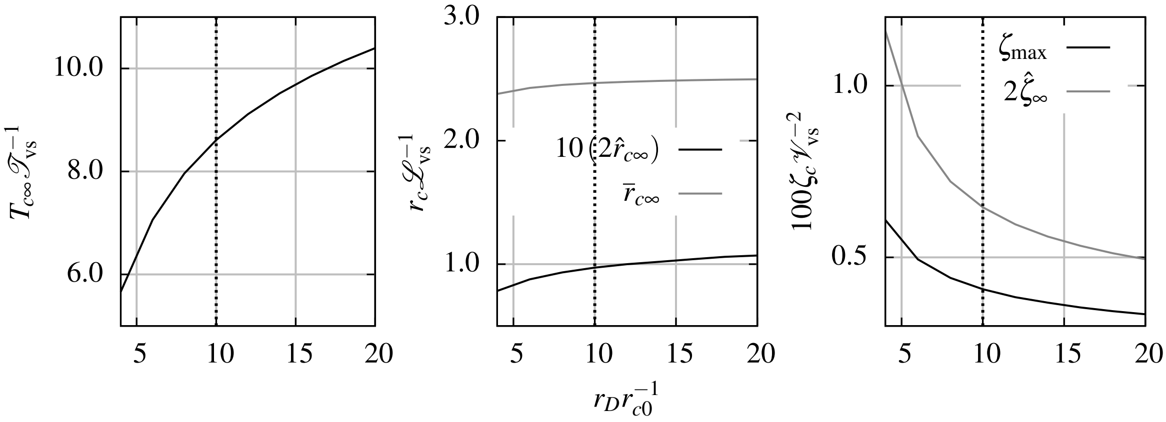

Fig. 5.10 Influence of r_D on the dynamical behaviour of a cavitating vortex. Conditions: $\gamma_{\mathrm{ini}} = 0.7$, $r_{a0} = 0.03\,\mathrm{m}$, $r_{c0} = 0.05\,\mathrm{m}$ and $\Gamma_b = 7.0\,\mathrm{m^2/s}$. From left to right: oscillation period at the end of the simulation, cavitation radius and radiated pressure.

Section 5.2 explains that the choice of the outer domain radius r_D can have an important impact on the dynamical behaviour of the vortex cavity. This has been investigated as well and the results are presented in Figure 5.10. The average cavity radius $\bar{r}_{c\infty}$ is nearly independent of r_D. However, all other quantities are influenced by the choice of r_D and the solution does not converge as $r_D \to \infty$.

This is a crucial aspect of the quasi two-dimensional approach used here. r_D turns out to be a free parameter which has to be chosen with care.

5.5.3 Effect of a reduced density around the cavitating core

As described in Section 5.2, VoCav2D-f2 is able to consider the influence of bubbles surrounding the cavitating core of a tip vortex. It is assumed that the presence of these bubbles result in a reduced density $\rho^\star$ which will affect the dynamics of the cavitating vortex core. Exemplary results are shown in Figure 5.11. A number of bubbles is distributed around the cavitating core according to the initially chosen reduced density $\rho^\star = 0.7\rho$ at $t = t_0$. It can be seen that the bubbles migrate to the center of the vortex continuously and finally disappear after a certain time. While travelling to the core, the bubble radius is fluctuating. In the present example, the initial cavitation radius r_{c0} is larger than the equilibrium radius and consequently the cavity undergoes a contraction. Due to the reduced density of the surrounding flow in the case $\rho^\star < \rho$, the pressure drop in the vortex is less pronounced and the cavity radius will experience a stronger contraction than for the case where no bubbles are present.

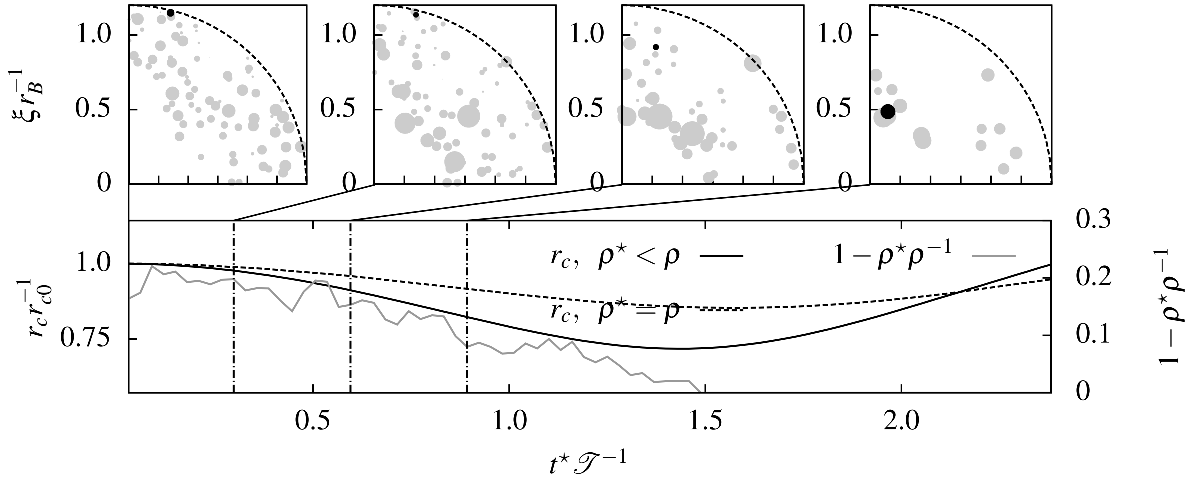

Fig. 5.11 Influence of bubbles surrounding the cavitating core of vortex segment. Conditions: $\Gamma_b = 11.5\,\mathrm{m^2/s}$, $\gamma_{\mathrm{ini}} = 0.652$, $r_{a0} = 0.07\,\mathrm{m}$, $r_{c0} = 0.07\,\mathrm{m}$, $\rho^\star\rho^{-1} = 0.7$ at $t^\star = 0$ and $r_B = 0.1\,\mathrm{m}$, $\mathscr{T} = 4\pi^2 {r_{a0}}^2 \Gamma_b^{-1}$. Top: visualisation of bubbles entrained by the vortex with a single bubble marked black, bottom: evolution of the cavitating core and the reduced density $\rho^\star$.

5.6 Convergence

The convergence behaviour of VoCav2D-f1 has been investigated by Gosda (2016). Now, the focus is put on carrying out a convergence study for the f2-formulation for the case $\rho^\star = \rho$. In this study, a large number of vortex segments arranged along the vortex axis is considered. The resulting cavitating tip vortex is exposed to a generic test scenario which is shown in Figure 5.12 and explained in the following. The duration of the simulation is $T_{\mathrm{sim}} = 0.25\,\mathrm{s}$. Within this period of time, the circulation of the generic propeller flow continually increases from $\Gamma_{b0} = 5.0\,{}^{m^2}\!/{}_{s}$ to $(1.0+a)\,\Gamma_{b0}$ with $a = 0.25$ and then decreases to the initial value (see Figure 5.12a). Vortex roll-up is not considered here, i.e. $\Gamma_{\text{ini}} = \Gamma_b$ and thus $\gamma_{\text{ini}} = 1.0$. All other vortex parameters are assumed to be constant as well: $r_{a0} = r_a = 0.04\,\text{m}$, $r_{c0} = 0.05\,\text{m}$ and $p_D = 100.0\,\text{kPa}$. For the sake of simplicity, the propeller radius is set to $R = {}^{D}\!/{}_{2} = 1.0\,\text{m}$, the number of revolutions to $n = 1.0\,\text{s}^{-1}$ and the ship speed to zero.

VoCav2D-f2 uses a two-level time discretisation (see Section 5.2). The surrounding vortex flow – here, in terms of circulation – is updated every $\tilde{t}_{[k]}$, and the Runge-Kutta scheme operates on a finer level of $\tilde{\tilde{t}}_{[j]}$, i.e. $\tilde{t}_{[k+1]} - \tilde{t}_{[k]} = \tilde{\tilde{t}}_{[j+n_{\text{sub}}]} - \tilde{\tilde{t}}_{[j]}$, where n_{sub} is the number of subdivisions.

Table 5.2 Relevant conditions for the convergence study.

Colour	Code	Time step size	n_{sub}
green	–	0.005 s	10000, 5000, 1000
grey	–	0.001 s	5000, 1000, 500, 100, 50
blue	D	0.0005 s	1000, 500, 100, 50
orange	C	0.0001 s	500, 100, 50, 10, 5, 1
black	B	0.00005 s	100, 50, 10, 5, 1
red	A	0.00001 s	10

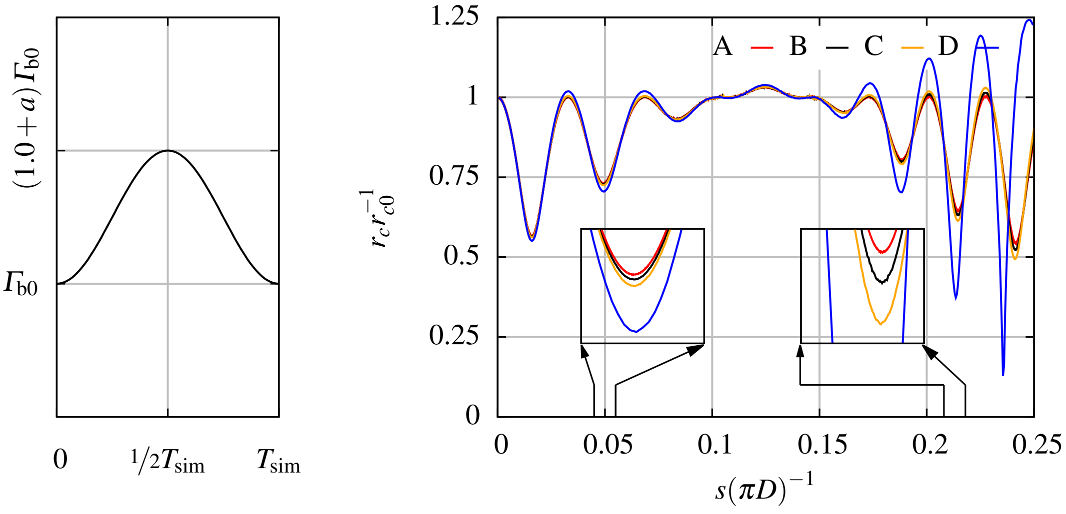

(a) Evolution of the blade circulation $\Gamma_b(t)$.

(b) Shape of the cavitating tip vortex $r_c(s)$ at $t = T_{\text{sim}}$.

Fig. 5.12 Generic test scenario. Left: generic blade circulation; right: predicted shape of the cavitating vortex for various time step sizes (see Table 5.2). The depicted cases are those with the respective maximum value of n_{sub}.

In Figure 5.12b, the shape $r_c(s)$ of the cavitating tip vortex is shown with s being the coordinate along the vortex axis originating from the propeller tip (see Figure 5.1 at the beginning of this chapter). The scenario has been simulated for different time step sizes and different numbers of substeps listed in Table 5.2. Obviously, when $\Gamma = \Gamma_{b0}$ at $t = 0$ and $t = T_{\mathrm{sim}}$, the constant initial cavitation radius chosen in this study is larger than the equilibrium radius since a contraction and strong fluctuations of the cavity radius occur under these conditions.

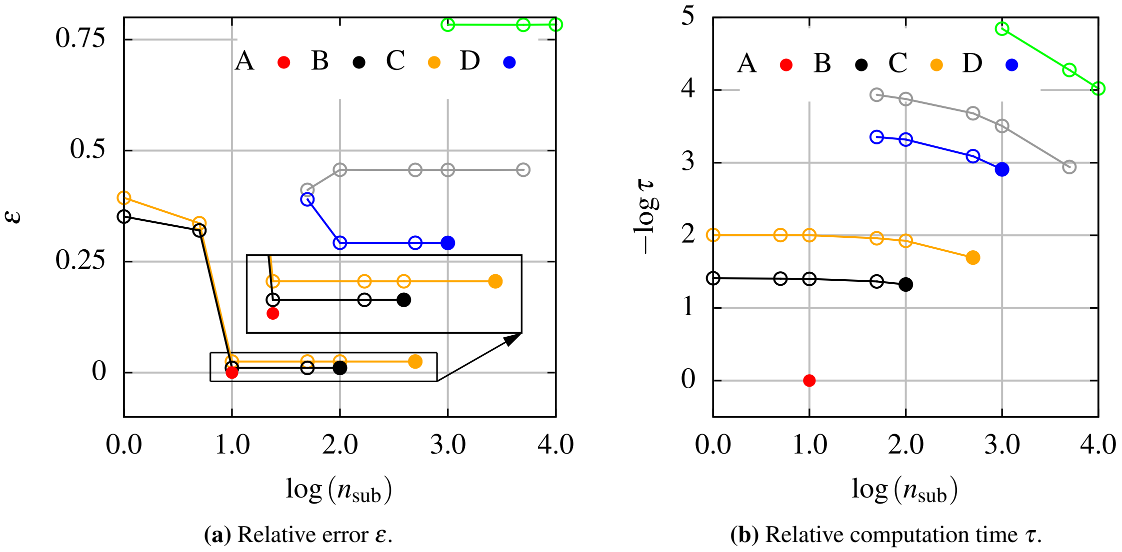

(a) Relative error ε.

(b) Relative computation time τ.

Fig. 5.13 Convergence behaviour of VoCav2D-f2 for various time step sizes and numbers of substeps n_{sub} (see Table 5.2).

In the figure, four different exemplary cases are shown (A through D). Numerical errors become significant in the sharp minima of the cavitation radius where the curvature is very high. If the time discretisation is too coarse, the solution becomes unstable which apparently happens in case D.

In the following, case A is considered to be the converged reference solution $\bullet_{\mathrm{ref}}$. A suitable measure for the convergence is then:

$$\varepsilon \equiv \frac{\sqrt{\int_0^{s_{\max}} \left(r_c - r_{c,\mathrm{ref}}\right)^2 \mathrm{d}s}}{\int_0^{s_{\max}} r_{c,\mathrm{ref}} \mathrm{d}s}. \tag{5.30}$$

Furthermore, the relative computation time τ is of interest. It is simply the ratio between the computation time of the particular case and the computation time needed to obtain the reference solution. Both quantities for the cases listed in the table are shown in Figure 5.13.

Apparently, the number of substeps n_{sub} does not have a significant effect on the accuracy of the solution as long as the number is not smaller than a certain limit value. The time step size, however, seems to be a more important parameter. A huge step towards the converged solution is made between case D and C, a further refinement does not improve the accuracy significantly (see Figure 5.13a). This is an important finding with respect to the computational time shown in Figure 5.13b since a factor of almost hundred lies between the converged reference solution A and solution C.

Chapter 6

Modelling of Propeller–Hull Interaction

All the elements presented in Chapters 4 and 5 are now assembled into one simulation method for the approximation of unsteady propeller cavitation and propeller-induced pressure fluctuations. A first idea of this hybrid method has already been given in the introductory Chapter 1. In the present chapter, the assumptions and interfaces required for assembling the hybrid simulation method are introduced.

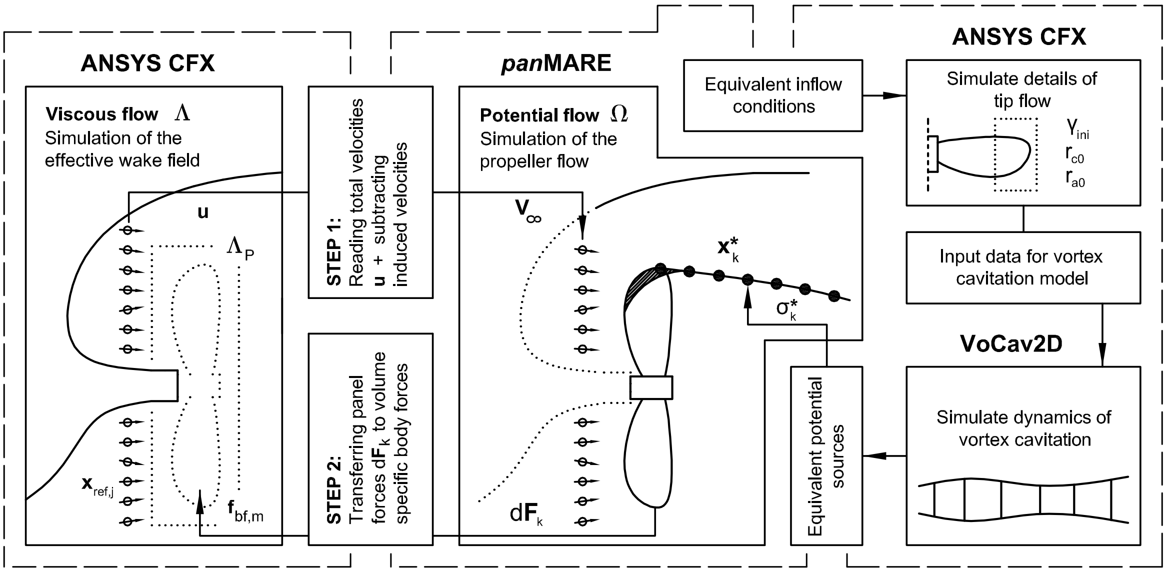

Fig. 6.1 Overall simulation method for the approximation of propeller cavitation and propeller-induced pressure fluctuations.

Figure 6.1 depicts the schematic chart of the overall simulation method. The panel method *pan*MARE is used in this thesis for determining the cavitating propeller flow and the evaluation of pressure fluctuations on the aft ship in the domain of potential flow Ω. The viscous hull flow in the domain of viscous flow Λ constituting the propeller inflow is treated by the RANSE solver ANSYS CFX. For a precise estimation of the unsteady propeller loads, the interaction between the viscous flow around the aft ship and the propeller has to be captured. An interface has to thus be established between Λ and Ω; here, this is accomplished by a body force coupling. The algorithm involved is described in Section 6.1.

As indicated in the figure, the domain of potential flow Ω essentially contains the propeller and the sections of the hull above the propeller where the pressure fluctuations are evaluated, whereas the viscous flow domain Λ contains only the bare hull. It is assumed that errors introduced due to restricting the hull geometry to the relevant region above the propeller are relatively small.

Not a part of the genuine potential flow solution, contributions to the overall hull pressure fluctuations due to the cavitating tip vortex (simulated by VoCav2D) have to be superimposed. The method applied to this problem is explained in Section 6.2. This section also addresses problems related to the different time step sizes used by *pan*MARE and VoCav2D. In the last section of this chapter, a schematic diagram showing the concatenation of all the modules and elements is presented.

6.1 Body Force Coupling Algorithm

Establishing an interface between *pan*MARE and the viscous flow solver ANSYS CFX for the calculation of the propeller inflow becomes possible via the concept of the *effective* wake field.

Whereas the *nominal* wake field is simply the velocity field measured behind a towed vessel under absence of the propeller, the effective wake field is the result of a complicated interaction between propeller suction and viscous hull flow; according to Carlton (1994, pp. 67f):

$$\{\text{effective wake field}\} = \{\text{nominal wake field}\} + \{\text{interaction velocities}\} \tag{6.1}$$

or, equivalently,

$$\{\text{effective wake field}\} = \{\text{total velocity field}\} - \{\text{propeller-induced velocities}\}\,. \tag{6.2}$$

The developed algorithm makes use of the definition given by Equation (6.2) and is based on a body force coupling approach – an approach that is well established (Choi and Kinnas, 2003; Greve et al., 2012; Zawadzki et al., 1997). A further validation of the approach based on the present implementation is shown in Section 7.2.

The basic idea behind the coupling approach is to represent the effect of the propeller by a distribution of body forces applied to the viscous flow domain Λ corresponding to the pressure distribution of the propeller blades. The pressure distribution in return is calculated by the panel method in the domain of potential flow Ω under consideration of the effective wake field, which has to be extracted from the viscous flow domain.

In every time step $t_{[i]}$, the algorithm performs two computation steps. For an illustration, see the left part of Figure 6.1.

Step 1 In the first step, the viscous flow solver is used to calculate the propeller inflow taking into account viscous effects due to the hull boundary layer. For this purpose, the velocity distribution $\mathbf{u}$ is extracted from Λ for an adequate number of reference points $\mathbf{x}_{\mathrm{ref},j}$ on a circular plane located approximately $0.1D$ upstream of the propeller position (see Figure 6.2b). Because of the body forces applied, this velocity distribution is affected by the induced velocities of the propeller $\mathbf{U}_P^+ = \nabla\Phi_P$ with $\nabla = (\partial/\partial x, \partial/\partial y, \partial/\partial z)$ (see Section 4.2). In order to obtain the effective wake field of the current time step $t_{[i]}$, according to Eq. (6.2), the induced propeller velocities have to be subtracted. The effective wake field is then used as reference velocity $\mathbf{V}_\infty$ for the panel method *pan*MARE:

$$\mathbf{V}_\infty\left(t_{[i]}\right) \approx \mathbf{u}\left(t_{[i-1]}\right) - \mathbf{U}_P^+\left(t_{[i-1]}\right), \tag{6.3}$$

for $\mathbf{x}_{\mathrm{ref},j}$. Since the induced velocities for the current time step are unknown, the values from the previous step $t_{[i-1]}$ are used for an approximation. Applying Eq. (6.3) involves a strong simplification of the flow since it implies that the reference velocity does not change in the direction of x.

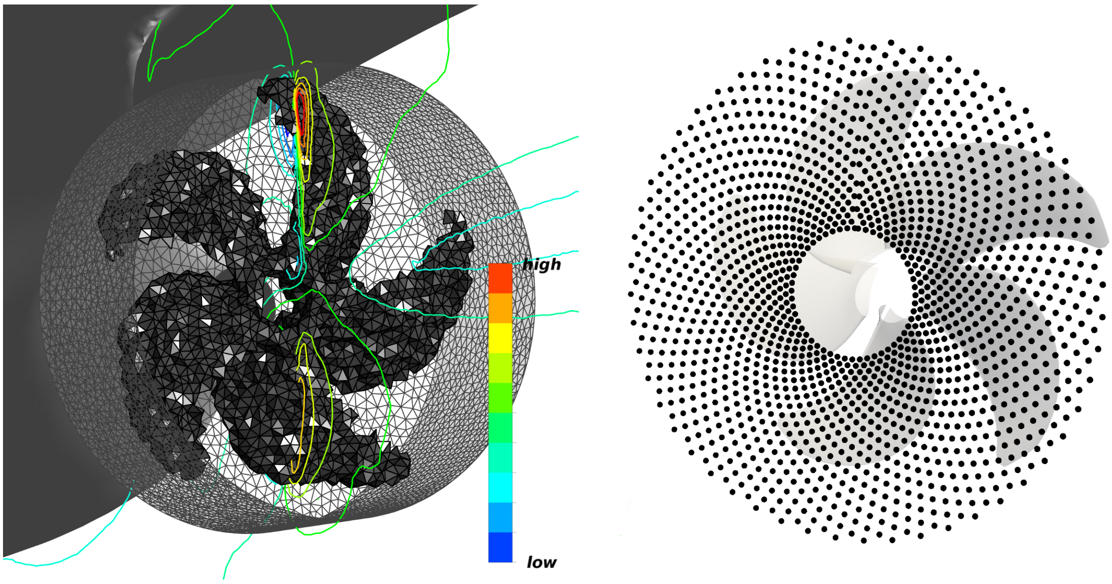

(a) Virtual propeller and pressure distribution.

(b) Reference points.

Fig. 6.2 Left: visualised virtual propeller for an exemplary instant of time and pressure contours due to the impact of body forces in Λ_P; right: typical distribution of reference points in for obtaining the effective wake field.

Step 2 The second step involves the distribution of equivalent body forces in the domain of viscous flow Λ. The mapping algorithm involved is able to convert the pressure distribution on the blades to volume-specific body forces and has been implemented with the help of ANSYS CFX user coding. It can handle both structured and unstructured meshes and takes into account the propeller shape, including pressure and suction side of the blades. Figure 6.3 illustrates the procedure in a simplified manner for two-dimensional grids where the propeller grid is idealised by two panels. For each time step, the panel method *pan*MARE provides the center $\mathbf{x}_k$ and the four vertices $\mathbf{x}_{c,l,k}$, $l = 1,...,4$ of each panel k (see subfigure (A) in Figure 6.3). The area A_k, pressure p_k and the normal vector $\mathbf{n}_k$ yield the force $\mathbf{F}_k = p_k A_k \mathbf{n}_k + \mathbf{F}_{\mathrm{fr},k}$ acting on the panel. $\mathbf{F}_{\mathrm{fr},k}$ is an empirically estimated friction force.

$\Lambda_P \subset \Lambda$ is defined as the part of the viscous flow domain containing the virtual propeller. All the mapping routines described in the following act on this subdomain. The volume mesh used by the RANSE solver ANSYS CFX consists of an arbitrary number of control volumes $\mathrm{d}V_m$ surrounding the grid vertices $\mathbf{x}_m$ (see Section 4.1).

First, the mesh near the propeller is analysed and an equivalent cell radius $r_{s,m}$ is assigned to each control volume $\mathrm{d}V_m$:

$$r_{s,m} = \beta \sqrt[3]{\mathrm{d}V_m}, \tag{6.4}$$

where $\beta = 1.0 \dots 2.0$ is a model parameter regulating how sharp the propeller shape is reproduced in the viscous flow domain. Knowing $r_{s,m}$ for each control volume, it is detected which panels k are intersected by the control volume m. This is done by means of the following definition:

$$a_{k,m} = \begin{cases} 1 & \text{if } \|\mathbf{x}_m - \mathbf{x}_k\| \le r_{s,m} \ \text{ or} \\ & \quad \|\mathbf{x}_m - \mathbf{x}_{c,l,k}\| \le r_{s,m},\ l = 1,\dots,4 \\ 0 & \text{else} \end{cases} \tag{6.5}$$

Furthermore, the number of panels intersected by the m-th control volume is of concern:

$$b_m = \begin{cases} 1 & \text{if } a_{k,m} = 0 \ \text{ for all } \ k \\ \sum_k a_{k,m} & \text{else} \end{cases} \tag{6.6}$$

In subfigure (B), cells intersected by panel 1, i.e. $a_{1,m} = 1$, are light grey, by panel 2 with $a_{2,m} = 1$ are dark grey and those intersected by both panels with $b_m = 2$ are shaded.

In order to calculate a volume-specific body force, a cell volume is needed which the force $\mathbf{F}_k$ is distributed over. This is obtained by

$$V_k = \sum_m \frac{a_{k,m}}{b_m} \mathrm{d}V_m \tag{6.7}$$

and illustrated in subfigure (C). The distribution of body forces $\mathbf{f}_{\mathrm{bf},m}$ added to the source term of the momentum equation (Eq. (4.2) or Eq. (4.7), respectively) is then given by

$$\mathbf{f}_{\mathrm{bf},m} = \sum_k \frac{a_{k,m}}{b_m} \frac{F_k}{V_k}; \tag{6.8}$$

see subfigure (D) in Figure 6.3. Cells intersected by both panels are charged with body force contributions originating from both panels.

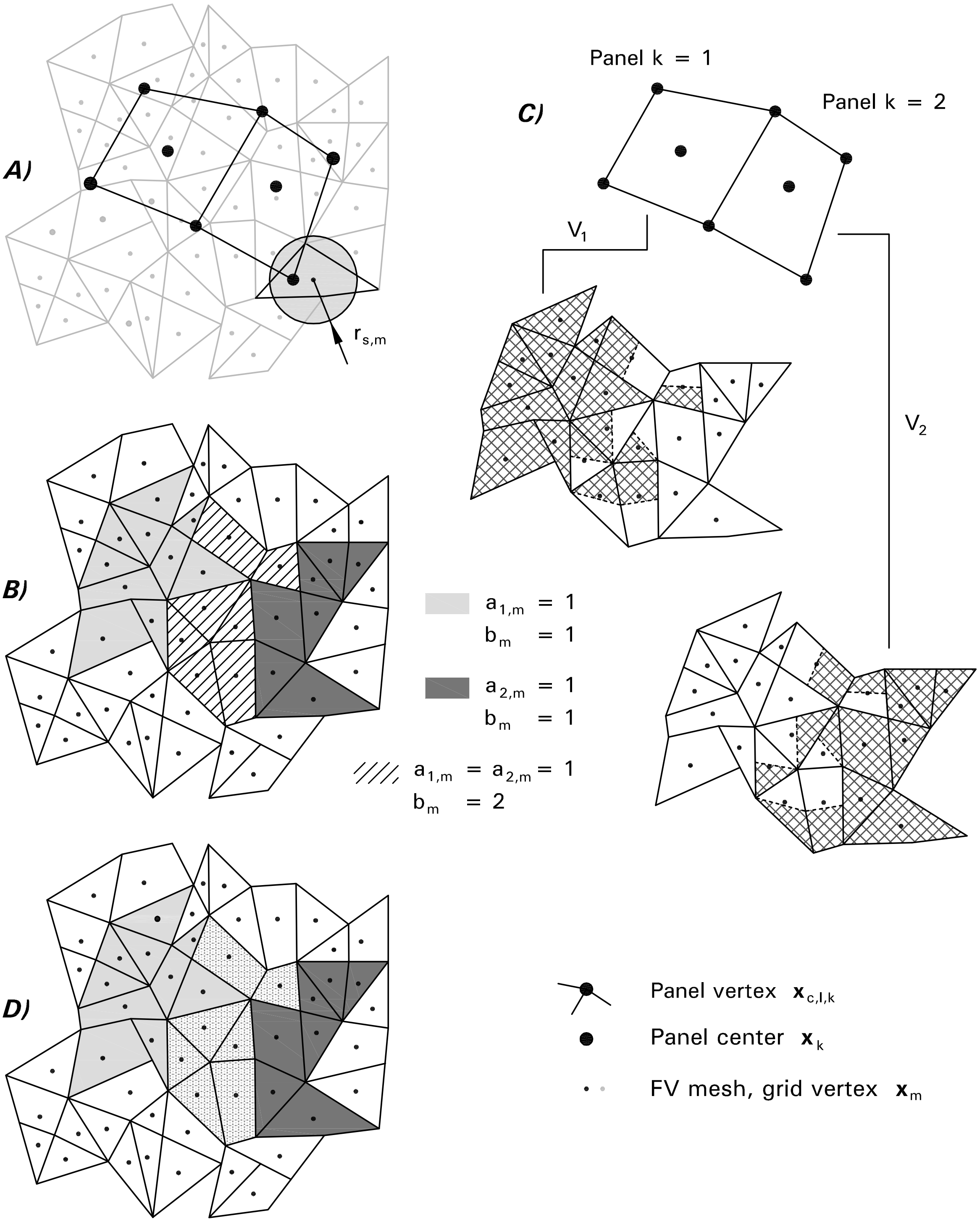

Fig. 6.3 Idealised cell arrangement illustrating the conversion from forces acting on panels to corresponding volume-specific body forces.

The method conserves the momentum introduced in the flow by the propeller, i.e. the condition

$$\sum_k F_k = \sum_m \mathbf{f}_{\mathrm{bf},m} \mathrm{d}V_m \tag{6.9}$$

is fulfilled at any time.[1]

In Figure 6.2a, those cells of Λ_P that comprise the virtual propeller are marked. The pressure distribution on a vertical plane at $y = 0$ shows that pressure and suction side of the propeller are clearly distinguishable. Due to the high propeller load caused by the non-uniform wake field, the pressure difference is much higher in the 12 o'clock position than in the 6 o'clock position.

6.2 Evaluation of Hull Pressure Fluctuations

To determine the pressure fluctuations p' on the part of the hull above the propeller in the domain of potential flow Ω, the unsteady flow on the hull surface S_H has to be simulated. The unsteady disturbance potential induced by the propeller Φ_P including the influence of sheet cavitation is known and can be obtained by means of *pan*MARE. A procedure is required to include the impact of the volume variations of the cavitating tip vortex.

VoCav2D delivers the unsteady shape of the cavitating tip vortex which is defined by a large number of segments k with the radius $r_{c,k} = r_{c,k}(t)$ and the position $\mathbf{x}_k^\star$ stringed together along the helical tip vortex axis (see Chapter 5). Following Szantyr (2006), or even earlier Weitendorf (1977), the pressure disturbance in the flow induced by tip vortex cavitation can be approximated by a line of potential sources located on the vortex axis. The volume variation of every segment can be associated to an equivalent source strength $\sigma_{c,k}^\star = \sigma_{c,k}^\star(t)$ with

$$\sigma_{c,k}^\star(t) = \pi \mathrm{d}l \frac{\partial \left(r_{c,k}^2 \right)}{\partial t}, \tag{6.10}$$

where dl is assumed to be the length of the segment. In other words, the source strength is equal to the segment's temporal volume variation. The potential induced at a certain distance d_k from such a point source is $\phi_k^\star(t) = -\sigma_{c,k}^\star (4\pi d_k)^{-1}$ (Katz and Plotkin, 2001, p. 49) and the overall disturbance potential induced by the volume variation of the cavitating potential $\Phi_{\mathrm{TV}} = \Phi_{\mathrm{TV}}(t)$ can be approximated by

$$\Phi_{\mathrm{TV}}(t) = \sum_k \phi_k^\star(t). \tag{6.11}$$

For the inviscid velocity $\mathbf{U}$ on the hull, the unsteady disturbance potential induced by the propeller Φ_P, including the influence of sheet cavitation and the unsteady disturbance potential Φ_{TV} due to the cavitating tip vortex, are considered. Two assumptions are made at this stage:

---

[1] Note that the method does not necessarily conserve the angular momentum and slight deficiencies may occur. Possible corrections for the exact conservation of angular momentum are proposed by Schenke (2015).

(1) The volume variation of the cavitating tip vortex does not affect the propeller flow in a significant way, and thus Φ_{TV} is neglected when determining Φ_P.

(2) The impact of the hull flow, which constitutes the propeller inflow $\mathbf{V}_\infty$, is dominated by viscous effects and it is assumed that these are sufficiently considered by the effective wake field which is obtained by the coupling approach described in the previous section. Consequently, the small impact of the boundary S_H can be neglected when Φ_P is determined.

Hence, when the inviscid hull flow is to be determined, Φ_P and Φ_{TV} are regarded as known quantities and one obtains:

$$\mathbf{U} = \nabla\left(\Phi_P + \Phi_{\mathrm{TV}} + \Phi_H\right), \tag{6.12}$$

where $\nabla = \left(\partial/\partial x, \partial/\partial y, \partial/\partial z\right)$ in the global coordinate system and Φ_H is the sought disturbance potential of the hull.

Similar to Eq. (4.27), the impermeability condition for the hull S_H reads:

$$\mathbf{U}\cdot\mathbf{n} = \nabla\left(\Phi_P + \Phi_{\mathrm{TV}} + \Phi_H\right)\cdot\mathbf{n} = 0, \quad \text{for all} \;\; \mathbf{x}\in S_H. \tag{6.13}$$

It is assumed that the hull is a non-lifting body and there is no need to model shed vorticity. By means of the panel method *pan*MARE, a distribution of sources and dipoles satisfying Eq. (6.13) can be found on the hull surface and, along with it, the pressure fluctuations p'.

Eq. (6.13) has a rather symbolic meaning – due to different time step sizes applied for the time discretisation of *pan*MARE and VoCav2D, this equation cannot be implemented directly. In the following, the discrete time steps of *pan*MARE are denoted as $t_{[i]}$, those of VoCav2D as $\widetilde{t}_{[k]}$. The time discretisation used by VoCav2D is much smaller than the one used by *pan*MARE; in other words: $t_{[i+1]} - t_{[i]} = \widetilde{t}_{[k+N]} - \widetilde{t}_{[k]}$, where N is an integer between 100 and 1000 depending on the particular case.

In order to solve the problem of merging the solutions obtained at different levels of time discretisation, there are two alternatives:

(1) It is possible because of the assumptions made above to interpolate the results for Φ_P and Φ_{TV} to a shared level of time discretisation. This could either be $t_{[i]}$, $\widetilde{t}_{[k]}$ or a third level of intermediate refinement. Eqs. (6.12) and (6.13) can than be evaluated by means of the panel method using the shared level.

(2) With the same rationale, the pressure disturbance caused by the propeller with sheet cavitation p'_{SC} and tip vortex cavitation p'_{TV} can be calculated separately and added up afterwards. The former can be evaluated using the panel method at discrete time steps $t_{[i]}$. In this case, Φ_{TV} is not considered when the impermeability condition stated by Eq. (6.13) is applied. The pressure disturbance induced by the cavitating tip vortex can be approximated by using a linearised form

of the Bernoulli equation:[2]

$$p'_{\mathrm{TV}} = -B_f \rho \frac{\partial \Phi_{\mathrm{TV}}}{\partial t}, \tag{6.14}$$

without the need of solving a boundary value problem. In this equation, $-\rho \partial\Phi_{\mathrm{TV}}/\partial t$ is the pressure disturbance induced by the cavitating tip vortex at a certain position on the hull surface – however, *without* the hull being present. Hence, the solid boundary factor B_f is introduced in order to approximate the effect of the presence of the hull surface (see Section 2.1). With Φ_{TV} being known, the numerical effort to calculate p'_{TV} is negligible and, hence, it can be easily derived at the fine time discretisation level $\widetilde{t}_{[k]}$. The overall pressure disturbance p' is then simply:

$$p' = p'_{\mathrm{SC}} + p'_{\mathrm{TV}}, \tag{6.15}$$

which makes it necessary to interpolate p'_{SC} to the level of $\widetilde{t}_{[k]}$.

Which of these strategies is the better one? Proceeding from the assumption that higher-order pressure fluctuations are predominantly caused by the cavitating tip vortex which requires a fine time resolution, it would not be reasonable to use $t_{[i]}$ as a shared time level because information would get lost. On the other hand, if the boundary value problem stated by Eqs. (6.12) and (6.13) was solved at intermediate time steps or even at each $\widetilde{t}_{[k]}$, this would be prohibitively expensive. Consequently, the first approach mentioned above does not seem to be the best choice.

The second approach may introduce a certain amount of uncertainty because of the solid boundary factor B_f. However, since the hull form is not too complex and the curvature only small, the use of a constant factor is assumed to be sufficient. Apart from this, the pressure signal due to the cavitating tip vortex p'_{TV} can be resolved in an accurate manner without any computational effort and no information gets lost due to insufficient temporal resolution. For this reason, the second approach is applied from now on.

6.3 Structure of the Overall Method

The last step towards the complete overall simulation method is concatenating all the modules and elements introduced before. This is explained in the present section. For an overview, consult Figure 6.4. Again, it is important to bear in mind that VoCav2D uses a much finer time discretisation $\widetilde{t}_{[k]}$ than *pan*MARE and ANSYS CFX, which operate on $t_{[i]}$.

At the beginning of $t_{[i]}$, data originating from $t_{[i-1]}$ are exchanged between *pan*MARE and ANSYS CFX by means of the coupling procedure described above. Then, for the current time step $t_{[i]}$, *pan*MARE determines the cavitating propeller flow, i.e. Φ_P, considering $\mathbf{V}_\infty$, and ANSYS CFX updates the viscous hull flow, using the distribution of propeller forces $\mathbf{f}_{\mathrm{bf},m}$. Hull pressure fluctuations

---

[2] In this particular case, other terms of the Bernoulli equation (4.25) than $\rho\partial\Phi/\partial t$ can be neglected without introducing a notable error.

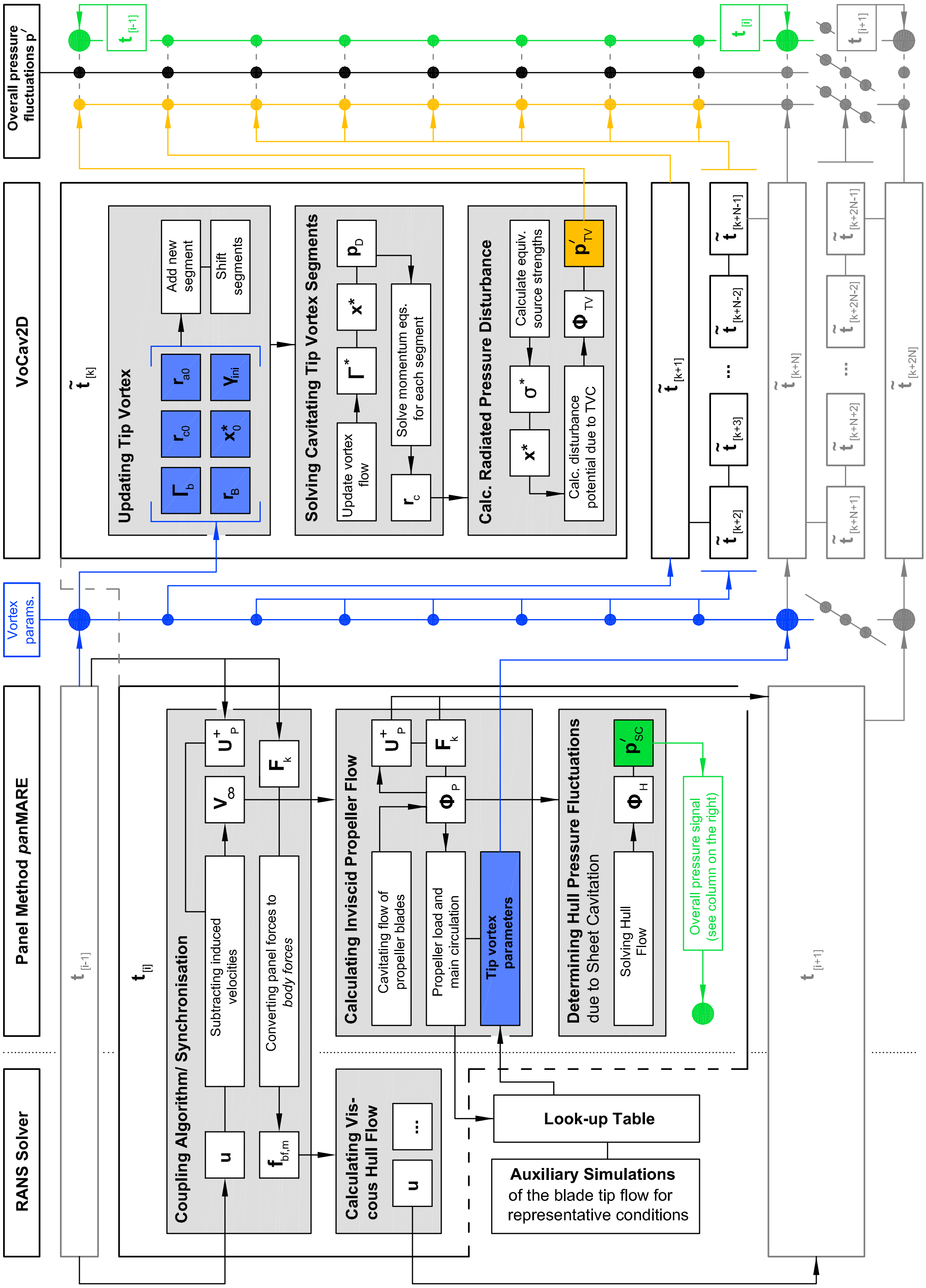

Fig. 6.4 Structure of the simulation method for the approximation of propeller cavitation and propeller-induced pressure fluctuations.

due to the propeller and sheet cavitation p'_{SC} (marked by green lines and symbols in the figure) are derived by *pan*MARE under consideration of the potential Φ_P of the cavitating propeller.

Meanwhile, VoCav2D simulates the dynamics of the cavitating tip vortex. Viscous flow simulations of the propeller blade have been made in advance in order to estimate the tip vortex parameters such as Γ_b, γ_{ini}, r_{c0} and so on depending on the instantaneous load of the propeller blade (see Section 5.4). These parameters are evaluated for every $t_{[i]}$ and are then interpolated to the finer time discretisation level $\widetilde{t}_{[k]}$. In the figure, this is indicated by the blue lines and boxes. After solving the momentum equations for each vortex segment as described in Section 5.2, the disturbance potential Φ_{TV} is evaluated and, by means of Eq. (6.14), p'_{TV} can be obtained for each time step $\widetilde{t}_{[k]}$ (see the yellow lines and symbols in the overview). Finally, p'_{TV} and p'_{SC} need to be added up to the overall pressure disturbance p', which is sketched in the right part of the overview.

Chapter 7

Validation of the Hybrid Simulation Method

In this chapter, the hybrid simulation method consisting of *pan*MARE, ANSYS CFX and VoCav2D is applied to the simulation of propeller-induced higher-order pressure fluctuations. The capabilities of the method are demonstrated by means of three examples – two container vessels and one ConRo vessel. Whenever available, experimental data is used for the validation.

This chapter starts with a presentation of the hull forms, the propellers and the operation conditions for the three vessels as well as the numerical grids used. Then, in Section 7.2, the body-force coupling procedure is validated by means of the full-scale data available for Ship A. Results for pressure fluctuations are presented in Section 7.3 for non-cavitating flow for all three vessels. A detailed analysis of the cavitating flow including the resulting higher-order pressure fluctuations is performed in Section 7.4.

7.1 Propellers, Hull Forms and Numerical Setup

In order to validate the hybrid simulation method for the prognosis of cavitation and resulting hull pressure fluctuations, the following three vessels are investigated numerically:

(1) The *ConRo Vessel Amandine* (from now on referred to as Ship **A**) is a slender ferry built at the Flensburger Schiffbau Gesellschaft and equipped with a controllable pitch propeller.

(2) The *KRISO Container Ship KCS*[1] (Ship **B**) is a classical container vessel; however, it has never been built and exists only as model. It is a widely accepted validation case for the development of experimental and numerical techniques (SIMMAN, 2008).

---

[1] Sometimes the KRISO Container Ship is called MOERI Container Ship.

Table 7.1 Relevant hull and propeller characteristics of the three vessels.

Ship		**A**	**B**	**C**
Propeller		P00A	P00B	P00C
Vessel name		Amandine	KCS	NN
Type		ConRo	Container	Container
Origin/ Shipyard		FSG	KRISO	NN
Origin/ Propeller manufacturer		SCHOTTEL	KRISO	MMG
Main dimensions hull				
Length b. pp.	L_{PP} [m]	186.22	230.00	223.57
Breadth	B [m]	26.20[2]	32.20	32.20
Design draught	T_D [m]	7.05	10.80	10.50
Design speed	V_s [kn]	19.00	24.00	23.18
Main dimensions propeller				
Type		1 × CPP	1 × FPP	1 × FPP
Sense of rotation		left-handed	right-handed	right-handed
Diameter	$D = 2R$ [m]	5.80	7.90	7.75
Number of blades	n_b [−]	4	5	5
Hub ratio	d_h/D [−]	0.277	0.180	0.170
Area ratio	$A_e/\frac{\pi}{4}D^2$ [−]	0.652	0.800	0.732
Design pitch ratio	$P_{0.7}/D$ [−]	1.135	0.997	0.977

(3) The third vessel (Ship **C**) is also a container vessel and has been the object of investigation during the BMWi joint research project NoiseLES. The main dimensions are comparable to those of Ship B.

During the BMWi joint research project KonKav II (Damaschke et al., 2014; Heinke and Richter, 2014; Lücke, 2014; Stoye, 2014), numerous full-scale data for Ship A were measured (see Section 3.1.2). These are used here for validation purposes in addition to the model test results available for all three vessels. The model tests were carried out in the cavitation tunnel of SVA Potsdam (Heinke and Jaksic, 2003; Heinke and Klose, 2016; Richter, 2012) and, in particular for Ship A, at HSVA Hamburg (Lücke and Johannsen, 2014).

The simulations carried out do not take into account effects due to the free water surface. Furthermore, appendages are not considered. This especially applies to the rudder, which clearly affects the propeller flow (Kracht, 1992). Constant inflow velocity and constant number of revolutions are assumed as well as fixed trim and sinkage. All simulations described in this chapter are conducted for full-scale conditions.

---

[2] This vessel has been equipped with additional floating elements in order to increase the floating stability after modifications of the deck structure. These elements are not taken into account for the simulations.

Table 7.2 Operation points of the three vessels. Some quantities are not contained in the reports; these have been derived from other quantities and are flagged by a question mark (?).

Ship		**A**			**B**	**C**
Operation point		OP00AD	OP00A1	OP00A2	OP00B	OP00C
		Design	Off	Off	Design	Design
CPP pitch		Design	D. $-5°$	D. $-3°$	–	–
Draught	D_{FP} [m]	7.05	6.32	6.32	10.80	11.52
	D_{AP} [m]	7.05	6.65	6.65	10.80	11.52
Speed	V_s [kn]	19.00	16.54	16.84	24.00	23.18
	V_s $[\mathrm{m/s}]$	9.77	8.51	8.66	12.35	11.92
Number of rev.	n $[\mathrm{min}^{-1}]$	103.02	103.20	103.02	104.7	104.10
	n $[\mathrm{s}^{-1}]$	1.717	1.720	1.717	1.745	1.735
Thrust coeff.	k_T $[-]$	0.220	0.179	0.206 (?)	0.172	0.196
Torque coeff.	$10k_Q$ $[-]$	0.404	0.291	0.350 (?)	0.285	0.302 (?)
Cav. number	σ_n $[-]$	*non-cavitating*			1.816	2.040
Cav. number	$\sigma_{n0.8}$ $[-]$	*operation conditions*			1.486	1.715

7.1.1 Relevant characteristics of hulls and propellers

Tables 7.1 and 7.2 summarise the main particulars of the three investigated vessels and the operation points taken into consideration. Both container vessels (Ships B and C) are quite similar with respect to their main dimensions. For Ship A, the ConRo vessel, two operation conditions are considered in addition to the design operation point. These conditions were adhered to during the full-scale measurement campaigns carried out for this ship.

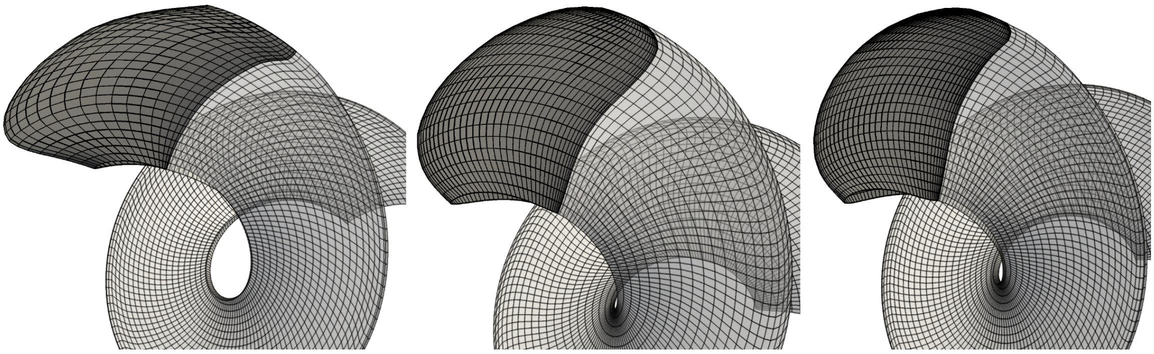

Fig. 7.1 Propeller blades P00A, P00B and P00C (from left to right.)

The propellers of the three ships are coded as P00A, P00B and P00C and are shown in Figures 7.1 and 7.2. Their main particulars are listed in Table 7.1. P00B and P00C are typical representatives of propellers for container vessels. Clearly, P00A has been designed to attain a higher comfort level – this is strongly indicated by a high skew angle, the reduced pitch at the blade tip and the large chord length in the middle. Furthermore, P00A is a controllable pitch propeller which explains the large hub ratio.

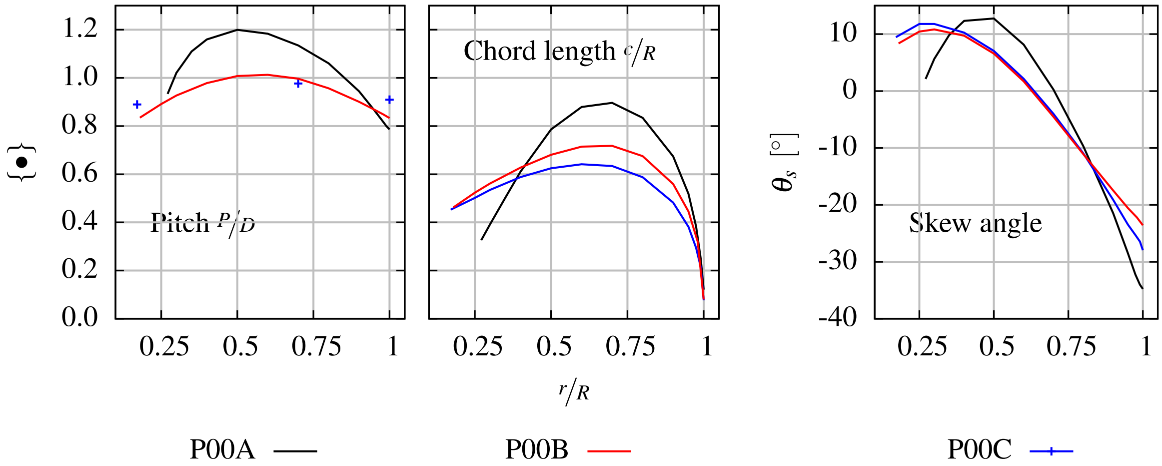

Fig. 7.2 Radial distributions of pitch $^P/_D$, chord length $^c/_R$ and skew angle for the three propellers. Some dimensions of P00C are confidentially.

Figures 7.3 through 7.5 show the aft ship geometry of the three vessels and the corresponding nominal wake field. The wake field of Ship A, with its slender hull form being typical for a ferry, is rather smooth and features a moderate peak in the 12 o'clock region, compared to the wake fields of the container vessels (Ships B and C). The hull shape directly above the propeller is convex in the case of Ships B and C, whereas for Ship A, there are concave portions of the hull above the propeller.[3]

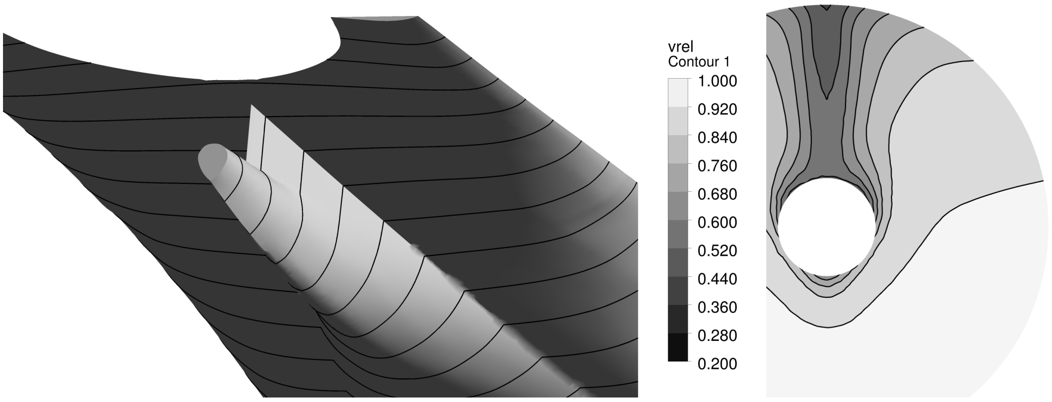

Fig. 7.3 Hull form in the aft ship region and simulated nominal wake field of Ship A, the ConRo vessel.

7.1.2 Viscous flow domain

In order to discretise the viscous flow domain Λ, a finite volume mesh around the hull needs to be constructed. This is shown in the following for Ships A and C (see Figures 7.6 and 7.8). For minimising blockage effects, the computational domain has to be sufficiently large. In this case,

---

[3] These portions are not part of the figure because they are above the water line at design draught and not included in the model of the viscous flow domain where the figure originates from.

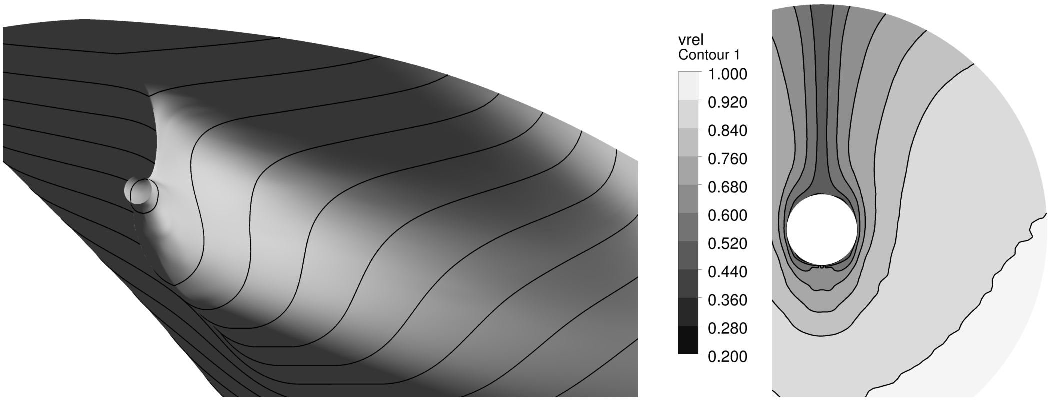

Fig. 7.4 Hull form in the aft ship region and simulated nominal wake field of Ship B.

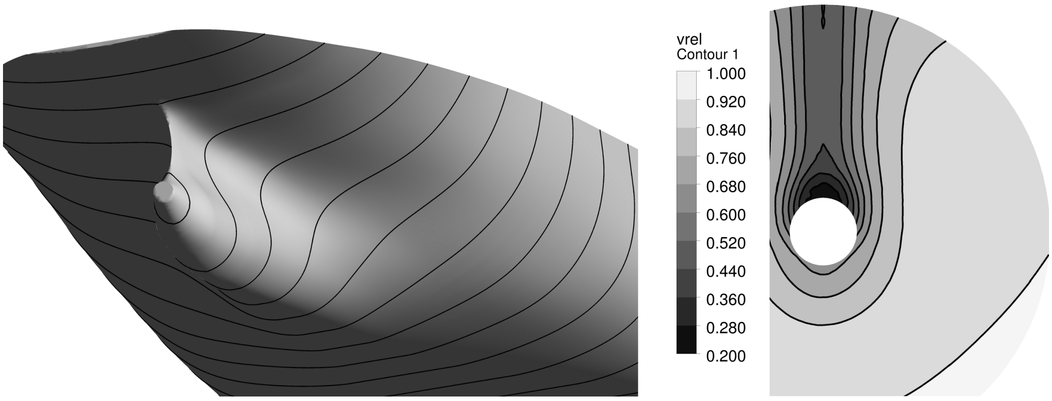

Fig. 7.5 Hull form in the aft ship region and simulated nominal wake field of Ship C.

$4.0L_{PP} \cdot 2.0L_{PP} \cdot 1.0L_{PP}$ (length · breadth · height of the domain) is chosen. Effects due to the free water surface are not taken into account and the upper wall terminating the domain is modelled as free slip wall. The hull itself is considered as no-slip wall. Effect of turbulence are approximated by the SST turbulence model (see Section 4.1).

Table 7.3 Discretisation of the viscous flow domain Λ.

Ship	**A**	**B**	**C**
Type	ConRo	Container	Container
Mesh type	unstructured	structured	unstructured
Turbulence model	SST	SST	SST
Spatial discretisation			
Number of cells in Λ	3.95 Mio.	5.97 Mio.	5.60 Mio.

Table 7.3 lists all relevant quantities of the finite volume meshes used for the three ships. Note that the propeller itself is not part of the computational domain Λ. However, in the mesh region Λ_P where the virtual propeller is located and the body-force coupling algorithm acts, the mesh density is

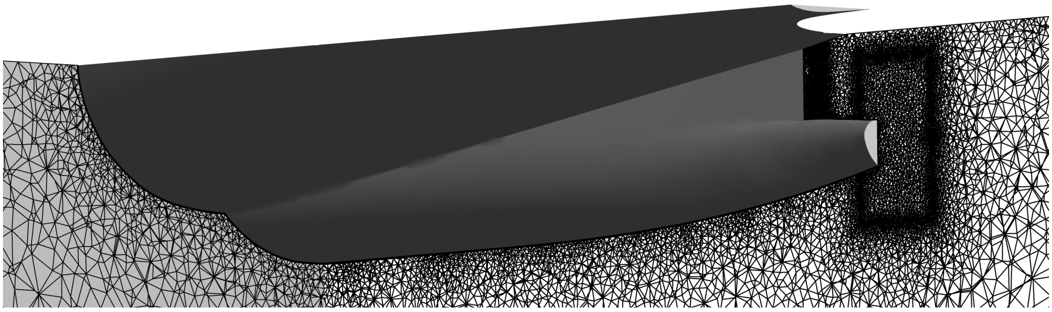

Fig. 7.6 Finite volume mesh of Λ used for Ship A.

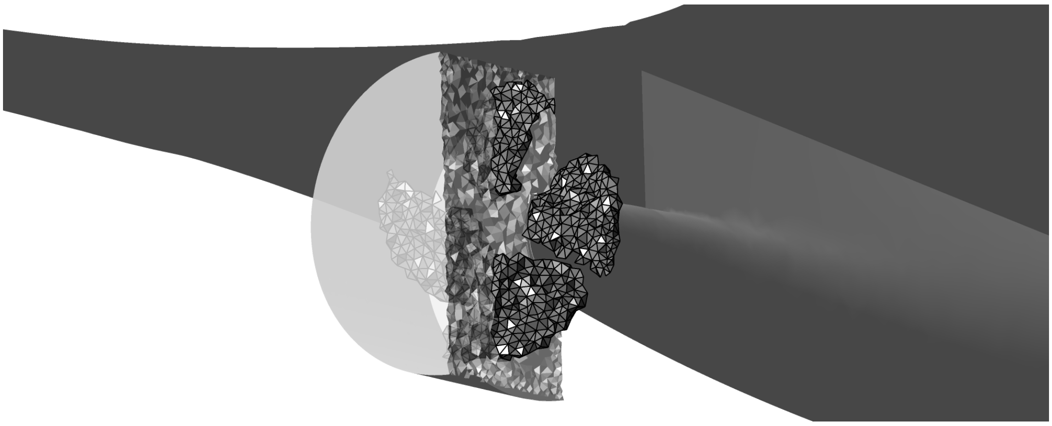

Fig. 7.7 Subdomain Λ_P containing the virtual propeller of Ship A. Marked cells are those with body forces due to the virtual propeller acting upon.

increased. Figures 7.7 and 7.9 show this part of the mesh. For a certain instant of time, those cells are marked in the figures which are involved in the body-force coupling procedure. The shape of the propeller becomes clearly visible in each case.

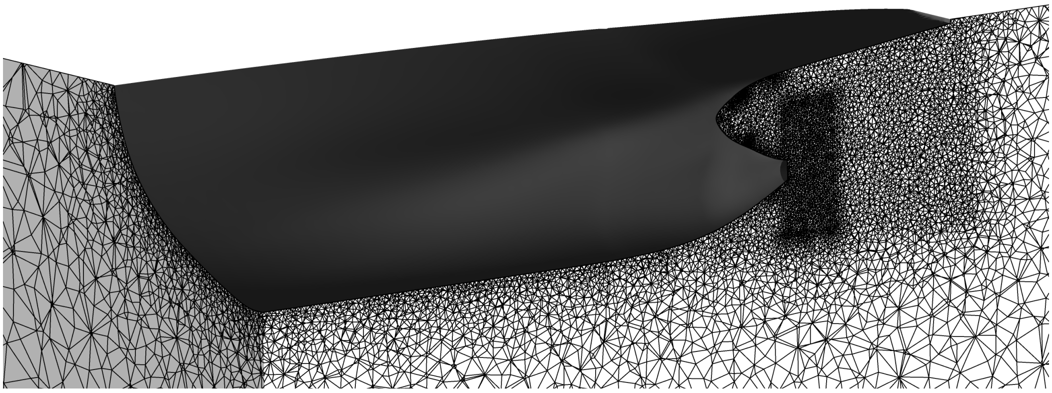

Fig. 7.8 Finite volume mesh of Λ used for Ship C.

As mentioned above, there are portions of the hull surface of Ship A directly above the propeller with a concave shape. These lie above the water line at design draught. When cruising at service

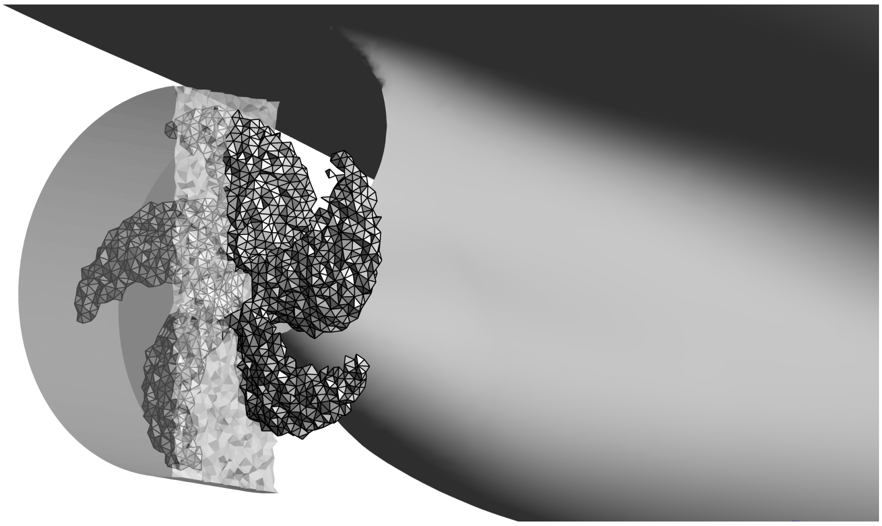

Fig. 7.9 See Figure 7.7; mesh for Ship C.

speed, these region will be wetted as well. Nevertheless, the numerical mesh of the viscous flow domain does not contain these concave parts (see Figure 7.6) since the effect on the wake field is considered to be small and mesh generation is facilitated.

The simulation of the viscous flow domain is of unsteady nature due to the rotation of the propeller. Because of the coupling algorithm applied, the time step size is the same as the one used for the simulations in the potential flow domain.

7.1.3 Potential flow domain

For all three cases considered here, the panel model of the potential flow domain Ω comprises the propeller itself inclusive the panels representing the trailing wake and the portion of the hull directly above the propeller. The propeller hub is not contained in the panel grid. The only purpose of the hull panels is to monitor pressure fluctuations – i.e. the average pressure niveau is not of interest. Thus, it is considered to be sufficient to only model a fraction of the hull and not the entire hull. The (physical) error introduced at the free cutting edges of the submodel is assumed to act locally and to decay sufficiently fast in order to not interfere with the results. The panel models for Ships A and C are shown in Figures 7.10 and 7.11.

Propeller P00A has experienced some modifications prior to meshing. In order to avoid heavily twisted panels at the blade tip, the chord length at the blade tip has been enlarged locally to a small extent and the skew has been slightly reduced. The hub ratio of the propeller is relatively large and the influence of the hub may thus become significant. To correct the error introduced by the missing representation of the hub, the pitch in the hub region has been slightly increased. Table 7.4 presents the discretisation parameters at one glance. Temporal and spatial discretisation of P00A is somewhat coarse since cavitation is not considered in this case (see Section 7.3 for an explanation). Time step size and angle increment are related by the constant number of revolutions.

Table 7.4 Discretisation of the potential flow domain Ω used in the simulations for the three vessels.

Ship	**A**	**B**	**C**
Propeller	P00A	P00B	P00C
Type	ConRo	Container	Container
Spatial discretisation			
Number of panels per blade	880	1400	1750
in radial direction	22	20	25
in chordwise direction	$2 \cdot 20$	$2 \cdot 35$	$2 \cdot 35$
Number of panels on hull surface	654	988	841
Time discretisation			
Angle increment	4.0°	2.880°	2.880°

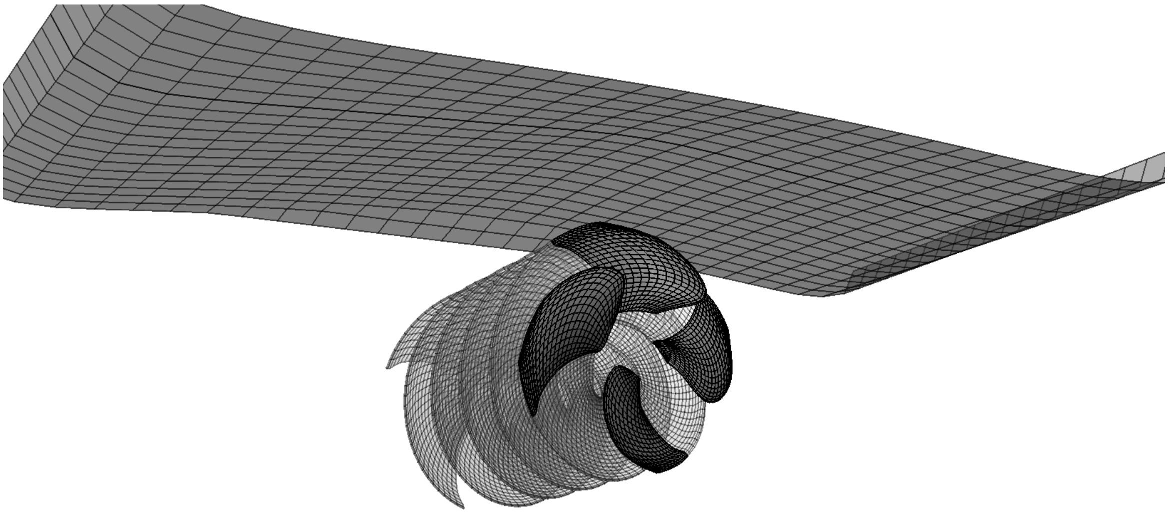

Fig. 7.10 Panel model of the potential flow domain Ω for Ship A, the ConRo vessel.

7.1.4 Tip vortex modelling

Tip vortex cavitation modelling is enabled for Ship B and Ship C. For the investigation of flow details at the blade tip, RANS simulations with very high grid density have been carried out in advance by means of ANSYS CFX. Only a single blade is taken into consideration and the influence of the other blades is captured by using a periodic boundary condition (see Section 4.1). The structured mesh used for the simulation is outlined in Figure 7.12 for the example of P00C. Three variants of the grid (9.0 Mio., 12.3 Mio. and 13.8 Mio. cells) and different turbulence models have been used in order to study the influence of the resolution on the results. The dynamics of the tip vortex cavity is simulated with the f2-formulation of VoCav2D. As mentioned in Section 6.2, the time step size used by VoCav2D-f2 is much finer than the one used by *pan*MARE and ANSYS CFX. In this case, a time step size of $0.0001\,s$ is used in the simulations. The length of the tip vortex is restricted to $0.75\pi D$, i.e. the cavitating tip vortex is only traced until it reaches the approximate position of the rudder leading

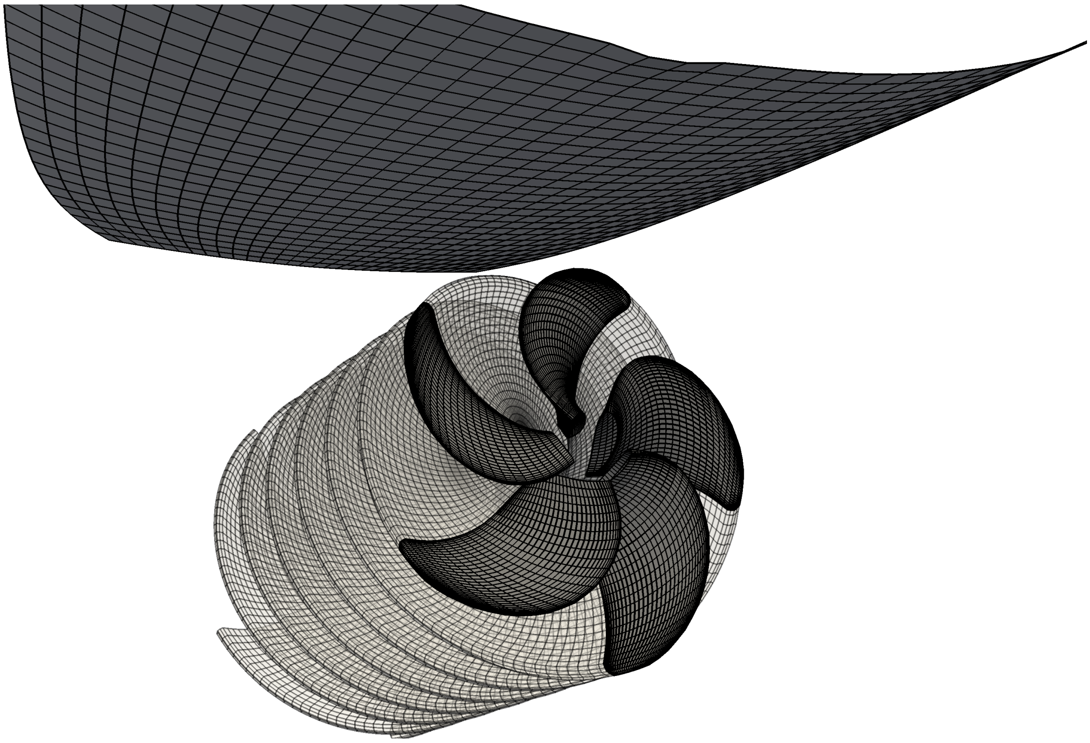

Fig. 7.11 Panel model of the potential flow domain Ω for Ship C.

edge. A solid boundary factor of $B_f = 1.95$ is selected to account for the presence of the hull when the pressure disturbance p'_{TV} is derived (see Section 6.2).

A determining parameter of the model is the outer domain radius r_D (see Chapter 5). Since a physical rationale for choosing a particular value is not known in the literature, it appears to be a free parameter. In Section 7.4, the influence of this parameter is studied. Furthermore, the exponent κ in Eq. (5.24) describing the tip vortex roll-up is a model parameter which has to be determined. In this case, κ is adjusted in a way that 99 % of the tip vortex circulation are reached after 0.75 revolutions.

In order to simulate the influence of bubbles surrounding the cavitating core, $\rho^\star\rho^{-1}$ at the birth of each vortex segment, i.e. $t^\star = 0$, and an average bubble radius have to be estimated. Theoretically, these are quantities ascertainable in experiments; however, such measurements are not known to the author and a rough guess is made at this point. The average bubble radius is defined as 0.0035 m and $\rho^\star\rho^{-1}$ is initialised with a value of 0.4.

7.2 Validation of the Coupling Procedure with Full-Scale Data

Prior to investigating pressure fluctuations and cavitation, the coupling procedure between ANSYS CFX and *pan*MARE is subjected to a validation scenario. The basic principle of the coupling procedure has been presented and validated several times (Greve et al., 2012; Wöckner-Kluwe, 2013; Zawadzki et al., 1997, e.g.). In addition to this, the detailed full-scale data provided by Damaschke et al. (2014)

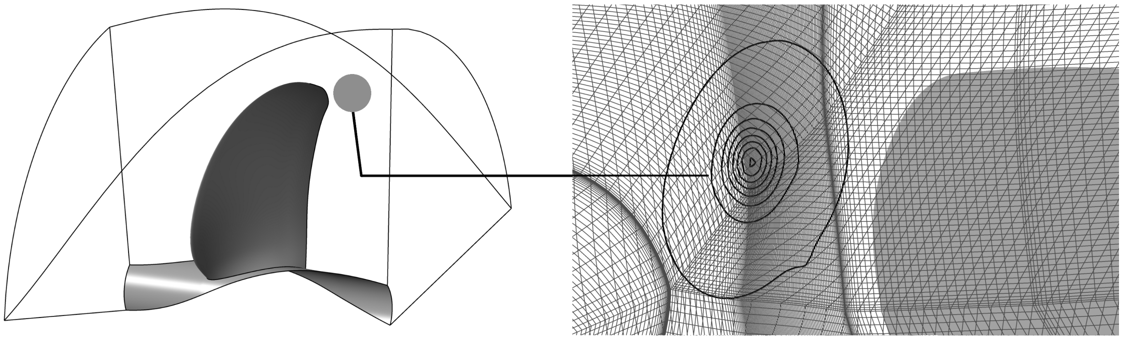

Fig. 7.12 Left: outline of the inner part of the numerical grid used for the investigation of flow details at the blade tip. The outer part is not shown. Right: resolution of the grid in the tip vortex region.

and Stoye (2014) are now applied in order to examine to which extent the results obtained by the coupling procedure reflect the full-scale conditions.

7.2.1 Total velocity field

Experimental data for the total velocity field directly in front of the propeller are available for the monitoring points sketched in Figure 7.13. These points are located on a slightly inclined plane in the direct vicinity of the propeller where the influence of the propeller is very large. Due to technical reasons, only the *x*- and *y*-component of the velocity field were recorded during the measurement campaigns.

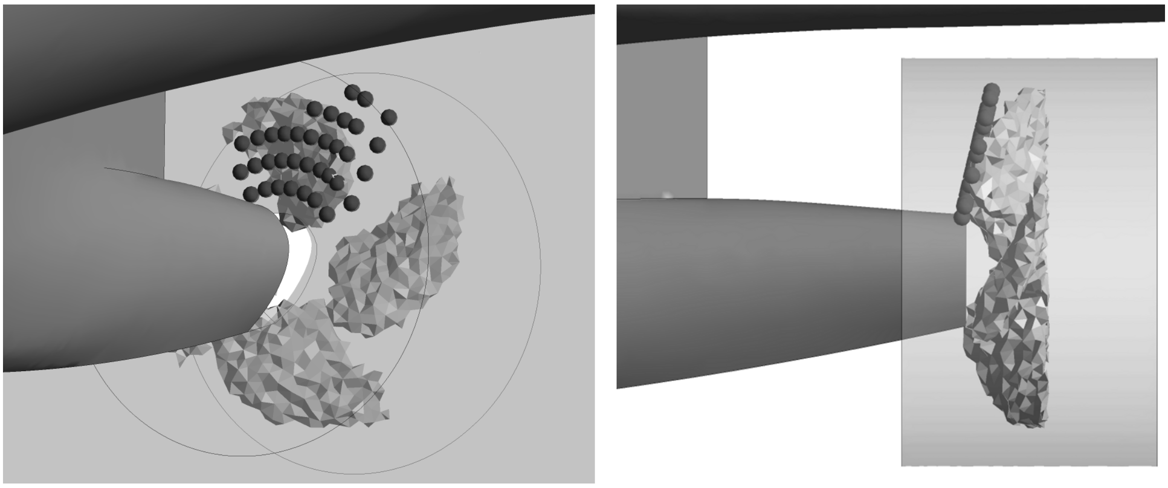

Fig. 7.13 Position of the monitoring points for the velocity measurement.

According to Heinke and Richter (2014), the operation point during the measurement campaigns is assumed to be best reflected by OP00A2, which is listed in Table 7.2. Figure 7.14 shows the acceleration of the flow behind the (virtual) propeller due to the action of the body forces.

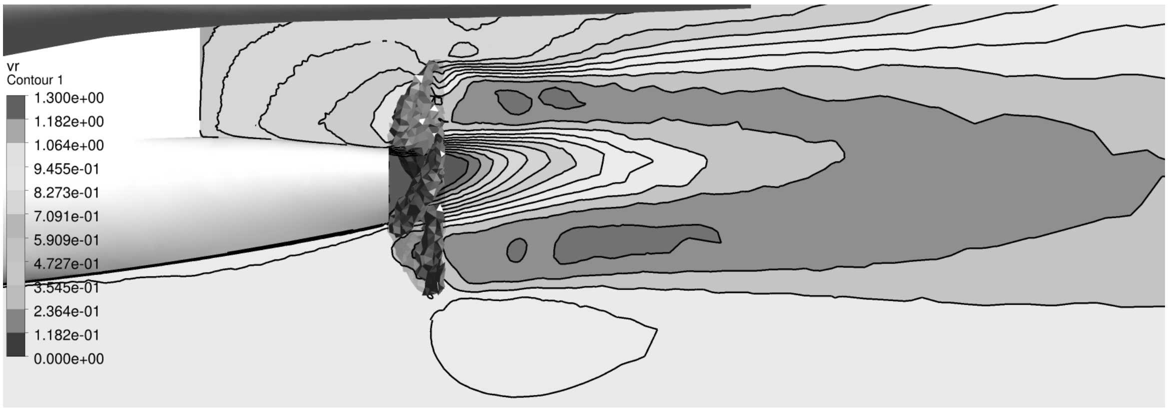

Fig. 7.14 Relative total axial velocity $u_x V_s^{-1}$ for a certain instant of time in a plane with $y = 0$.

To examine this further, the mean relative velocities in front of the propeller,

$$\varepsilon_{u_x} \equiv \frac{\overline{u_x}}{V_s} \quad \text{and} \quad \varepsilon_{u_y} \equiv \frac{\overline{u_y}}{V_s}, \tag{7.1}$$

are introduced at this point. $\overline{u}_x$ and $\overline{u}_y$ are time-averaged velocity components in the direction of x and y, respectively. Apart from the mean velocities, full-scale data is available for the velocity fluctuations $u_{x,\max} - u_{x,\min}$ and $u_{y,\max} - u_{y,\min}$ induced by the periodical passage of the propeller blades. These are made dimensionless by the ship speed and one obtains:

$$\varepsilon_{\hat{u}_x} \equiv \frac{u_{x,\max} - u_{x,\min}}{V_s} \quad \text{and} \quad \varepsilon_{\hat{u}_y} \equiv \frac{u_{y,\max} - u_{y,\min}}{V_s}. \tag{7.2}$$

It has been indicated in Section 3.1.2 that data gathered from the full-scale observations are affected by a number of uncertainties and some care must be exercised when a comparison with the simulation results is made. In particular, when the velocity was recorded for the monitoring points, this did not happen simultaneously for all points but in four separate campaigns. These are listed in Table 7.5. It can be seen that a significant amount of time passed between the individual campaigns and it has to thus be assumed that environmental conditions changed from campaign to campaign. In order to make this apparent, the full-scale data presented in Figures 7.15 and 7.16 are coloured according to the campaign the respective measured value originates from.

With respect to the mean velocity, the agreement between simulation and full-scale measurement presented in Figure 7.15 is, in general, satisfying. However, in this case, there is a trend of slightly overestimating the velocity deficit in the wake peak region at $\varphi = 0°$, which can be most clearly asserted for $r/R = 0.55$.

In the case of the velocity fluctuations $\varepsilon_{\hat{u}_x}$ and $\varepsilon_{\hat{u}_y}$, there are two possibilities to extract the information from the numerical solution. On the one hand, it is possible to directly consider the viscous flow solution obtained from the viscous flow domain Λ. On the other hand, use can be made

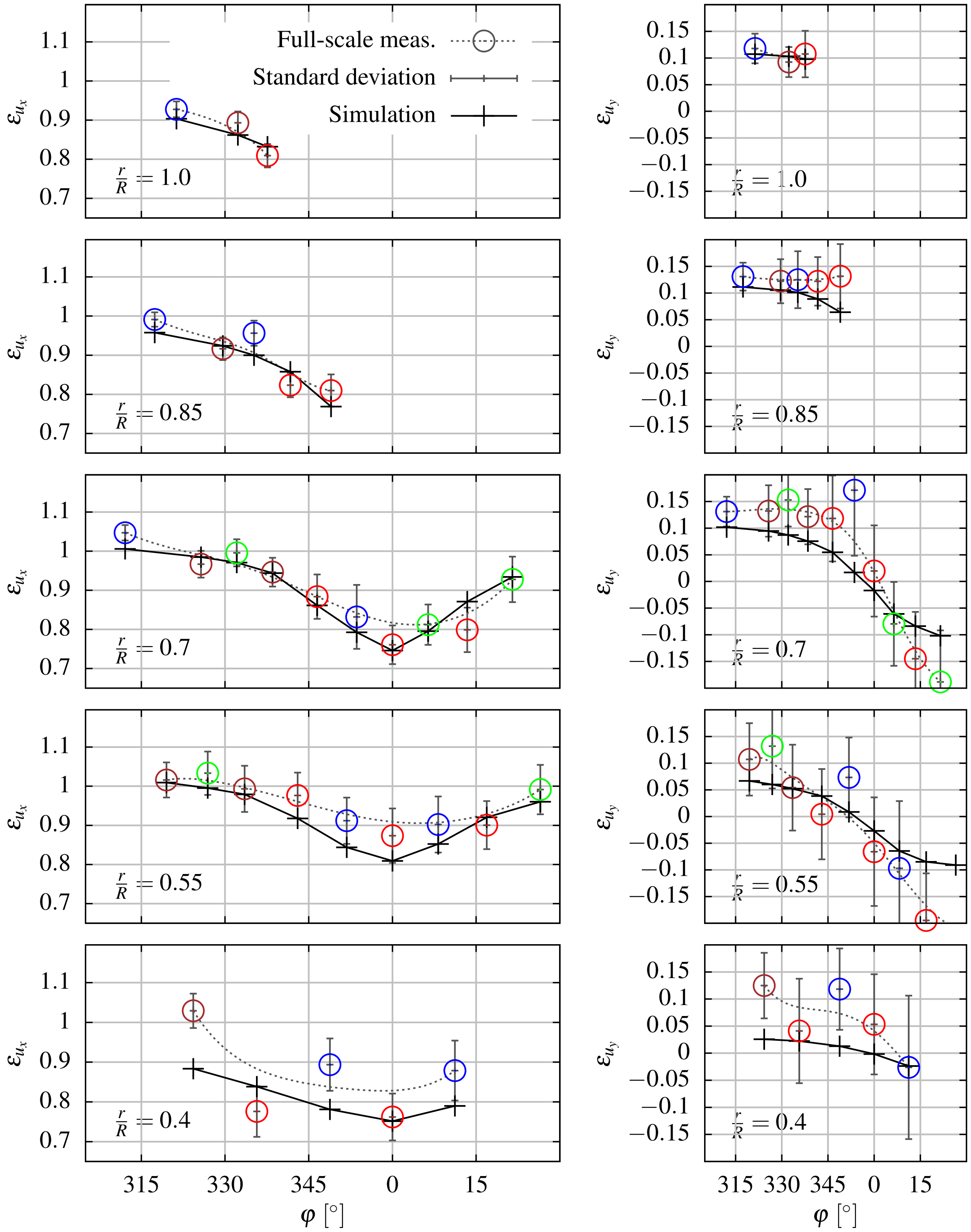

Fig. 7.15 Mean relative velocity components ε_{u_x} (left column) and ε_{u_y} (right column) of the total velocity field for Ship A; comparison between simulation and full-scale measurement for five different radii r/R in the propeller plane.

Table 7.5 Four campaigns for the measurement of the total velocity field for Ship A, the ConRo vessel.

Campaign	1	2	3	4
Duration (year 2013)				
Start	11.05. 23:30h	12.05. 10:40h	13.05. 02:00h	13.05. 12:20h
End	12.05. 02:35h	12.05. 12:25h	13.05. 04:50h	13.05. 13:45h
Colour code in Figures 7.15 and 7.16				
Colour	red	brown	blue	green

Table 7.6 Propeller thrust and propeller torque for Ship A at different operation conditions.

Operation point		OPA00A1	OPA00A2	OPA00AD
Numerical prediction				
Thrust coefficient	k_T [-]	0.178	0.206	0.216
Torque coefficient	$10k_Q$ [-]	0.299	0.350	0.405
Experimental results				
Thrust coefficient	k_T [-]	0.179	–	0.220
Torque coefficient	$10k_Q$ [-]	0.291	–	0.404

of Eq. (6.2) and *pan*MARE can be applied to calculate the unsteady total velocity field in the domain of potential flow Ω. As seen in Figure 7.16, the results obtained by both variants are quite different. The fluctuation of the velocity field observed in the viscous flow domain Λ is underrated, whereas the prediction with the help of *pan*MARE yields a good agreement with the full-scale measurement data.

How can this be explained? The total velocity calculated by *pan*MARE is basically a superposition of the background flow $\mathbf{V}_\infty$ and the propeller-induced velocity (see Eq. 4.23 in Section 4.2). The greatest part of the velocity fluctuation is contained in the propeller-induced velocities which are part of the solution given by *pan*MARE under consideration of the impermeability boundary condition on the propeller blades. This is important to highlight since this particular condition is not enforced by the virtual propeller present in the viscous flow domain. A wall in terms of the propeller surface is not present here; only a distribution of body forces emulates the presence of the propeller. In other words, the propeller model used here based on the body-force coupling is not able to render the displacement effect of the blades. This effect becomes important if regions in the close vicinity of the propeller, as in the present case, are of interest. As a consequence, pressure fluctuations observed in the domain of viscous flow are most likely underrated as well.

7.2.2 Propeller thrust and torque

Apart from the mean propeller thrust and torque listed in Table 7.6, periodic fluctuations of thrust and torque due to the inhomogeneity of the inflow are an important feature that needs to be predicted properly by the simulation method. For the operation point OP00A1, full-scale measurement data is available for the fluctuations of shaft torque (Stoye, 2014).

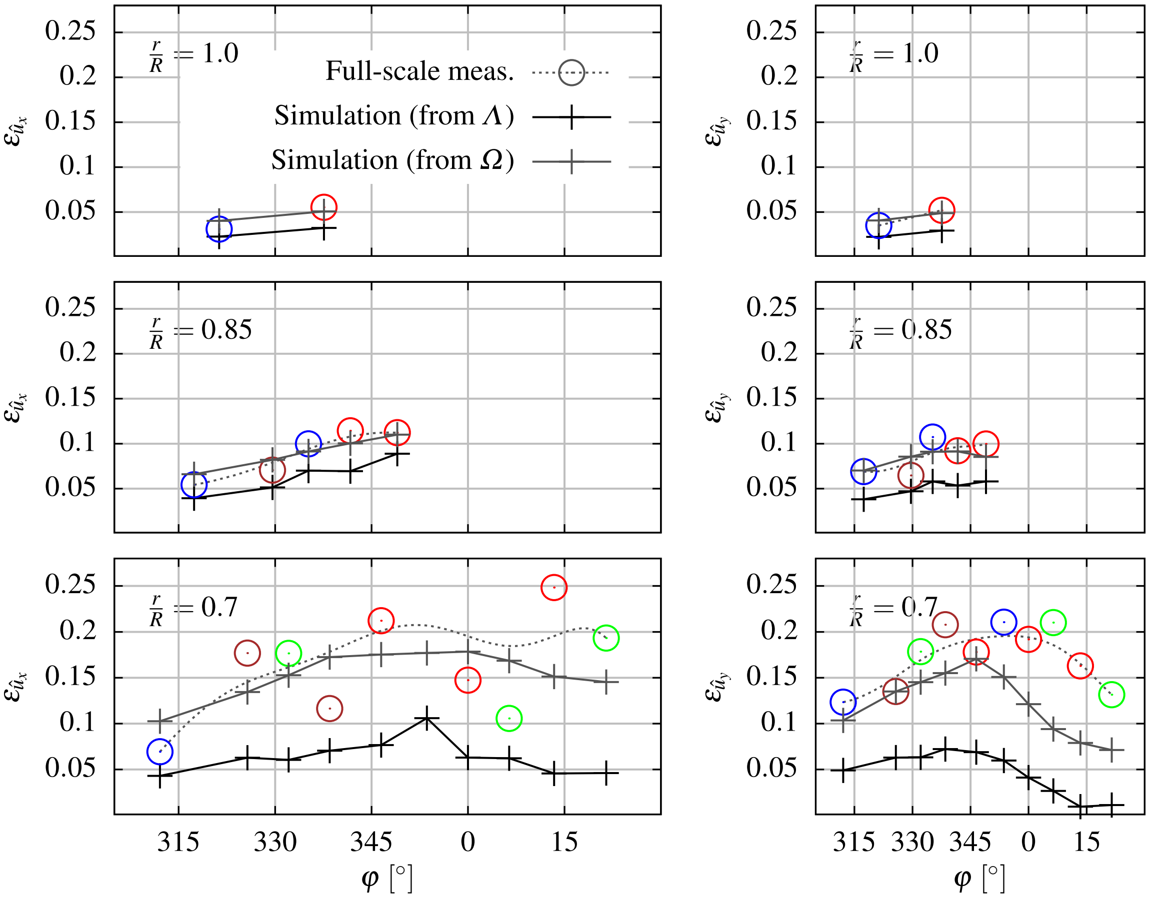

Fig. 7.16 Propeller-induced fluctuations of the velocity in the direction of x and y for Ship A in a dimensionless representation by means of $\varepsilon_{\hat{u}_x}$ and $\varepsilon_{\hat{u}_y}$; comparison between simulation and full-scale measurement for five different radii r/R in the propeller plane.

In order to relate the measured fluctuations of torque transferred by the shaft $\hat{Q}_{\text{shaft}}$ to the torque fluctuations acting on the propeller as a result of the varying hydrodynamic forces $\hat{Q}$, a vibration analysis taking into account all relevant components of the propulsion train has been carried out, yielding a transfer function $Y(\omega) = \hat{Q}_{\text{shaft}}\widehat{Q}^{-1}$ depending on the angular frequency ω of the torsional vibration (Abdel-Maksoud et al., 2014).

In the left part of Figures 7.17 and 7.18, simulation results with respect to thrust and torque acting on the individual propeller blades and on the entire propeller are shown in a dimensionless representation. The relative fluctuations of the order q,

$$\varepsilon_{\hat{T}^{[q]}} = \frac{\hat{T}^{[q]}}{T} \quad \text{and} \quad \varepsilon_{\hat{Q}^{[q]}} = \frac{\hat{Q}^{[q]}}{Q}, \tag{7.3}$$

of thrust and torque (fluctuating with qnn_b), are shown on the right side of the respective figures. A comparison with measurement data is made only for first-order torque fluctuations $\varepsilon_{\hat{Q}^{[1]}}$ (see Figure 7.17). Determining the transfer function Y mentioned above is affected by a number of uncertainties

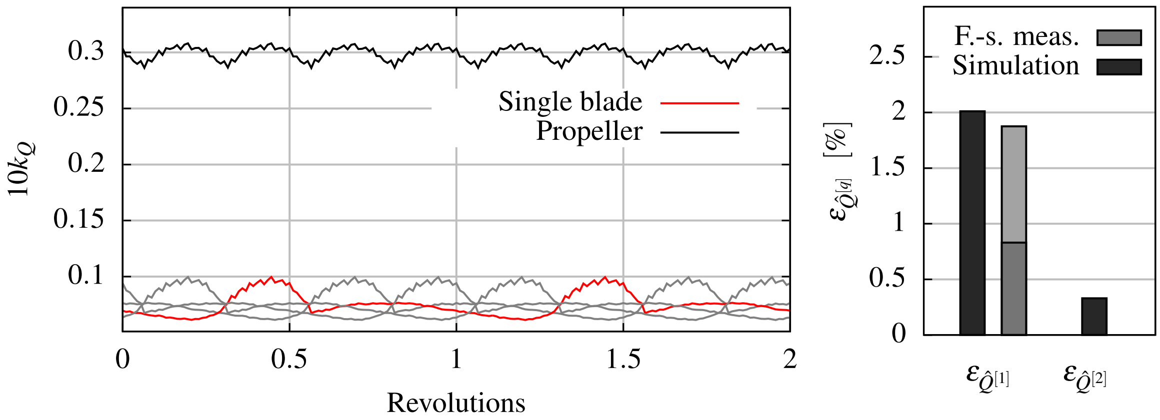

Fig. 7.17 Fluctuations of propeller torque for Ship A at OP00A1.

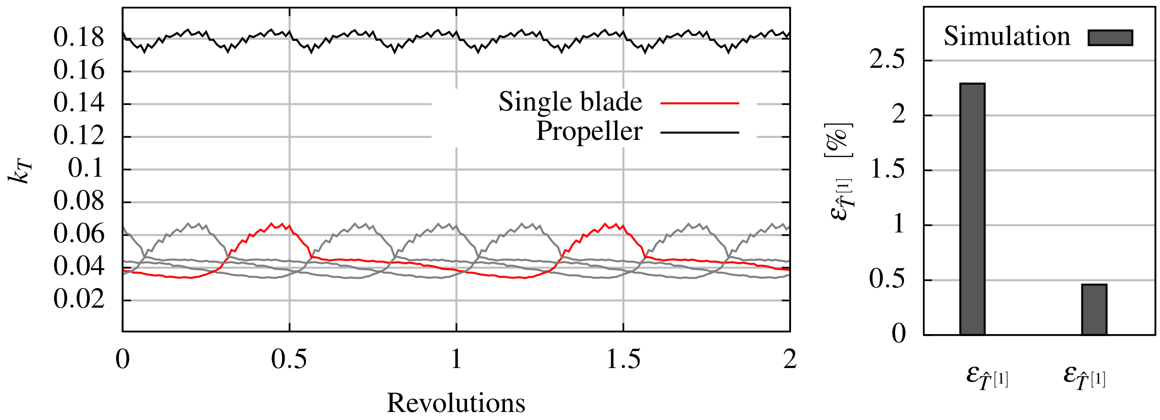

Fig. 7.18 Fluctuations of propeller thrust for Ship A at OP00A1.

and only an interval can be specified containing the assumable full-scale fluctuation of hydrodynamic torque. This interval is marked by the two grey boxes in the figure. It can be seen that the simulated fluctuation of torque is fractionally larger than the measured one.

7.3 Pressure Fluctuations for Non-Cavitating Flow

An important condition for predicting correct pressure fluctuations induced by cavitating propellers is that the induced pressure fluctuations for *non-cavitating* flow are determined with sufficient accuracy. This can only be assured if the wake field of the ship is predicted correctly. It has been shown in the previous section by means of Ship A that the simulation method is able to determine the unsteady total velocity field upstream of the propeller. For the other two vessels, experimental data is available in form of the nominal wake field measured during model tests. This is shown in Figure 7.19 for all three vessels investigated in the present study. One has to keep in mind that dummy models

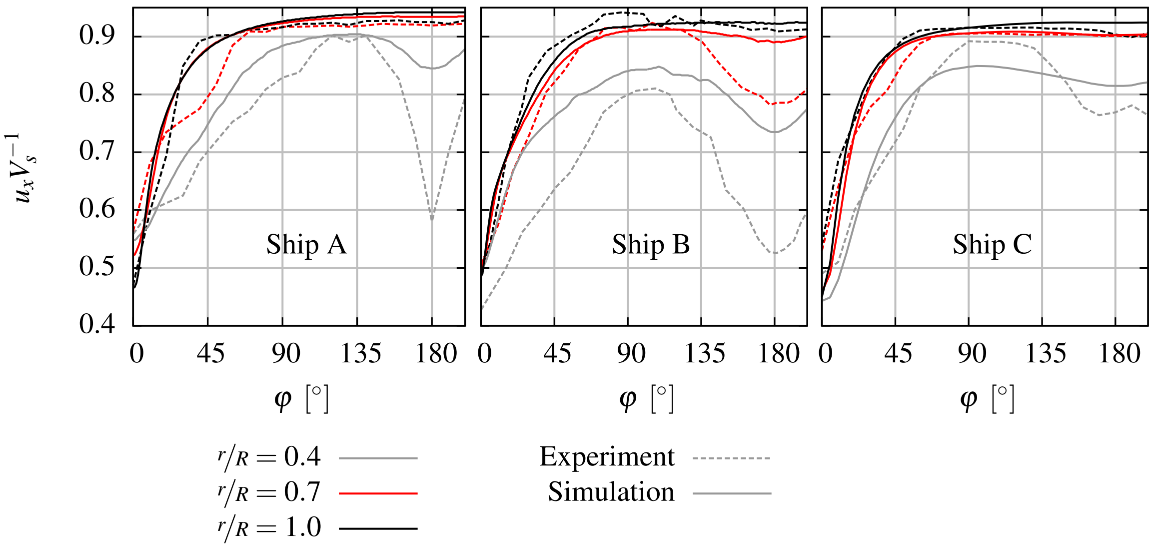

Fig. 7.19 Comparison between simulated and measured nominal wake field for the three ships.

with wake screens have been used for the experiments in order to emulate the full-scale wake field, whereas for the numerical simulations with ANSYS CFX, the geometrically similar hull forms are modelled. In this respect, the agreement between experiment and simulation demonstrated in the figure is acceptable, especially when the velocity deficit in the wake peak zone around $\varphi = 0^\circ$ is considered. Notable discrepancies occur for $r/R = 0.4$ at $\varphi = 180^\circ$ where the influence of the gondola becomes important. The biggest share of the propeller load, however, is generated at the outer radial fractions of the propeller, which leads to the conclusion that the nominal wake field is reproduced in a sufficiently accurate manner.

Throughout this thesis, pressure fluctuations p' and amplitudes $\hat{p}$ are brought to a dimensionless representation by means of the coefficients

$$k_{p'} \equiv \frac{p'}{\rho n^2 D^2} \quad \text{and} \quad k_{\hat{p}} \equiv \frac{\hat{p}}{\rho n^2 D^2}. \tag{7.4}$$

Similarly, $k_{\hat{p}[q]}$ refers to the amplitude of the q-th harmonic component of the pressure signal.

ConRo vessel (Ship A) Cavitation tunnel experiments were carried out within the project KonKav II by two ship model basins for Ship A in order to investigate pressure fluctuations (Heinke and Richter, 2014; Lücke, 2014). The operation point OPA001 was used in the experiments. Furthermore, also for OPA001, full-scale data with respect to pressure fluctuations have been made available by Lücke. A complicated cavitation pattern was observed during the full-scale measurements campaign for Ship A. This is due to the reduced pitch of the propeller at OPA001. The pattern is described in Section 2.5.2 and can be characterised by the interaction between leading edge vortex and trailing vortex. Sheet cavitation has not been observed. Attempts to simulate the interaction between two cavitating

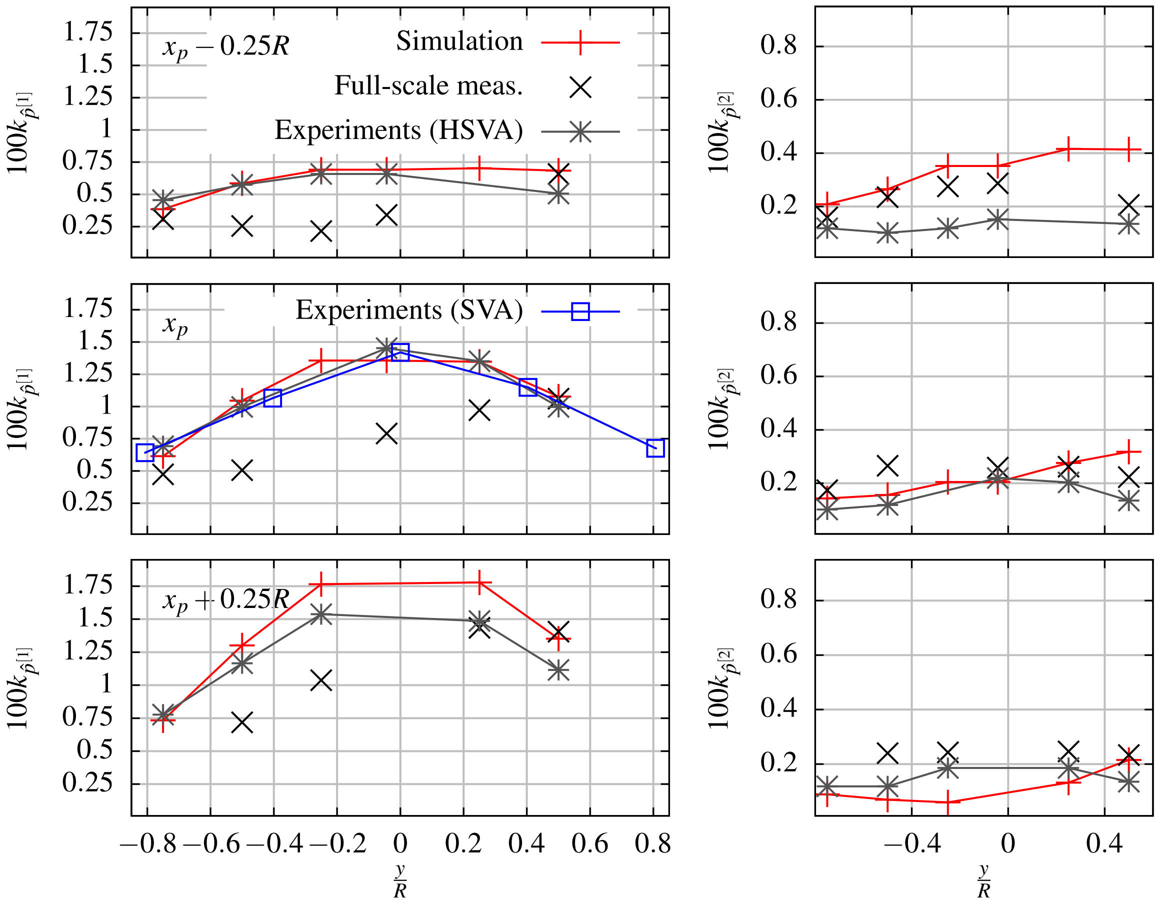

Fig. 7.20 Propeller-induced pressure fluctuations of first (left column) and second order (right column) for Ship A at OPA001 without cavitation at three levels $x = x_p - 0.25R$, $x = x_p$ and $x = x_p + 0.25R$; x_p marks the propeller plane.

vortices have not been made in the present thesis. It is assumed that this cavitation pattern does not affect the first-order and second-order pressure fluctuations treated in this section in a significant way. Therefore, the results of the full-scale measurement campaign can be used for the validation of the method for non-cavitating flow conditions, although cavitation is present.[4] In Figure 7.20, simulation results with respect to hull pressure fluctuations are shown for Ship A. A good agreement with the model test results is obtained for $k_{\hat{p}^{[1]}}$; numerically predicted second-order fluctuations are on the same level as those obtained in the experiments. However, some discrepancies become apparent when the numerical and experimental data are compared to the full-scale measurements. Generally, the level of pressure fluctuations in this case is quite low ($k_{\hat{p}} = 0.75$ corresponds to $\hat{p} = 0.763\,\mathrm{kPa}$, for example) and small inaccuracies of the experimental or numerical model can affect the result. These discrepancies may possibly arise from the overestimation of the wake peak indicated in the previous

---

[4] This assumption can be justified by the fact that in this particular case – according to model test experiments (Heinke and Richter, 2014; Lücke, 2014) – first-order pressure fluctuations are not altered by the presence of cavitation in a significant manner.

section. Additionally, it can be speculated that the ship's motion in the seaway, which has not been taken into account in the simulation and the experiments, could have an influence on the recorded pressure signal.

Container vessels (Ships B and C) Numerical simulations with respect to non-cavitating pressure fluctuations are also carried out for the container vessels, for which the operation points OP00B and OP00C for non-cavitating flow are adjusted. The results and a comparison with cavitation tunnel experiments are shown in Figures 7.21 and 7.22.

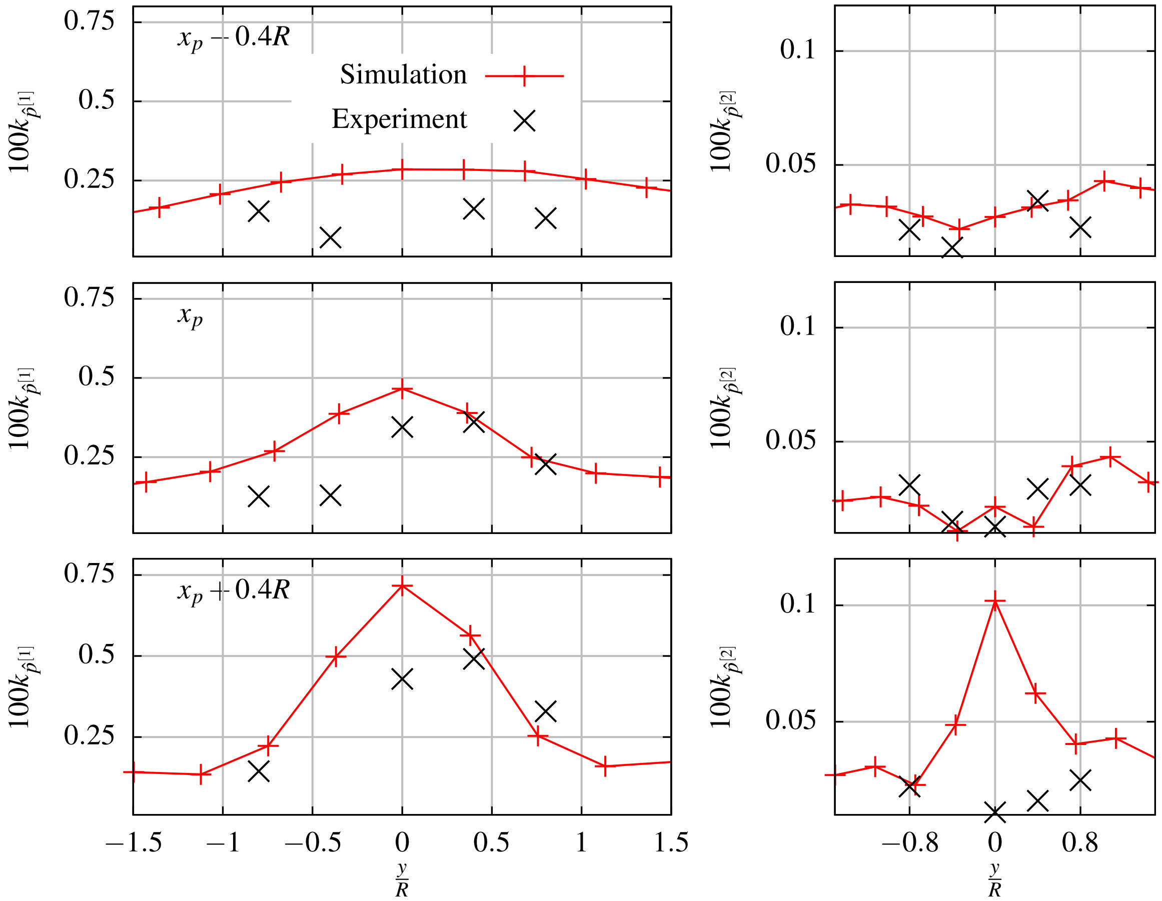

Fig. 7.21 Propeller-induced pressure fluctuations of first (left column) and second order (right column) for Ship C without cavitation at three longitudinal positions $x = x_p - 0.4R$, $x = x_p$ and $x = x_p + 0.4R$; x_p marks the propeller plane.

In the case of Ship C, monitoring points are located on three sections with $x = \text{const.}$ (see Figure 7.21). For the middle section located directly above the propeller, the numerical results sufficiently reflect the flow behaviour observed during the experiments. However, when locations upstream and downstream of the propeller are considered, larger deviations can be observed. In particular for $k_{\hat{p}[1]}$ at $x = x_p - 0.4R$, the rudder influence might become important. The numerically forecast trend of $k_{\hat{p}[2]}$ at $x = x_p + 0.4R$, i.e. in front of the propeller, differs in a qualitative manner from the experiments.

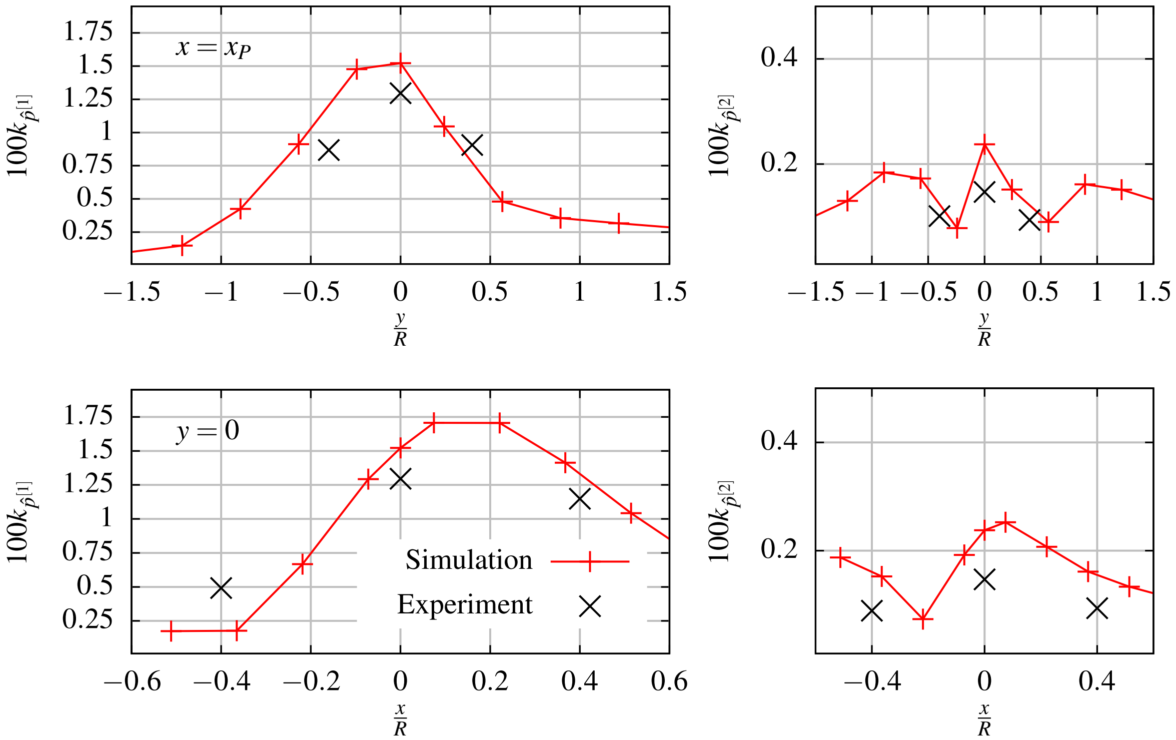

Fig. 7.22 Propeller-induced pressure fluctuations of first (left column) and second order (right column) for Ship B without cavitation in the propeller plane at $x = x_p$ and in the longitudinal direction at $y = 0$.

Similar to the case of Ship A, the level of pressure fluctuations is very low here, which especially holds for second-order fluctuations, and any inaccuracy of the numerical model can lead to significant deviations.

For Ship B, pressure fluctuations were recorded for five monitoring points in a crosswise arrangement with the center being located directly above the propeller. The agreement between experiment and simulation for $k_{\hat{p}[1]}$ and $k_{\hat{p}[2]}$ shown in Figure 7.22 is acceptable.

7.4 Selected Results for Cavitating Flow

Cavitating flow conditions are considered for both container vessels – Ships B and C. In this section, simulation results are discussed in greater detail only for Ship C. In this respect, some of the RANS simulation results for the flow details at the blade tip are presented in Section 7.4.1. Input parameters for the tip vortex cavitation model are generated by means of these simulations. Cavity patterns for various angular positions of the blade are presented in Section 7.4.2 as well as a comparison between numerically predicted and measured pressure fluctuations in Section 7.4.3.

7.4.1 Flow details at the blade tip

By means of detailed RANS simulations, input data for VoCav2D have been generated. The procedure is described in Section 5.4. In order to figure out the initial core radius r_{a0} and γ_{ini}, i.e. the relation between initial circulation Γ_{ini} of the tip vortex and the bound blade circulation Γ_b, the tip flow directly downstream the trailing edge is evaluated. This is shown for the exemplary case of propeller P00C at $J = 0.65$ in Figure 7.23. Obviously, the distribution of circumferential velocity $u_\varphi(\xi)$ can be described with a sufficient degree of accuracy by a fitted Burgers vortex, which can be seen in the left diagram of Figure 7.23a.

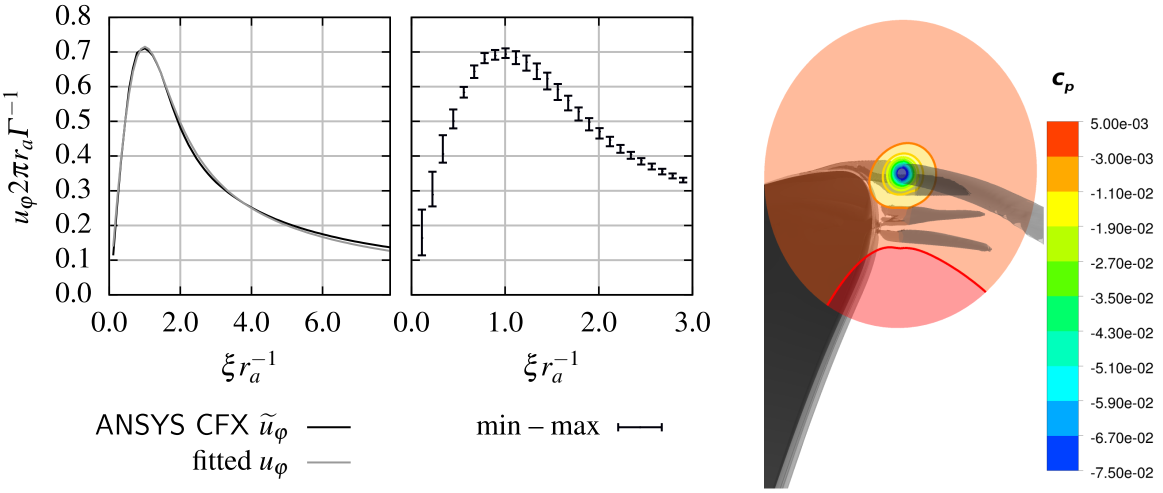

(a) Distribution of circumferential velocity. **(b)** Pressure distribution.

Fig. 7.23 Distribution of circumferential velocity and pressure in the tip vortex region and fitted Burgers vortex model for P00C and exemplary operation conditions.

It is assumed that the results depend on the grid resolution in the tip region and the applied turbulence model. To study this further, various simulations with different grids (9.0 Mio., 12.3 Mio. and 13.8 Mio. cells) and turbulence models (the SST model with and without curvature correction, the k–ε model and the k–ω model; see Section 4.1.2) are carried out. The results of this investigation are compiled in the right diagram of Figure 7.23a where the margins of deviations according to the varied numerical parameters are shown in a dimensionless form. The highest impact can be detected in the region $\xi < r_a$. The uncertainties occurring when Γ_{ini} and r_{a0} are determined using the fine mesh configurations with 12.3 Mio. and 13.8 Mio. cells are less than 1 % for the circulation and approximately 2.5 % for the viscous core radius. Values obtained by simulations with the coarse mesh (9.0 Mio. cells) differ by appr. 7 % from the results with the fine mesh configurations.

By relating the cavity thickness at the trailing edge in the tip region of the propeller η_{TE} to the initial cavitation radius r_{c0}, the interaction between sheet cavitation and tip vortex cavitation can be taken into account (see Section 5.3). For this purpose, RANS simulations are conducted for various homogeneous inflow velocities under consideration of cavitation. The results are shown in Figure

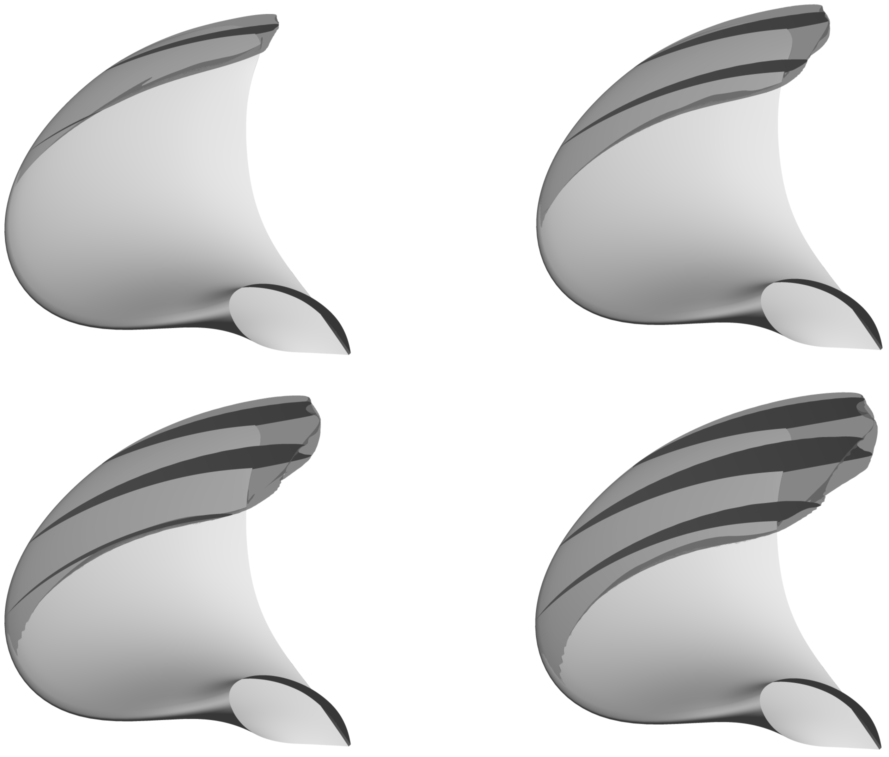

Fig. 7.24 Simulated cavity shape for P00C in homogeneous inflow at $J = 0.65, 0.55, 0.45, 0.35$ (from top left to bottom right); cavitation number set according to OP00C.

7.24 and exhibit a typical behaviour of sheet cavitation with a growing cavity thickness at increasing propeller load. Figure 7.25 shows the interpolated input data used for the simulation of the cavitating tip vortex with VoCav2D-f2 extracted from the RANS simulations for the case of P00C.

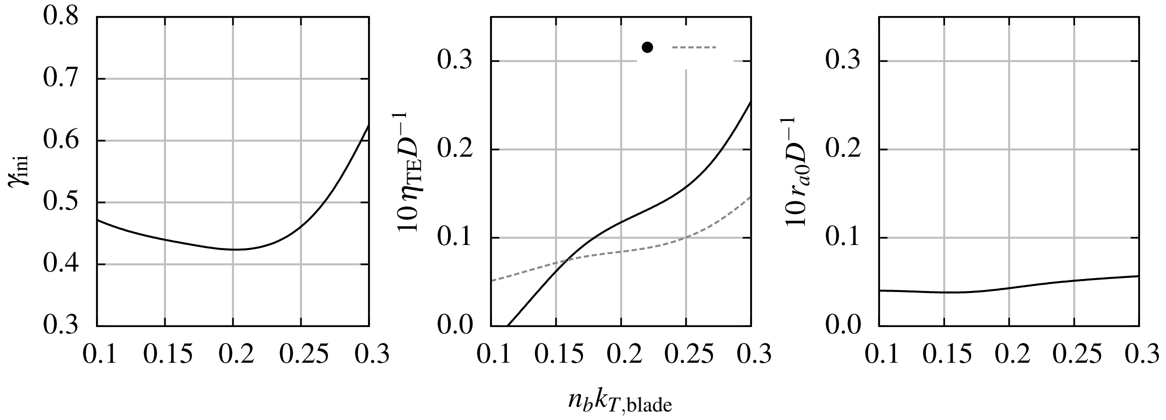

Fig. 7.25 Input parameters for the simulation of the cavitating tip vortex plotted against the corresponding blade load for non-cavitating flow. • marks curve of $10\left(2r_{c,\mathrm{eq}}\right)D^{-1}$ according to Eq. (2.22) using $\gamma_{\mathrm{ini}}\Gamma_b$ as circulation.

7.4.2 Cavitation pattern

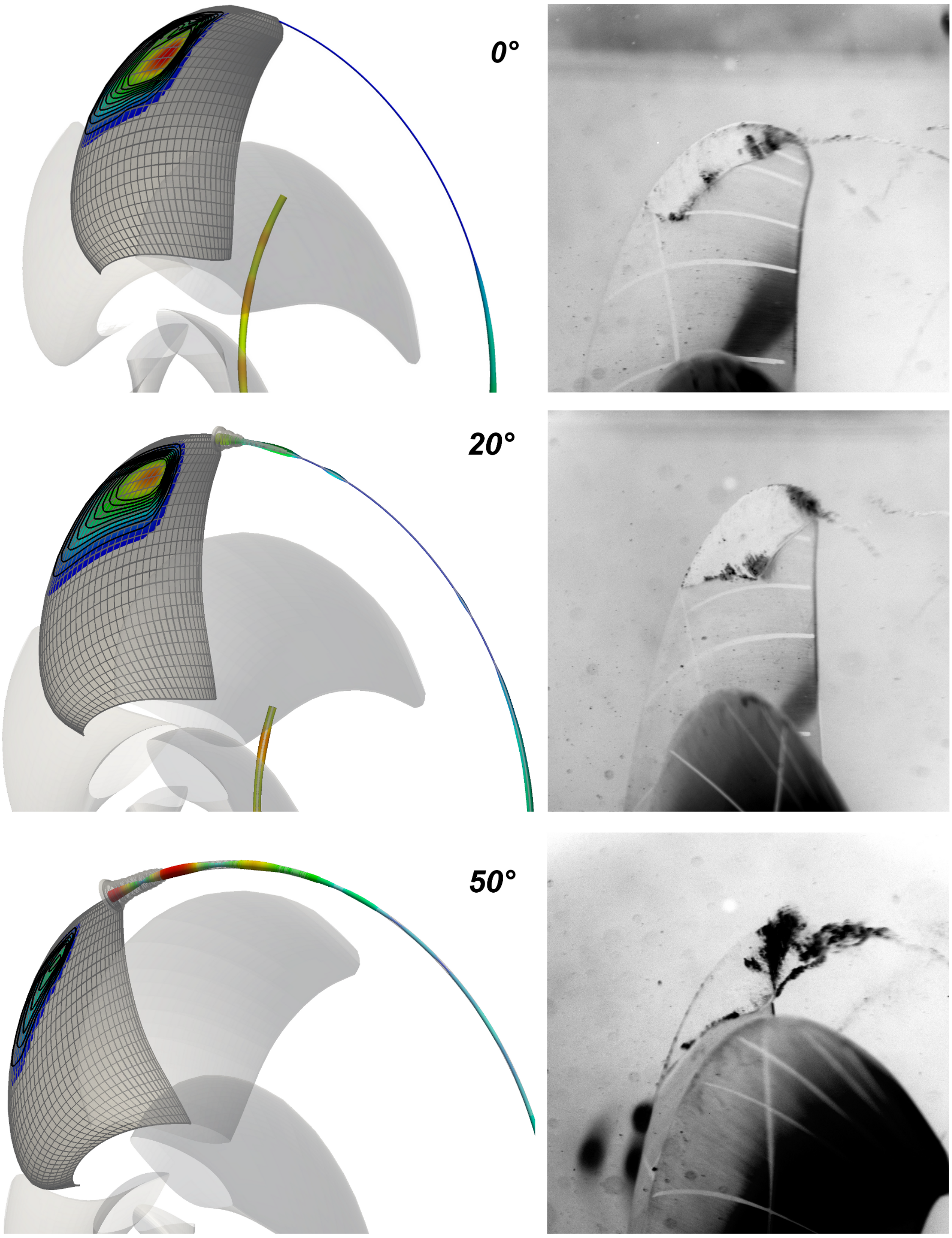

Fig. 7.26 Comparison between simulated and experimentally observed cavitation pattern of P00C. Cavity thickness and cavitation radius made dimensionless by $\frac{D}{100}$; see Figure 7.27.

The cavitation pattern in terms of unsteady sheet cavitation on the propeller blades and the cavitating tip vortex is shown in Figures 7.26 and 7.27 for propeller P00C. A comparison with experimental data is made in Figure 7.26 for three angular positions. It can be seen that, with respect to sheet cavitation, the agreement between simulation and experiment is not optimal. Indeed, the cavity area and, presumably, the cavity volume is reflected properly. However, some deviations occur with respect to precisely locating the zones of the blade surface covered by sheet cavitation. When approaching the angular position of $\varphi = 0°$, the cavitating tip vortex is rather weak since the blade has reached this position originating from a region of low blade loading. Then, in the position of 20°, sheet cavitation extends to regions beyond the trailing edge and widens the cavitating tip vortex. Although, sheet cavitation predicted by *pan*MARE for $\varphi = 20°$ terminates upstream of the trailing edge, the detailed RANS simulations carried out in advance for the propeller predict such a behaviour. This is why a widened tip vortex can be observed in the simulation results despite the fact that there is no contact visible between sheet cavitation simulated by *pan*MARE and the cavitating tip vortex. At $\varphi = 50°$, the thickness of sheet cavitation at the trailing edge increases even more, leading to a further

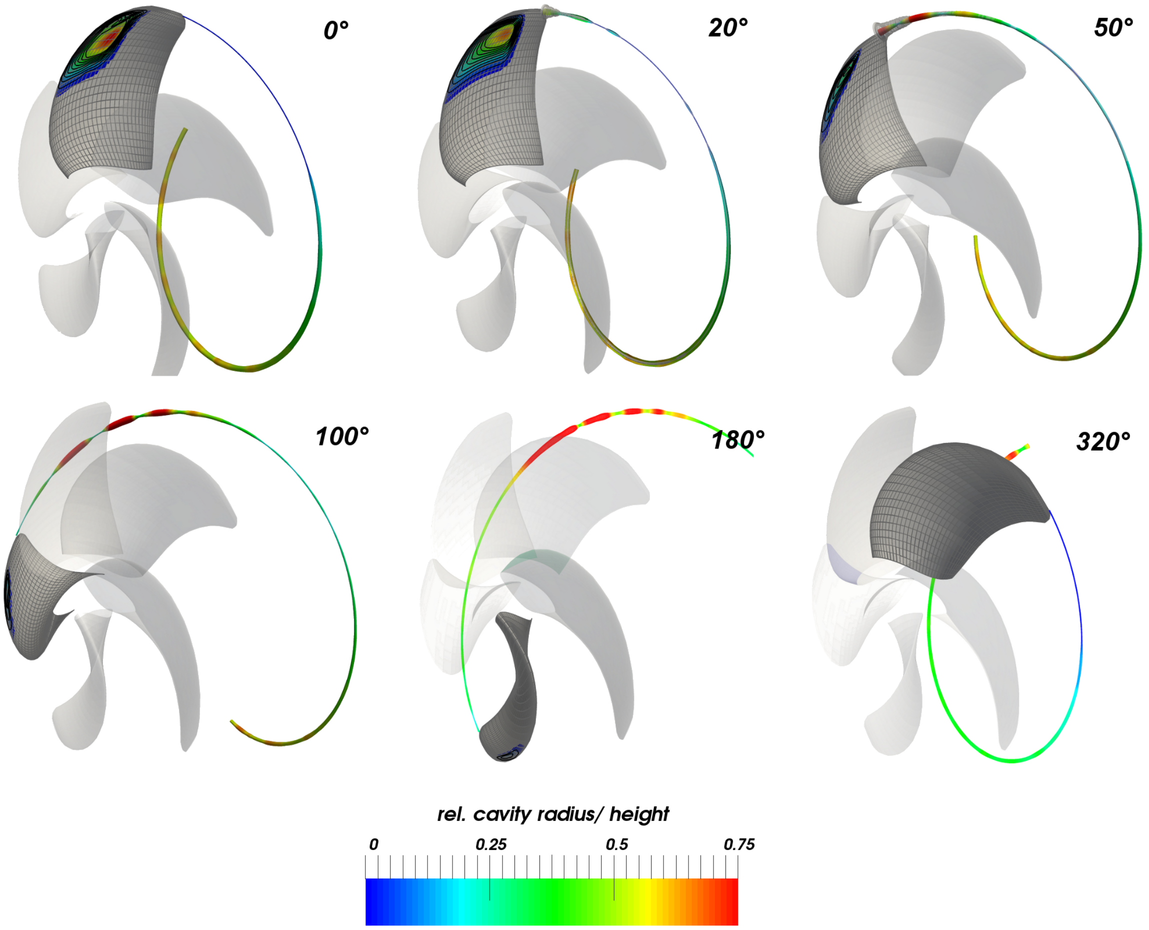

Fig. 7.27 Simulated cavitation pattern of P00C for six angular positions. Cavity thickness and cavitation radius made dimensionless by $\frac{D}{100}$.

widening of the tip vortex. Simultaneously, disintegration takes place and bubbly flow surrounds the cavitating vortex. This is indicated in the simulation results by the opaque grey envelope covering portions of the cavitating tip vortex in the direct vicinity of the trailing edge.

The further development of the tip vortex is shown in Figure 7.27. Portions of the tip vortex born at $\varphi = 50^\circ$ feature a large cavitation radius undergoing strong fluctuations. These portions are swept away by the flow while maintaining their approximate vertical position. The intensity of the tip vortex in terms of cavity radius decreases when the blade leaves the wake peak zone. Due to the upward vertical velocity component of the wake field, the lowest intensity is observed in angular positions around $\varphi = 270^\circ$.

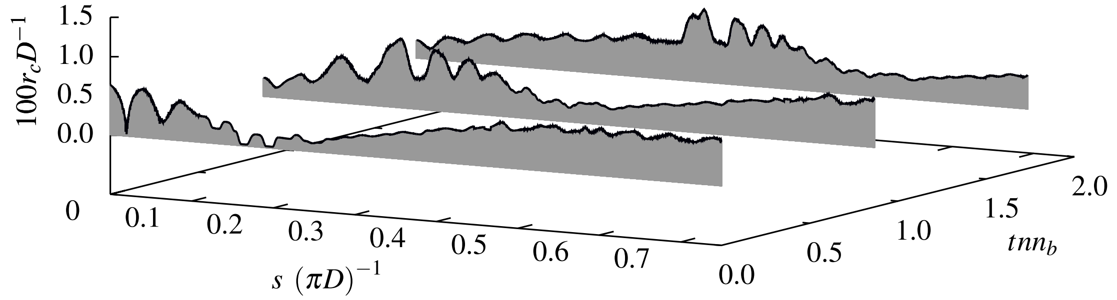

Fig. 7.28 Shape $r_c(s)$ of the tip vortex cavity for three instants of time for the first three-quarter revolution $s \leq 0.75\pi D$.

Figure 7.28 offers a more detailed view of the evolution of the tip vortex cavitation shape. At $t = 0$ in the figure, a group of segments with large cavitation radii is generated at the trailing edge $s = 0$. Obviously, the blade has passed the wake peak region at this moment. This group is apparently swept away by the flow. It can furthermore be observed that the average cavitation radius of this group grows while travelling downstream. This is a result of the increase of circulation from Γ_{ini} to Γ_b due to vortex roll-up. It can be gathered from the figure that the maximum cavitation radius ranges around 0.065 m, which can be considered as a realistic value.

7.4.3 Higher-order pressure fluctuations

Finally, the results with respect to propeller-induced pressure fluctuations are presented. In Figure 7.29a, the pressure signal monitored on the hull directly above the propeller is shown for four different cases: (1) due to the cavitating tip vortex of a single blade, (2) the signal originating from all n_b tip vortices, (3) the pressure signal of the cavitating propeller without taking into account tip vortex cavitation and (4) the overall signal including the effect of tip vortex cavitation.

By means of Fourier analysis, the frequency spectrum of the signal can be obtained, and the result is shown in Figure 7.29b. For the moment, only consider the red curves in the figure. The frequency spectrum of the pressure signal due to a single cavitating tip vortex is shown in the lower diagram and reveals a hump between $2.5\,nn_b$ to $4.5\,nn_b$ and a smaller one around $7\,nn_b$.[5] This is in perfect accordance with the considerations on the characteristic frequencies of tip vortex cavitation made in Section 2.6.2. The periodic summation of the single blade signal results in the signal being radiated by all n_b cavitating tip vortices and sharp discrete components emanating at multiples q of the blade frequency nn_b. This is shown in the upper diagram of Figure 7.29b.

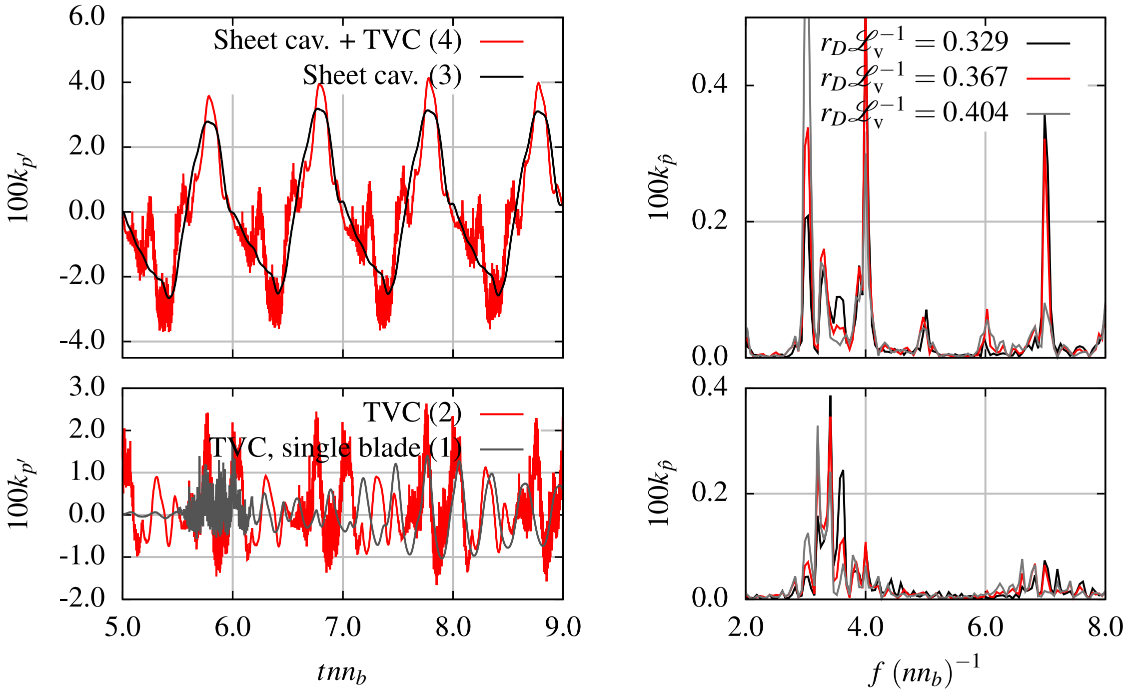

(a) Different contributions to the overall pressure signal; $r_D\mathscr{L}_v = 0.367$.

(b) Influence of r_D on the frequency spectrum. Top: TVC complete propeller; bottom: single blade.

Fig. 7.29 Pressure signal due to the cavitating propeller P00C considering sheet cavitation and tip vortex cavitation recorded in a monitoring point directly above the propeller.

As mentioned in Chapter 5, the outer domain radius r_D occurring in Eq. (5.9) is *de facto* a free parameter since there is no physical rationale for choosing a particular value. Therefore, the influence of this parameter is studied in the following. What is missing for such a study, is a suitable reference length. In this context, it is important to recall the findings of Section 5.5.2, where it has been shown that the average cavitation radius of a single vortex segment is nearly independent of r_D (whereas oscillation frequency and radiated pressure are highly affected by this quantity).

It is thus possible to use the average cavitation radius or anything proportional to it as suitable reference length $\mathscr{L}_v$ in the following study. Since the same value of r_D is used for all segments

---

[5] What is called ‘hump’ here is actually an agglomeration of peaks at frequency intervals n^{-1} (see Section 2.6 for an explanation).

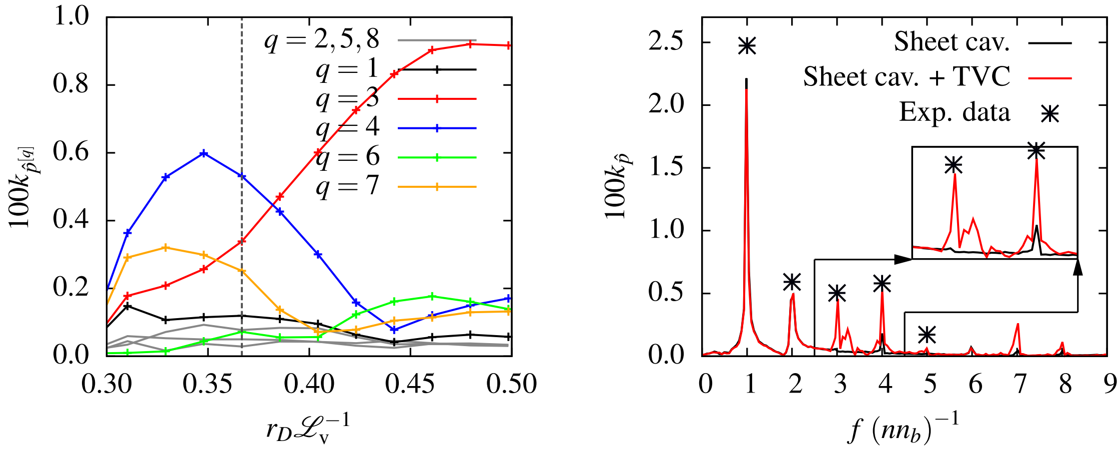

(a) Influence of r_D on higher-order pressure fluctuations.

(b) Exemplary frequency spectrum observed in the monitoring point directly above the propeller; $r_D = 0.367\mathscr{L}_\mathrm{v}$.

Fig. 7.30 Left: influence of r_D on higher-order pressure fluctuations with dashed line indicating the value used in the simulations; right: frequency spectrum of pressure signal with and without tip vortex cavitation.

constituting the cavitating tip vortex, the average cavitation radius of the entire tip vortex is applied for this purpose. Combining Eq. (2.21) and Eq. (2.22) yields $r_{c,\mathrm{eq}} \propto k_T D \sigma_n^{-0.5} \equiv \mathscr{L}_\mathrm{v}$, where $\sigma_n = 2(p_\infty - p_v)\rho^{-1}n^{-2}D^{-2}$ has been used.

The influence of r_D is depicted in Figure 7.29b. The results represented by the red curves in the figure have been obtained with an outer domain radius of $r_D = 0.367\mathscr{L}_\mathrm{v}$, which is approximately ten times the average cavitation radius of the tip vortex. Consider now the frequency spectrum for the single blade case shown in the lower diagram. Increasing r_D to $r_D = 0.404\mathscr{L}_\mathrm{v}$ leads to a slight shift of the hump towards lower frequencies; a decrease results in the opposite. Although the shifting of the hump is rather small in both cases, the spectrum representing the pressure signal radiated by all n_b tip vortices (shown in the upper diagram) is highly affected by the choice of r_D. It can be clearly seen that the peaks at multiples of blade frequency change significantly depending on the radius r_D.

Studying the influence of r_D on the results is continued in Figure 7.30a, where the dimensionless harmonic pressure amplitudes $k_{\hat{p}[q]}$ due to tip vortex cavitation are plotted against r_D for $q = 1, 2, \ldots 8$. It can be seen that in this particular case, components with $q = 3, 4$ and $q = 7$ (i.e. those associated to three, four and seven times blade frequency) are very sensitive towards changes of r_D.

A comparison with experimental data is shown in Figures 7.30b and 7.31. The best agreement between experiment and simulation could be obtained with $r_D = 0.367\mathscr{L}_\mathrm{v}$, i.e. the outer domain radius is chosen to be approximately ten times larger than the average cavitation radius of the tip vortex. In Figure 7.30b, the frequency spectrum of the pressure signal recorded on the hull directly above the propeller is shown. Experimental results are marked by an $*$ in the diagram. It can be seen that without considering the influence of tip vortex cavitation, there is a significant underestimation of third-order and fourth-order pressure fluctuations.

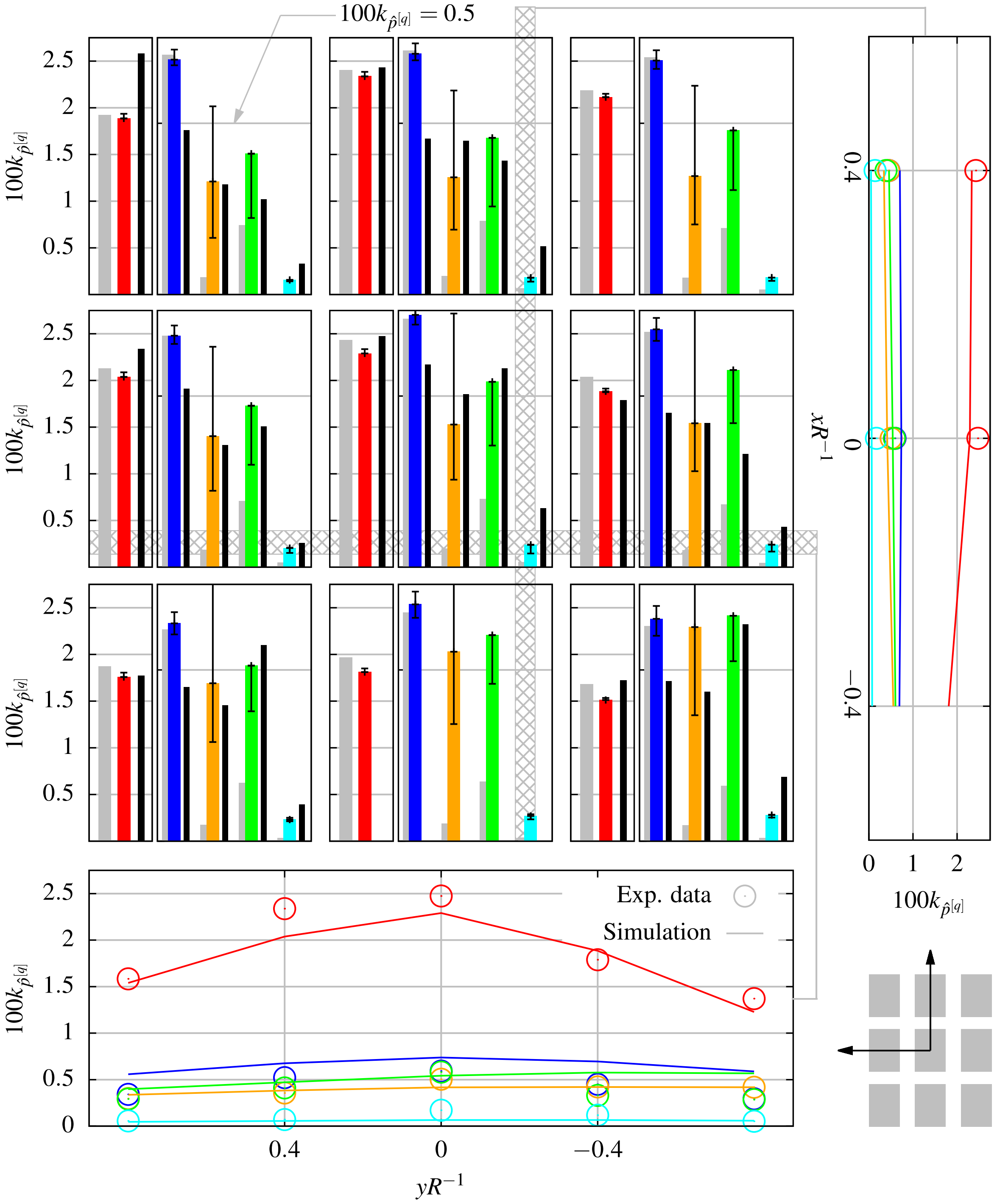

Fig. 7.31 Pressure fluctuations $k_{\hat{p}[q]}$ induced by propeller P00C; comparison between simulation and experiment. Colour code: 🟥 $q = 1$, 🟦 $q = 2$, 🟧 $q = 3$, 🟩 $q = 4$ and ■ $q = 5$. Thin black boxes indicate experimental results, grey boxes indicate simulation results without the tip vortex cavitation model being active. $\top$ and $\perp$ mark the interval the solution ranges in when r_D is varied between $r_D = 0.329\mathscr{L}_\mathrm{v}$ and $r_D = 0.404\mathscr{L}_\mathrm{v}$. No experimental results are available for subdiagrams without thin black boxes.

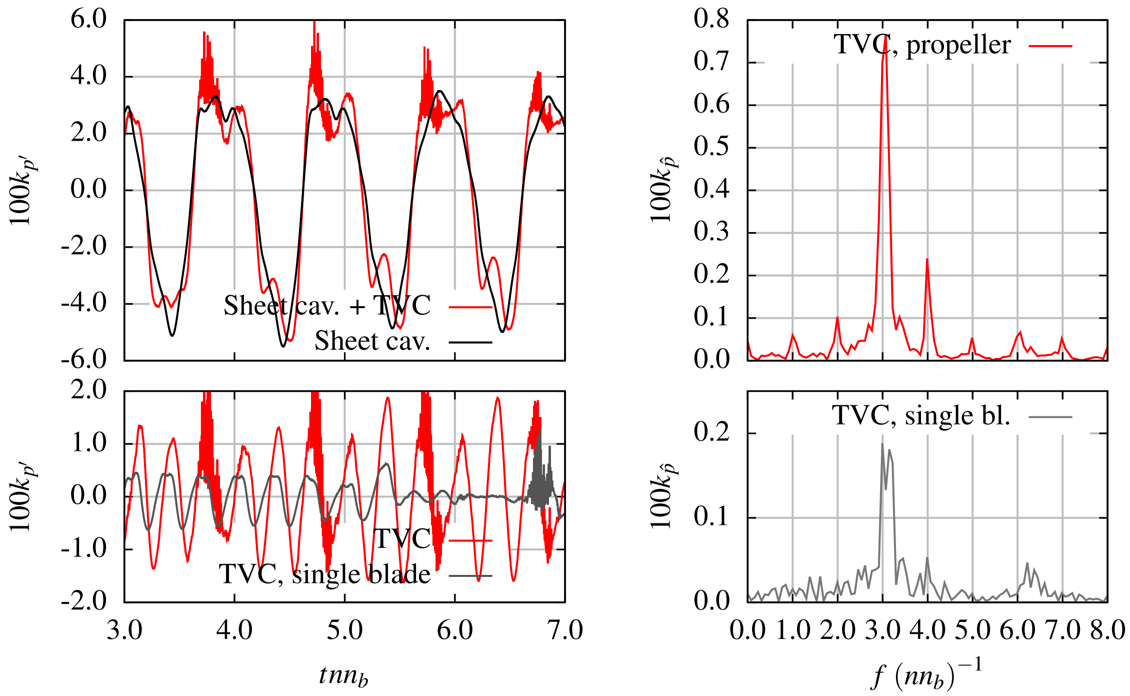

(a) Different contributions to the overall pressure signal.

(b) Frequency spectrum of the pressure signal. Top: TVC complete propeller; bottom: single blade.

Fig. 7.32 Pressure signal due to the cavitating propeller P00B considering sheet cavitation and tip vortex cavitation recorded in a monitoring point directly above the propeller.

Figure 7.31 shows the measured and computed harmonic amplitudes for a variety of monitoring points. Grey columns refer to the simulation results without taking into account tip vortex cavitation, thin black columns are measured values, and coloured columns represent simulation data with enabled tip vortex cavitation model for $r_D = 0.367\mathscr{L}_\text{v}$. Note that different scales are used in the diagrams for first-order and for higher-order fluctuations. To further illustrate the dependence on r_D, intervals (defined by interval boundaries $\top$ and $\perp$) comprising the range of solutions when r_D is varied between $r_D = 0.329\mathscr{L}_\text{v}$ and $r_D = 0.404\mathscr{L}_\text{v}$, have been added to the figure. The overall agreement between experiment and simulation is satisfying; however, one has to keep in mind that the parameter r_D has been adjusted in a way to obtain a best match between simulation and experiment.

A simulation similar to the one for Ship C is conducted for Ship B and propeller P00B using the same setting for the outer domain radius r_D, i.e. r_D is chosen ten times larger than the average cavitation radius. Similar to Figure 7.29, the influence of tip vortex cavitation on the pressure signal is illustrated in Figure 7.32. Looking at the frequency spectrum due to a single cavitating tip vortex in the lower diagram of Figure 7.32b, it can be observed that the hump tends to be located closer to frequencies of $3nn_b$ than to $4nn_b$. As a consequence, the contribution due to all n_b cavitating tip vortices leads to a strong amplification of the third harmonic order, which is shown in the upper diagram of the figure.

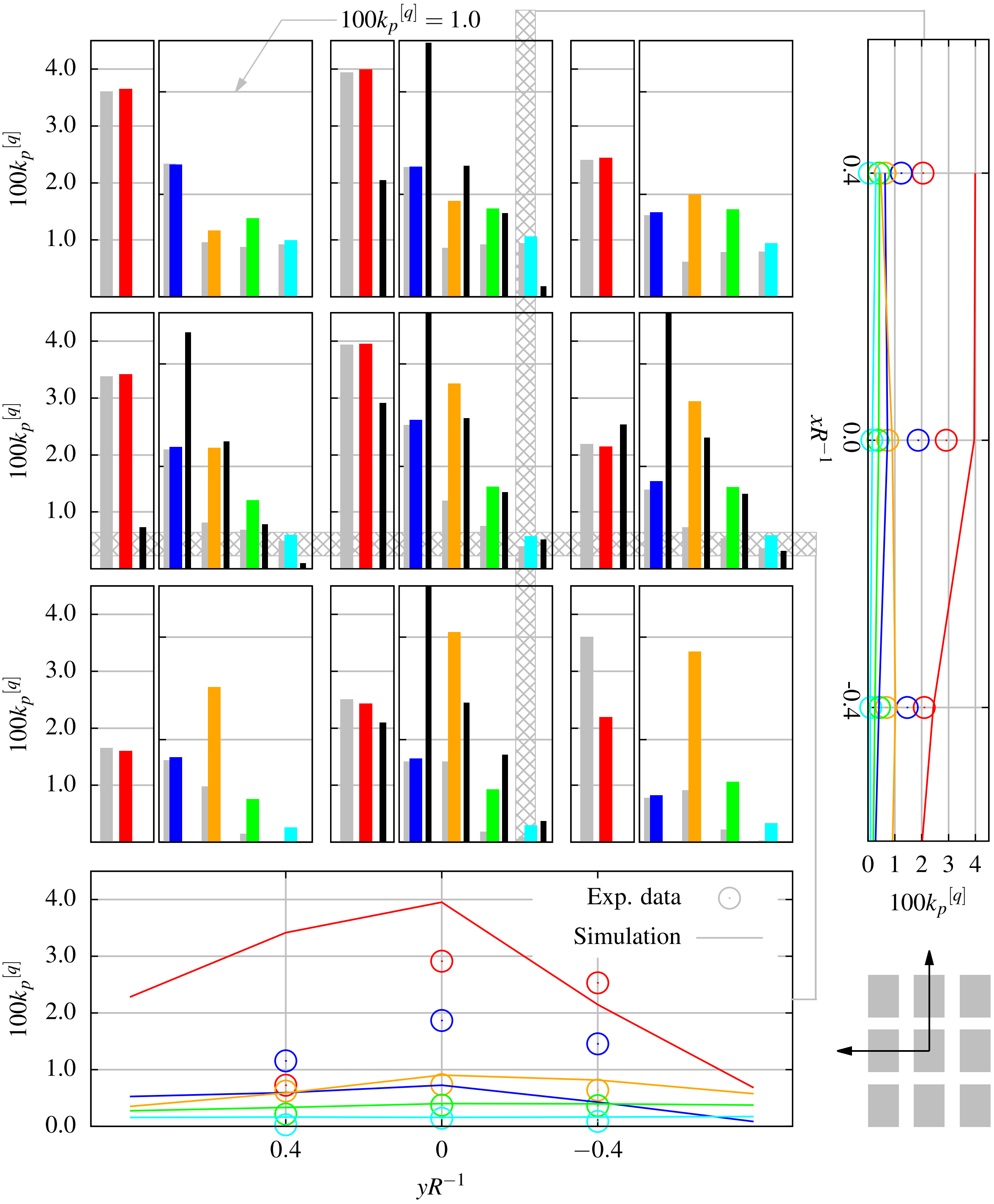

Fig. 7.33 Pressure fluctuations $k_{\hat{p}^{[q]}}$ induced by propeller P00B; comparison between simulation and experiment. See caption of Figure 7.31 for the colour code. No experimental results are available for subdiagrams without thin black boxes.

The agreement between experiment and simulation in case of Ship B and propeller P00B shown in Figure 7.33 is not thoroughly satisfying. On the one hand, higher-order fluctuations with $q = 3,4,5$

are predicted well for most of the monitoring points. On the other hand, the method fails when predicting second-order pressure fluctuations and only partially yields good results for first-order fluctuations. Here, the amplitudes are predicted well for three of five monitoring points.

First-order and second-order pressure fluctuations are dominated by sheet cavitation and most likely the reason for the respective deviations between measurement and simulation can be found in the numerical representation of sheet cavitation. This is discussed in Section 8.1 and Chapter 9.

Chapter 8

Investigation of Scale Effects

Scale effects on cavitation and propeller-induced pressure fluctuations have already been discussed in Section 3.1, where the basic principles of model test techniques were explained. In the present chapter, two selected phenomena related to Reynolds number scale effects are investigated numerically:

(1) aspects of the wake scale effect due to the hull boundary layer on propeller load, sheet cavitation and resulting pressure pulses

(2) the effect of the blade boundary layer thickness on the dynamic behaviour of cavities inside the viscous core of the tip vortex

Both effects are highly relevant in practice. Whereas ship model basins apply corrections to overcome the wake scale effect, no such correction exists for the second type of scale effect. The first effect is investigated and explained for the propeller of the KRISO Container Ship (Ship B; see Table 7.1 in Section 7.1). Then, scale effects on moderate and developing tip vortex cavitation are treated. Here, a generic test scenario on the basis of real propeller flows is applied.

8.1 Wake Scale Effect

8.1.1 Influence on propeller load

In order to illustrate what is meant by wake scale effect, consider Figure 8.1. In subfigure (a), the numerically predicted nominal wake field of Ship B is depicted – in model scale $u_{x,m}V_m^{-1}$ and for the full-scale version $u_{x,s}V_s^{-1}$. Due to the relatively thicker hull boundary layer, the model scale wake field exhibits a much more distinct wake peak region than the full-scale pendant. To examine this further, the wake scale ratios

$$\delta_{u_x} = \frac{u^*_{x,s} - u^*_{x,m}}{u^*_{x,s}}, \quad \delta_{u_y} = \frac{u^*_{y,s} - u^*_{y,m}}{u^*_{y,s}} \quad \text{and} \quad \delta_{u_z} = \frac{u^*_{z,s} - u^*_{z,m}}{u^*_{z,s}} \tag{8.1}$$

of the particular velocity components with $u^*_{\bullet,s} = u_{\bullet,s}V_s^{-1}$ and $u^*_{\bullet,m} = u_{\bullet,m}V_m^{-1}$ are introduced here. For the case of the nominal wake field of Ship B, these quantities are plotted in Figure 8.1b for ${}^r/_R = 0.7$. Apparently, the intensity of the wake scale effect depends on the angular position and on the particular velocity component. The effect upon the axial velocity component u_x is large in the wake peak region around $\varphi = 0°$; however, the vertical and transversal components are even more influenced by the wake scale effect. Strong influences on the transversal component u_y can be observed in the position of 90°, whereas the vertical component u_z experiences the highest impact in the positions of 0° and 180°, and no effect is detectable for $\varphi = 90°$.

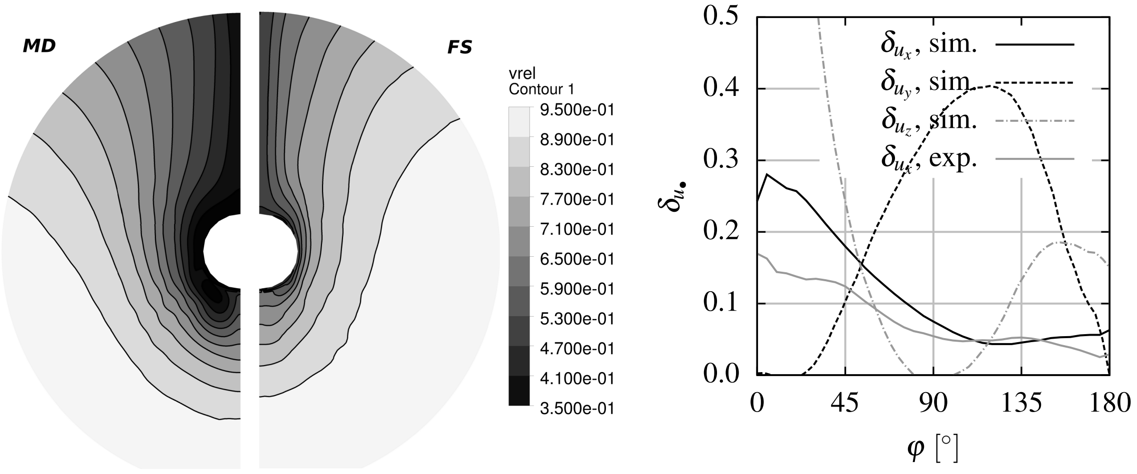

(a) Axial velocity field. **(b)** Wake scale ratios $\delta_{u_\bullet}$.

Fig. 8.1 Comparison between the nominal wake field of the full-scale version of Ship B and the model.

Regarding the propeller load distribution, the role of wake scale effects for the velocity components u_y and u_z is a minor one since the z-component of the flow becomes important in the 90°-position and the y-component in the 0°-position. What remains in this case, is the important wake scale effect on the velocity component u_x.

In order to investigate influences of the wake scale effect on propeller load, sheet cavitation and propeller-induced hull pressure fluctuations, a second simulation campaign is conducted for model scale conditions, in addition to the simulations already carried out for the full-scale version of Ship B (see Chapter 7). To begin with, no cavitation is considered. The scale factor between model and full-scale version is $\lambda = 31.6$. OP00B is used as operation point for the full-scale version $\bullet_s$, and the operation point of the model $\bullet_m$ is initially set in a way that identity of Froude number is fulfilled, i.e. $n_m = \sqrt{\lambda} n_s$ and $V_m = \sqrt{\lambda^{-1}} V_s$. Considering the aforementioned, the fundamental condition of k_T-identity applying for model tests will not be met when V_m is used as the advance speed for the model. Therefore, the advance speed of the model has to be increased to a value of V'_m until the condition $k_{T,m} = k_{T,s}$ is fulfilled. Fulfilling k_T-identity exactly requires an iterative procedure.

Alternatively and with less effort, the corrected model speed can be obtained by

$$V_m' \approx \kappa_m V_m \quad \text{with} \quad \kappa_m = \frac{\overline{u}_{x,s}}{V_s}\frac{V_m}{\overline{u}_{x,m}}, \tag{8.2}$$

where $\overline{u}_{x,s}$ and $\overline{u}_{x,m}$ are the area-averaged axial velocities in the propeller plane measured for V_s and the uncorrected model advance speed V_m, respectively. In this case, an increase of $\kappa = 1.12$ needs to be applied.

For validation purposes, results obtained by model test experiments involving the use of two dummy models are used (Heinke and Jaksic, 2003): one exhibiting the wake field of the model and the other one emulating the velocity distribution of the full-scale version of the ship. This particular experimental setting allows for studying the influence of the different velocity distributions of the model and full-scale wake field. Both models are equipped with a rudder, which is not accounted for in the simulation.

For non-cavitating flow, the measured thrust coefficient for BP00B (see Table 7.2) is $k_T = 0.172$. In the simulations, $k_{T,m} = 0.173$ $(+1.2\,\%)$ and $k_{T,s} = 0.164$ $(-4.7\,\%)$ are obtained, which is considered to be sufficiently consistent.

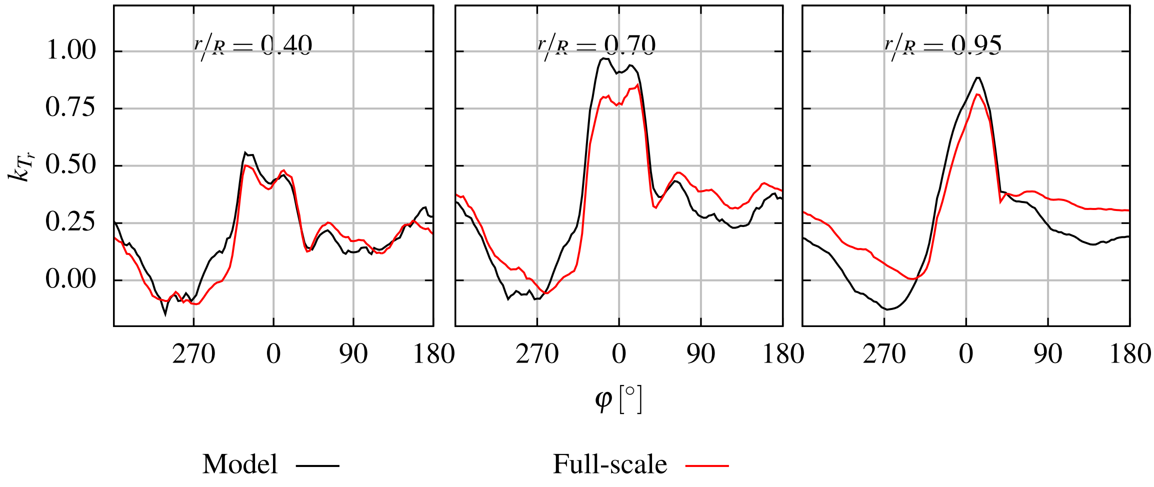

Fig. 8.2 Radial thrust coefficient k_{T_r} for P00B under full-scale and model conditions.

The influence of the wake scale effect on the propeller load for non-cavitating flow is shown in Figure 8.2 in terms of the radial thrust coefficient

$$k_{T_r} = \frac{\mathrm{d}T}{\rho n^2 D^2 c \mathrm{d}r}, \tag{8.3}$$

where $\mathrm{d}T$ is the thrust acting on a small radial portion $\mathrm{d}r$ of the propeller with the chord length $c\,(r)$. It can be seen in the figure that the influence is large for $r/R = 0.7$ in the position $\varphi = 0°$. Note the effect of increasing the model speed from V_m to V_m': Indeed, k_T-identity is nearly achieved, but significant differences occur when the radial and angular load distributions are considered. The blade load is still overestimated by the model in the wake peak zone and underrated for nearly all other blade positions.

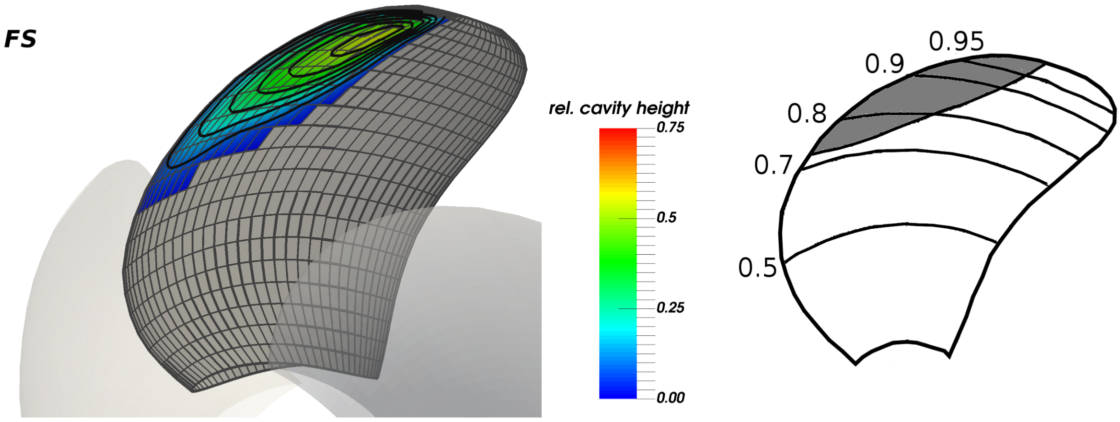

Fig. 8.3 Comparison between predicted and experimentally observed cavity shape and thickness $100\eta D^{-1}$ for full-scale conditions and $\varphi = 0°$.

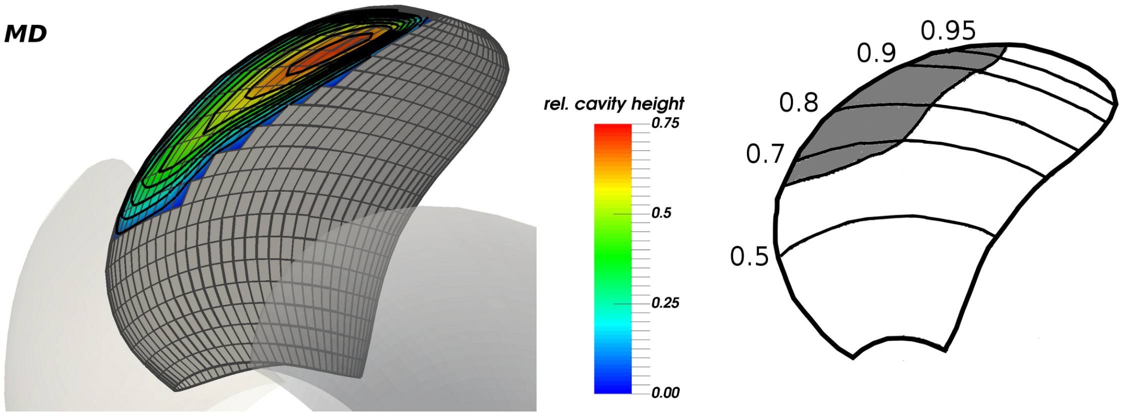

Fig. 8.4 Comparison between predicted and experimentally observed cavity shape and thickness $100\eta D^{-1}$ for model conditions and $\varphi = 0°$.

8.1.2 Sheet cavitation and resulting pressure fluctuations

What is the effect of the difference between model and full-scale wake field on the extent of sheet cavitation? Refer to Figures 8.3 through 8.5, which show sheet cavitation on the blades for the blade angles of $\varphi = 0°$ and $\varphi = 340°$. Particularly for $\varphi = 0°$, the extent of sheet cavitation in the radial direction is different when comparing model and the full-scale scenario. This is shown consistently by both the simulation and the experiments.

First-order pressure fluctuations are predicted in a sufficiently accurate manner for the model. The comparison between experiment and simulation is shown in Figure 8.6. Experiments show a

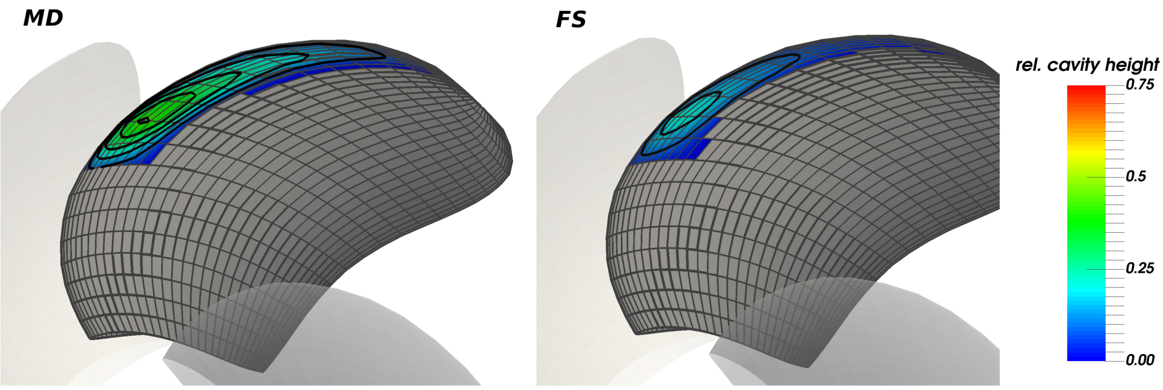

Fig. 8.5 Comparison of cavity shape and cavity thickness $100\eta D^{-1}$ between model (left) and full-scale version (right) for $\varphi = 340°$.

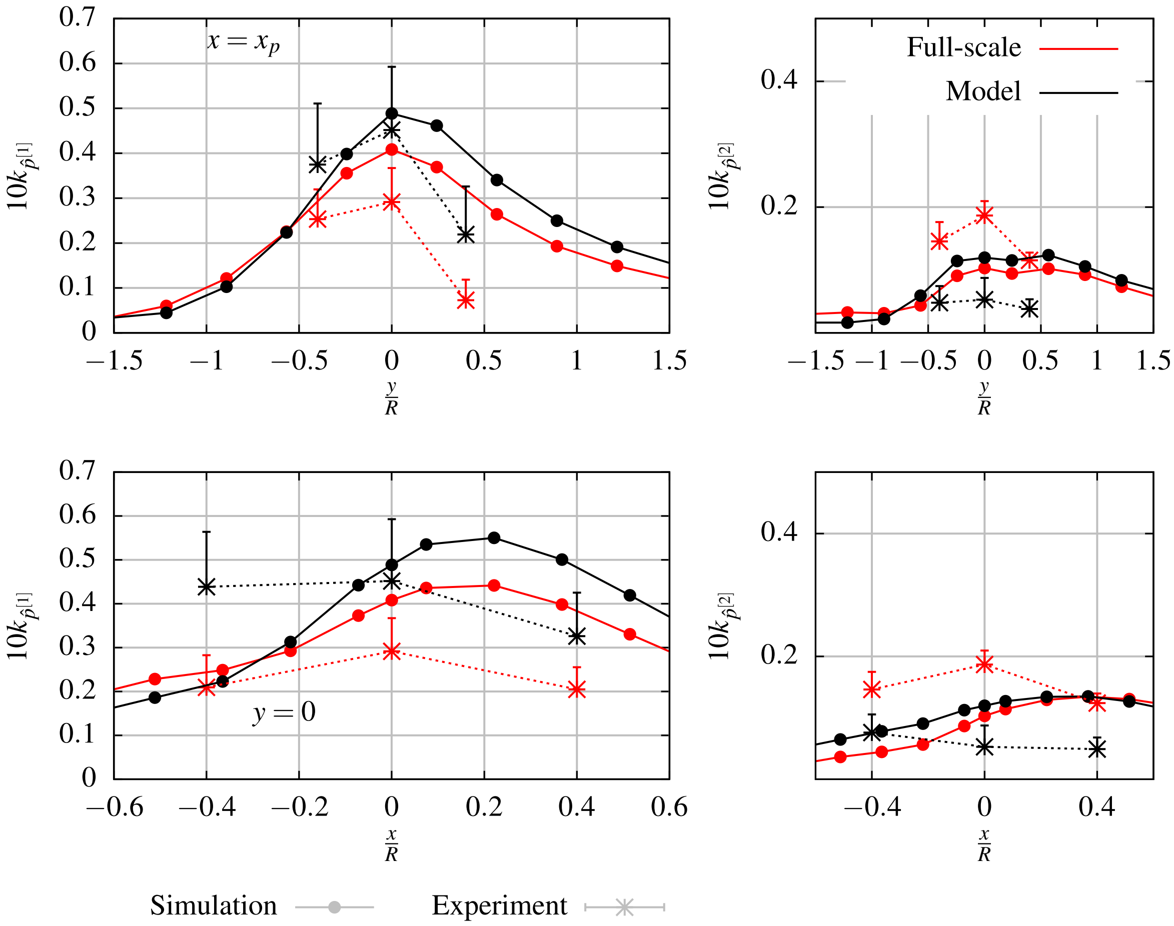

Fig. 8.6 Hull pressure fluctuations induced by P00B including effects of sheet cavitation for model and full-scale conditions; comparison between simulation and experiment. ⊤ and ⊥ mark the interval which measured pressure fluctuations range in when the cavitation number is lowered from $\sigma_{n0.8} = 1.486$ (⊥) to 1.382 (⊤).

significant decrease of first-order amplitudes for the full-scale scenario, which is a trend reproduced in the simulations. With respect to second-order fluctuations, the simulation method fails at predicting. This has already been shown by the results in Section 7.4 and the question arises why.

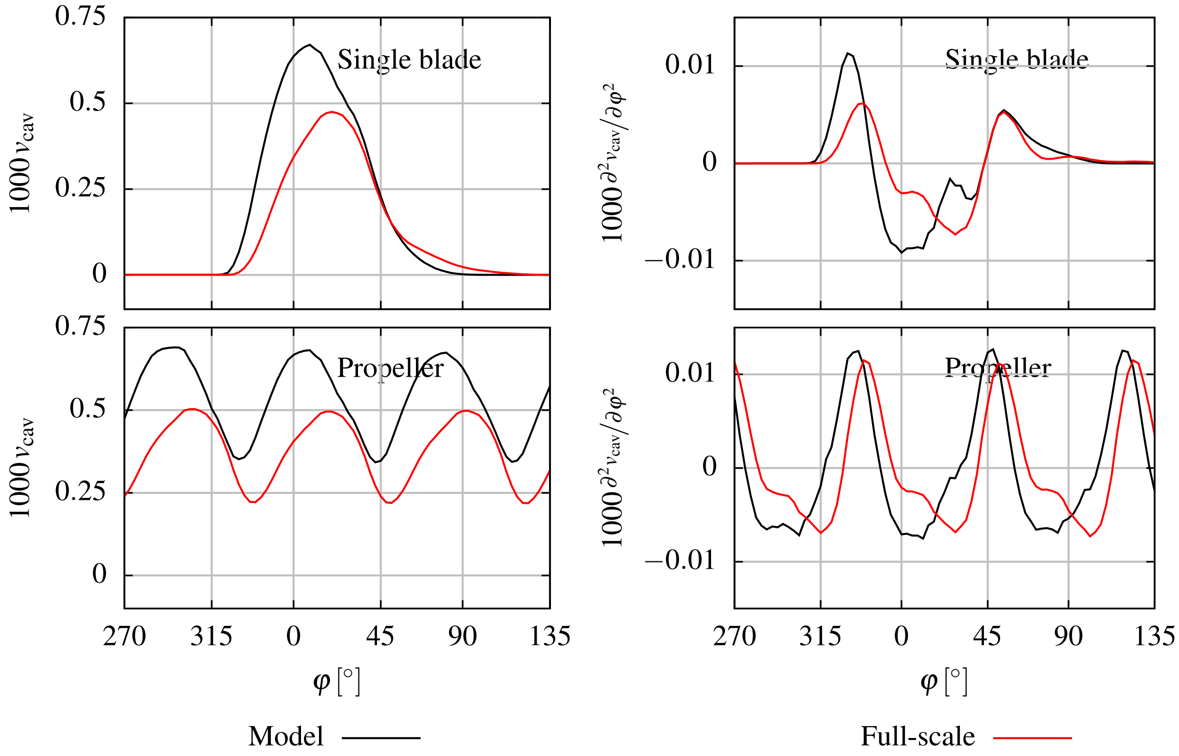

Fig. 8.7 Dimensionless cavity volume $v_{\text{cav}} = V_{\text{cav}} R^{-3}$ and second time derivative of the cavity volume ${}^{\partial^2 v_{\text{cav}}}/_{\partial\varphi^2}$ with $\partial\varphi \propto \partial t$; comparison between model and full-scale conditions.

The simulation results with respect to the extent of sheet cavitation for the model and the full-scale scenario appear to be plausible all in all and are consistent with the experimental observations. It is thus helpful to have a closer look at the unsteady cavitation volume plotted in the left diagrams of Figure 8.7 and to recall the explanations made in Section 2.6. There, it has been shown that two features of the unsteady sheet cavitation volume are especially important: the life span T_{lc} of the cavitation volume and the final phase of the shrinking process where the second time derivative of the cavitation volume can get large. Consider now the upper left diagram in the figure, depicting the unsteady cavitation volume of a single blade. Clearly, it is plausible that the maximum cavitation volume of the model is larger than for the full-scale case. However, the shrinking process of sheet cavitation for the full-scale case (red curve) can be characterised by a gentle decay than by quick disappearance. Such a behaviour differs from the typical shrinking and disappearance of sheet cavitation shown in Section 2.6.

Due to the less pronounced wake peak of the full-scale ship, one would expect a shorter life span T_{lc} of sheet cavitation for the full-scale scenario. This is also encouraged by the angular blade load distribution shown in Figure 8.2, especially for ${}^{r}/_{R} = 0.95$. Indeed, the growing process sets in later, but owing to the overly smooth decay, the life span of the full-scale sheet cavitation is even longer than for the model case. This leads to underestimated second-order pressure fluctuations. Insofar, the simulation results are consistent, and one is left with finding an explanation for the representation of the cavity volume evolution given in this particular case. It can be speculated that probably the applied pressure recovery model handling the flow at the sheet cavitation closure (see Section 4.2) yields to an inaccurate representation of the shrinking process of the cavitation volume (see Section 9.2 for a further discussion).

8.2 Tip Vortex Cavitation

8.2.1 Relation between viscous core radius and Reynolds number

It has been shown in Section 2.4.1 that the trailing vortex of a lifting surface originates from the rolled-up shear layer shed from the trailing edge. The thickness of the shear layer depends on the boundary layer thickness of the lifting surface and so does the structure of the trailing vortex and the tip vortex. McCormick was the first who suggested such a correlation (Arndt, 1995). To be more specific, the following relation between the boundary layer thickness δ on the lifting surface and the viscous core radius r_a of the tip vortex can be formulated (Arndt, 1995):

$$\frac{\delta}{c_0} \propto \left(\frac{r_a}{c_0}\right)^2, \tag{8.4}$$

with c_0 being a representative chord length. Since $\delta \propto c_0 \mathrm{Re}^{-m}$, one obtains

$$\left(\frac{r_a}{c_0}\right)^2 \propto \mathrm{Re}^{-m}. \tag{8.5}$$

The exponent m ranges somewhere between 0.2 and 0.5 depending on whether the flow is laminar or turbulent. For instance, Amromin (2006) proposes a two-range scaling procedure with $m = 0.4$ for low Reynolds numbers and $m = 0.24$ for large ones.

The following example shall illustrate the problem. For propeller flows, a suitable Reynolds number definition is governed by $\mathrm{Re} \propto nDc_0$, and the ratio between full-scale Reynolds number Re_s and the model pendant Re_m is then $\mathrm{Re}_s \mathrm{Re}_m^{-1} = n_s n_m^{-1} \lambda^2$, where λ is the scale ratio. Applying Eq. (8.5) yields $(\lambda r_{a,m})\, r_{a,s}^{-1} = \left(n_s n_m^{-1}\right)^{m/2} \lambda^m$.

Usually, the identity of Froude number is abandoned when carrying out model tests, which allows for setting the number of revolutions of the model propeller n_m as high as possible in order to evoke turbulent flow. Typical values are $D_s = 8.0\,\mathrm{m}$, $\lambda = 30.0$, $n_s = 1.67\,\mathrm{s}^{-1}$ and $n_m = 25.0\,\mathrm{s}^{-1}$. Using these exemplary values and $m = 0.24$, one gets $(\lambda r_{a,m})\, r_{a,s}^{-1} = 1.63$, which means that the relative viscous core radius (i.e. related to the propeller diameter) observed in the model experiment is more than 60 % larger than the one of the full-scale tip vortex. The viscous core radius is a governing parameter of the

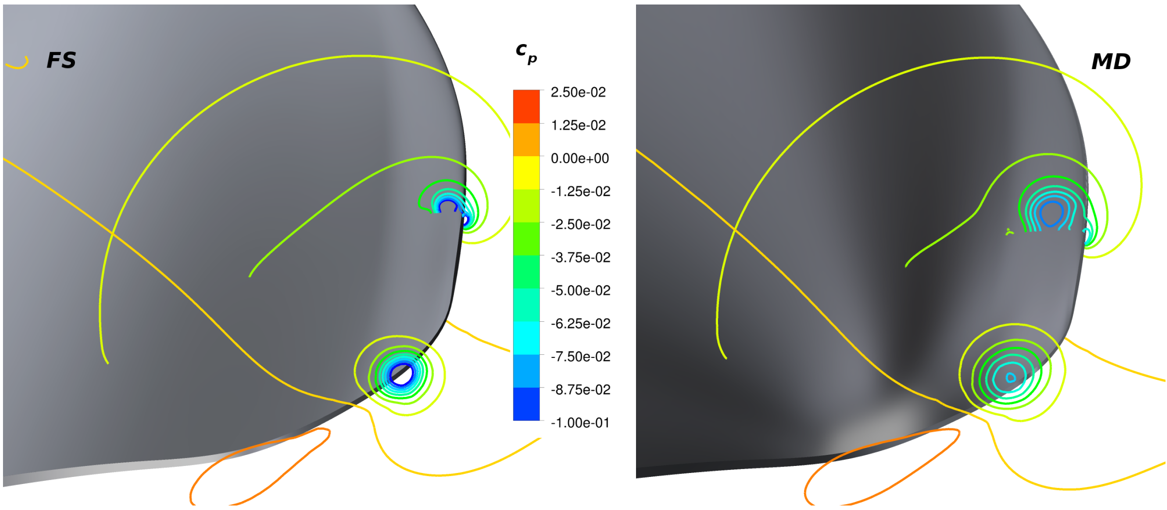

Fig. 8.8 Pressure drop in the core of a propeller tip vortex for P00C and $J = 0.65$, non-cavitating flow conditions; comparison between model (right) and full-scale conditions (left).

vortex flow and this certainly has strong implications on the onset of tip vortex cavitation and on the dynamical behaviour cavities inside the viscous core.

In Figure 8.8, concentric isolines of pressure indicate the presence of vortical structures at the blade tip. The flow simulation has been conducted by means of ANSYS CFX for propeller P00C (see Table 7.1) and non-cavitating flow conditions. It can be clearly observed that, due to the relatively smaller viscous core radius, the pressure drop in the core of the full-scale tip vortex is much more intense.

8.2.2 Influence on cavities inside the viscous core region

In the following, a generic test scenario is developed which allows for studying the influence of viscous effects on moderate and developing tip vortex cavitation. In contrast to the previous part of the thesis in which always developed tip vortex cavitation has been assumed disregarding the actual formation process of the cavity inside the vortex, the focus is now put on a scenario which sets in shortly after the onset of moderate tip vortex cavitation and exclusively involves cases where $r_c < r_a$ in the initial phase and viscous effects play an important role.

It is not the intention to simulate the exact formation mechanisms of tip vortex cavitation. Rather, a large number of nuclei and bubbles is observed in the tip vortex regime and the effect of different viscous core radii is studied. To make the problem feasible for a numerical treatment with the methods available, some simplifications have to be made.

Use is made of VoCav2D-f1 with the limitation that only bubbles in the center of the vortex at $\xi = 0$ can be treated, i.e. any influences acting on the bubbles while transiting to the core are not considered. Furthermore, the two-dimensional momentum equations are applied to model the dynamical behaviour of initially spherical bubbles, i.e. cylindrical ‘bubbles’ are treated here. Nevertheless, it is assumed

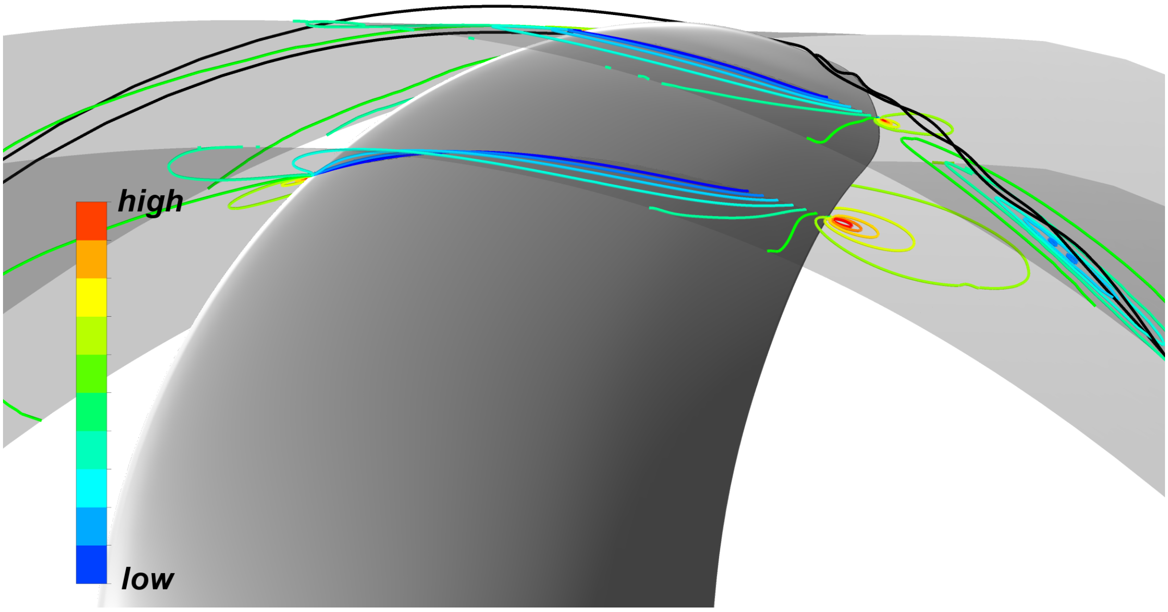

Fig. 8.9 Path of a bubble which is entrained by the tip vortex and pressure field experienced by this bubble.

that the qualitative observations yielded in the following numerical investigation can shed some light on the Reynolds number scale effects on tip vortex cavitation.

The applied test scenario is motivated by Figure 8.9. Two situations are considered:

(1) No coherent forms of cavitation are present on the blade and the tip vortex does not feature a cavitating core at its center. Nuclei and small bubbles travelling along the blade surface in the tip region and being attracted by the tip vortex are considered.

(2) There are minor regions of cavitation at the blade tip and a small cavitating core of the tip vortex may have formed already, which, however, is neglected in the following study. Bubbles may break off the cavity sheet and be absorbed by the tip vortex.

In both situations, the scenario sets in when nuclei and bubbles have passed the trailing edge of the blade. The pressure in this region and imposed on the bubbles will be affected by the stagnation point near the trailing edge (see Figure 8.9). When leaving this region, the bubble will experience a pressure drop. Simultaneously, due to the vortex roll-up, the circulation of the tip vortex increases.

The numerical study carried out here consists of numerous simulations of bubbles with different sizes subjected to a variety of flow conditions. In order to cover a wide range of possible flow conditions, the increase of circulation $\Gamma^\star$ from Γ_{ini} to Γ_b is modelled by a generic function with varying parameters, which is shown in Figure 8.10a. To mimic the pressure drop from stagnation pressure p_{D0} to the surrounding pressure behind the blade tip $p_{D\infty}$, the pressure p_D at $\xi = r_D$ is modelled by the set of functions shown in Figure 8.10b.

Table 8.1 summarises the most important parameters of the numerical study, which consists of five campaigns – one for each of the initial viscous core radii r_{a0} listed in the table. All quantities

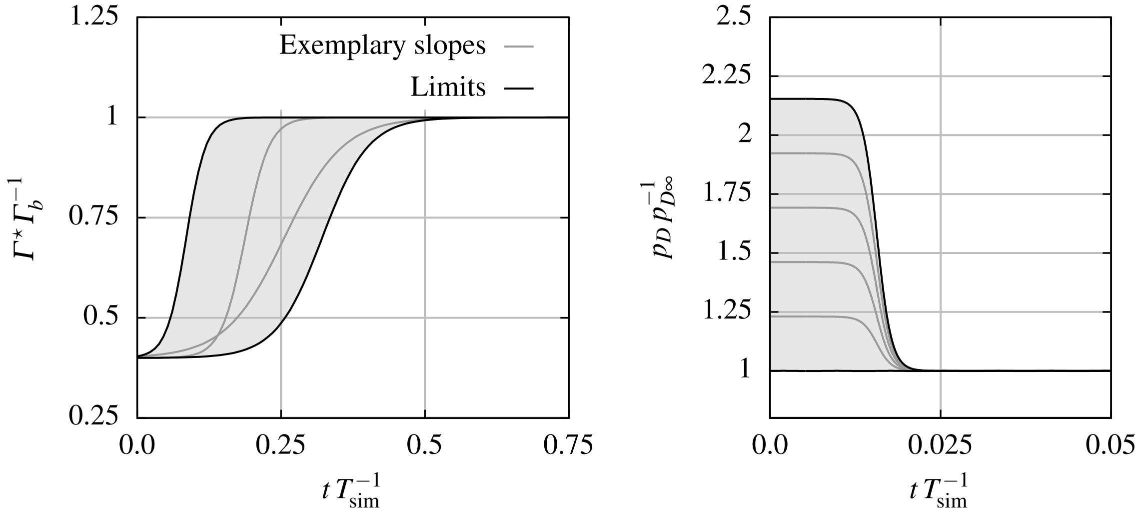

(a) Increase of circulation. **(b)** Drop of surrounding pressure p_D.

Fig. 8.10 Generic increase of vortex circulation and generic pressure drop with varying parameters.

Table 8.1 Relevant conditions and quantities used in the study.

Quantity			Value
Max. circulation	Γ_b	$[\mathrm{m}^2/\mathrm{s}]$	5.0
Ini. circulation	Γ_{ini}	$[\mathrm{m}^2/\mathrm{s}]$	2.0
Ini. core radius	$r_{a0,i}$	[m]	0.03, 0.04, 0.05, 0.06, 0.07
Ini. cavitation radius	r_{c0}	[m]	0.0001 . . . 0.003
	$\dot{r}_{c0}$	$[\mathrm{m}/\mathrm{s}]$	0
Ambient pressure	$p_{D\infty}$	[Pa]	130000.0
Max. stagnation pressure	p_{D0}	[Pa]	280000.0
Outer domain radius	r_D	[m]	0.5

and dimensions have been chosen to be representative for propeller tip flow. Each campaign consists of $N_b = 3000$ bubble simulations, i.e. the total number of simulations accumulates to 15000. For each such simulation, the initial bubble radius r_{c0} is randomly determined. Furthermore, those parameters regulating the increase of circulation and the pressure drop are drawn by lot based on a uniform distribution. These constitute the vortical flow surrounding the bubble. The pressure of non-condensable gases p_{g0} inside the bubble is adjusted in a way that for a given surrounding flow, r_{c0} coincides with the equilibrium cavitation radius at $t^\star = 0$.

Exemplary simulation results are shown in Figure 8.11 for the three cases A, B and C and two viscous core radii. The simulation parameters for these cases are listed in Table 8.2. In the figure, the evolution of the cavitation radius r_c is shown in the upper diagrams. In the lower diagrams, the radiated pressure resulting from the oscillation of the cavitation radius in terms of ζ (see Eq. 5.29 in

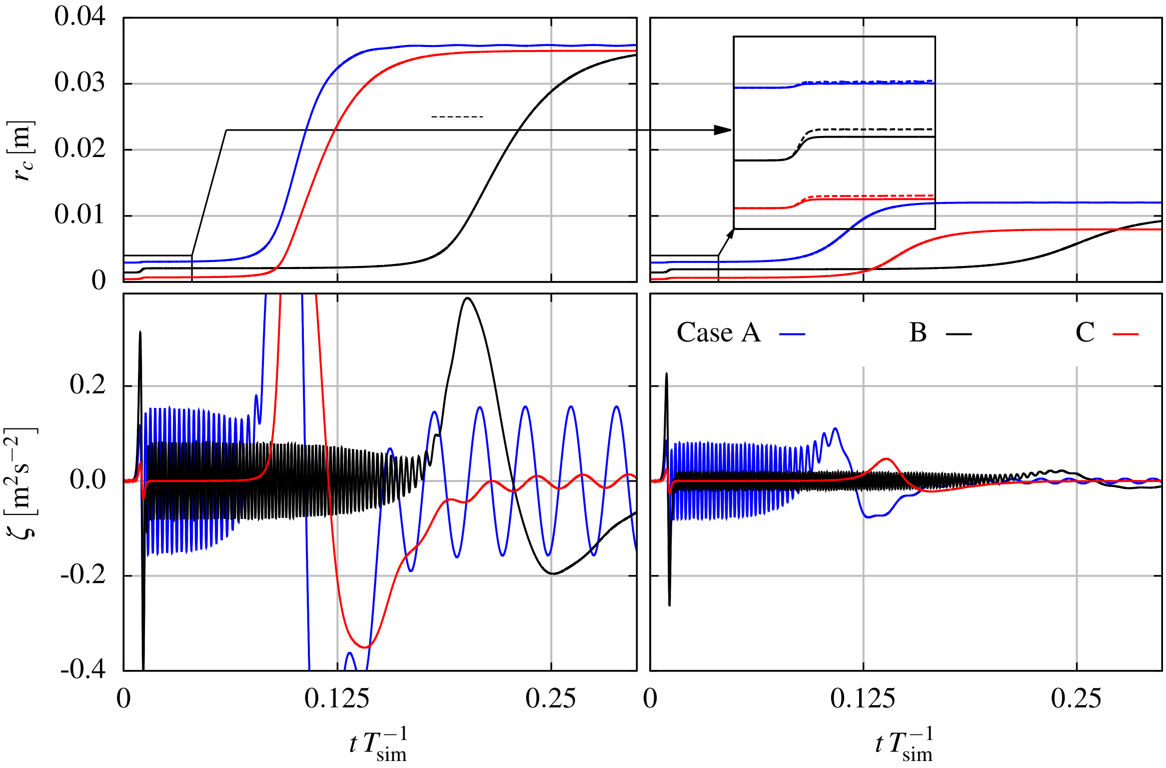

Fig. 8.11 Three exemplary bubble evolutions for the cases listed in Table 8.2. Left: $r_{a0} = 0.04\,\text{m}$; right: $r_{a0} = 0.06\,\text{m}$.

Section 5.5.2) is plotted. The diagrams on the left show results for $r_{a0} = 0.04\,\text{m}$, those on the right for $r_{a0} = 0.06\,\text{m}$ resembling model flow conditions.

In the simulations, a life span of $T_{\text{sim}} = 0.8\,\text{s}$ has been considered, and it can be observed in Figure 8.11 that in the present scenario, a bubble undergoes three phases. The first phase starts directly after the pressure drops from p_{D0} to $p_{D\infty}$, the third phase is characterised by steady state oscillations at the end of its life span when $\Gamma^\star = \Gamma_b$. The second phase refers to the transition from the first to the third phase. For small viscous core radii r_a, it is likely that the cavitation radius grows beyond the viscous core in this phase. Oscillations of the bubble radius are hardly visible in the figure; however, they are present – otherwise there would not be any radiated pressure in terms of ζ. The three exemplary shown cases demonstrate the strong dependency of the evolution of the bubble on the initial conditions and on the viscous core radius.

It can be seen in the magnification that the pressure jump from p_{D0} to $p_{D\infty}$ causes a small but sudden increase of cavitation radius followed by oscillations at high frequencies in the range between 500 Hz and 5000 Hz depending on the particular case. These frequencies are related to broadband propeller noise than to notably higher-order pressure fluctuations.

The three cases considered here reveal the influence of the viscous core radius on the behaviour of the bubble. Oscillations are effectively damped by a larger viscous core radius and also the final mean cavitation radius at the end of the simulation is smaller in this case.

Table 8.2 Initial cavitation radius and flow conditions for the three cases shown in Figure 8.11.

Case	Colour	r_{c0} [m]	r_{a0} [m]	$^{t}/_{T_{\mathrm{sim}}}$ when $\Gamma^{\star} \geq$		$p_D p_{D\infty}^{-1}$
				$105\,\%\,\Gamma_{\mathrm{ini}}$	$99\,\%\,\Gamma_{\mathrm{b}}$	
A	blue	$2.935 \cdot 10^{-3}$	0.04, 0.06	0.080	0.226	1.048
B	black	$1.426 \cdot 10^{-3}$	0.04, 0.06	0.182	0.478	1.641
C	red	$4.329 \cdot 10^{-4}$	0.04, 0.06	0.058	0.278	1.814

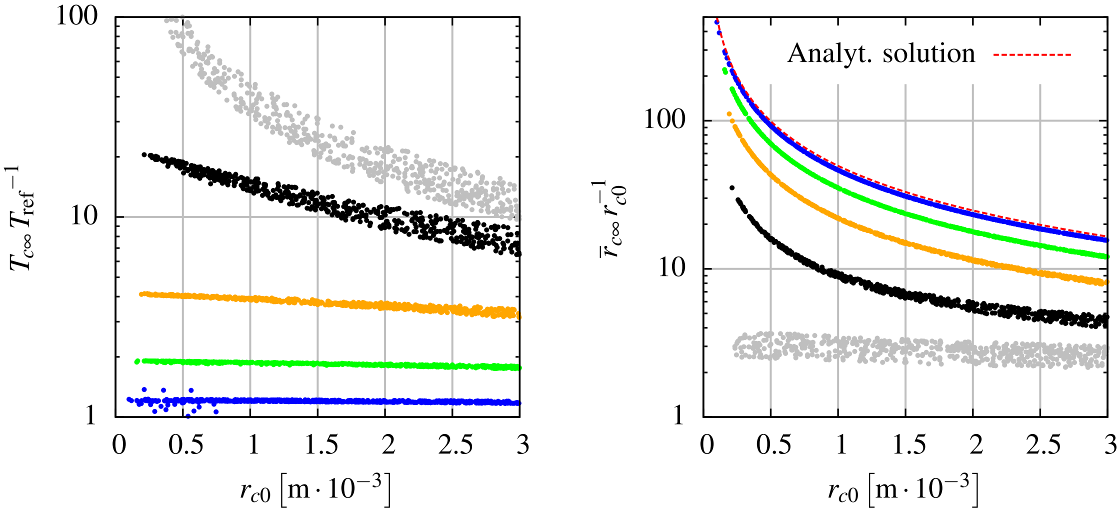

(a) Oscillation period $T_{c\infty}$.

(b) Mean cavitation radius $\overline{r}_{c\infty}$.

Fig. 8.12 Simulation results with respect to oscillation period $T_{c\infty}$ and mean cavitation radius $\overline{r}_{c\infty}$ at the end of the simulation. Every fifth data point is plotted using the following colour code: ● $r_{a0} = 0.03\,\mathrm{m}$; ● $r_{a0} = 0.04\,\mathrm{m}$; ● $r_{a0} = 0.05\,\mathrm{m}$; ● $r_{a0} = 0.06\,\mathrm{m}$; ● $r_{a0} = 0.07\,\mathrm{m}$.

To address this problem in a more systematic manner, the focus is now put on the steady state oscillations in the third phase of the bubble's life. In Figure 8.12, simulation results of all bubbles in terms of oscillation period $T_{c\infty}$ and mean cavitation radius $\overline{r}_{c\infty}$ are shown. They are made dimensionless by the analytical oscillation period T_{ref} given by Eq. (2.19) in Section 2.4.2 using $\overline{r}_{c\infty}$ as cavitation radius and the initial cavitation radius r_{c0}, respectively. Additionally, the analytical equilibrium cavitation radius according to Eq. (2.22) has been plotted in Figure 8.12b. Five distinctive point clouds can be seen, each associated to a certain viscous core radius. A clear tendency can be asserted: the smaller the viscous core radius, the less the influence of viscosity and the less the difference between analytical and numerical solution. Also consider the scattering of the point clouds. In the case of the small viscous core radius $r_a = 0.03\,\mathrm{m}$ (blue point clouds in the figures), there is almost no scattering, which indicates a weak dependency on initial conditions, i.e. the final state of the bubble is always the same. On the contrary, when examining the results for $r_a = 0.07\,\mathrm{m}$ (grey point cloud), the final state is strongly affected by initial conditions.

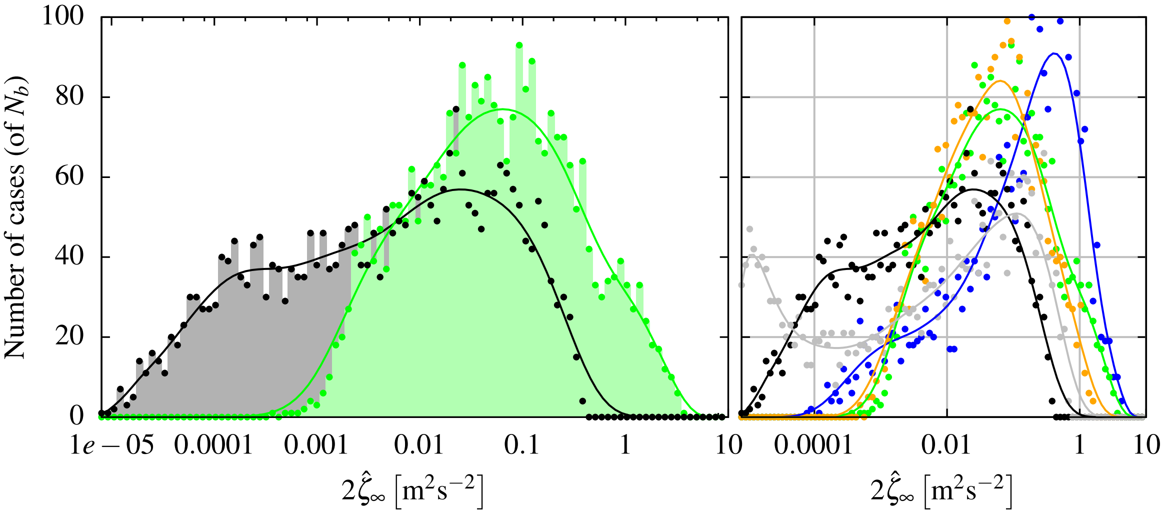

Fig. 8.13 Radiated pressure of a bubble $\hat{\zeta}_\infty$ for various flow conditions at the end of the simulation evaluated in a histogram. N_b is the number of simulated bubbles per campaign. The color code used is explained in the caption of Figure 8.12.

The influence on the radiated pressure in terms of $\hat{\zeta}_\infty$ is depicted in Figure 8.13. For each viscous core radius, a histogram with logarithmic bin width has been generated. In the left part of the figure, the two histograms for $r_a = 0.04\,\text{m}$ (green) and $r_a = 0.06\,\text{m}$ (dark grey/ black) are shown. In the right part, the results with respect to all five core radii are presented; however, for clarity, only the best-fit curves are plotted. Apparently, large amplitudes of radiated pressure are effectively prevented by larger viscous core radii.

Caution is advised when drawing conclusions with respect to higher-order pressure fluctuations as addressed in Section 7.4. As already highlighted at the beginning of this section, the situation addressed here is different: Here, a small tip vortex cavity, i.e. a bubble or a nucleus, is initialised with equilibrium radius, and oscillations are exclusively excited by an imposed change of the surrounding vortical flow, leading to much weaker radiated pressure disturbances at relatively high frequencies compared to the case where fully developed tip vortex cavitation and interaction with sheet cavitation are involved.[1] This scenario reflects the conditions of moderate or developing tip vortex cavitation in an idealised manner – a situation in which a strong dependence on viscous effects can be asserted.

---

[1] Reynolds number scale effects (i.e. the influence of the viscous core radius) on developed propeller tip vortex cavitation and resulting pressure fluctuations have been recently investigated by Gosda et al. (2018) by means of a generic propeller flow case. In the study, the `f1`-formulation has been applied for simulating tip vortex cavitation.

Chapter 9

Discussion and Conclusions

In this final chapter, achievements are summarised, results are discussed and proposals with respect to future developments are made.

9.1 Summary of Important Results and Findings

The aim of the present thesis was to develop a simulation method for the prediction and investigation of higher-order hull pressure fluctuations induced by cavitating propellers, i.e. fluctuations occurring with blade frequency nn_b and multiples $q \geq 2$ of it. It has been hypothesised that the interaction between sheet cavitation and tip vortex cavitation is primarily responsible for notable pressure fluctuations of higher order.

Two container vessels have been investigated by the developed method with respect to cavitating and non-cavitating propeller flow as well as induced hull pressure fluctuations. In addition, the propeller flow of a ConRo vessel has been simulated with respect to propeller flow and non-cavitating pressure fluctuations. A comparison to full-scale measurement data has been conducted for this case. The overall agreement with experimental results, especially for higher-order pressure fluctuations induced by the cavitating propeller, is very promising. However, there are still some shortcomings that indicate the method needs to be further improved in order to be entirely applicable to industrial propeller design. Apart from this, the following important results shall be emphasised:

(1) The results obtained indicate that this study's hypothesis can be accepted as true: Notable higher-order pressure fluctuations originate from the interaction between sheet cavitation and tip vortex cavitation. Sheet cavitation in the tip region extending beyond the trailing edge of the blade leads to a widening of the cavitating tip vortex. This can be primarily observed when the propeller blade traverses the wake peak region. Portions of the tip vortex originating in this phase undergo strong pulsations and effectively radiate pressure disturbances. On the contrary, as shown by the simulation results presented in Section 5.5.2, a cavitating tip vortex performing only small oscillations around the equilibrium cavitation radius does not contribute to pressure fluctuations in a significant manner.

(2) Two aspects of scale effects due to different Reynolds numbers of model and full-scale ship have been investigated. The results can be summarised as follows:

   - Sheet cavitation on the propeller blades is strongly affected by the wake scale effect, leading to lower first-order pressure fluctuations for the full-scale ship than predicted for the model, in general. Higher-order pressure fluctuations are also influenced by sheet cavitation dynamics. This will be discussed in the next section.
   - Smaller Reynolds numbers lead to a relatively thicker boundary layer on the blade of the model propeller and consequently to a relatively larger viscous core radius of the tip vortex. The simulations carried out show that this especially affects the formation process of tip vortex cavitation and smaller bubbles being present in the viscous core, i.e. cases with $r_c < r_a$.

The question may arise how reliable the numerical results and the presented method are. Because only conventional propeller flows at moderate operation conditions as observed in the present cases are considered, special issues such as vortex bursting or vortex–vortex interaction are excluded from the following discussion.

9.2 Further Discussion of the Results

The simulation tool introduced in this study is a combination of three numerical methods being combined by adequate interfaces. It is assumed that each method on its own is sufficiently accurate. ANSYS CFX is a validated commercial code and the assumption may hold for it. The applied panel code *pan*MARE has been tested several times in the present scope of application as well.

In the case of the tip vortex cavitation model, the situation is not entirely clear, since a validation has only happened indirectly by comparing predicted and measured pressure fluctuations which is affected by some uncertainties. But there are some more indications speaking for the validity of the tip vortex cavitation model. With respect to VoCav2D, the solution method for the momentum equations for a single vortex segment, experimental results provided by Choi and Ceccio (2007) could be reproduced well using the f1-formulation for the case $r_c, r_{c0} < r_a$ (see Section 5.5). Furthermore, the method provides results similar to those presented by Bosschers (2009c). These results refer to a single vortex segment – but what about the entire cavitating tip vortex? Apart from the indirect validation by considering higher-order pressure fluctuations, the rules of thumb given in Section 2.6 can provide a basis for estimating the plausibility of the results. By means of Eq. (2.24), the frequency range of oscillations of the cavitation radius can be roughly estimated and the respective estimate agrees well with the numerical predictions. Furthermore, comparisons with analytical formulae disregarding the effect of viscosity have been made throughout the thesis wherever possible (see Sections 5.5 and 8.2). It could be consistently shown that for cases with small viscous core radius, the numerical results tend against the analytical results.

In the following, some problems concerning the overall simulation method will be addressed which may attract a critical discussion and should be considered in future work:

(1) The most critical issue with respect to modelling tip vortex cavitation by a quasi two-dimensional approach is the need of defining the outer radius of the vortex flow domain r_D. Since r_D is an argument of the ln-function in the governing Rayleigh-Plesset equation (5.9), it is not possible to set r_D to infinity. Hence, an appropriate value has to be found, which is problematic since there is apparently no physically motivated rationale to find a particular value. In the present work, r_D has been chosen in a way that is approximately ten times the average cavitation radius of the tip vortex. Using this value, a good agreement between simulated and measured pressure fluctuations could be obtained.

(2) The interaction between tip vortex cavitation and sheet cavitation in the blade tip region has been approximated by initialising the cavitation radius with half of the cavity thickness at the trailing edge or the equilibrium cavitation radius, whichever is larger. This may approximate the effect of how oscillations of the cavity inside the tip vortex are excited. However, the full interaction cannot be captured by such a simplified approach. More clarification is required in order to fully understand the complex flow pattern in the blade tip region. Scale effects may also play an important role here, which in turn will affect the behaviour of tip vortex cavitation and thus hull pressure fluctuations.

(3) Initial values for the tip vortex cavitation model are obtained by detailed RANS simulations of the blade tip flow. This is deemed necessary because the solution for the flow in the propeller tip region obtained by panel methods is not accurate enough. In order to reduce the computational effort, steady state RANS simulations for representative propeller loads are carried out. It remains questionable if these conditions are entirely representative for the inhomogeneous wake field the propeller is operating in. Furthermore, for the sheet cavitation volume and consequently for the cavity thickness at the trailing edge, it is shown by Falcão de Campos et al. (2006) that a phase error is introduced by the present quasi steady procedure. Most likely, the ratio γ_{ini} between initial circulation and bound blade circulation is also affected by this type of error. This aspect requires further clarification.

(4) Details of the roll-up process have not been taken into account. Instead, the vortex roll-up has simply been predetermined by involving heuristics to a certain extent. Furthermore, the full-scale flows considered here are most likely of a turbulent nature. These effects have also been disregarded when modelling tip vortex cavitation.

(5) It has been observed during the experiments that remainders of the disintegrating sheet cavitation surround the main tip vortex cavity in a flow region close to the propeller tip. In the f2-formulation, these are taken into account by a number of spherical bubbles placed around the vortex axis, and their presence is assumed to reduce the ambient density from ρ to $\rho^{\star}$. The influence of the reduced density on $r_c(t)$ is shown in Section 5.5. Certainly, this is a gross

simplification of the real flow conditions since a close look at the flow in this region reveals that remainders of the sheet cavitation are not whirring randomly. Rather, secondary vortex structures become visible (whereof the re-entrant jet vortex mentioned in Section 2.5 is the most prominent representative), each attracting agglomerations of smaller bubbles. These smaller vortices merge with the tip vortex. The role of these secondary vortex structures with respect to pressure fluctuations in the considered frequency range is not clear. Furthermore, the initial bubble distribution constitutes an additional parameter of the model which has to be determined. With respect to this, little information is available.

(6) It has been shown in Section 2.6 that growth and shrinkage of sheet cavitation can affect higher-order pressure fluctuations. The numerical flow simulations made for the KRISO Container Ship (Ship B) reveal a larger deviation between measured and calculated second-order pressure fluctuations for full-scale conditions. In Section 8.1, the unsteady sheet cavitation volume has been depicted in Figure 8.7. An untypical behaviour during the shrinking phase can be seen. Probably, the underlying model for sheet cavitation integrated in the panel method is not exact enough to accurately capture the shrinking process. This may be due to the pressure recovery model applied to mimic the flow in the vicinity of the cavity closure (see Section 4.2). Indications justifying this assumption are given by Dang and Kuiper (1998) who emphasise the importance of taking into account the re-entrant jet dynamics. According to them, the treatment of the flow in the closure region of sheet cavitation has an effect upon the calculated cavitation volume.

(7) In the experimental campaigns, a rudder was attached to the dummy model which has not been included in the numerical model. The effect of the rudder is twofold. On the one hand, the tip vortex gets significantly disturbed when it impinges the rudder surface. On the other hand, the propeller load is influenced by the presence of the rudder (Kracht, 1992).

9.3 Recommendations for Future Work

Based on the issues listed above, some recommendations can be made for future work. With respect to modelling, the most urgent improvements are discussed in the following.

(1) More clarity on the outer domain radius r_D should be attained. Either the current choice of r_D has to be confirmed by more experimental data or – even better – a formulation of the tip vortex cavitation model has to be found without this parameter. This is generally the case for compressible flow (Choi et al., 2009) or for a three-dimensional flow situation. For instance, if oscillations of a cavitating vortex ring are considered, this parameter does not occur in the respective equation (Franc and Michel, 2005, pp. 227ff). A solution for a helical vortex is not known to the author, but such a solution could possibly be figured out. Instead of cylindrical vortex segments, segments of the helix could then be modelled. Beyond this, further improvement could be obtained by an entirely three-dimensional approach.

(2) As sheet cavitation also plays an important role for higher-order pressure fluctuations and is the determining part of first-order fluctuations, some effort should be devoted to the improvement of sheet cavitation modelling. In particular, the treatment of the sheet cavitation closure by the panel method does not seem to be satisfactory now. Modelling effects due to the re-entrant jet as proposed by Dang and Kuiper is complicated for three-dimensional geometries. Additionally, a relatively fine panel mesh is needed for the computations that has to be adapted during the iteration process. Furthermore, the accuracy of the solution near the blade tip should be improved.

(3) Alternatively, instead of using a panel method to simulate the propeller flow including sheet cavitation, this could be done by the RANSE solver. The viscous flow domain would then not only contain the hull but also the propeller. Auxiliary RANS simulations of the propeller flow which are necessary when the current approach is applied, could be bypassed and along with it the problems discussed under point 2 in the previous section. The overall computational effort would not be significantly larger. However, a reliable procedure is needed which automatically analyses the tip flow in order to continuously generate input parameters for the tip vortex cavitation model.

(4) The influence of the rudder should be considered in future work. Modelling the distortion of the tip vortex when impinging the rudder will be challenging.

Apart from modelling aspects, some effort should be devoted to experimental procedures. Validation of models for propeller cavitation usually happens either indirectly by means of radiated pressure disturbances or by means of a visual comparison of the cavity extent. A significant step towards better validation could be made if the unsteady sheet cavity volume was measured and compared to simulation results. With respect to tip vortex cavitation, the measured unsteady cavitation radius along the vortex axis would be a highly valuable quantity. Attempts to measure cavitation characteristics have already been made by, for example, Damaschke et al. (2013).

9.4 Conclusions

In this work, a hybrid simulation method for the investigation and prediction of hull pressure fluctuations induced by cavitating propellers operating in the effective wake field has been developed and tested. Special attention has been devoted to higher-order fluctuations, i.e. those associated to multiples of the blade frequency. Tip vortex cavitation and its interaction with sheet cavitation have been recognised as major source of these pressure fluctuations. The developed model for tip vortex cavitation is based on a segmentation of the tip vortex, i.e. the actually three-dimensional flow problem is broken down to a two-dimensional flow problem which is much easier to handle.

The overall agreement of the numerical results in terms of pressure fluctuations, cavitation and propeller load is generally satisfying. Especially with respect to higher-order pressure fluctuations, a good agreement could be obtained. However, some shortcomings of the method exist. These have been discussed in Section 9.2 and should be considered as a starting point for future development.

References

M. Abdel-Maksoud, D. Hänel, and U. Lantermann. Modeling and computation of cavitation in vortical flow. *International Journal of Heat and Fluid Flow*, 36(6):1065–1074, 2010.

M. Abdel-Maksoud, T. Rung, S. Yakubov, B. Cankurt, and P. Schiller. KonKav I – Korrelation von Kavitationseffekten unter Berücksichtigung der Wassereigenschaften. Technical report, Hamburg University of Technology, Hamburg, Germany, 2013.

M. Abdel-Maksoud, T. Rung, S. Berger, M. Scharf, S. Völkner, and M. Javanian. KonKav II – Korrelation von Kavitation unter Berücksichtigung des Nachstroms: Numerische Modellierung. Technical Report FDS/013-2014/KonKav-II-1, Hamburg University of Technology, Hamburg, Germany, 2014.

M. Abdel-Maksoud, U. Barkmann, S. Kinnas, L. Lübke, and Y.Tian, editors. *Second Workshop on Cavitation and Propeller Performance – Fourth International Symposium on Marine Propulsors smp'15*, Austin, USA, 2015.

W. Abels. *Zuverlässige Prognose propellererregter Druckschwankungen auf die Außenhaut mittels Korrelation direkter Berechnung*. PhD thesis, Hamburg University of Technology, Hamburg, Germany, 2006a.

W. Abels. Reliable Prediction of Propeller Induced Pulses on the Aftbody by Correlation [of] Direct Calculation. In *6th International Symposium on Cavitation CAV2006*, Wageningen, The Netherlands, 2006b.

J. Ackeret. Über stationäre Hohlwirbel. *Ingenieur-Archiv*, 1(4):339–402, 1930.

P. Alwardt, K.-Y. Chao, W. H. Isay, and N. Westphal. Berechnung der Druckverteilung, der Kavitationserscheinungen sowie der induzierten Druckschwankungen an der Außenhaut für Propeller im Nachstrom. *STG Annual*, 76:423–450, 1982.

E. Amromin. Two-range scaling for tip vortex cavitation inception. *Ocean Engineering*, 33:530–534, 2006.

ANSYS. ANSYS CFX 15.0 Documentation. Technical report, ANSYS Inc., Canonsburg, USA, 2014.

R. E. A. Arndt. *Fluid Vortices*, chapter Vortex Cavitation, pages 731–782. Springer, 1995.

R. E. A. Arndt, C. C. S. Song, M. Kjeldsen, J. He, and A. Keller. Instability of Partial Cavitation: A Numerical/Experimental Approach. In *23rd Symposium on Naval Hydrodynamics*, Val de Reuil, France, 2000.

J.-A. Astolfi, D. H. Fruman, and J.-Y. Billard. A model for tip vortex roll-up in the near field region of three-dimensional foils and the prediction of cavitation onset. *European Journal of Mechanics B/Fluids*, pages 757–775, 1999.

H.-J. Baiter. Advanced Views on Cavitation Noise. In *International Symposium on Propulsors and Cavitation*, Hamburg, Germany, 1992.

H.-J. Baiter, F. Gruneis, and P. Tilmann. An Extended Base for the Statistical Description of Cavitation Noise. In *International Symposium on Cavitation Noise*, New York, USA, 1982.

F. Bakir, R. Rey, A. G. Gerber, T. Belamri, and B. Hutchinson. Numerical and Experimental Investigations of the Cavitating Behavior of an Inducer. *International Journal of Rotating Machinery*, 10: 15–25, 2004.

G. Bark and W. B. van Berlekom. Experimental Investigations of Cavitation Dynamics and Cavitation Noise. In *12th Symposium on Naval Hydrodynamics*, Washington D.C., USA, 1978.

G. K. Batchelor. Axial flow in trailing vortices. *Journal of Fluid Mechanics*, 20(4):645–658, 1964.

L. Berghult. Propeller induced tip vortex noise as function of blade area and blade-tip loading. In *International Conference on Propeller Cavitation NCT'50*, Newcastle, UK, 2000.

J. Bosschers. Investigation of hull pressure fluctuations generated by cavitating vortices. In *First International Symposium on Marine Propulsors smp'09*, Trondheim, Norway, 2009a.

J. Bosschers. Modelling and analysis of a cavitating vortex in 2D unsteady viscous flow. In *7th International Symposium on Cavitation CAV2009*, Ann Arbor, USA, 2009b.

J. Bosschers. Modelling and analysis of a cavitating vortex in 2D unsteady viscous flow. In *9th International Conference on Hydrodynamics*, Shanghai, China, 2009c.

J. Bosschers. On the relation between tonal and broadband content of hull pressure spectra due to cavitating ship propellers. In *9th International Symposium on Cavitation CAV2015*, Lausanne, Switzerland, 2015.

C. E. Brennen. *Cavitation and Bubble Dynamics*. Oxford University Press, New York, USA, 1995.

J. P. Breslin. The Pressure Field Near a Ship Propeller. *Journal of Ship Research*, 1:57–66, 1958.

J. P. Breslin and S. Tsakonas. Marine Propeller Pressure Field Due to Loading and Thickness Effects. *Transactions of the Society of Naval Architects and Marine Engineers*, 67:386–422, 1959.

J. P. Breslin, R. J. van Houten, J. E. Kerwin, and C.-A. Johnsson. Theoretical and Experimental Propeller-Induced Hull Pressure Arising from Intermittent Blade Cavitation, Loading and Thickness. *Transactions of the Society of Naval Architects and Marine Engineers*, 90:111–151, 1982.

R. L. Bristol, J. M. Ortega, P. S. Marcus, and Ö. Savaş. On cooperative instabilites of parallel vortex pairs. *Journal of Fluid Mechanics*, 517:331–358, 2004.

I. N. Bronstein, K. A. Semendjajew, G. Musiol, and H. Mühlig. *Taschenbuch der Mathematik*. Verlag Harri Deutsch, 6th edition, 2005.

B. Budich, S. J. Schmidt, and N. A. Adams. Numerical Investigation of a Cavitating Model Propeller Including Compressible Shock Wave Dynamics. In *Fourth International Symposium on Marine Propulsors smp'15*, Austin, USA, 2015.

J. S. Carlton. *Marine Propellers and Propulsion*. Butterworth-Heinemann Ltd., 1994. ISBN 0 7506 1143 X.

J. S. Carlton and P. A. Fitzsimmons. Cavitation: Some Full Scale Experience of Complex Structures and Methods of Analysis and Observation. In *27th American Towing Tank Conference*, St. John's, Canada, 2004.

G. Chahine. *Fluid Vortices*, chapter Bubble Interactions with Vortices, pages 783–828. Springer, 1995.

J. Choi and S. Ceccio. Dynamics and noise emission of vortex cavitation bubbles. *Journal of Fluid Mechanics*, 575:1–26, 2007.

J. Choi, C.-T. Hsiao, G. Chahine, and S. Ceccio. Growth, oscillation, and collapse of vortex cavitation bubbles. *Journal of Fluid Mechanics*, 624:255–279, 2009.

J.-K. Choi and S. A. Kinnas. Prediction of Unsteady Effective Wake by an Euler Solver/Vortex Lattice Coupled Method. *Journal of Ship Research*, 47(2):131–144, 2003.

N. Damaschke, W. Kröger, S. Borchert, and S. Höhne. KonKav I – Korrelation von Kavitationseffekten unter Berücksichtigung der Wassereigenschaften: Teilprojekt Entwicklung der Messmethoden. Technical report, University of Rostock, Rostock, Germany, 2013.

N. Damaschke, A. Kleinwächter, E. Ebert, and R. Kostbade. KonKav II – Korrelation von Kavitationseffekten unter Berücksichtigung des Nachstroms: Teilprojekt Großausführungsmessung. Technical report, University of Rostock, Rostock, Germany, 2014.

J. Dang and G. Kuiper. Re-Entrant Jet Modelling of Partial Cavity Flow on Two-Dimensional Hydrofoils. In *Third International Symposium on Cavitation CAV1998*, Grenoble, France, 1998.

C. del Pino, L. Parras, M. Felli, and R. Fernandez-Feria. Structure of trailing vortices: Comparison between particle image velocimetry measurements and theoretical models. *Physics of Fluids*, 23: 1–12, 2011.

W. J. Devenport, M. C. Rife, S. I. Liapis, and G. J. Follin. The structure and development of a wing-tip vortex. *Journal of Fluid Mechanics*, 312:67–106, 1996.

A. Eberle, A. Rizzi, and E. H. Hirschel. *Numerical Solutions of the Euler Equations for Steady Flow Problems*, volume 34 of *Notes on Numerical Fluid Mechanics*. Vieweg, Braunschweig, Germany, 1992.

J. W. English. Cavitation Induced Hull Surface Pressures – Measurements in a Water Tunnel. In *RINA Symposium on Propeller Induced Ship Vibration*, London, UK, 1979.

J. A. C. Falcão de Campos, G. Vaz, and J. Bosschers. Influence of the Reduced Frequency on the 2-D Partial Cavitation Behaviour for a Foil in a Gust. In *Sixth International Symposium on Cavitation CAV2006*, Wageningen, The Netherlands, 2006.

N. Fine. *Non-linear Analysis of Cavitating Propellers in Nonuniform Flow*. PhD thesis, Massachusetts Institute of Technology, Cambridge, USA, 1992.

J.-P. Franc and J.-M. Michel. *Fundamentals of Cavitation*. Springer, 2005.

D. H. Fruman, P. Cerutti, T. Pichon, and P. Dupont. Effect of Hydrofoil Planform on Tip Vortex Roll-Up and Cavitation. *Journal of Fluids Engineering*, 117:162–169, 1995.

K. Fujiyama. Numerical Simulation of Ship Hull Pressure Fluctuation Induced by Cavitation on Propeller with Capturing the Tip Vortex. In *Fourth International Symposium on Marine Propulsors smp'15*, Austin, USA, 2015.

M. Gaschler. *Numerical Modelling and Simulation of Cavitating Marine Propeller Flows*. PhD thesis, Hamburg University of Technology, Hamburg, Germany, 2017.

R. Gosda. *Numerical Investigation of the Interaction between a Viscous Line Vortex and a Cylindrical Cavitation Bubble in the Viscous Core Region*. Bachelor thesis, Hamburg University of Technology, Hamburg, Germany, {www.panmare.de → Publications → 2016}, 2016.

R. Gosda, S. Berger, and M. Abdel-Maksoud. Investigation of Reynolds Number Scale Effects on Propeller Tip Vortex Cavitation and Propeller-Induced Hull Pressure Fluctuations. In *10th International Symposium on Cavitation CAV2018*, Baltimore, USA, 2018. [submitted to CAV2018].

S. I. Green. *Fluid Vortices*, chapter Wing Tip Vortices, pages 427–470. Springer, 1995.

E. M. Greitzer, C. S. Tan, and M. B. Graf. *Internal Flow*. Cambridge University Press, Cambridge, USA, 2004.

M. Greve. *Non-viscous calculation of propeller forces under consideration of free surface effects*. PhD thesis, Hamburg University of Technology, Hamburg, Germany, 2015.

M. Greve, K. Wöckner-Kluwe, M. Abdel-Maksoud, and T. Rung. Viscous-Inviscid Coupling Methods for Advanced Marine Propeller Applications. *International Journal of Rotating Machinery*, 2012. doi: 10.1155/2012/743060.

T. Hachmann, M. Abdel-Maksoud, D. Hänel, and U. Lantermann. Application of Vortex Confinement Method in Combination with Two-Way Euler-Lagrangian Coupling Approach for the Prediction of Cavitating Propeller Tip Vortex Flows. In *Second International Symposium on Marine Propulsors smp'11*, Hamburg, Germany, 2011.

D. P. Hart, A. Acosta, and A. Leonard. Observations of Cavitation and Wake Structure of Unsteady Tip Vortex Flows. In *International Symposium on Propulsors and Cavitation*, Hamburg, Germany, 1992.

H.-J. Heinke. The Influence of Test Parameters and Wake Field Simulation on the Cavitation and the Propeller Induced Pressure Fluctuations. In *STG Colloquium on Cavitation*, Hamburg, Germany, 2003.

H.-J. Heinke and D. Jaksic. Untersuchung des Einflusses des Nachstromfeldes (Modell oder Großausführungsnachstrom) auf die Kavitation und die Druckschwankungen am KRISO Containerschiff KS 621. Technical Report 2852, SVA Potsdam, Potsdam, Germany, 2003.

H.-J. Heinke and R. Klose. Acoustic Measurements with the Propeller P1724 in the Full-Scale Wake Field of a 3600 TEU Container Vessel. Technical Report 4465, SVA Potsdam, Potsdam, Germany, 2016.

H.-J. Heinke and H. Richter. KonKav II – Korrelation von Kavitationseffekten unter Berücksichtigung des Nachstroms: Nachstrombeeinflussung durch das Dummymodell. Technical Report 4238, SVA Potsdam, Potsdam, Germany, 2014.

J. L. Hess. Panel Methods in Computational Fluid Dynamics. *Annual Review of Fluid Mechanics*, 22: 255–274, 1990.

E. H. Hirschel. *Recent Contributions to Fluid Mechanics*, chapter Considerations of the Vorticity Field on Wings, pages 129–137. Springer, Berlin, 1982.

E. H. Hirschel. Vortex Flows: Some General Properties, Modelling, Configurational and Manipulation Aspects. In *14th Applied Aerodynamics Conference*, New Orleans, USA, 1996.

T. Hommes, J. Bosschers, and H. W. M. Hoeijmakers. Evaluation of the radial pressure distribution of vortex models and comparison with experimental data. In *9th International Symposium on Cavitation CAV2015*, Lausanne, Switzerland, 2015.

C.-T. Hsiao and G. Chahine. Scaling of Tip Vortex Cavitation Inception for a Marine Open Propeller. In *27th Symposium on Naval Hydrodynamics*, Washington D.C., USA, 2008.

C.-T. Hsiao, J. Ma, and G. L. Chahine. Simulation of Sheet and Tip Vortex Cavitation on a Rotating Propeller Using a Multiscale Two-Phase Flow Model. In *Fourth International Symposium on Marine Propulsors smp'15*, Austin, USA, 2015.

J. Hundemer. *Entwicklung eines Verfahrens zur Berechnung der instationären potenzialtheoretischen Propellerumströmung*. PhD thesis, Hamburg University of Technology, Hamburg, Germany, 2013.

E. Huse. The Magnitude and Distribution of Propeller-Induced Surface Forces on a Single-Screw Ship Model. Technical Report 100, Norwegian Ship Model Experiment Tank, 1968.

E. Huse. Pressure Fluctuations on the Hull Induced by Cavitating Propellers. Technical Report 111, Norwegian Ship Model Experiment Tank, 1972.

IMO. *IMO MEPC.1/Circ.833: Guidelines for the Reduction of Underwater Noise from Commercial Shipping to Address Adverse Impacts on Marine Life*. International Maritime Organization, London, 2014.

W. H. Isay. *Kavitation*. Schiffahrts-Verlag Hansa, Hamburg, 1989.

W. H. Isay. Eine Näherungslösung für das Geschwindigkeits- und Druckfeld eines Flügelspitzenwirbels in turbulenter Strömung. Technical Report 516, Institut für Schiffbau der Universität Hamburg, Hamburg, 1991.

16th International Towing Conference, Leningrad, Russia, 1981. ITTC.

17th International Towing Conference, Gothenburg, Sweden, 1984. ITTC.

18th International Towing Conference, Kobe, Japan, 1987. ITTC.

19th International Towing Conference, Madrid, Spain, 1990. ITTC.

B. Ji, X. W. Luo, R. E. A. Arndt, X. Peng, and Y. Wu. Large Eddy Simulation and theoretical investigations of the transient cavitating vortical flow structure around a NACA66 hydrofoil. *International Journal of Multiphase Flow*, 68:121–134, 2015.

C. Johannsen. Investigation of Propeller-Induced Pressure Pulses by Means of High-Speed Video Recording in the Three-Dimensional Wake of a Complete Ship Model. In *22nd Symposium on Naval Hydrodynamics*, Washington D.C., USA, 1998.

C. Johannsen, E. van Wijngaarden, T. Lücke, H. Streckwall, and J. Bosschers. Investigation of Hull Pressure Pulses Making Use of Two Large Scale Cavitation Test Facilities. In *8th International Symposium on Cavitation CAV2012*, Singapore, 2012.

C. A. Johnsson, O. Rutgersson, S. Olsson, and O. Björheden. Vibration Excitation Forces from a Cavitating Propeller. Model and Full Scale Tests on a High Speed Container Ship. In *11th Symposium on Naval Hydrodynamics*, London, UK, 1976.

T. Kanemaru and J. Ando. Numerical Analysis of Tip Vortex Cavitation on Marine Propeller Using a Simple Surface Panel Method SQCM. In *Fourth International Symposium on Marine Propulsors smp'15*, Austin, USA, 2015a.

T. Kanemaru and J. Ando. Numerical Analysis of Tip Cavitation on Marine Propellers with Wake Alignment Using a Simple Surface Panel Method SQCM. In *9th International Symposium on Cavitation CAV2015*, Lausanne, Switzerland, 2015b.

J. Katz and A. Plotkin. *Low-Speed Aerodynamics*. Cambridge University Press, Cambridge, UK, 2nd edition, 2001.

A. P. Keller and E. A. Weitendorf. A Determination of Free Air Content and Velocity in Front of the Sydney Express Propeller in Connection with Pressure Fluctuation Measurements. In *12th Symposium on Naval Hydrodynamics*, Washington, D.C., 1979.

A. Konno, K. Wakabayashi, H. Yamaguchi, M. Maeda, N. Ishi, S. Soejima, and K. Kimura. On the mechanism of the bursting phenomena of propeller tip vortex cavitation. *Marine Science and Technology*, 6:181–192, 2002.

N. Kornev. *Propellertheorie*. Shaker Verlag, Aachen, Germany, 2009.

A. M. Kracht. On Propeller–Rudder Interaction. In *International Symposium on Propulsors and Cavitation*, Hamburg, Germany, 1992.

G. Kuiper. New Developments around Sheet and Tip Vortex Cavitation on Ships' Propellers. In *4th International Symposium on Cavitation CAV2001*, Pasadena, USA, 2001.

G. Kuiper. Cavitation in Ship Propulsion: Vortex Cavitation. Technical report, Delft Technical University, Delft, The Netherlands, 2012. [Lecture notes].

L. Larsson, B. Regnström, K.-J. Han, G. Bark, and N.Bathfield. Numerical optimisation of propeller-hull configurations at full-scale. *Journal of Marine Engineering and Technology*, 5(1):27–33, 2006.

H. Lee. *Modeling of Unsteady Wake Alignment and Developed Tip Vortex Cavitation*. PhD thesis, The University of Texas at Austin, Austin, USA, 2002.

J.-B. Leroux, J. A. Astolfi, and J. Y. Billard. An Experimental Study of Unsteady Partial Cavitation. *Transactions of ASME*, 126:94–101, 2004.

P. Ligneul. Theory of Tip Vortex Cavitation Noise of a Screw Propeller operating in a Wake. In *17th Symposium on Naval Hydrodynamics*, Washington D.C., USA, 1989.

K. Lucas. *Thermodynamik*. Springer, 2006.

T. Lücke. Untersuchung zur Entstehung und Beseitigung von Propeller Tip Vortex Bursting. In *Statustagung Schifffahrt und Meerestechnik 2006*, Hamburg, Germany, 2006.

T. Lücke. KonKav II – Korrelation von Kavitationseffekten unter Berücksichtigung des Nachstroms: Bordmessungen und Nachstrombeeinflussung durch Liner. Technical Report 1679 (K47-14), Hamburgische Schiffbau-Versuchsanstalt, Hamburg, Germany, 2014.

T. Lücke and C. Johannsen. Modellversuche im HYKAT mit Linern – Messfahrtzustand, Schiff 1 – Projekt: KonKav II. Technical Report K 10-14, HSVA Hamburg, Hamburg, Germany, 2014.

K. Lüders and G. von Oppen. *Lehrbuch der Experimentalphysik: Mechanik, Akustik, Wärme – Band 1*. de Gruyter, Berlin, Germany, 2008.

V. P. Morozov. Theoretical analysis of the acoustic emission from cavitation line vortices. *Journal of Soviet Physics Acoustics*, 19(5):468–471, 1974.

N. Okamura, R. Fujino, and T. Tanaka. An Experimental Investigation of the Mechanism and the Pressure of Counter-Rotating Vortices on a CPP at the Off-Design Condition. In *20th Symposim on Naval Hydrodynamics*, Santa Barbara, USA, 1994.

K.-J. Paik, H.-G. Park, and J. Seo. RANS simulation of cavitation and hull pressure fluctuation for marine propeller operating behind-hull condition. *International Journal of Naval Architecture and Ocean Engineering*, 5:502–512, 2013a.

K.-J. Paik, H.-G. Park, and J. Seo. URANS Simulation of Cavitation and Hull Pressure Fluctuation for Marine Propeller with Hull Interaction. In *Third International Symposium on Marine Propulsors smp'13*, Launceston, Australia, 2013b.

G. Patience. Developments in marine propellers. *Proceedings of the Institution of Mechanical Engineers, Part A: Journal of Power and Energy*, 205:77–88, 1991.

P. Pennings, J. Westerweel, and T. van Terwisga. Cavitation tunnel analysis of radiated sound from the resonance of a propeller tip vortex cavity. *International Journal of Multiphase Flow*, 83:1–11, 2016.

P. C. Pennings, J. Bosschers, J. Westerweel, and T. J. C. van Terwisga. Dynamics of isolated vortex cavitation. *Journal of Fluid Mechanics*, 778:288–313, 2015.

W. R. C. Phillips. The turbulent trailing vortex during roll-up. *Journal of Fluid Mechanics*, 105: 451–467, 1981.

A. E. Raestad. Tip vortex index – an engineering approach to propeller noise prediction. *The Naval Architect*, Jul/Aug, 1996.

H. Richter. Druckimpulsmessungen und Kavitationsbeobachtungen mit dem Modellpropeller HSVA2824 in schiffsähnlicher Zuströmung mit Dummymodell DM78 im Kavitationstunnel. Technical Report 3894, SVA Potsdam, Potsdam, Germany, 2012.

RINA Symposium on Propeller Induced Ship Vibration, London, UK, 1979. RINA.

W. Rodi. *Turbulence Models and Their Application in Hydraulics – A state-of-the-art review*. A. A. Balkema, Rotterdam, The Netherlands, 1993.

H. E. Saunders. *Hydrodynamics in Ship Design*, volume I. The Society of Naval Architects and Marine Engineers, New York, USA, 1957.

H. Schade and E. Kunz. *Strömungslehre*. de Gruyter, Berlin, Germany, 2nd edition, 1989.

M Scharf. Weiterentwicklung eines Modells zur effizienten Simulation partieller Schichtkavitation auf Basis eines parallelisierten Paneelverfahrens. Master's thesis, Technische Universität Hamburg-Harburg, Hamburg, Germany, 2014.

S. Schenke. Assessment of propulsion efficiency for hull-propeller systems. Master's thesis, Hamburg University of Technology, Hamburg, Germany, 2015.

B. Schuiling, F. H. Lafeber, A. van der Ploeg, and E. van Wijngaarden. The Influence of the Wake Scale Effect on the Prediction of Hull Pressure due to Cavitating Propellers. In *Second International Symposium on Marine Propulsors smp'11*, Hamburg, Germany, 2011.

K. W. Shin. DES of Tip Vortex Cavitation. In *19th Numerical Towing Tank Symposium*, St Pierre d'Oléron, France, 2016.

SIMMAN. KRISO Container Ship (KCS), 2008. URL http://www.simman2008.dk/kcs/container.html. [Online; accessed August 2016].

K. T. Skaar and A. E. Raestad. The Relative Importance of Ship Vibration Excitation Forces. In *RINA Symposium on Propeller Induced Ship Vibration*, London, UK, 1979.

H. Söding. Vibrationen von Schiffen I. Technical Report 23, Institut für Schiffbau der Universität Hamburg, Hamburg, Germany, 1987. [Lecture notes].

H. Söding, G. Jensen, M. Abdel-Maksoud, and W. Fricke. Ship Vibrations. Technical report, Hamburg University of Technology, Hamburg, Germany, 2014. [Lecture notes].

T. Stoye. KonKav II – Korrelation von Kavitationseffekten unter Berücksichtigung des Nachstroms: Entwicklung eines Verfahrens zur Bewertung des Großausführungsnachstroms. Technical report, Flensburger Schiffbau-Gesellschaft, Flensburg, Germany, 2014.

H. Streckwall. Numerical Models for Cavitation and Propeller Pressure Fluctuations. In *STG Colloquium on Cavitation*, Hamburg, Germany, 2003.

SVA. Potsdam Propeller Test Case (PPTC), 2017. URL http://www.sva-potsdam.de/pptc-propeller-test-case-verwandte-projekte. [Online; accessed April 2017].

J. A. Szantyr. A Computational Model of the Propeller Cavitating Tip Vortex Interacting with the Rudder. In *6th International Symposium on Cavitation CAV2006*, Wageningen, The Netherlands, 2006.

W. Thompson (Lord Kelvin). Vibrations of a Columnar Vortex. *Philosophical Magazine and Journal of Science*, 10:155–169, 1880.

E. Truckenbrodt. *Fluidmechanik – Band 2*. Springer, Berlin, 1989.

T. van Terwisga, E. van Wijngaarden, J. Bosschers, and G. Kuiper. Achievements and challenges in cavitation research on ship propellers. *International Shipbuilding Progress*, 54:1–22, 2007.

T. J. C. van Terwisga, E. van Wijngaarden, J. Bosschers, and G. Kuiper. Cavitation Research on Ship Propellers – A Review of Achievements and Challenges. In *6th International Symposium on Cavitation CAV2006*, Wageningen, The Netherlands, 2006.

E. van Wijngaarden. *Prediction of Propeller-Induced Hull-Pressure Fluctuations*. PhD thesis, Maritime Research Institute Netherlands, Wageningen, The Netherlands, 2011.

E. van Wijngaarden, J. Bosschers, and G. Kuiper. Aspects of the Cavitating Propeller Tip Vortex as a Source of Inboard Noise and Vibration. In *ASME Fluids Engineering Division Summer Meeting and Exhibition FEDSM2005*, Houston, USA, 2005.

G. Vaz. *Modelling of Sheet Cavitation on Hydrofoils and Marine Propellers using Boundary Element Methods*. PhD thesis, IST, UTL, Lisbon, Portugal, 2005.

F. Vesting. *Marine Propeller Optimisation – Strategy and Algorithm Development*. PhD thesis, Chalmers University of Technology, Gothenburg, Sweden, 2015.

W. S. Vorus. *Vibration*. The Principles of Naval Architecture. The Society of Naval Architects and Marine Engineers, Jersey City, USA, 2010.

G. Wang. The influence of solid boundaries and free surface on propeller-induced pressure fluctuations. *Norwegian Maritime Research*, (2):34–46, 1981.

E. A. Weitendorf. *Kavitationseinflüsse auf die vom Propeller induzierten Druckschwankungen*. PhD thesis, Technische Universität Hannover, Hannover, Germany, 1976.

E. A. Weitendorf. Der kavitierende Spitzenwirbel eines Propellers und die daraus resultierenden Druckschwankungen. *Schiffstechnik*, 24:237–251, 1977.

Wikimedia Commons. Different types of cavitation around a propeller, 2008. URL https://commons.wikimedia.org/wiki/File%3ACavitation.svg. [Online; accessed February 2017].

Wikipedia Encyclopedia. Poisson summation formula, 2017. URL https://en.wikipedia.org/wiki/Poisson_summation_formula. [Online; accessed February 2017].

D. C. Wilcox. *Turbulence Modeling for CFD*. DCW Industries, La Cañada, USA, 3rd edition, 2006.

R. Williams, A. J. Wright, E. Ashe, L. K. Blight, R. Bruintjes, R. Canessa, C. W. Clark, S. Cullis-Suzuki, D. T. Dakin, C. Erbe, P. S. Hammond, N. D. Merchant, P. D. O'Hara, J. Purser, A. N. Radford, S. D. Simpson, L. Thomas, and M. A. Wale. Impacts of anthropogenic noise on marine life: Publication patterns, new discoveries, and future directions in research and management. *Ocean and Coastal Management*, 115:17–24, 2015.

C. H. K. Williamson, T Leweke, D. J. Asselin, and D. M. Harris. Phenomena, dynamics and instabilities of vortex pairs. *Fluid Dynamics Research*, 46:1–23, 2014.

K. Wöckner-Kluwe. *Evaluation of the Unsteady Propeller Performance behind Ships in Waves*. PhD thesis, Hamburg University of Technology, Hamburg, Germany, 2013.

J.-Z. Wu, H.-Y. Ma, and M.-D. Zhou. *Vortical Flows*. Springer, Berlin, Germany, 2015.

S. Yakubov, B. Cankurt, T. Maquil, P. Schiller, M. Abdel-Maksoud, and T. Rung. Euler–Euler and Euler–Lagrange Approaches to Cavitation Modelling in Marine Applications. In *Fourth International Conference on Computational Methods in Marine Engineering – MARINE 2011*, Hamburg, Germany, 2011.

I. Zawadzki, D. Fuhs, and J. Gorski. Integration of a Viscous Flow RANS Solver with an Unsteady Propulsor Force Code. Technical report, Caderock Division, Naval Surface Warfare Center, Maryland, USA, 1997.

O. Zeman. The persistence of trailing vortices: A modeling study. *Physics of Fluids*, 7(1):135–143, 1995.